PROTEIN ADSORPTION CONTROLLED BY MULTIVALENT IONS

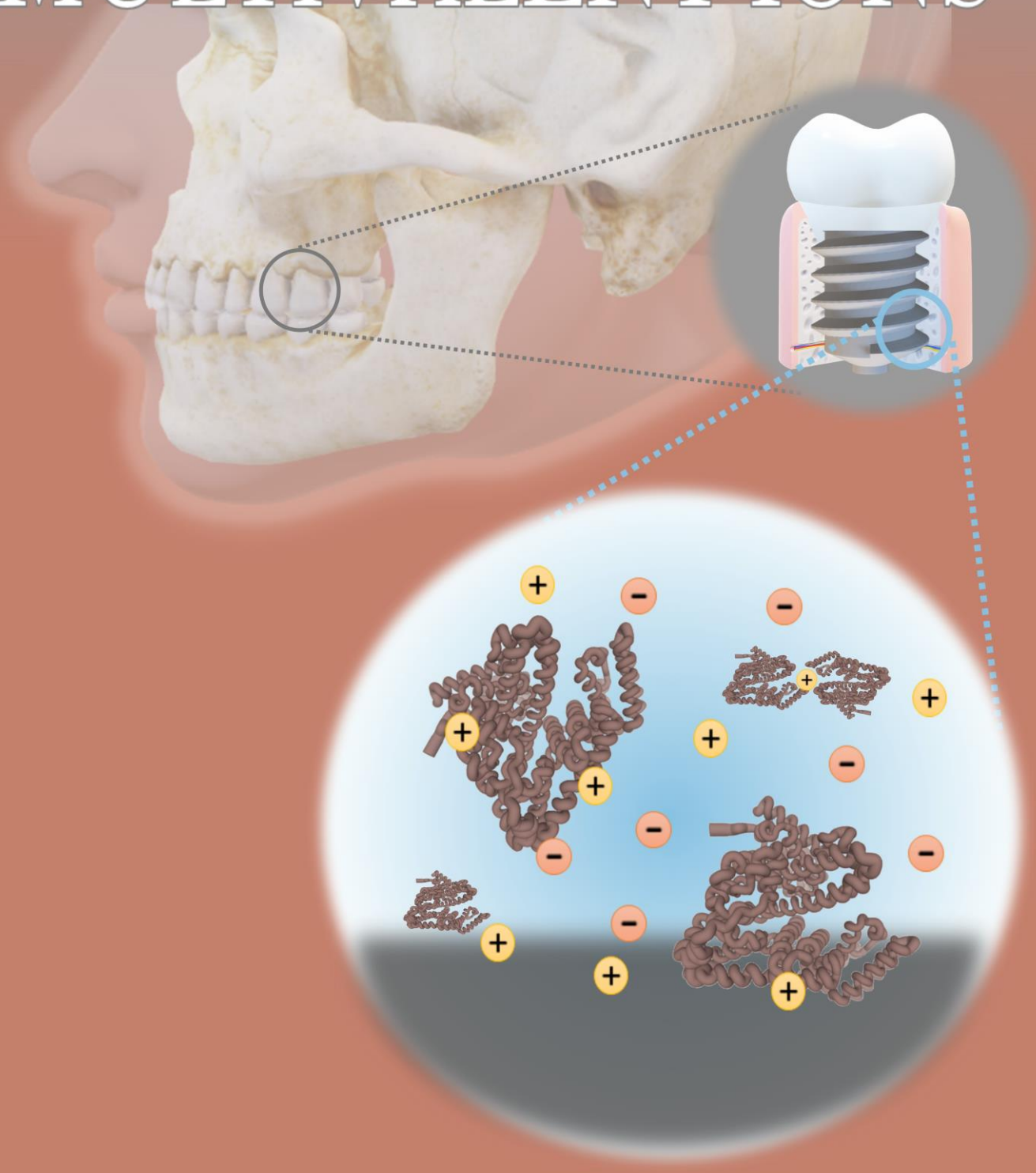

Madeleine R. Fries

Protein adsorption controlled by multivalent ions

Dissertation

der Mathematisch-Naturwissenschaftlichen Fakultät

der Eberhard Karls Universität Tübingen

zur Erlangung des Grades eines

Doktors der Naturwissenschaften

(Dr. rer. nat.)

vorgelegt von

Madeleine R. Fries

aus Freiburg

Tübingen

2020

Gedruckt mit Genehmigung der Mathematisch-Naturwissenschaftlichen Fakultät der Eberhard Karls Universität Tübingen.

Tag der mündlichen Qualifikation:	05.03.2021
Stellvertretender Dekan:	Prof. Dr. József Fortágh
1. Berichterstatter:	Prof. Dr. Frank Schreiber
2. Berichterstatter:	Prof. Dr. Marcus Scheele
3. Berichterstatter:	Prof. Dr. Oliver Bäumchen

Für meine Familie.

The cover is based on the supplementary cover of the Langmuir Journal (volume 37, issue 1) published on the January 12, 2021.

CONTENTS

Abstract

Proteins are a substantial, and integral matter for life on earth since they are required, e.g. to transport nutrients, to regulate body functions, and to form the building blocks of muscles, skin, and hair. Depending on their structure and function, proteins can be divided into four groups: fibrous, globular, disordered, and membrane proteins. Globular proteins are water-soluble, spherical proteins and can show a rich phase behaviour featuring aggregation, liquid-liquid phase separation (LLPS), re-entrant condensation, and crystallisation in the presence of multivalent salts. Consequently, the dominant interactions are electrostatic forces. The knowledge about the driving force of the bulk phase behaviour is crucial to guide and manipulate the phase behaviour since certain aggregations are desired, whereas for example the formation of amyloid fibrils contribute to diseases such as Alzheimer.

In this dissertation, the rich phase diagram of globular proteins with multivalent salt is utilised to investigate protein adsorption. Protein adsorption, meaning the accumulation or aggregation of proteins at a solid interface, occurs in numerous areas from medicine to food processing. Especially in the context of biomaterials, protein adsorption can be both an advantage and disadvantage since it facilitates biocompatibility, but can also induce a foreign body response, which leads to the rejection of an implant. While the general functions of proteins are well understood, less is known about underlying dominant molecular interactions which drive protein adsorption. The aim of this dissertation is to shed light on the dominant interactions driving and parameters influencing the adsorption behaviour such as protein type, cation and anion type, solvent, temperature, and surface properties. The main findings are summarised in the subsequent paragraphs.

In the first results chapter, the correlation between bulk phase behaviour and protein adsorption at a net negatively charged surface as a function of the salt concentration is established. Re-entrant adsorption at the interface is observed, which reflects the bulk re-entrant condensation behaviour in an intriguing way measured by a reduced second virial coefficient (measure for dominant bulk interactions). The experimental findings can be described by the multivalent-ion-activated patchy particle model within the framework of classical density functional theory, which reduces the adsorption trend found to dominant electrostatic interactions between proteins and with the surface.

In the second part, the effects of temperature and protein concentration on the protein adsorption are investigated, which induce simple adsorption or (diverging) wetting layer formation upon approaching bulk phase separation. Approaching LLPS increases attractive short-ranged interactions in the system facilitating the onset of a wetting transition. Through variations in protein concentration and temperature, LLPS formation can be promoted or prevented in the bulk solution. The wetting layer contains significantly

more water trapped within the (protein) layer compared to a simple adsorption layer illustrating different layer morphologies between an adsorption and wetting layer. The experimental findings are in good agreement with the theoretical descriptions of ion-activated attractive patches experiencing an attractive wall potential within the framework of classical density functional theory.

In the third part, the role of anions and cations on bovine serum albumin (BSA) in the bulk and at the interface are investigated. The bulk phase behaviour not only depends on the cation type used, but also on the anion type, which leads to different phase behaviours for different salts. Chloride is found to be 'neutral' in the sense that it neither affects the bulk nor interface behaviour of proteins, whereas for weakly hydrated anions (iodide salts), the established ion-activated patchy model is not valid since it neglects anion interactions. These anion interactions are assumed to consist of an interplay of electrostatic and hydrophobic interactions due to the different BSA binding sites for iodide. The phase transitions at the interface can also be induced by specific interface properties, whether these behaviours are reflected in bulk or not (i.e. bulk-independent adsorption), which emphasises the interplay of the substrate and bulk properties relating to protein adsorption.

In the fourth part, the influence of anion type and solvents (includes different isotopes) on β-lactoglobulin (BLG) in the bulk and at the interface are investigated. The bulk and interface behaviour of BLG is not influenced by the anion used due to BLG's weak affinity to anions and its preference for cation binding. In addition, BLG does not show an isotope effect. This could be explained with its predominant β-sheet structure, in which isotope substitution does not occur. At the interface, a much denser packing of the adsorption layer for BLG compared to BSA is found, which could explain why BLG crystallises and BSA does not.

In the fifth part, preliminary results on surface modifications and their influence on protein adsorption are discussed. The parameters investigated include the surface charge, roughness (topography), and hydrophobicity, as well as substrates with implant coatings and protein-repellent properties and should be viewed as an outlook and starting point for future endeavours.

A striking comparison between the bulk and interface behaviours of BLG and BSA is drawn in the conclusions summarising previous and current findings to explain the system behind protein adsorption and its underlying mechanisms. The knowledge of the mechanisms behind protein adsorption allows the targeted manipulation of parameters influencing protein adsorption such as temperature, salt type and concentration, and surface properties. This presents new prospects in the investigation of protein crystallisation through controlled nucleation at interfaces, which is particularly of relevance in the fields of pharmacology and biomaterials.

DEUTSCHE ZUSAMMENFASSUNG

Proteine sind ein substanzieller und integraler Bestandteil für Leben auf der Welt. Sie werden unter anderem benötigt, um Nährstoffe zu transportieren, Körperfunktionen zu steuern und Grundbausteine für Muskeln, Haare und Haut zu formen. Je nach Struktur und Funktion können Proteine in vier Gruppen unterteilt werden: Faserförmige, kugelförmige, ungeordnete und Membranproteine. Kugelförmige Proteine sind wasserlöslich. Sie zeigen in Gegenwart von mehrfach geladenen Ionen ein komplexes Phasenverhalten, welches Aggregation, Flüssig-Flüssig-Phasentrennung (FFPT), "re-entrant condensation" (durch erhöhte Salzkonzentration induziertes Auflösen der kondensierten Phase), und Kristallisation aufweisen kann. Folglich sind die dominanten Wechselwirkungen elektrostatischer Natur. Das Verständnis über die treibende Kraft des Phasenverhaltens der Proteine in Lösung ist wichtig für dessen gezielte Steuerung und Manipulation. Hierbei können bestimmte Aggregationen erwünscht sein, wohingegen beispielsweise die Bildung von Amyloidfibrillen zu Krankheiten wie Alzheimer beitragen kann.

In dieser Dissertation wird von dem komplexen Phasendiagramm von kugelförmigen Proteinen mit mehrfach geladenen Salzen Gebrauch gemacht, um Proteinadsorption zu untersuchen. Proteinadsorption, im Sinne von Akkumulation and Aggregation von Proteinen an einer festen Oberfläche, tritt in vielen Bereichen von Medizin bis hin zur Lebensmittelindustrie auf. Besonders im Bereich der Biomaterialien kann Proteinadsorption Vor- und Nachteil zugleich sein, da es einerseits die Biokompatibilität ermöglicht, zum anderen jedoch auch die Fremdkörperantwort einleiten kann, die zur Abstoßung des Implantats führt. Während die allgemeinen Funktionen von Proteinen gut verstanden sind, ist wesentlich weniger über die zugrundeliegenden dominanten molekularen Wechselwirkungen bekannt, welche Proteinadsorption steuern. Das Ziel dieser Dissertation ist Aufschluss über die dominanten Wechselwirkungen und Parameter, welche das Adsorptionsverhalten beeinflussen, zu geben. Dazu gehören unter anderem der Proteintyp, der Anionen- und Kationentyp, das Lösungsmittel, die Temperatur und die Substrateigenschaften. Die Hauptergebnisse werden im Folgenden zusammengefasst.

Im ersten Ergebnisteil dieser Arbeit wird der Zusammenhang zwischen dem Phasenverhalten in Lösung und Proteinadsorption an einer netto negativ geladenen Oberfläche in Abhängigkeit von der Salzkonzentration hergestellt. "Re-entrant adsorption" (ein nicht-monotoner Anstieg der Adsorption) an der Oberfläche wird beobachtet, welche das "re-entrant condensation"-Verhalten in der Lösung wiederspiegelt und durch Messungen des reduzierten zweiten Virialkoeffizienten (Maß der dominanten Wechselwirkungen in Lösung) bestimmt wurde. Die experimentellen Erkenntnisse können im Rahmen der Dichtefunktionaltheorie mit einem durch mehrfach geladene

Ionen aktiviertem Teilchenmodell (engl. *multivalent-ion-activated attractive patchy particle adsorption model*) beschrieben werden. Dieses Modell reduziert das beobachtete Adsorptionsverhalten auf dominante elektrostatische Wechselwirkungen zwischen den Proteinen untereinander und mit dem Substrat.

Im zweiten Teil wird der Effekt von Temperatur und Proteinkonzentration auf den Proteinadsorptionsprozess untersucht. Diese können entweder einfache Adsorption oder die Bildung einer Benetzungsschicht (engl. *wetting layer*) bei Annäherung an den Bereich der Phasentrennung induzieren. Bei Annäherung an den FFPT-Bereich steigen die attraktiven kurzreichweitigen Wechselwirkungen in dem System, welche die Entstehung eines Benetzungsübergangs ermöglichen. Durch die Variation der Proteinkonzentration und Temperatur kann die FFPT-Bildung in der Lösung begünstigt oder verhindert werden. Die Morphologien der Adsorptions- und Benetzungsschicht unterscheiden sich voneinander. Die Benetzungsschicht hat signifikant mehr Wasser in sich gebunden im Vergleich zu der Adsorptionsschicht. Die experimentellen Ergebnisse sind in guter Übereinstimmung mit der theoretischen Beschreibung des Systems durch mehrfach geladene Ionen aktivierten Bereiche, welche einem attraktiven Wandpotential ausgesetzt sind.

Im dritten Teil wird die Rolle des Anionentyps und Kationentyps auf Rinderserumalbumin (BSA) in Lösung und an Oberflächen untersucht. Das Phasenverhalten in Lösung hängt hierbei nicht nur von dem verwendeten Kationentyp ab, sondern auch von dem Anionentyp, welcher zu unterschiedlichem Phasenverhalten bei Verwendung von verschiedenen Salzen führt. Für Chlorid wurde ein neutrales Verhalten beobachtet im Sinne, dass es weder das Verhalten in Lösung noch an der Oberfläche beeinflusst. Für schwach hydrierte Anionen (wie z.B. Jodidsalze), hingegen kann das eingeführte, durch mehrfach geladene Ionen aktivierte Teilchenmodell nicht angewandt werden, da es keine Wechselwirkungen mit Anionen berücksichtigt. Diese Anionenwechselwirkungen bestehen vermutlich aus einem Wechselspiel von elektrostatischen und hydrophoben Wechselwirkungen verursacht durch die unterschiedlichen Bindestellen von Jodid an BSA. Die Phasenübergänge an der Oberfläche können durch spezifische Substrateigenschaften ausgelöst werden, egal ob sich das Verhalten in Lösung widerspiegelt oder nicht. Dies betont das Wechselspiel der Eigenschaften des Substrats und der Lösung in Bezug auf Proteinadsorption.

Im vierten Teil wird der Einfluss des Anionentyps und des Lösungsmittels (beinhaltet verschiedene Isotope) auf β-Lactoglobulin (BLG) in Lösung und an Oberflächen untersucht. Weder das Verhalten von BLG in Lösung noch an der Oberfläche, wird durch die verwendeten Anionen beeinflusst. BLG bevorzugt die Bindung von Kationen und hat nur eine geringe Affinität zu Anionen. Zudem zeigt BLG keinen Isotopeneffekt. Dies kann mithilfe der dominierenden β-Faltblattstruktur von BLG erklärt werden, da in dieser kein Isotopenaustausch stattfindet. An der Oberfläche bildet BLG eine wesentlich dichter gepackte Adsorptionsschicht im Vergleich zu BSA. Dies könnte erklären, warum BLG kristallisiert, wohingegen BSA das nicht macht.

Der fünfte Teil widmet sich vorläufigen Ergebnissen von Oberflächenmodifikationen und deren Einfluss auf Proteinadsorption. Die untersuchten Parameter beinhalten Oberflächenladung, Topografie (Rauigkeit), und Hydrophobie, sowie Substrate mit Implantatbeschichtungen und proteinabweisende Oberflächen. Dieser Teil sollte als Ausblick und Anknüpfungspunkt für zukünftige Untersuchungen betrachtet werden.

In diesem Zusammenhang wird ein eindrucksvoller Vergleich zwischen dem Phasen- und Oberflächenverhalten von BSA und BLG im Diskussionskapitel gezogen, welcher bisherige und aktuelle Erkenntnisse zusammenfasst, um das System und die zugrundeliegenden Mechanismen hinter Proteinadsorption zu erklären. Die Kenntnis von den zugrundeliegenden Mechanismen in Proteinadsorption ermöglicht dessen gezielte Manipulation durch beeinflussende Parameter wie zum Beispiel Temperatur, Salztyp und -konzentration, und Oberflächeneigenschaften. Dies eröffnet neue Möglichkeiten der Untersuchung von Proteinkristallisation durch kontrollierte Nukleation an Oberflächen, was von besonderer Relevanz in Bereichen der Pharmazie und Biomaterialien ist.

I. FUNDAMENTALS

1 Introduction

What do milk production, antiarthritic drugs, and surgical instruments have in common? In all these applications, proteins play an important role, more specifically, the process of protein adsorption. In the past decades, this topic was under investigation in numerous research fields ranging from biology to medicine to material science [1]. In the following, a brief overview of accomplishments and applications is given, which should further motivate this topic and emphasise its relevance.

In food processing, proteins can form emulsions, foams or food colloids [2–4]. Those can be used for protein-based microparticulation to facilitate texture modification in low-fat yoghurt or as fat replacers in ice cream or cheese [5–7]. For healthy balanced diets in non-fat foods and clear beverages, milk protein-based nanovesicles allow nanoencapsulation of hydrophobic nutraceuticals, which are otherwise unstable in solution [8]. Furthermore, edible whey protein coatings are found to improve the storage life of groceries such as sunflower oil, peanuts, fruits and vegetables by providing an oxygen barrier [9–11]. Nevertheless, unwanted reactions and by-products can be induced through protein fouling [2,12] on containers in the production chain. A special case is membrane fouling [13,14], which occurs often in beverages and cheese manufacturing [15], when ultrafiltration is an essential step in its production. Contamination through bacteria, fungi etc. must be prevented. Thus, a sanitary and sterile production of food must be achieved [16], e.g. through stabilisers such as ionic surfactants forming complexes with protein, and thus, lowering protein adsorption on surfaces [17].

Roughly 16 % of the human body is composed of proteins [18,19], which facilitate essential body functions and come with a wide range of properties. Subsequently, proteins (in their crystalline form) are crucial for drug production, either to treat the deficits of the body's own protein or suppress the body's immune response to a drug [20–22]. In pharmacology, bovine serum albumin (BSA) is added to anticancer drugs in pH (lat. *potentia hydrogenii*) -responsive release systems [23] to improve the water solubility and provide reactive sites for multivalent coupling of bioactive molecules [24–26]. BSA is also used as a carrier for multiple drugs such as antiarthritic drugs [27] or in the treatment of drug overdoses through the use of albumin-containing dialysates to allow extracorporeal removal of endogenous toxins [28,29].

In tissue engineering [30], proteins can be incorporated into the scaffolds via electrospinning [31] facilitating controlled drug delivery and release of bioactive agents, such as BSA, to produce bio-functional tissue scaffolds [32–37]. Even protein-based tissue adhesives (BSA-glutaraldehyde/'Bioglue') have been developed, which find application in cardiovascular surgery for, e.g., haemostasis [38–40]. Successful cell adhesion on biomaterials depends on the combination of different proteins adsorbing to the interface

[41]. Serum albumin is the fastest protein to adsorb on any solid surface [42] (**Figure 1.1**) and can prevent the adhesion of platelets, thus forming a hemocompatible surface, whereas fibrinogen adsorption initiates blood coagulation [43,44].

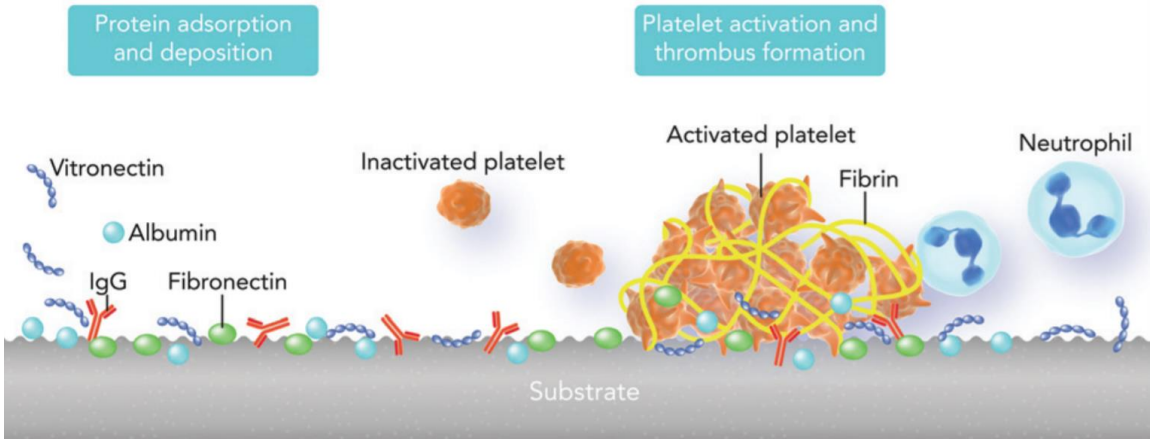

***Figure 1.1**: The foreign body response to a biomaterial. The initial interaction of the substrate is primarily with proteins and depends on the implant's surface properties. After successful protein adsorption, different reactions can be initiated depending on the specific protein adsorbed, e.g. platelet adhesion through fibronectin binding, which is followed by platelet activation for fibrous encapsulation (wound healing). From Ref.* [45].

Depending on the function of the implant, specific protein adsorption is desired or undesired. For all implants, such as bypass, heart valves, or stents, blood clotting must be prevented by suppressing the binding of fibrinogen, while maintaining hemocompatibility [46–48]. This can be achieved either by precoating of albumin for arterial protheses, thus diminishing coagulation activation [49,50] and improving blood compatibility [51,52] or through protein-resistant surfaces [53]. In contact lenses (hydrogels), protein adsorption to the lens prevents the initiation of the foreign body response (**Figure 1.1**) [54], but also induces the risk of allergic reactions [55]. Hence, body's own proteins can also be toxic by-products influencing cell viability and function e.g. in 3D organ/tissue printing [56].

Biocompatibility and osseointegration are two important properties of prosthetics and artificial joints. These favour protein adsorption, but could also facilitate unfavourable interactions with bacteria etc. that could lead to apoptosis or biofilm formation, and thus, infections [57]. Here, the understanding of protein adsorption is essential to produce blood-compatible surfaces [58] on the one hand, but prevent inflammatory response of the body [59] on the other. UV-light treatment of dental implants is one method to destroy formed biofilms on the surface, while improving albumin adsorption and osteoblast attachment. It was found that specific surface properties can tune and control protein adsorption. A hydrophilic surface is better for the hemocompatibility [60,61]. Negatively charged surface sites induce protein adsorption and platelets adhesion [60,62], as well as, activate other blood plasma proteolytic systems such as leukocyte adhesion, blood coagulation, fibrinolysis, and thrombus formation [63–65]. In addition to surface properties, bulk properties can also stimulate adsorption. Ions present in the body fluids can mineralise on the surface of bioglass implants and stimulate osteoblast adhesion,

differentiation, and bone growth [66]. In hydrogels, protein patterning [67] allows the development of artificial cytoskeletal or extracellular matrix mimics, which can be regulated by the concentration of crosslinking proteins or divalent cations [68].

The above paragraphs illustrate how complex protein adsorption is and how it depends on numerous different parameters such as protein charge, polarity, protein shape, as well as temperature, ionic strength, and substrate properties. So far, protein adsorption to non-biological substrates is well investigated [1,42,69–75]. Yet not much research is conducted on the influence of multivalent ions on protein adsorption at the solid-liquid interface [76,77], which induce complex protein phase transitions (e.g. liquid-liquid phase separation (LLPS), re-entrant condensation (RC), crystallisation) [78–80], and thus, allow the tailoring of interactions in a controlled manner. The broadness and variety in the occurrence of protein adsorption, as well as the complexity, and diversity of its structure, demand the search for universal mechanisms on a molecular level, and thus, facilitate a potent research topic. Its relevance makes it always current.

On these grounds, this dissertation focuses on understanding effects underlying the protein adsorption behaviour, its correlation with the bulk protein phase behaviour, as well as interactions dominating and parameters tuning protein adsorption such as temperature, (multivalent) salt, solvent, and surface properties. Fundamental differences in phase and adsorption behaviour are found depending on protein type, salt type, and substrate type, and thus, the driving force and underlying physical properties are understood, which guide protein adsorption and bulk phase behaviour, thus enabling the control, prediction and manipulation of protein adsorption and adsorption phenomena. In Chapter 2, intra- and intermolecular interactions are introduced that contribute to protein adsorption such as protein-protein, protein-salt and protein-interface interactions, which are defined by the properties of the proteins and interface, as well as external parameters such as salt concentration and temperature. This chapter serves as a background on the topic of protein adsorption and outlines past research. The above mentioned examples highlight two globular proteins, bovine serum albumin (BSA) [81] and β-lactoglobulin (BLG) [82], which are the most abundant proteins in blood and in milk, respectively, and the main proteins used in this dissertation. In Chapter 3, these proteins, as well as the salts and substrates used are described and their preparation explained. Complementary methods such as ellipsometry, quartz-crystal microbalance with dissipation monitoring (QCM-D), neutron reflectivity (NR), ultraviolet-visible spectroscopy (UV-Vis), and infrared spectroscopy (ATR-FTIR) are used to determine the thickness, density, viscosity, hydration, and structure of the adsorbed protein layer, which are explained in Chapter 4 in combination with further experimental methods. These chapters sum up and highlight the fundamentals needed to understand the results presented in Chapters 5 to Chapter 9 of this dissertation. The result sections are divided by topic and focus on different aspect and properties, which guide and define protein adsorption.

In the first result chapter, the correlation between bulk and adsorption behaviour is established, which is supported by a theoretical patchy particle model (Chapter 5).

In the second part, bulk-instability-induced wetting transition is theoretically and experimentally explained (Chapter 6). In the third part, anion- and cation-induced BSA bulk and adsorption behaviour are established (Chapter 7). In the fourth part, the role of anions and isotopes on BLG bulk and interface behaviour is investigated (Chapter 8). In the last result chapter, different surface properties generated by metal coatings, self-assembled monolayer (SAM) coatings, and electrochemical manipulation of the substrate are tested and their effect on protein adsorption (Chapter 9). Chapter 10 provides a comparison between BSA and BLG, which summarises essential differences and similarities between the two proteins and the main findings of this dissertation. In Chapter 11, an outlook is given discussing open questions and their implications for future research.

2 Background

In this chapter, the fundamentals, theories, and concepts related to protein adsorption are introduced. The determination of the adsorption properties of a protein on a substrate is only possible if the interaction of the components of the systems are known (**Figure 2.1**). Subsequently, the chapter is organised according to interaction groups such as protein-protein, protein-salt, and protein-interface interactions. Hence, intra-, and intermolecular interactions of proteins have to be considered, as well as their interactions with the solvent and substrate. Natural occurring forces in and between proteins and their environment (i.e. hydrogen bonds, van der Waals, hydrophobic and electrostatic interactions) are explained, as well as the artificial manipulation of these forces through variations in internal (i.e. within the system) and external parameters such as pH, pressure, temperature, or salt (**Figure 2.1**). In the last section, theoretical descriptions of proteins and protein adsorption are introduced based on these concepts.

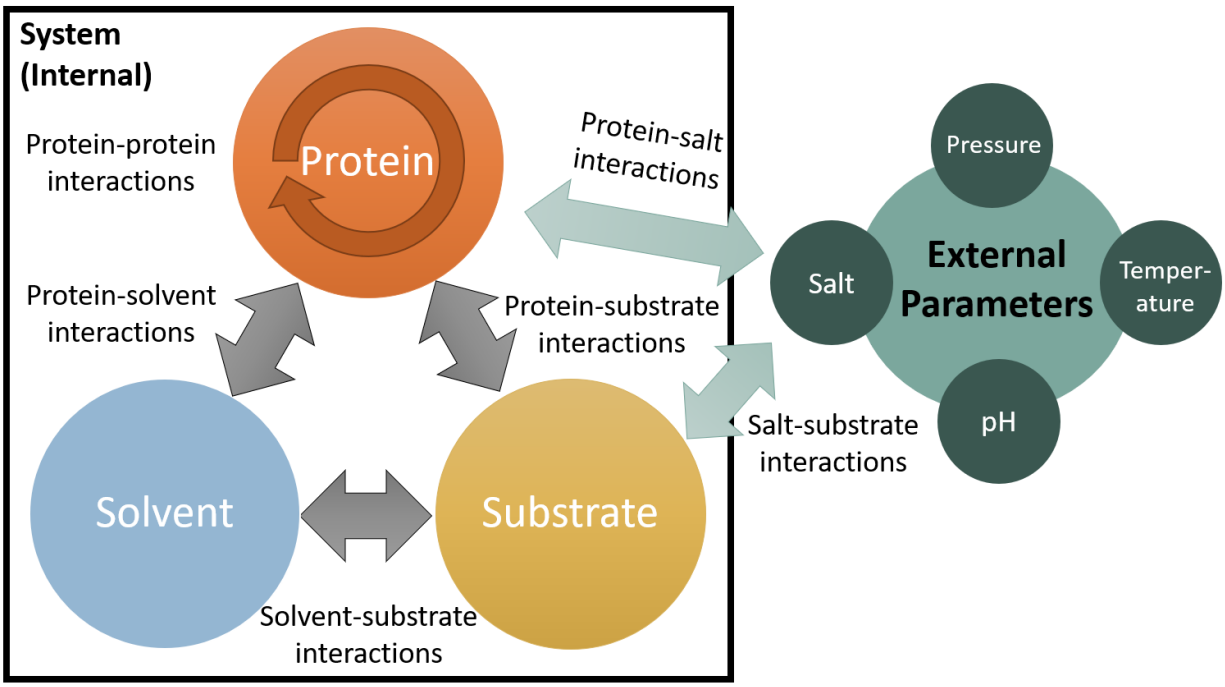

Figure 2.1: Protein adsorption depends on numerous interaction forces introduced by the different components. The setup with the least components consists of one type of protein in a solvent adsorbing onto an interface. These three components induce different interactions within a system and depend on external parameters e.g. salt, pH, pressure, and temperature.

2.1 Intramolecular Interactions in Proteins

Interactions in and between molecules can be organised in different groups, i.e., attractive/repulsive, or intramolecular/intermolecular forces. Here, the structure and interaction forces within a protein are discussed leading to its spatial structure.

Proteins have a highly complex structure, which can be rationalised in four complexity levels: the primary structure, the secondary structure, the tertiary structure, and the quaternary structure [83]. The primary structure is the sequence of amino acids connected through peptide bonds (i.e. covalent bonds). Covalent bonds describe intramolecular forces (within the molecule) meaning amino acids are chemically bond and share an electron pair [84].

The secondary structure is constructed by hydrogen bonds, which can lead to α-helix and β-sheet formations of the amino acid sequence (**Figure 2.2**). Hydrogen bonds are formed between a hydrogen and an electronegative atom such as oxygen, sulphur or nitrogen. These hydrogen bonds can either be within one protein (intramolecular interactions or also interact with the solvent e.g. water and thus induce solvent-protein interactions (**Figure 2.2**). Hydrogen bonds in general are found to increase thermal stability within proteins [85].

The tertiary structure leads to the spatial form of the protein with different types of contributing forces. These forces are disulphide bonds, which are a form of covalent bonds and link sulfhydryl groups (-SH) (**Figure 2.2**). Another attractive force is hydrophobic interactions experienced by non-polar atoms/groups, which do not mix well with water [86]. Thus, they form hydrophobic patches within the protein to exclude water also known as 'burying' of non-polar groups (**Figure 2.2**).

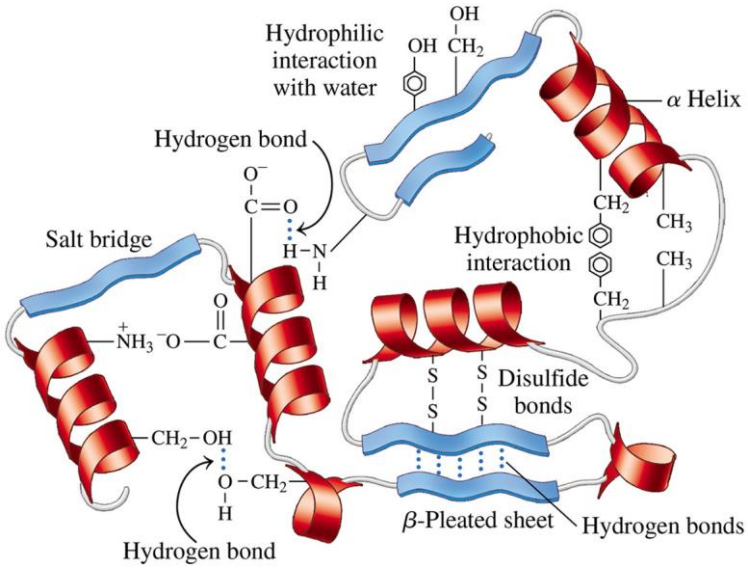

Figure 2.2: Molecular forces leading to the 3D structure of protein with hydrogen bonds forming the secondary structure and disulphide bonds, hydrophobic interactions, and electrostatic (salt bridges) interactions contributing to the tertiary structure. From Ref. [87].

Without hydrophobic interactions counterbalancing the hydrophilic interactions within the protein and its solvent, the protein would unfold. Thus, a combination of hydrogen and hydrophobic interactions is needed for a stable, globular protein structure [88]. In the presence of charges, Coulomb interactions, also known as electrostatic forces, are induced as an attractive force between two oppositely charged atoms/ions illustrated as a salt bridge in **Figure 2.2** [89]. Those can also be repulsive if the amino acid residues carry the same charge.

Forces, which are not depict in the sketch, but also contribute to the tertiary protein structure are e.g. van der Waals (vdW) interactions. The vdW forces define the interactions between dipoles. One type of vdW force is dispersion, which describes the attractive force between two molecules due to temporarily induced dipole moments through fluctuating charge distributions [90]. Dispersion forces are found to enhance the thermal stability of helical structures within a protein [91]. Other types of vdW interactions are Keesom force between dipole and dipole and Debye interactions between dipole and induced dipole [92]. The closest distance between overlapping non-binding amino acid branches is defined by steric repulsion, which describes a repulsive force between overlapping electron clouds. The driving force behind all other interaction forces could be argued to be entropic interactions [93]. All molecules try to increase their entropy since this is energetically favoured and maximises their accessible configurations. Side-chain entropy in native proteins is found to increase thermostability [94], but also account for the distribution of side chains on the protein surface and rationalise α-helix propensities [95], while conformational entropy regulates protein binding activity [96].

***Table 2.1**: Typical noncovalent interactions and their energy dependence on distance. There are different types of van der Waals interactions: dipole-induced dipole (Debye force), dipole-dipole (Keesom force), two induced dipoles (dispersion). r: distance of interactions. From Ref.* [97].

Noncovalent interaction		Energy dependence on distance
Charge–charge	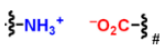	1/r
Charge–dipole	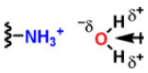	$1/r^2$
Dipole–dipole	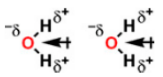	$1/r^3$
Charge-induced dipole	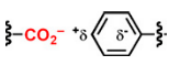	$1/r^4$
Dipole-induced dipole	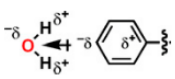	$1/r^5$
Dispersion	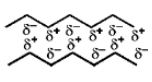	$1/r^6$
H-bond	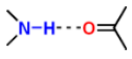	Complicated ~$1/r^2$
Steric repulsion	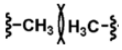	$1/r^{12}$

If a protein consists of multiple subunits, which is not applicable to all proteins, its spatial arrangement is described by the quaternary structure and depends on the above-mentioned interactions, e.g. hydrogen bonds, vdW and electrostatic interactions [90]. A prominent example is haemoglobin.

All these different interactions have different ranges (**Table 2.1**) and strengths with the weakest being steric repulsion and Debye interactions (2-10 kJ/mol). Thus, their contributions to the overall protein structure are not as strong and compete with e.g. hydrogen bonds (10-40 kJ/mol). Electrostatic interactions (400-4000 kJ/mol) are stronger than most covalent bonds (150-1100 kJ/mol) [89], hence have a crucial influence not only on the protein structure itself, but also on its interactions with other molecules. Consequently, the role of electrostatic interactions must be understood and is one focus of this dissertation. Through the use of multivalent ions, additional electrostatic interactions are induced to the systems investigated, which are further discussed in Chapter 2.3.

2.2 Protein-Protein Interactions

After introducing the relevant intramolecular interactions, the next complexity level is intermolecular interactions. Intermolecular interactions incorporate protein-solvent, protein-protein, protein-substrate interactions. In this section, the focus is on possible protein-protein interactions and their phase behaviour.

2.2.1 DLVO Theory

Considering all interactions within a protein that lead to its final globular structure, the solvent-exposed groups can be charged/uncharged, polar/non-polar, and hydrophilic/hydrophobic.

Depending on the protein surface and its dominant interactions, it interacts differently with other proteins in solution. The interaction potential $V(D_{pp})$ between two (charged) proteins can be described with the DLVO (Derjaguin-Landau-Verwey-Overbeek) theory (**Figure 2.3**) [98,99]. The classical DLVO theory only considers attractive vdW and repulsive electrostatic interactions between two charged particles and how these result in a net repulsive or attractive force depending on the protein-protein distance D_{pp} (**Figure 2.3**). This leads to either a fast approach or separation of the two proteins meaning the binding or repulsion of two molecules [86]. The DLVO theory can be used to estimate protein-protein interactions for appropriate systems, yet, it is important to bear in mind that the theory fails to account for further underlying competing interactions, such as hydrophobic, steric repulsion, entropic repulsion or depletion interactions and short-range, protein-specific processes e.g. lock-and-key, ligand-receptor mechanisms between proteins (**Figure 2.3**).

A parameter for the strength of the overall protein-protein interactions is the (osmotic) reduced second virial coefficient B_2/B_2^{HS} [100–103] obtained via small-angle X-ray scattering (SAXS) measurements (for more information see Chapter 4.3).

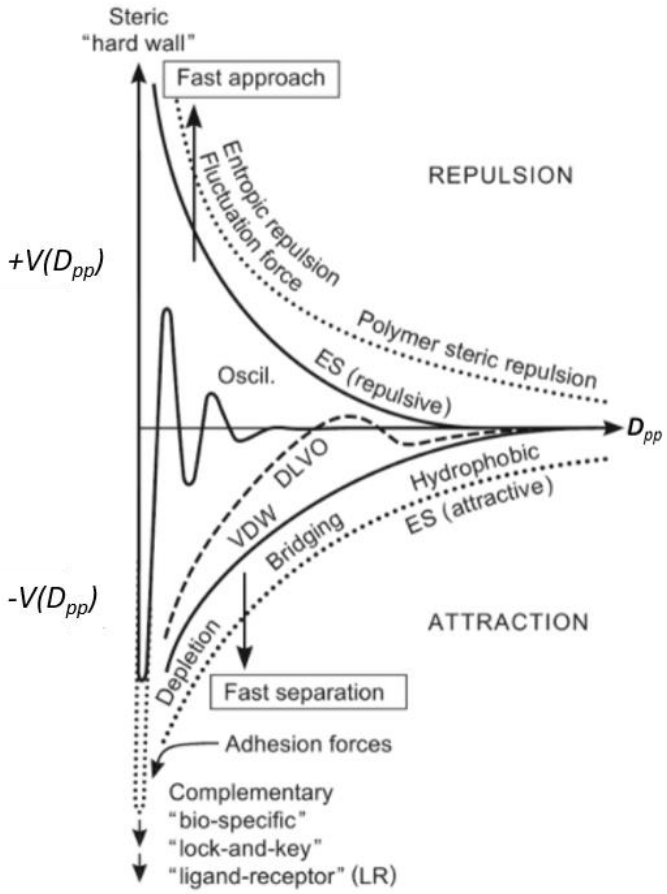

Figure 2.3: DLVO theory describing the interaction potential (dashed line) between two macromolecules with complex, interfering repulsive electrostatic and attractive vdW interactions (solid lines). Other contributing forces (dotted lines) such as depletion, hydrophobic interactions are also depicted in the plot, which are not considered in the DLVO theory. ES: electrostatic interactions. Oscil.: Oscillation based on solvation forces. Modified from Ref. [86].

2.2.2 Phase Diagram

Proteins give rise to a phase diagram, in which only two stable phases exist, i.e. gas and crystal, since short-range attractions dominate in the temperature-protein concentration plane (**Figure 2.4**) [104]. The phase diagram consists of four prominent phase boundaries: the solidus line, the solubility line, the liquid-liquid coexistence line (binodal), and the glass line [105]. The solidus and solubility lines define the temperature and protein concentration, above which only a solid crystal or gas phase occurs. In between these lines, a gas-crystal phase exists. The gas-crystal spinodal, in turn, confines a metastable region up to the solubility line, in which decomposition sets in for a coexistence of crystal and gas phase. Below the critical point, the total free energy of the system is minimised, if the system separates into two phases [106]. This leads to metastable liquid-liquid phase separation into a dilute and dense protein phase. The liquid-liquid binodal defines the area, below which phase separation is thermodynamically favourable and the system goes from a one-phase state to a two-phase state (**Figure 2.4**). Phase separation can occur in two ways either by nucleation or by spinodal decomposition. For nucleation (between the binodal and spinodal), the system needs an increase in free energy, which is not needed for spinodal

decomposition (below the spinodal) [106,107]. At sufficiently high volume fractions, a glass line may impose a slow-down of mobility, and thus creates an arrested state of the dense phase interrupting LLPS formation, which is described in literature as arrested spinodal decomposition [108–111]. In a more general approach, the phase diagram could also be expressed in terms of the second virial coefficient B_2 instead of temperature [101].

This phase diagram helps to understand the formation of protein aggregation, gels, and especially protein crystallisation. The presence of LLPS promotes a two-step nucleation pathway. Through the formation of small dense droplets, the formation of nuclei is supported [112,113]. In addition, the formation of the dense droplets can accelerate crystallisation due to the reduction of the free energy barrier near the critical point and below [114,115]. This two-step crystallisation deviates from the classical nucleation theory (CNT) through the formation of an intermediate phase before crystallisation [116,117]. For more information on the fundamentals of protein crystallisation see Refs. [113,118,119].

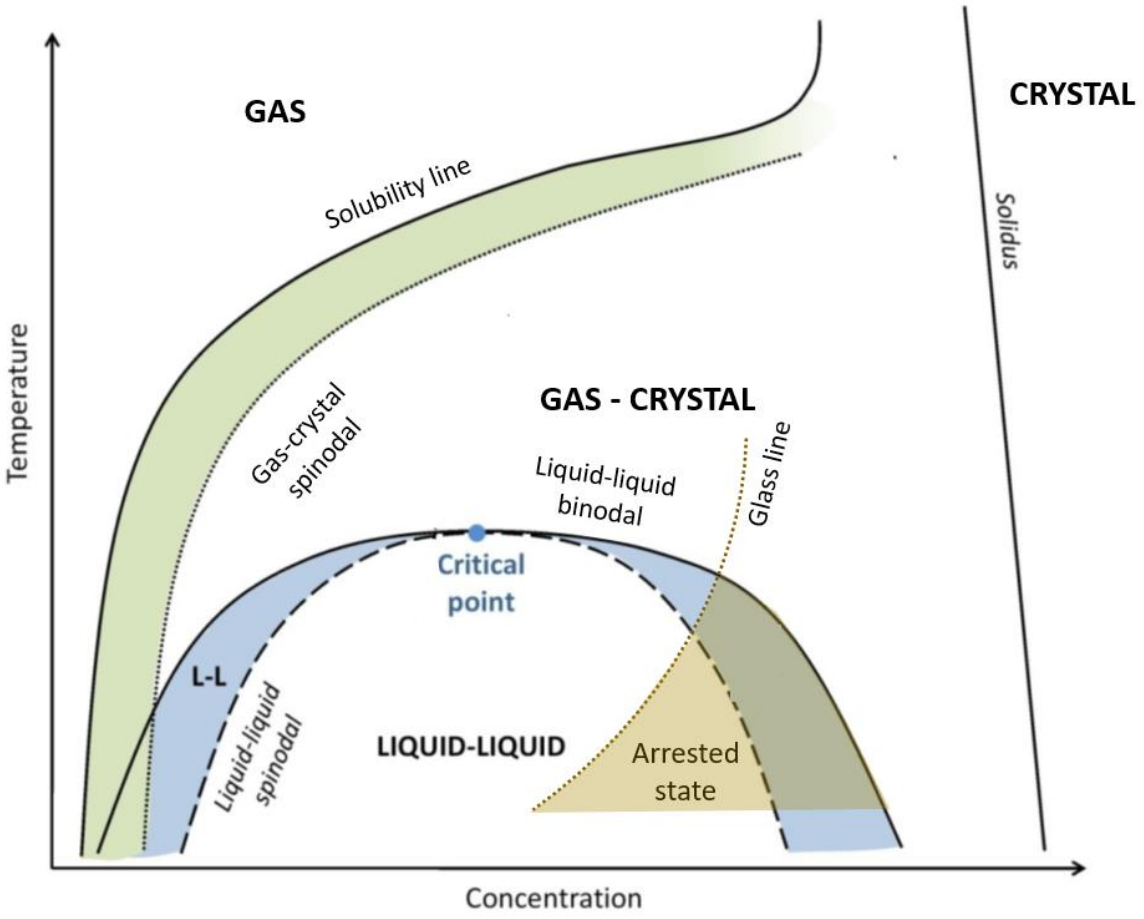

Figure 2.4: Protein phase diagram of the temperature plotted against the protein concentration. Due to dominating short-range attractive forces, only the crystal and gas phase are stable defined by the solidus and solubility line. Below the liquid-liquid binodal, the system forms two metastable liquid phases either by nucleation or spinodal decomposition. The phase separation pathway depends on its position between the binodal and spinodal or below the liquid-liquid spinodal, which can promote protein crystallisation. Below the glass line, the dense phase forms an arrested state. Modified from Ref. [120].

2.3 Protein-Salt Interactions

The protein-protein interactions established in the chapter above can be manipulated through e.g. the addition of salt. This is a precise tool to control and guide the dominant interactions in the protein system. According to the DLVO theory, the interaction potential between two charged proteins becomes more attractive by increasing the salt concentration in solution (from curve 1 to 5) in **Figure 2.5** [121]. Thus, the DLVO theory can be used and is successfully applied to predict pH and ionic strength trends of protein-protein interactions [102,122,123]. Nevertheless, the DLVO theory has its limitations. One major drawback is its use of the Poisson-Boltzmann theory, which simplifies salt ions to point charges and consequently, does not account for ion-ion interactions, non-electrostatic interactions (e.g. hydrophobic interactions), properties of the salt type used (e.g. valency), or inhomogeneity of charge distribution [123–125].

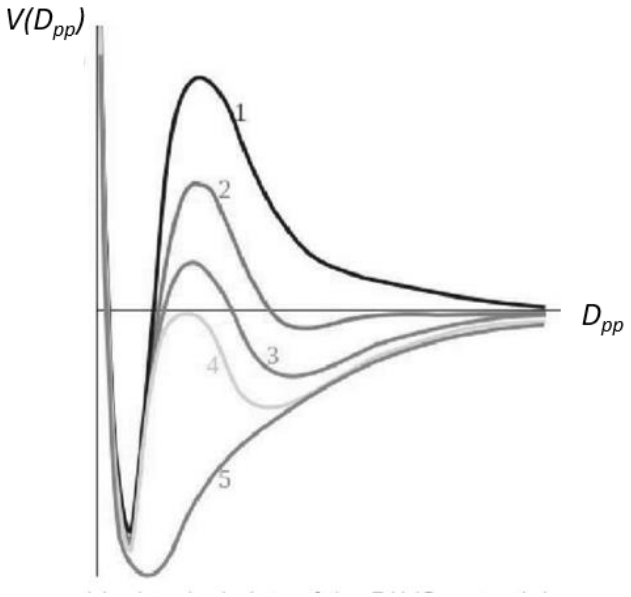

***Figure 2.5**: DLVO theory. Through the increasing addition of salt (1-5), the net interaction potential experienced between two proteins changes dramatically. Modified from Ref.* [121].

2.3.1 Hofmeister Series

Besides the DLVO theory, other theories and series are established describing ion-specific effects on globular proteins. The Hofmeister series, for example, is an empirical series ranking cations and anions according to their ability to 'salt-out' and 'salt-in' proteins (**Figure 2.6**) [126]. 'Salting-out' describes the formation of aggregates due to the addition of salt, which increases the protein stability, and surface tension of the protein, while decreasing the risk of denaturation (for denaturation see Chapter 2.6.1). 'Salting-in' describes the opposite ion-induced effect of solubilised proteins with decreased protein stability and increased risk of denaturation [127]. For the past century, numerous publications have looked into the behaviour of ions and proteins in relation to the Hofmeister series, yet not all agree on the same order of ions [128–136].

In **Figure 2.6**, the colour bars around some ions indicate the variations in ranking positions in different publications. Specific protein properties, protein/salt concentrations, or pH are found to invert the direct Hofmeister series partially or completely, known as the partially altered and reverse Hofmeister series for anions and cations (**Figure 2.7**) [137,138]. With these determining factors, the behaviour of ions with proteins can be well predicted and subsequently their phase behaviour.

2.3.2 Lyotropic Series

Another series, which sometimes can be used interchangeably with the Hofmeister series [139,140], but not exclusively is the lyotropic series [102,132,141]. The lyotropic series ranks ions according to their interactions with water (solvent-protein interactions) (**Figure 2.6**). Here, the terms kosmotropic and chaotropic are established. Kosmotropes are strongly hydrated ions with a structured water layer, thus are 'structure-markers' [86].

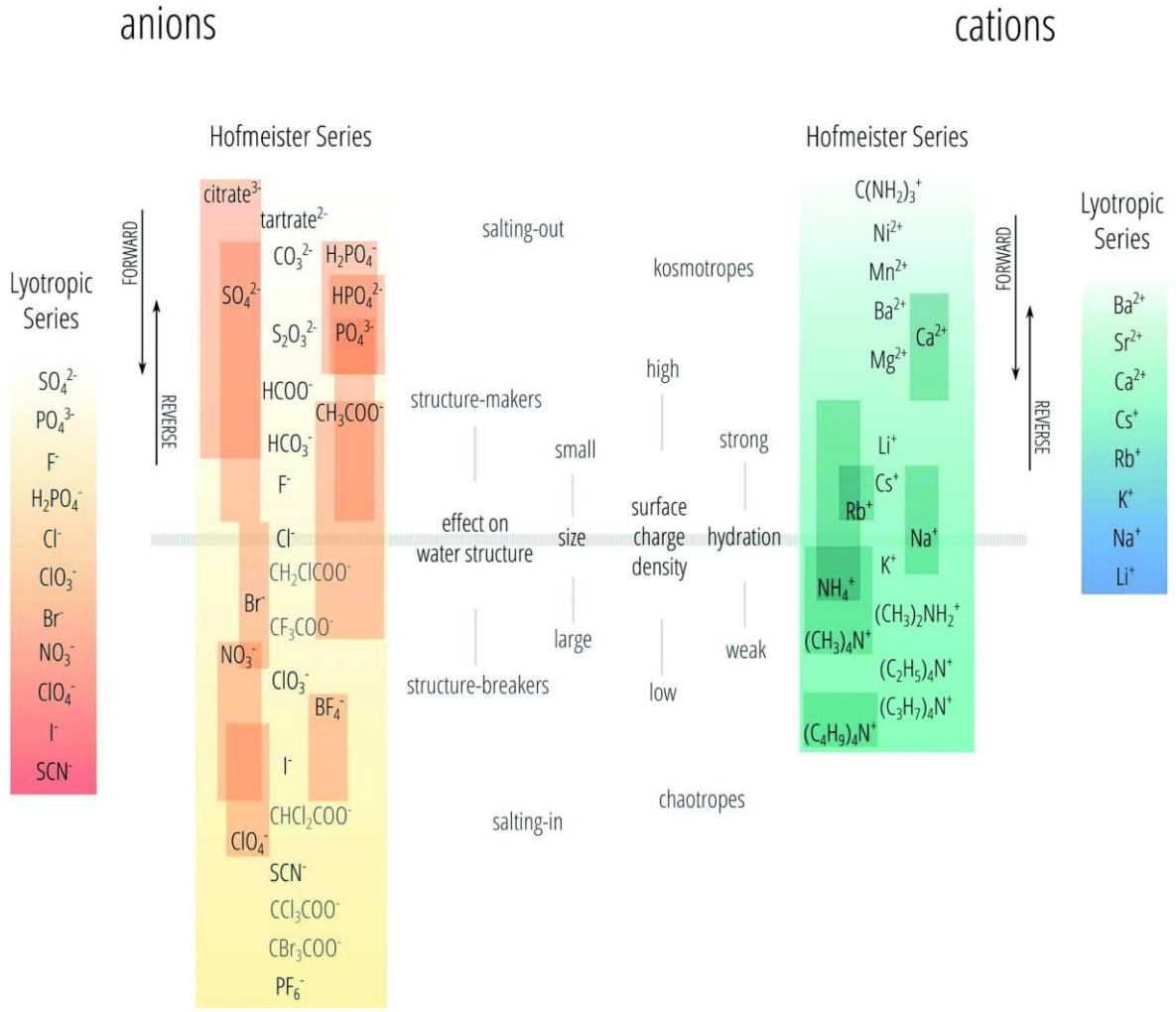

***Figure 2.6**: Hofmeister and lyotropic series. According to the Hofmeister series, ions can be ordered by their ability to 'salting-out' globular proteins. The lyotropic series organises cations and anions according to their interaction with water (kosmotropic/chaotropic). The colour bars around some anions or cations indicate an uncertainty about the accurate ranking position due to contradictory literature, as well as the grey-coloured haloacetates (anions) illustrate uncertainties of positioning compared to the traditional anions. From Ref.* [132].

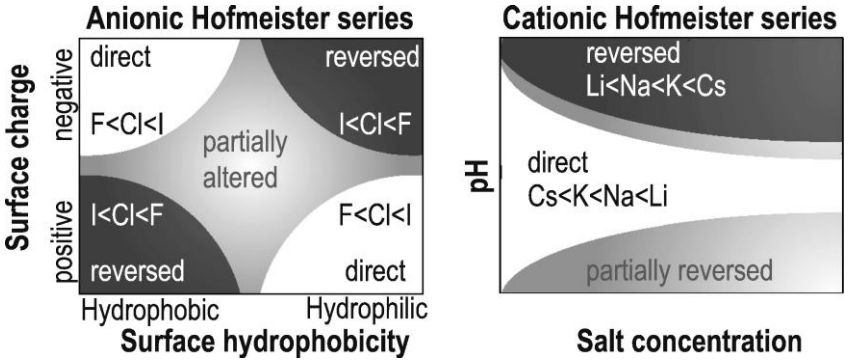

Figure 2.7: Depending on the surface hydrophobicity, surface charge and pH, the cation, and anion behaviour deviates from the classical direct Hofmeister series. From Ref. [137].

In comparison to chaotropes, these ions are 'structure-breakers' and are defined by their weak hydration and structureless water layer. In Figure 2.6, the similarities and differences in the order of cations and anions between the Hofmeister und lyotropic series are visualised. Consequently, different ion-specific effects arise in protein solutions depending on the salts added leading to the manipulation of the phase behaviour.

2.3.3 Salt-Induced Protein Phase Behaviour

Some proteins, such as the proteins investigated (BSA and BLG), do not show any complex phase behaviour unless salts are added. Through the addition of monovalent salt, gel formation and aggregation of BLG can be promoted and be modulated with changes in temperature and pH [142]. At high ionic strength, the aggregation process can lead to sedimentation through phase separation [143]. The aggregation is increased with divalent salts compared to monovalent salt [3,144], which is also reflected in the strength of the gel. Both salts (monovalent and divalent) induce gelation by non-specific charge screening effects, but divalent salts (here: calcium) also contribute to gel formation by a specific cross-linking (ion bridging) effect [5,145]. This ion bridging effect occurs only, if the attractive interactions between ion and protein are sufficiently strong, which is not the case for monovalent salts.

Ion bridging enhances cluster formation, and thus promotes protein crystallisation [146], which is found for BLG with divalent salts ($CdCl_2$ [147] and $ZnCl_2$ [78]), as well as trivalent salts (YCl_3) [148]. Another special phase feature found only for higher valent salts, i.e. trivalent salt such as YCl_3, $LaCl_3$, $HoCl_3$, $CeCl_3$, $La(NO_3)_3$, $FeCl_3$, and $AlCl_3$, is called re-entrant condensation (RC) [79,80,149–152]. Re-entrant condensation is induced at high salt concentrations by charge inversion of the protein due to ion binding and bridging and a subsequent non-monotonous reduction in attractive protein-protein interactions [79,150,153]. This illustrates not only how multivalent salts can induce a rich and complex protein phase behaviour by changing the electrostatic protein and solvent interactions leading to RC, LLPS, and protein crystallisation, but also how the knowledge about these mechanisms can help to control and guide protein phase behaviours and correlated phenomena. In this context, specific isotope-, anion-, and cation-dependent effects are found [152,154,155].

More information on the bulk phase behaviour and influencing parameters are found in the respective result chapters. A detailed review about effects of multivalent ions on biomolecules can be found in Ref. [156].

2.4 Solvent-Surface Interactions

By introducing an interface to a solution, two scenarios can occur: wetting and spreading. Those depend on the surface tension and surface energy of the respective substrate and solvent used. In solids, the surface free energy G is defined by the work spent in forming a unit area of a solid surface [157]. They can be divided into two major groups: high-energy (G = 200–5000 mJ/m^2) and low-energy surfaces (G = 10–50 mJ/m^2) [158]. In high energy surfaces, usually strong chemical bonds stabilise the substrate and the substrate is hydrophilic e.g. silicon dioxide with G = 287 mJ/m^2 [159]. In low energy surfaces, however, van der Waals interactions stabilise the structure [157] and the substrates are hydrophobic e.g. OTS-coated substrate with G = 19.8 mJ/m^2 [160]. Thus, typically van der Waals and hydrogen interactions guide and induce different intermolecular interaction depending on the substrate properties [161].

In liquids, the surface free energy results from the work that is be needed to bring the molecules from the bulk phase to its surface to form a new surface with a solid material. Liquids tend to minimise their number of interface molecules to decrease the surface energy [157]. When a solution droplet is placed on a solid substrate, three wetting states are possible: complete wetting, partial wetting, and complete de-wetting/dryness (**Figure 2.8**) [162]. These different states can be expressed in terms of the spreading parameter S (**Equation 2.1**). Note that the surface free energies G are equivalent to the interfacial surface tensions between the three components ($G = \gamma$), if the surface is flat [158].

$$S = \gamma_{SV} - (\gamma_{SL} + \gamma) \tag{2.1}$$

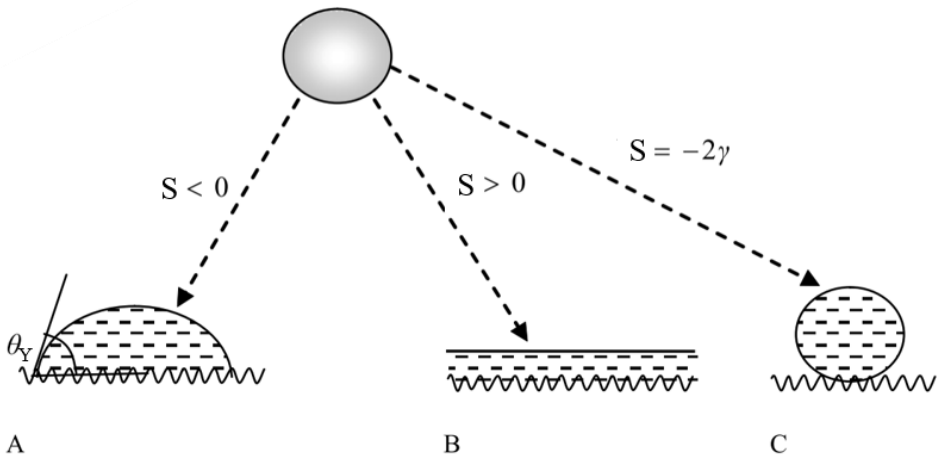

***Figure 2.8**: Three possible wetting states. (A) Partial wetting for S < 0. The droplet has a contact angle θ_Y with the substrate. (B) Complete wetting for S > 0. (C) Complete de-wetting for S = -2γ. Modified from Ref.* [157].

γ_{SV} describes the surface tension between the solid and air, γ_{SL} is the surface tension between the solid and liquid and γ is the surface tension between the liquid and air. If the liquid spreads on an interface ($S > 0$), it reduces its surface energy. However, if the difference between surface energies between the liquid and substrate is too wide, it does not spread since this is not energetically favoured. Hexane (G = 18.4 mJ/m^2) [159], for example, is a good solvent for trichloro(octadecyl)silane (OTS) (G = 19.8 mJ/m^2) [160] since their surface energies are similar to each other leading to mixing and complete wetting on an OTS-coated silicon wafer. In the case of partial wetting ($S < 0$), the droplet forms a specific contact angle θ_Y with the interface, which facilitates the determination of material-specific surface tensions via contact angle measurements (explained in Chapter 4.11), and thus, can proof e.g. the success of a coating procedure.

Additionally, desired solvent-surface interactions can be achieved through surface modifications, which can be permanent through e.g. coatings, and functionalisation [46,58,163,164] or temporary through e.g. plasma treatment inducing hydrophilicity [165]. The surface modifications applied in this dissertation are explained in Chapter 3.3.2. Further surface properties, i.e. surface roughness, surface heterogeneity, and surface morphology, influence the wetting behaviour and increase the complexity of the interaction properties. Detailed information on this topic can be found in Refs. [157,162]. Note that the term wetting has two definitions in this dissertation. In the context of contact angle measurements and surface free energies, it describes the ability of a liquid to maintain contact with a solid substrate [157], whereas wetting discussed in the context of protein adsorption (Chapter 6) defines an excess surface adsorption of an adsorbate (e.g. proteins) due to long-range interactions [166].

2.5 Protein-Surface Interactions

All of the above introduced bulk interactions are relevant in the context of protein-surface interactions illustrating the numerous parameters influencing protein adsorption. On the one hand, intramolecular interactions control the shape and state (i.e. folded/unfolded) of the proteins and intermolecular interactions lead to a specific protein phase behaviour. On the other hand, depending on the substrate properties, different protein-surface interactions can occur and determine whether the proteins adsorb to the surface (dominant attractive interactions) or not (dominant repulsive interactions). In the following paragraph, some examples are given on how certain surface properties influence protein adsorption. For further information see Refs. [1,42,69–73,167].

Surface modifications showed that when wetting is decreased (i.e. surface becomes more hydrophobic) through e.g. SAM coatings, protein adsorption increases for BSA and decreases for collagen [168,169], which is due to the strong hydrophobic nature of BSA compared to collagen. Plasma treatment of the substrate increases wettability temporarily and increases protein adsorption of plasma proteins, but reduces blood platelet adhesion [170].

Furthermore, the surface charge is found to change the adsorption behaviour. In blood coagulation, negatively charged surface charges activate the plasmatic coagulation system starting with the adsorption of BSA, whereas positively charged surfaces stimulate blood platelet adhesion and activation [171]. Most proteins are net negatively charged at neutral pH. A negatively charged interface can induce electrostatic repulsion of proteins from the interface creating a steric barrier [172–174]. This illustrates the interplay of protein and interface properties [175] leading to surface-protein interactions.

Protein adsorption is a dynamic process with a multitude of interfering interactions. Depending on the surface tension and the strength of dominant interactions, the protein can partially or completely unfold (i.e. denature) and/or adsorb in a different orientation (**Figure 2.9**) [176,177]. The tendency of a protein to unfold or undergo conformational changes upon adsorption also depends on its thermodynamic stability and can be organised into three groups: 'hard' proteins with a high thermodynamic stability (e.g. lysozyme), 'soft' proteins with low thermodynamic stability (e.g. BSA) and a 'middle' group with intermediate stability (e.g. BLG) [72,178]. Upon adsorption, proteins induce lateral interactions, which can enhance adsorption or desorption and lead to a dense or loose packing (**Figure 2.9**) [1]. In a protein mixture, the Vroman effect describes a competitive dynamic process, in which first the proteins with the highest mobility adsorb and later being replaced by slower proteins with higher affinity, also known as overshooting adsorption (**Figure 2.9**) [43,73,179]. In overshooting adsorption, partial desorption of the adsorbed proteins leads to unique features in the adsorption kinetics (growth curve) [1]. The dynamic adsorption process can be described via kinetic models, which are based on mathematical approaches to protein adsorption and are further discussed in Chapter 2.7.

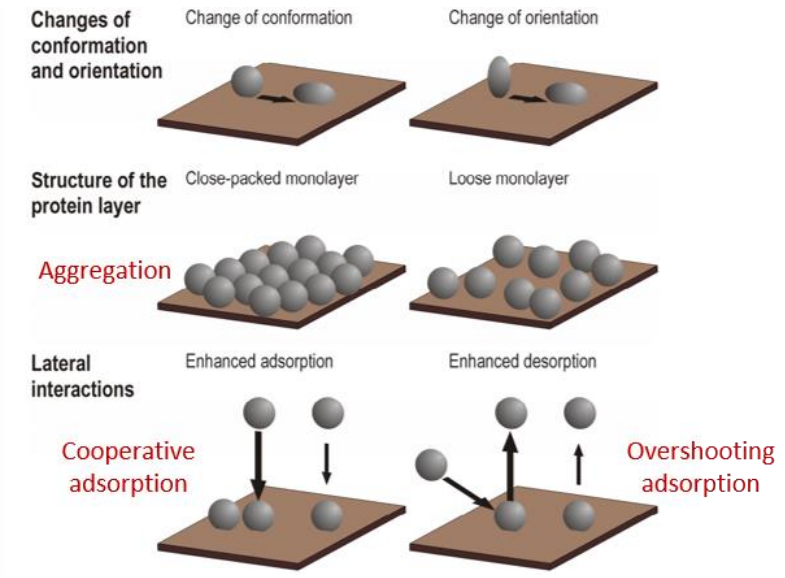

***Figure 2.9**: Different surface-induced effects occur in protein adsorption from orientation changes, to conformation changes, to cooperative adsorption, aggregation, and overshooting adsorption leading to desorption. Cooperative adsorption describes the pre-adsorption of one protein, which promotes the adsorption of another protein. These effects influence and change the adsorption kinetics and protein layer resulting. Modified from Ref.* [180].

2.6 External Parameters

Protein adsorption and bulk behaviour also depend on external parameters such as salt, temperature, pH, pressure, and composition. The manipulation through salt/ionic strength is thoroughly discussed in Chapter 2.3. Here, the focus is on other parameters and general effects associated with them.

2.6.1 Temperature

The protein phase behaviours investigated in this dissertation are highly temperature sensitive meaning their bulk phase behaviour shifts and changes with temperature [181]. Two types of temperature-dependent mechanism can lead to the formation of LLPS. Either LLPS forms below a critical solution temperature defined as the upper critical solution temperature (UCST) [182] (illustrated in **Figure 2.4**) or above a critical temperature known as the lower critical solution temperature (LSCT) resulting in an inverted LLPS binodal [155]. UCST-LLPS is guided by the framework of entropy and enthalpy of mixing/de-mixing with a positive value of the enthalpy of mixing, whereas the LCST-LLPS is thermodynamically driven resulting in a gain in entropy caused by the release of bound water molecules and a negative enthalpy of mixing [183]. The investigated proteins show a dependence on salt concentration and temperature (LCST-LLPS or UCST-LLPS) [155,183].

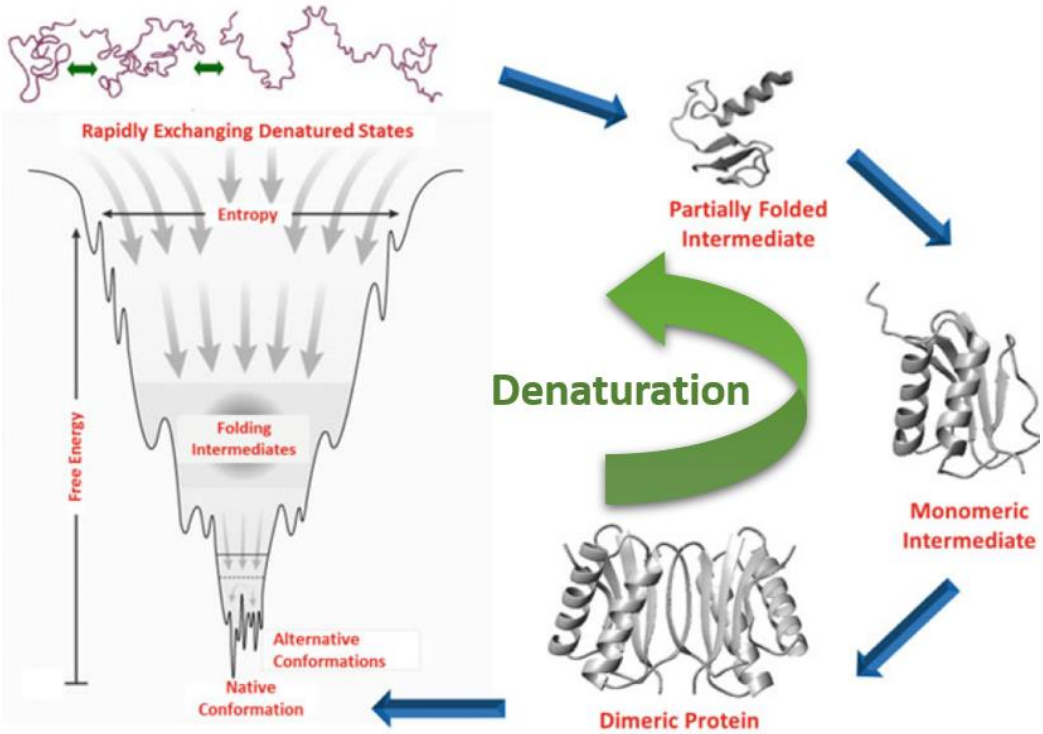

Figure 2.10: Protein folding (blue arrows) and denaturation (green arrow). The energy landscape illustrates the dependence of the protein confirmation on the free energy. In protein folding, the aim is to reach the global minimum in free energy since the native structure is thermodynamically stable at this point. In denaturation, the protein starts with an intact native structure and unfolds in multiple intermediates, called molten globule states, leading to the complete unfolding of the protein. Modified from Ref. [184].

The temperature range is limited by thermal denaturation. The denaturation temperature of proteins defines their melting point. The melting point of BSA is at 65 °C [153] and for BLG at 78 °C [185,186]. Denaturation occurs in two-steps for proteins existing as dimers (e.g. BLG), first, the dissociation of dimers leading to conformation changes in the protein from native to molten globule structure and in the next step to the loss of secondary structures, thus complete unfolding (**Figure 2.10**) [185,187]. The definition of denaturation is: 'simply a major change from the original native structure, without alteration of the amino acid sequence, i.e., without severance of any of the primary chemical bonds which join one amino acid to another' [188]. Thus, denaturation [178] can not only be caused by heat, but also through pH changes (Chapter 2.6.2) [188], pressure changes [189] or adsorption on an interface (i.e. unfolding of soft proteins) [190].

At the interface, temperature changes lead to adsorption or desorption of proteins, as well as denaturation at high temperatures [153,191], which correlates with changes in entropy and kinetics.

2.6.2 pH

Depending on the pH in solution, proteins carry different charges. The isoelectric point (pI) defines the pH of neutral net charge of a protein (**Table 3.1**). Below the pI, proteins are positively charged and above negatively charged [192]. Besides the net charge of the protein, the pH also determines the protein structure/conformation. For example, BSA exists in four forms: basic form (B) above pH 9, normal form (N) from pH 9 to 4.5, fast form (F) from pH 4.0 to 3.5, and extended form (E) from pH < 3.5 (**Figure 2.11**) [81,193]. Consequently, the pH also correlates with the stability of the globular protein structure. The E form can be assumed to be denatured and not functional (**Figure 2.10**).

In bulk, pH values far from the pI promote gel formation and, close to the pI, phase separation [143]. Protein adsorption of most proteins, for instance bovine serum albumin and whey proteins, is diminished when the pH deviates from the pI due to increasing repulsive protein-protein interactions [75,194,195]. Additionally, changes in the pH can lead to different orientation of the protein on the interface [196].

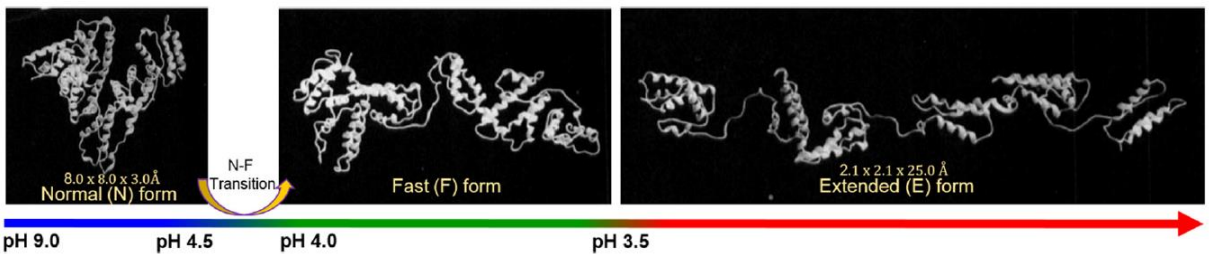

***Figure 2.11**: Three of the pH-dependent BSA conformations. In most systems, BSA has its normal (N) form, but below its pI changes its shape to the fast (F) form. The extended (E) form can be argued to be not functional anymore. From Ref.* [197].

2.6.3 Pressure

The atmospheric pressure on earth is 1 bar. With a high pressure cell, values up to 2500 bar can be achieved [198]. An increase in pressure is found to induce enhanced adsorption for lysozyme, which becomes a 'soft' protein under these conditions [198,199], yet it also increases the risk of denaturation [200–202].

2.6.4 Composition

Besides salt, also other molecules can be added to modify the bulk interactions. One option is the addition of polymers. Due to the addition of a non-adsorbing polymer such as polyethylene glycol (PEG), tuneable depletion interactions can be introduced to induce LLPS formation and/or crystallisation, and thus, can be used to modulate the attractive intermolecular interactions [182,203].

2.7 Theoretical Descriptions of Proteins and Protein Adsorption

Theoretical descriptions, including modelling and simulations, can help to describe and investigate phenomena not feasible in experiments, e.g. via molecular dynamic simulations, or provide the supporting model explaining the driving force behind protein adsorption and bulk behaviour, e.g. patchy model for proteins.

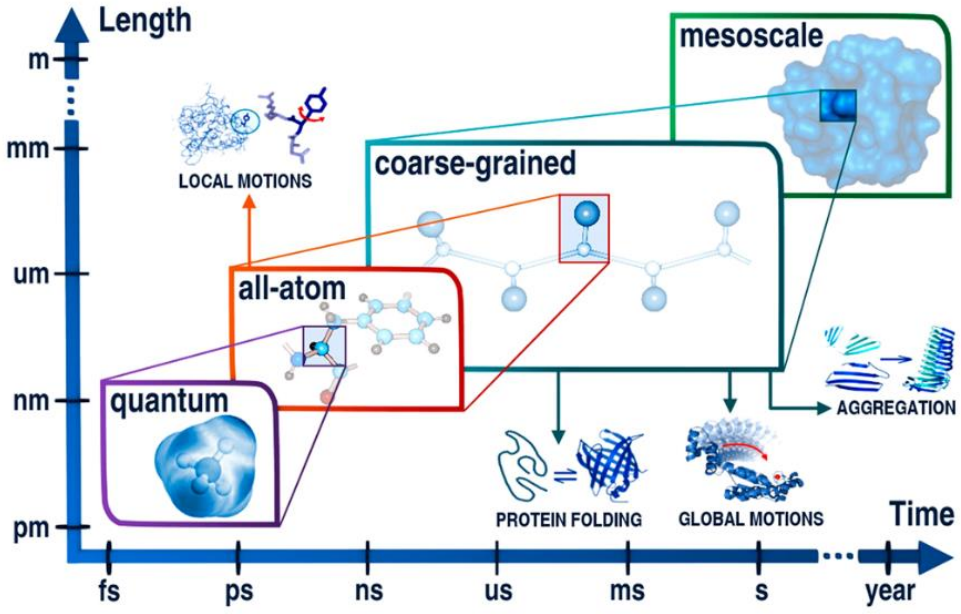

Figure 2.12: Depending on theoretical model, the application range allows the investigation of different phenomena at different time and length scales. From Ref. [204].

While the above-mentioned, empirical series and forces portrait all existing interactions within the system investigated, theoretical models and simulations are needed for the description of the dominating interactions underlying certain assumptions and simplifications.

These simplifications can be expressed amongst others with different resolution ranges from quantum to mesoscale (Figure 2.12). In the following paragraphs, some theoretical descriptions are introduced, which are relevant in this dissertation.

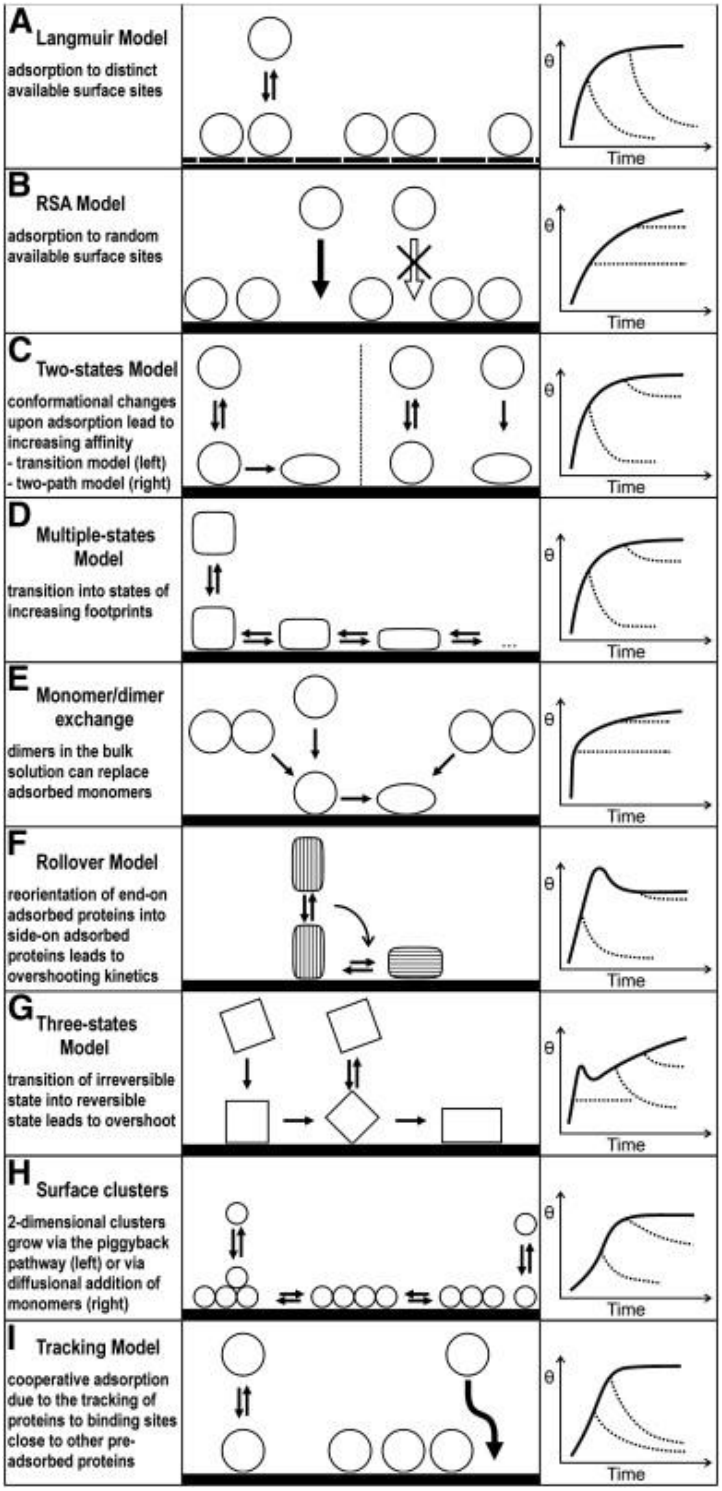

Figure 2.13: Overview of different kinetic models describing protein adsorption on a solid interface. On the left side, the name of the model and a brief description are written. In the middle, a sketch illustrates the binding mechanism. On the right side, the underlying real-time adsorption growth curve are plotted. Here, the dashed lines illustrate the curve change if desorption occurs in the system. From Ref. [1].

Proteins are often described with coarse-grained models to investigate protein dynamics and interactions [204]. The protein phase behaviour can be described with a patchy particle model for some globular proteins [205–207]. It hereby simplifies proteins to hard spheres with attractive patches to account for the protein-protein interactions [208]. For globular protein with trivalent salt, the ion-activated attractive patchy particle model was established by Roosen-Runge et al. [209] describing the complex phase behaviour. The dominant intermolecular interactions are hereby electrostatic, other interactions may slightly influence the phase behaviour, but can be neglected. This model is the basis for the theoretical description of the protein adsorption trends founds and more information is provided in the corresponding result sections (Chapter 5 & 6).

Protein adsorption can be described via kinetic models to account for the adsorption growth curve [1] (**Figure 2.13**) or via the density functional theory (DFT), which defines the protein density profile on the interface protruding into the bulk solution [210]. The most well-known adsorption model is the Langmuir model describing the adsorption of a monolayer via a desorption and adsorption rate [211]. This is the starting point for most, more complex, kinetic models, which consider cooperative adsorption, overshooting adsorption, aggregation or conformational changes (**Figure 2.13**) [153,212–215]. The DFT allows the investigation of inhomogeneous density distribution such as intermolecular interactions at the liquid-vapor interface or spinodal decomposition [216,217]. In this dissertation, DFT is applied to obtain the density profile of adsorbed proteins to an attractive wall (for more information see Chapter 5 & 6).

Computational approaches [218] to simulate larger systems and all-atom systems include molecular dynamics (MD) simulations and Monte Carlo (MC) simulations. MC simulations can be used to investigate systems with certain probability distributions such as intermolecular (i.e. ion-protein, protein-protein) interactions [219] and protein denaturation on interfaces [220]. MD simulations allow the investigation of dynamic processes in the nanosecond time range [221] such as protein aggregation and unfolding [222], as well as protein adsorption (**Figure 2.14**) [223–225].

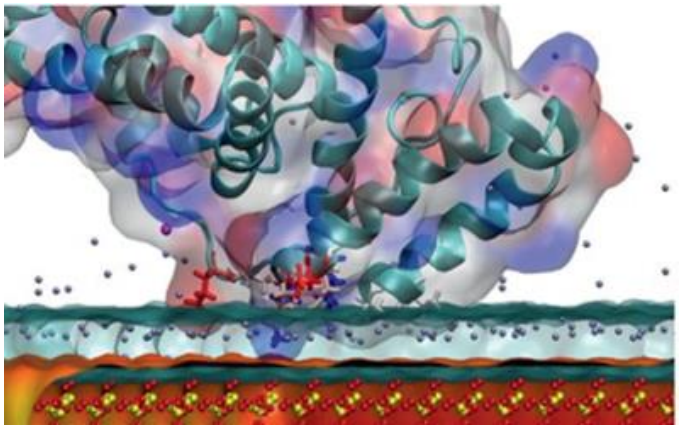

***Figure 2.14**: Molecular dynamic simulations of an adsorbed BSA molecule on a hydrophobic interface. MD simulations provide information on an atomic level. From Ref.* [226].

3 Materials

In this chapter, the materials used in this dissertation are introduced and their fundamental properties and function explained and compared within one material class. The emphasis is on the different types of proteins, salts, substrates, and coatings utilised, as well as the sample and substrate preparation.

3.1 Globular Proteins

Depending on their structure and function, proteins can be divided into four groups: fibrous, globular, disordered, and membrane proteins [227,228]. Globular proteins define spherical, water-soluble proteins and can be divided into four structural classes, namely all-α, all-β, α+β and α/β, depending on their secondary structure [229]. In this dissertation, the focus is on BSA and BLG. They belong, respectively, to the group of all-α and all-β proteins (**Figure 3.1**) [230], thus, provide information on proteins of the opposite structure spectrum.

3.1.1 Bovine Serum Albumin (BSA)

Bovine serum albumin (BSA) is the most abundant blood protein in the circulatory system. It contributes to the regulation of the blood pressure, blood pH [231], and the circulation of plasma, as well as functions as an carrier for fatty acids and ligands [81]. BSA is net negatively charged at pH 7 (**Figure 3.1 (A) & (C)**) and consists of 583 amino acids. It is obtained from Sigma Aldrich/Merck (Germany) in form of a lyophilised powder (No. A7906) with a purity of ≥ 98 % and produced with heat shock fractionation. More properties are listed in **Table 3.1**.

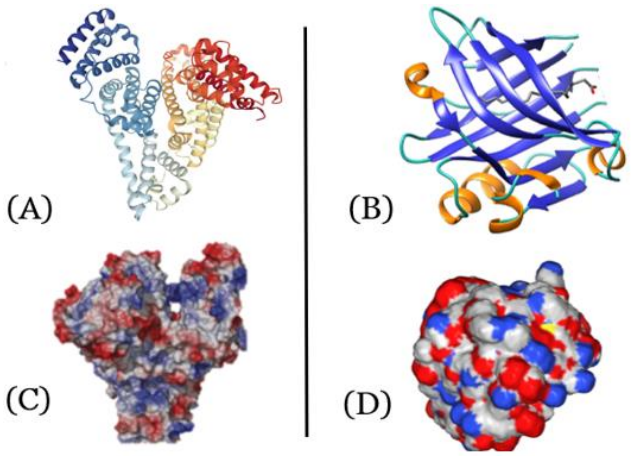

Figure 3.1: *Globular structure of BSA (PDB ID: 3V03) and BLG (PDB ID: 1BEB). In (A) and (B), the secondary structure of BSA* [232] *and BLG* [233] *are illustrated, and in (C) and (D), their surface charge distributions induced by the amino acid residues (red: negatively charged, blue: positively charged, grey: non-polar)* [234,235].

Table 3.1: Relevant properties of BSA and BLG are listed below. The information is obtained from the following Refs. [195,235–245].

Properties	BSA (MONOMER)	BLG (DIMER)
Molar mass M_w (kDa)	66.7	36.6 (18.3)
Extinction coefficient ${\varepsilon_{0.1\,\%}}^{279\,nm}$ (ml/(mg*cm))	0.667	0.96
Radius R_p (nm) (Monomer)	3.5	2.35
Gibbs free energy of transfer from water (kcal\mol)	-5.1	-1.7
Anion binding index $\sum(NH^+)/\lvert\sum(COO^-) - \sum(OH)\rvert$	29	4.6
Secondary structure (%)		
α-helices	66	15
β-sheets	21	54
Charge at pH 7 (e)	-10	-10
Isoelectric point pI (pH)	4.6	5.2
LLPS	LCST	UCST

3.1.2 Beta-Lactoglobulin (BLG)

Beta-lactoglobulin (BLG) is the dominant whey protein in milk [82]. It contributes to the transport of hydrophobic ligands such as vitamin D and cholesterol [233,246,247]. BLG is net negatively charged at pH 7 (**Figure 3.1 (B) & (D)**) and consists of 162 amino acids. It is obtained from Sigma Aldrich/Merck (Germany) in form of a lyophilised powder (No. L3908) with a purity of ≥ 90 % via chromatography. More properties are listed in **Table 3.1.**

All protein stock solutions are prepared with degassed Milli-Q water at 20 °C and need two days for complete dissolution of the protein powder, followed by the determination of the final protein concentration (c_p) with UV-Vis absorbance measurements (see Chapter 4.4). The Milli-Q water has a total organic carbon value of 1.7 ppb or µg/l and a resistivity of 18.2 MΩ*cm at 25 °C. Degassing via a vacuum pump removes dissolved gases within water e.g. oxygen, which can cause bubble formation on interface and disrupt measurements [248]. Another precaution is to seal the solution with Parafilm to slow down the dissolution of gas. Due to the risk of bacteria and fungi growth [249], a stock solution is only used for up to three weeks, depending on the protein type, and is stored in the fridge. The working protein concentration is either 5, 20, or 50 mg/ml depending on the system investigated.

Table 3.2: *Relevant ion properties taken from Refs.* [250–257]. *Note that nitrate (NO_3^-) is included in this table for comparison reasons discussed in Chapter 7.*

Properties	Y^{3+}	La^{3+}	Cl^-	NO_3^-	I^-
Molar mass (10^{-3} kg/mol)	88.91	138.91	35.45	62.01	126.91
Charge (e)	3	3	-1	-1	-1
Effective radius (Å)	1.019	1.216	1.81	2.0	2.2
Ionisation potential (kJ/mol)	3795	3474	-	-	-
Electron affinity (kJ/mol)	-	-	349	378	295
Refraction (10^{-6} m^3/mol)	2.4	2.74	8.63	10.43	18.95
Structural entropy (J/(K*mol))	-	-	58	66	117
Enthalpy aq. (kJ/mol)	-723.4	-707.1	-167.2	-205	-55.19
Gibbs energy aq. (kJ/mol)	-693.8	-683.7	-131.2	-108.7	-51.57
Volume aq. (cm^3/mol)	-57.3	-55.6	23.3	34.5	41.7
Hydration number	12	10.3	2.0	2.0	1.6
Softness	-0.69	-0.75	-0.09	0.03	0.5
Polarisability ($Å^3$/atom)	22.7	31.1	2.18	-	4.7
Electronegativity	1.11	1.04	2.82	-	2.27
Water structure	0.77	0.78	-0.61	-0.68	-1.09
Ionic aqueous surface tension (nm/(m*M))	-	-	0.90	0.15	-0.05
Heat capacity (J/(K*mol))	-	-	-237	-234	-288
B-coefficient (dm^3/mol)	-	0.576	-0.007	-0.046	-0.068
Number of ions bound to BSA[1] at pH 5	-	-	8	19	48

[1] The concentration of added anion was 0.1 mol/kg and the protein concentration 0.3 mM/l, which is equivalent to the protein concentration used of 20 mg/ml.

3.2 Salts

Salts are a natural component in the human body and food [258] and can change the charge distribution in systems, consequently, modify the interactions and possible

functions. All salts are purchased from Sigma Aldrich/Merck (Germany), namely, sodium chloride (NaCl) anhydrous beads with a purity of 99.99 % (product No. 450014), yttrium chloride (YCl_3) anhydrous powder with a purity of 99.99 % (product No. 451363), lanthanum chloride ($LaCl_3$) anhydrous beads with a purity of ≥ 99.99 % (product No. 449830), yttrium iodide (YI_3) anhydrous flakes with a purity of 99.9 % (product No. 413011), and lanthanum iodide (LaI_3) anhydrous beads with a purity of 99.9 % (product No. 413674). The different combinations of cation and anion types facilitated a detailed investigation on ion-specific effects, e.g. on proteins [126,137,259,260], which depend on their properties listed in **Table 3.2**.

All salt stock solutions are prepared with degassed Milli-Q water with a final salt concentration (c_s) of 100 mM or 200 mM. The stock solutions are sealed with Parafilm to slow down the dissolution of gas.

3.3 Substrates and Coatings

3.3.1 Silicon Dioxide (SiO_2)

SiO_2 is a cornerstone component used in fixation of implants in the skeletal system/ bone replacement [261–263]. Its well-defined and characterised surface makes it a great model surface for solid-liquid protein adsorption investigations. SiO_2 is negatively charged and hydrophilic, once submerged under water [264,265]. For ellipsometer measurements, standard p-doped (boron) Si wafer are used with an (111) orientation, a resistivity of 1-10 Ω*cm, and a thickness of 475 nm ± 15 nm with a native oxide layer of roughly 1.7 nm. Before use, the Si wafers are cleaned in the ultrasonic bath with acetone, isopropanol, and water for 5 min in each solution at 50 °C. Depending on the experimental method and type of substrate, slightly different cleaning procedures are applied ex situ and in situ.

For QCM-D measurements, quartz sensors with SiO_2 coating are purchased from Biolin Scientific (Sweden) (product No. QS-QSX303). Depending on ex-situ and in-situ cleaning, the cleaning procedures differed. Ex-situ cleaning is performed in an ultrasonic bath with acetone, isopropanol, and water for 5 min in each solution. The in-situ cleaning within the QCM-D flow cell allowed the re-use of the same samples and is done with 10 ml of Hellmanex (2 %), isopropanol, and water each pumped through the cell with a flow rate of 0.5 ml/min.

For ATR-FTIR measurements, a trapezoidal polished silicon crystal with a SiO_2 layer is provided by ISIS (Rutherford Appleton Laboratory, UK). Depending on ex-situ and in-situ cleaning, the cleaning procedures differs. Ex-situ cleaning is performed in an ultrasonic bath with acetone, isopropanol, and water for 5 min in each solution followed by 15 min of ozone treatment (O_3). Ozone is formed by UV-C rays of 184.9 nm wavelength, which are absorbed by oxygen, and gets rid of organic residues on surfaces by the reduction of organic contaminants into harmless H_2O, CO_2 and NO_x [266–268]. The in-situ cleaning within the ATR flow cell allowed the re-use of the same sample and is done with 5 ml of Hellmanex (2 %), isopropanol, and water, each pushed through the cell with a syringe.

For NR measurements, silicon crystals (dimensions: 50 × 80 × 15 mm) with a polished 80 × 50 mm face and a (111) orientation from Siltronix (France) are provided with a native oxide layer. The surface roughness (σ) is roughly 3 Å. The ex-situ cleaning started with a quick rinse with water followed by 15 min of ozone treatment. Afterwards, the blocks are cleaned in piranha acid (water: sulfuric acid: hydrogen peroxide; ratio 5:4:1) for 20 min at 80 °C. Immediately before the solid-liquid cell assembly under water, the blocks are put in the ozone cleaner again for another 15 min to obtain a perfectly hydrophilic, dust-free surface. The in-situ cleaning within the NR flow cell allowed the re-use of the same sample. A syringe pump is used to push first 15 ml of Hellmanex (2 %) and then water through the cell.

3.3.2 Coatings

A well-characterised and defined surface such as Si wafers can be the basis for surface modifications. Depending on the method applied, the specific Si samples described in Chapter 3.3.1 are coated with other materials changing their surface properties. One approach is the coating of solid (metal) materials through e.g. sputtering [269]. Another is the liquid deposition of self-assembled monolayers (SAMs) [270], which come in a big variety of chemical modifications/ functional groups and self-adsorb on an interface forming a monolayer. In the following sections, the surface modifications used in this dissertation are introduced and the preparation procedure is explained.

3.3.2.1 TiO_2 (Anatase)

Anatase is used in dental implants. It is known for its decomposition of organic material under UV light (photocatalysis) and UV-induced superhydrophilicity, thus improving osseointegration and the formation of a basal layer [165,271,272]. For these samples, the (crystalline) anatase coating are produced by tempering amorphous TiO_2 at 450 °C for 3 h by Medentis medical GmbH (Bad Neuenahr-Ahrweiler, Germany) in collaboration with Prof. Geis-Gerstorfer (Universitätsklinikum Tübingen) [273,274]. Anatase has a (101) orientation and is roughly 500 μm thick. More information on its characterisation and properties can be found in Refs. [274–276]. Before use, the anatase-coated samples are cleaned in the ultrasonic bath with isopropanol and water for 5 min in each solution. After protein adsorption experiments, to allow re-use, an additional cleaning step in Hellmanex (2 %) is necessary prior to the general cleaning procedure to get rid of adsorbed organic material.

3.3.2.2 Gold (Au)

Gold is a common substrate, yet by itself, it is hard to clean and to obtain a defined surface [277]. Thus, these substrates are used as the basis for thiol-coated surfaces described in Chapter 3.3.2.3. For QCM-D measurements, quartz sensors with Au coating are purchased from Biolin Scientific (Sweden) (product No. QS-QSX301). For NR measurements, the blocks described above (Chapter 3.3.1) are sputter-coated with gold in a Denton Discovery 550 sputtering chamber at NIST centre for Nanoscience and Technology (USA) provided by ISIS (Rutherford Appleton Laboratory, UK).

3.3.2.3 Self-assembled Monolayers (SAMs)

Self-assembled monolayers (SAMs) are ordered molecular assemblies of organic molecules, which are defined by a specific head and end group [270,278]. Through exposition of these molecules in solution to a solid interface, the self-assembly process and growth mechanism on substrate is initiated [279,280]. In **Figure 3.2**, the adsorption process illustrated is a simplification ignoring present solvent molecules and parallel occurring events. The SAM molecules start to distribute themselves randomly on the interface in a lying-down orientation (**Figure 3.2 (A)**) forming a complete lying-down monolayer (**Figure 3.2 (B)**). Over time, the number of molecules on the surface increases, and thus, the pair interactions between molecules increase as well [281]. The tails start to rise vertically allowing the formation of dense islands (**Figure 3.2 (C)**). In the last step, the molecules undergo conformational changes from a gauche to all-trans formation to form a densely packed, highly ordered monolayer (**Figure 3.2 (D)**) [279]. Depending on their composition, different surface materials are favoured for self-organisation and adsorption on an interface, e.g. gold or silicon [270,280,282]. The tails can be chemically modified depending on the desired properties of the coated substrate. The two specific molecules used for SAM formation in this dissertation are described in the following paragraphs.

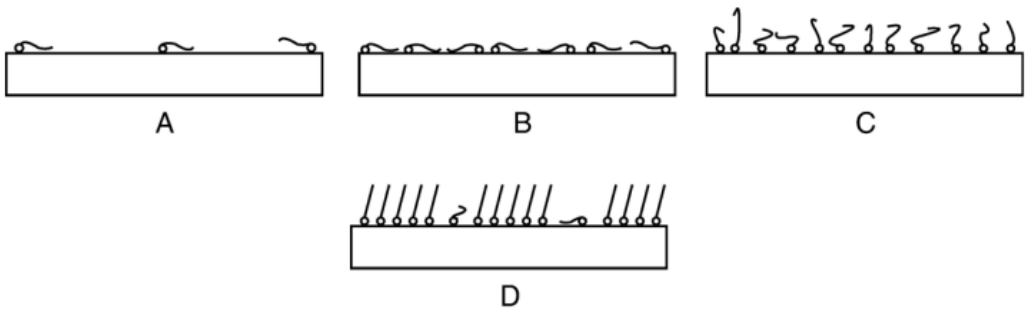

***Figure 3.2**: Self-assembled monolayer formation on solid substrate. In (A) and (B), initially low coverage and lying-down orientation of the molecules can be observed. (C) At higher coverage, the tails start to rise from interface in gauche formation. (D) The molecules undergo conformational change to all-trans conformation to form the final vertically bound monolayer. Modified from Ref.* [279].

Thiols are known to bind to gold surfaces with the sulfanyl group (head) [280,283]. Triethylene glycol mono-11-mercaptoundecyl ether (TEG) ($HS(CH_2)_{11}(OCH_2CH_3)_3OH$) shown in **Figure 3.3** belongs to the group of thiols and is purchased from ProChimia Surfaces (Poland) (Product No. TH 001-m11.n3-0.2). Its molecular weight (M_W) is 336.53 g/mol and has a purity of > 95 % and a density of 1.03 g/ml. For the thiol coating process, 500 µM of TEG is dissolved in ethanol (HPLC 99 %) under argon atmosphere to prevent interactions with oxygen and water. The gold substrates are cleaned with isopropanol and water in the ultrasonic bath for 10 min in each solution and ozone treated for 15 min prior to functionalisation to create a defined and clean surface for adsorption. The samples are then incubated for 18 hours in the TEG/ethanol solution and afterwards rinsed with ethanol and dried with argon. After functionalisation, the substrates are hydrophilic and negatively charged due to the hydroxyl termination. The contact angle should be 31 ± 2° and the SAM layer is 1.8 ± 0.3 nm thick [284]. The samples are sealed

from air and light and stored in the fridge to slow down degradation. This specific thiol is known for its protein-repellent properties [285]. More information on thiol-specific properties can be found in the Refs. [286–288].

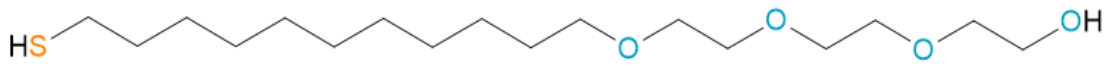

***Figure 3.3**: Structural formula of triethylene glycol mono-11-mercaptoundecyl ether belonging to the group of thiols with its characteristic head sulfanyl group and three ethylene glycol groups. Image is generated with software ACD/ChemSketch.*

Silanes are known to bind to silicon surfaces with its silane group (head) [289]. Trichloro(octadecyl)silane (OTS) ($CH_3(CH_2)_{17}SiCl_3$) shown in **Figure 3.4** belong to the organosilane and is obtained from Sigma Aldrich/Merck (Germany) with a purity of ≥ 90 % (product No. 104817). It has a M_W of 387.93 g/mol and a density of 0.984 g/ml. For the silane coating process, 1.5 mM of OTS is dissolved in hexane (98.29 %) under argon atmosphere to prevent interactions with oxygen and water. Prior to SAM solution preparation, hexane is dried with calcium chloride ($CaCl_2$) to minimise SAM exposure to water since this hinders the SAM formation [290]. The silicon substrates are cleaned as described in Chapter 3.3.1 and with an additional cleaning step with ozone for 15 min prior to functionalisation to create a defined and clean surface for adsorption. The samples are then incubated for 180 min in the OTS/hexane solution and afterwards rinsed with hexane and dried with argon. After functionalisation, the substrates are neutrally charged and hydrophobic due to the methyl termination [291,292]. The value of the contact angle from literature is around 98.2° and the SAM layer is roughly 2.3 nm thick [279,293]. The samples are sealed from air and light to slow down degradation. More information on properties and growth of OTS can be found in the Refs. [160,291,292,294–296].

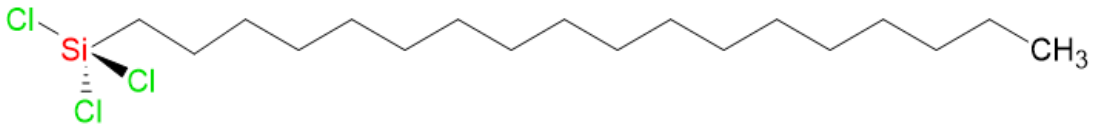

***Figure 3.4**: Structural formula of trichloro(octadecyl)silane belonging to the group of silanes. Image is generated with software ACD/ChemSketch.*

4 Experimental Methods

In this chapter, the experimental methods utilised to investigate protein adsorption at a solid-liquid interface are introduced and explained. Hereby, the emphasis is on scattering methods, which are powerful tools to analyse and investigate both solid and liquid samples. The full electromagnetic spectrum consists of a multitude of radiation types such as X-rays, ultraviolet, visible or infrared light (**Figure 4.1**), which are defined by their wavelength. With a single radiation type or the combination of selected radiation, different parameters can be measured. In the following sections, the individual methods and underlying radiation types are presented, as well as their specific purpose for this dissertation. Furthermore, complementary methods are described, which are used to determine and characterise protein bulk and phase behaviours. This chapter focuses on the operation mode and underlying physical mechanism of the experimental methods, thus providing the basic knowledge needed for the analysis and interpretation of the presented data in the result section.

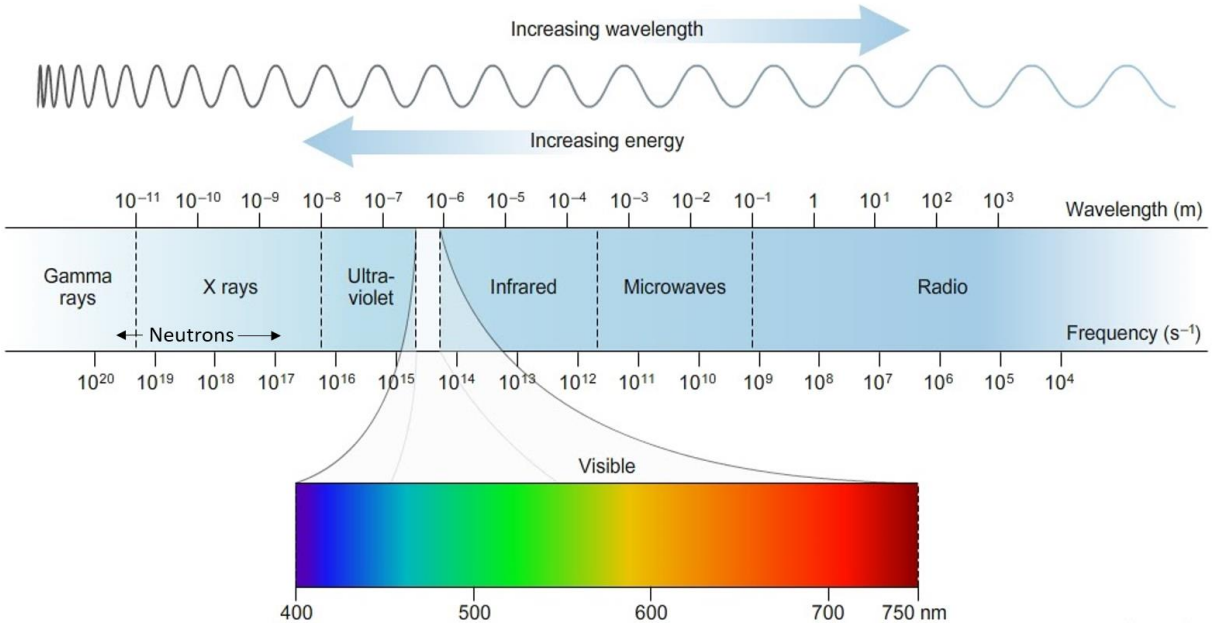

Figure 4.1: *The electromagnetic spectrum can be divided into different radiation types. Each radiation type is defined by a specific wavelength range. In addition, the neutron wavelength is indicated in the spectrum for a complete overview. Modified from EM spectrum, by Macmillan Learning, 2008 (https://sites.google.com/site/chempendix/em-spectrum). Copyright 2008 by Sapling Learning.*

4.1 Ellipsometry

Ellipsometry is used for the determination of optical properties, namely the refractive index n and the extinction coefficient ε, or the thickness d of thin films [297]. It hereby measures the polarisation ρ of an incident (polarised) beam after reflection from a substrate. The polarised light contains two polarisation directions - a perpendicular (s) and parallel (p) component with respect to the substrate plane of incidence (sample). The incident light is (usually) linearly polarised and hits the sample at an incident angle θ_0. Depending on the material(s) investigated, the beam undergoes a polarisation change to elliptically polarised light upon reflection on the substrate as depicted in **Figure 4.2**. The polarisation ρ of elliptically polarised light can be described for spectroscopic ellipsometry with two parameters: the amplitude ratio ψ and the phase shift Δ between the s- and p-component in **Equation 4.1**, which originate from the reflection, transmission and superposition of the beam components on and through the individual substrate layers [298].

$$\rho \equiv \tan(\psi)\, e^{i\Delta} \equiv \frac{r_\mathrm{p}}{r_\mathrm{s}} \equiv \frac{\left(\frac{E_\mathrm{rp}}{E_\mathrm{ip}}\right)}{\left(\frac{E_\mathrm{rs}}{E_\mathrm{is}}\right)} \tag{4.1}$$

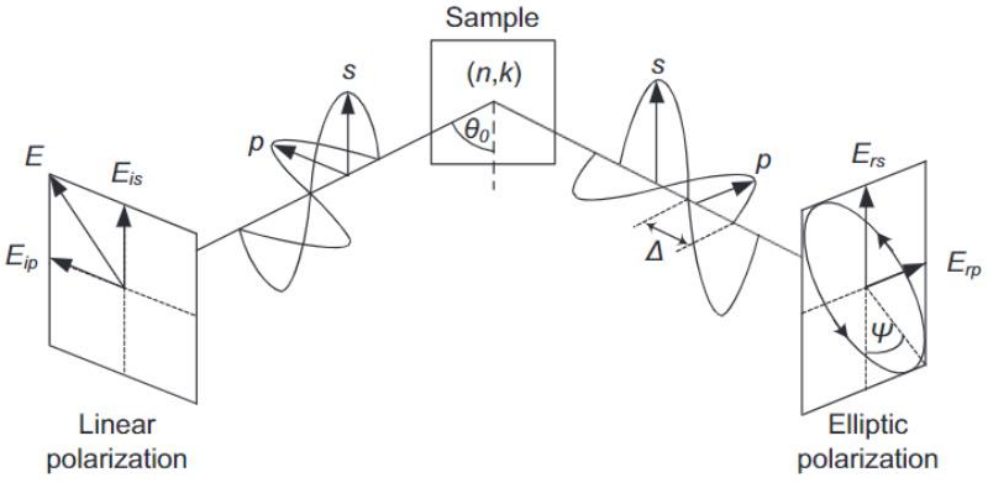

Figure 4.2: Basic principle of ellipsometry. Incident, linearly polarised light is reflected, transmitted, and superimposed at the individual substrate layers leading to a polarisation change, which can be measured in the form of a phase change Δ *and amplitude ratio* ψ*. From Ref.* [299].

According to Maxwell's theory [300], the Fresnel reflection coefficients, r_s and r_p, describe the relative contributions of each component x, y to electric field E_{yx} [301]. For multiple interfaces (substrate (2) – film (1) - ambient material (0)), this leads to **Equation 4.2**, from which the complex refractive index $\tilde{n}$ and film thickness d can be derived (**Equation 4.3**) [301]. Since these two parameters are intertwined, the thickness of the individual layers or the optical properties need to be known for successful data fitting and analysis. Fresnel coefficients of the p-component at the substrate-film interface and at the film-ambient interface are denoted $r_{12\mathrm{p}}$ and $r_{01\mathrm{p}}$, respectively.

$$r_{\mathrm{p}} = \frac{r_{01\mathrm{p}} + r_{12\mathrm{p}} e^{-i2\beta}}{1 + r_{01\mathrm{p}} r_{12\mathrm{p}} e^{-i2\beta}} \tag{4.2}$$

$$\beta = 2\pi \left(\frac{d}{\lambda}\right) \tilde{n} \cos\theta_0 \tag{4.3}$$

A M-2000 ellipsometer by J.A. Woollam (USA) is operated with the CompleteEASE and WVASE 32 software for data collection and analysis. A white xenon-arc lamp is used as the light source in the variable-angle spectroscopic ellipsometer (VASE). The rotating compensator provides another polarisation change to circularly polarised light, thus, cancelling out source and detector polarisation and facilitating the determination of all Stokes parameters [302]. This type of ellipsometer measures beam intensity and translates them into the parameters ψ and Δ. For more information on the ellipsometer type and data collection see Refs. [298,301–303].

The ellipsometer can be used for different kinds of samples. On the one hand, it is used in air to determine layer thicknesses of solid substrates, e.g. OTS-coated substrates. For this purpose, spectroscopic scans from 40° to 75° at 300 revs/meas over the complete spectrum from 245 to 1697 nm are taken. For data analysis and fitting, the Cauchy model [298,299,303] is applied, see **Equation 4.4**.

$$n(\lambda) = A + \frac{B}{\lambda^2} + \frac{C}{\lambda^4} \tag{4.4}$$

For OTS, the fitting parameters used are A = 1.45, B = 0.01 nm^2, and C = 0 nm^4 [279] and for anatase the 'tiO2_tl`model of the WVASE software [304]. On the other hand, real-time solid-liquid measurements are performed to investigate protein adsorption to obtain the adsorbed protein layer thickness [305–307]. Due to absorbance of the proteins at certain wavelengths, the area of interest is limited from 500 to 900 nm and measurements are performed in a home-made measurement cell [308] at the Brewster angle of the substrate (here: 68° for SiO_2 in water) [302,309,310]. At the Brewster angle, the p-polarised beam transmits through the sample without reflection, thus the sensitivity for the substrate is increased and the difference between r_p and r_s is maximised [299,301]. Dynamic scans allow for real-time data collection, thus providing adsorption kinetics. The adsorption time is set to 1 h, which is sufficiently close to equilibrium conditions. The optical constants of the individual layers are taken from the following references for model fitting: Si [311], SiO_2 [311], H_2O [312]. Specifically for BSA, a Cauchy layer with A = 1.43, B = 0.01 nm^2 and C = 0 nm^4 is chosen (in literature the value of A varies from 1.42 to 1.45 for BSA) [313–316]. Through the step-by-step construction of a fitting model, the final adsorption layer *d* can be determined very precisely (**Figure 4.3**). The effective thickness *d* assumes a volume fraction of 1, which is laterally averaged over the measured surface. All measurements are repeated at least three times to ensure their reproducibility and to estimate real standard deviations as statistical error bars. The systematic errors (e.g. wavelength and angle calibration of the ellipsometer) are substantially smaller. For more information on measurement procedure and model fitting see Ref. [308].

Another type of ellipsometry is the single-wavelength ellipsometry or phase-modulated ellipsometry (PME). Here, the light source is a He/Ne laser, and the setup contains a photoelastic birefringence modulator instead of a compensator, which achieves higher sensitivity and less noise in the collected data. The measured parameters (x and y) are correlated with the real and imaginary part of the measured polarisation change and thus with Ψ and Δ [317]. In collaboration with the Oxford University (UK), the Picometer ellipsometer of Beaglehole Instruments (New Zealand) is operated with the IgorPro 6 software. More information on this ellipsometer type can be found in Refs. [303,318,319].

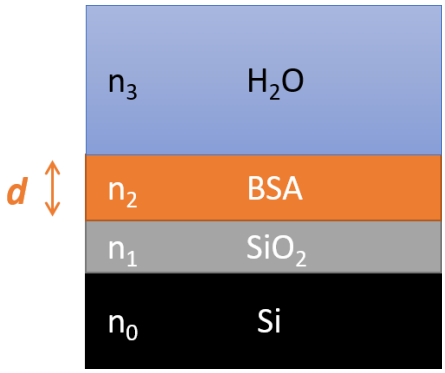

Figure 4.3: *Illustration of the model used for the analysis of the ellipsometry data consisting of the optical constants of the individual layers, namely silicon, silicon dioxide, BSA, and water.*

4.2 Neutron Reflectivity (NR)

Neutron reflectivity (NR) is a powerful method to investigate soft matter such as the surface chemistry of surfactants, polymers, lipids [288] or proteins, as well as solid films, e.g. Langmuir-Blodgett films, multilayers, bacterial membranes [320] or surface magnetism of magnetic multilayers or superconductors [321]. Depending on the sample, NR allows investigations on the solid-liquid, solid-solid, solid-air or liquid-liquid interfaces with external variable parameters such as shear, pressure, temperature, applied magnetic field or electric field [322].

Similar to the ellipsometer (Chapter 4.1), neutron reflectivity is based on the principle of transmission through and reflection on media. Thus, Snell's law and the Fresnel equations can be applied, and **Equations 4.2** & **4.3** are also valid for NR. One difference, due to the different radiation type, is the definition of the refractive index n for neutrons in **Equation 4.5**. It depends on the (neutron) wavelength λ and the scattering length density (SLD) ρ_{SLD} of the medium [322].

$$n = 1 - \frac{\lambda^2 \rho_{\mathrm{SLD}}}{2\pi} \tag{4.5}$$

ρ_{SLD} is defined by the number of atoms per unit volume and coherent scattering length [323], which results in material-specific SLD values due to different atomic compositions. Typical SLDs for materials used in this dissertation can be found in **Table 4.1.**

One advantage of neutrons is the possibility of solvent contrast variation meaning the H/D substitution within one sample. Nuclei scatter neutrons with different amplitudes [321]. For hydrogen and deuterium, this results in opposite phases and thus vastly different ρ_{SLD} (Table 4.1). This benefits the data quality and analysis without changing the chemical structure or disrupting the sample [321].

Table 4.1: Scattering length densities of different materials used in this dissertation for model fitting from Refs. [321,324–328].

Material	ρ_{SLD} (10^{-6} Å^{-2})
H_2O	-0.56
D_2O	6.35
Si	2.07
SiO_2	3.5
Au	4.41
Hydrated thiol	0.15
Deuterated thiol	0.77
BLG in H_2O	1.72
BLG in D_2O	1.84
BSA in H_2O	1.8
BSA in D_2O	3.0

For specular reflectivity, the magnitude of the wavevectors $k_i = k_r$ (Figure 4.4), thus, the magnitude of the scattering vector or the momentum transfer q can be described by Equation 4.6 [323].

$$q = k_r - k_i = \frac{4\pi}{\lambda} \sin\theta_0 \tag{4.6}$$

The reflectivity $R(q)$ only depends on q and can be described by the kinematic approximation (for $q >> q_c$, critical scattering vector) for samples with more than one inhomogeneous layer by Equation 4.7 [329].

$$R(q) \approx \frac{16\pi^2}{q^4} \left(\Delta\rho_{SLD}\right)^2 \tag{4.7}$$

$\Delta\rho_{SLD}$ denotes the difference in SLD between the materials. Total reflectance occurs at a material-specific critical angle θ_c defined by Equation 4.8 [323]. The critical angle correlates with the critical scattering vector q_c (Equation 4.9). To check for proper sample alignment, the control of q_C is valuable, which is known as the critical edge in reflectivity curves. For Si, the critical angle is at 0.047 deg/Å [329].

$$\sin\theta_c = \sqrt{\frac{\lambda^2 * \rho_{SLD}}{\pi}} \tag{4.8}$$

$$q_c = \sqrt{16\pi\Delta\rho_{SLD}} \tag{4.9}$$

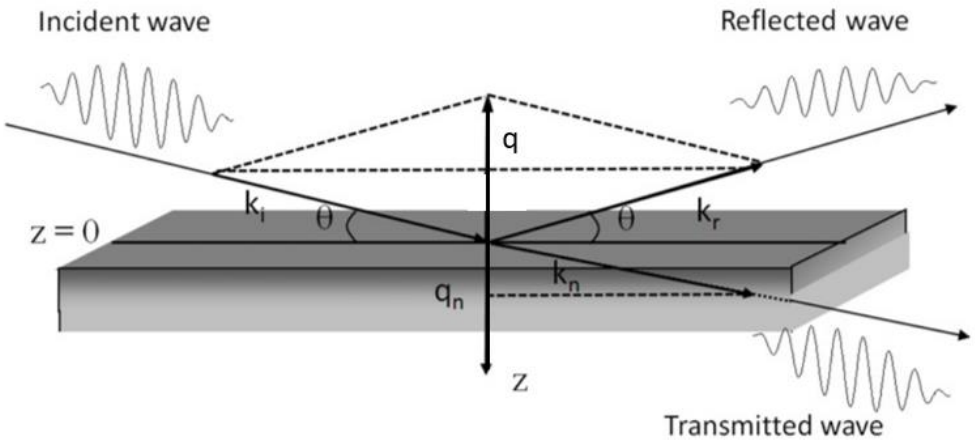

Figure 4.4: Specular reflection is defined by an incident beam with a wave vector $\vec{k_i}$ entering at an incident angle of θ_i. It is reflected and transmitted at the interface according to Snell's law. The magnitude of the scattering vector is defined by q. Modified from Ref. [323].

Surface roughness σ can modify the specular reflectivity curve and add another momentum transfer q_x in x-direction known as diffuse scattering (not illustrated in the image). It can be accounted for either with the Debye-Waller factor or the Nevot-Croce factor [330]. The measured reflectivity data as a function of q can be analysed with a one-layer model for the adsorbed protein layer as illustrated in **Figure 4.5**. Hereby, the layer thickness, density, roughness, and hydration, as well as kinetics, can be extracted. For more information on the fundamentals of neutron reflectivity, see Refs. [321–324,329,331–334].

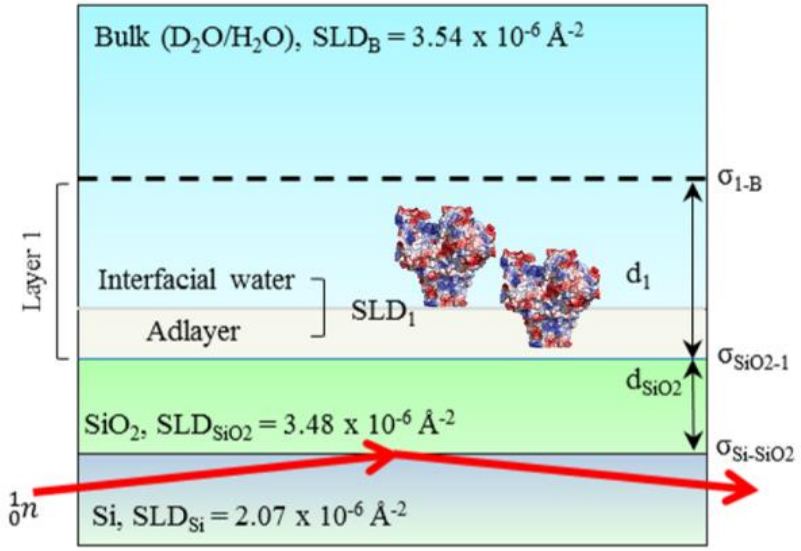

Figure 4.5: Sample structure and model composition. Each layer has its specific SLD with an unknown thickness and roughness. Prior substrate characterisation can help to determine as many parameters as possible to have fewer fitting parameters in the final model. The adsorbed proteins with the interfacial water are considered as one layer in this model. Modified from Ref. [335].

In this dissertation, protein adsorption at the solid-liquid interface is investigated with a solid-liquid flow cell [321] to obtain information about the kinetics and adsorption structure (hydration, thickness, roughness, density). For surface charge manipulation of the substrate, an electrochemical three-electrode solid-liquid NR cell consisting of a platinum grid as a counter electrode and a platinum wire at the reference electrode is utilised. The working electrode is the substrate, which is a p-doped Si NR block (see Chapter 9.3). Beam times were granted at the beamlines INTER and POLREF at ISIS/Rutherford-Appleton laboratory (UK) and at the beamline D17 at the Institute Laue-Langevin (ILL, Grenoble) (for data see Chapter 8 & 9 and Appendix A and C). For more information on the setup and characteristics of the different beamlines see the following Refs. for INTER [336,337], for POLREF [337–339], and for D17 [329,340].

In the measurement procedure, first, the salt/protein mixture in D_2O is injected into the solid-liquid cell at a flow rate of 2 mL/min using an Aladdin programmable syringe pump (model AL1000-220) and after 20 min of equilibration time, the first neutron reflectivity measurement is started. The inlet to the liquid cell is connected to a valve pump with connections to the syringe pumps and a liquid chromatography pump (L7100 HPLC pump, Merck, Hitachi), which allows for easy exchange of the solution within the (3 mL volume) solid-liquid sample cell. For solvent contrast, D_2O is exchanged with H_2O int the next step. A total of 10 ml solution is pumped through the cell at a speed of 1.5 ml/min and given at least 20 min for isotope substitution. After roughly 1 h of real-time protein adsorption, the cell is flushed with pure water to estimate the amount of irreversibly adsorbed proteins. A detailed description of the experimental setup can be found in Ref. [308]. A broad band neutron beam with wavelengths from 1 to 12 Å is used. The reflected intensity is measured as a function of the momentum transfer q. The collimated neutron beam is reflected from the silicon-liquid interface at different glancing angles of θ_0 = 0.6, 1.2, and 2.3°. For data recording, different institute-specific software packages (Nomad, mantid etc.) are used at the different beamlines.

For data analysis, the RasCAL2019 software package is used, which employs an optical matrix formalism (described in detail by Born and Wolf [341]) to fit layer models representing the interfacial out-of-plane structure. In this approach, the interface is described as a series of layers, each characterised by its scattering length density (SLD) listed in **Table 4.1**, thickness, and roughness. Interfacial roughness is implemented in terms of an error function, according to the approach by Nevot and Croce [342]. The reflectivity for an initial model is calculated based on known sample parameters, such as substrate, its oxide layer, and the solvent, and compared with the experimental data. A least squares minimisation is used to adjust the fit parameters and to reduce the differences between the model reflectivity and the data. In all cases, the simplest possible model (i.e. least number of layers, which is usually a one-layer model), which adequately describes the data, is selected. Error analysis of the fitted parameters is carried out using Rascal's Bayesian error algorithm [343,344]. The resulting plots contain fits and corresponding real space structure of the sample layer system, as well as 95 % confidence intervals (see Chapter 8 and Appendix C).

Another similar method based on the same mechanisms and principles is X-ray reflectivity (XRR). With X-rays, the electron density is measured instead of the neutron density [345]. The benefits of XRR are better q resolution and higher q values, whereas disadvantages are the induced radiation damage and less contrast variation options compared to NR [329,346,347]. Examples of XRR data are given in Appendix A.

4.3 Small-Angle X-ray Scattering (SAXS)

Small-angle X-ray scattering (SAXS) is another scattering method used to investigate protein-protein interactions in solution [348]. In this dissertation, the focus is on elastic scattering ($k_{in} = k_{out}$). The X-ray beam hereby hits the sample perpendicular to its orientation and leads to a deflection of the beam due to scattering at the proteins in solution (**Figure 4.6**). The deflection can be expressed with the momentum transfer q (**Equation 4.6**), which is directly correlated to the beam angle 2θ. In contrast to NR, θ describes half of the scattering angle (for SAXS) compared to the incident and scattering angle according to the law of reflection (for NR).

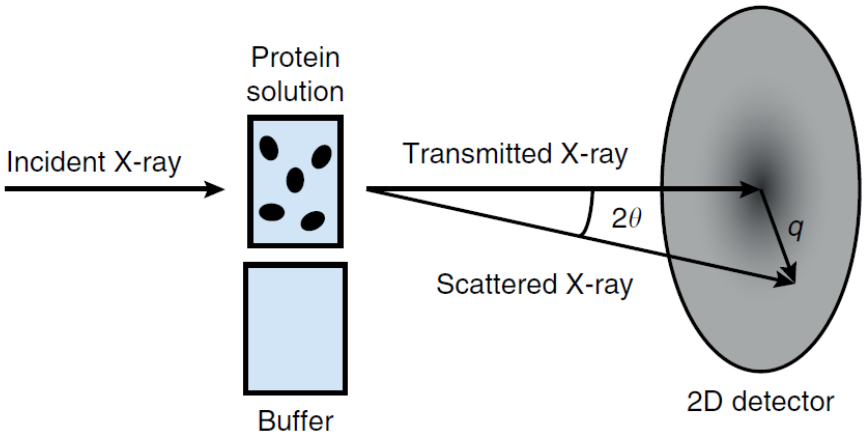

***Figure 4.6**: Schematic of a SAXS experiment. The incident beam hits the protein solution and depending on the bulk properties, a certain fraction of the beam is transmitted and scattered leading to a sample-specific interference pattern. The deflection of the beam due to scattering can be expressed with the momentum transfer q. From Ref.* [348].

The measured scattering intensity $I(q)$ as a function of q is defined in **Equation 4.10** for spherical particles [349,350].

$$I(q) = \Phi_V \, V_{\text{Particle}} \, (\Delta\rho)^2 P(q) S(q) \tag{4.10}$$

Φ_V denotes the volume fraction of the particles in solution, V_{Particle} the partial volume of the particle investigated, $\Delta\rho$ the difference in scattering cross section between particle and solvent, $P(q)$ the form factor of the particles and $S(q)$ the structure factor. $S(q)$ is proportional to the osmotic compressibility of the system and can be expressed by a series of virial coefficients. These coefficients are related to the second virial coefficient B_2 and depend on the interaction pair potential $U(r)$ between particles in solution [351]. Depending on the phase diagram, $U(r)$ can be approximated as a screened Coulomb, hard

sphere, or sticky hard sphere potential [352–355]. Below 3 mM YCl_3, a screened Coulomb potential is assumed and above 4 mM a sticky hard sphere potential [349]. B_2 defines the second viral coefficient of the bulk solution (**Equation 4.11**) [355].

$$B_2 = 2\pi \int_0^\infty dr\, r^2 \left[1 - e^{-U(r)/k_B T}\right] \tag{4.11}$$

The effective interactions between proteins are reflected in the behaviour of the reduced second virial coefficient B_2/B_2^{HS}. The second viral coefficient of hard spheres is defined by $B_2^{HS} = 16\pi R_p^3/3$, where R_p is the radius of the protein [152]. In the scope of this dissertation, experimental B_2/B_2^{HS} values were determined using SAXS at the beamline ID02 of the European Synchrotron Radiation Facility (Grenoble, France) [154]. For more information on the theoretical background of the method and derivation of the equations, the reader is referred to Refs. [349–351,356].

4.4 Ultraviolet-Visible (UV-Vis) Spectroscopy

Ultraviolet-visible (UV-Vis) spectroscopy allows the determination of the protein stock solution concentration via absorbance measurements and solution turbidity determination by transmittance measurements [357,358]. The UV-Vis spectrophotometer measures the ratio of the transmitted intensity I through the sample to the intensity of the incident light I_0, to calculate the absorbance A of the solution (**Equation 4.12**) [359].

$$A(\lambda) = \log_{10} \frac{I_0}{I} = -\log T_{UV} \tag{4.12}$$

The term I/I_0 is defined as transmittance T_{UV} and can be used to determine the turbidity of the solution and consequently the phase transitions c^* and c^{**} [360,361]. The solution is scanned from 400 to 800 nm and the average transmittance value from 700 to 800 nm is used to calculate the solution turbidity in percentage.

Most proteins, containing aromatic amino acids, show an absorbance maximum at 279 nm, thus, a range from 200 to 400 nm is scanned for each concentration determination [358].

$$A(\lambda) = \varepsilon\, c\, d_{UV} \tag{4.13}$$

Via the Beer-Lambert law [362] (**Equation 4.13**), the protein-specific extinction coefficient $\varepsilon_{0.1\,\%}^{279nm}$ (**Table 3.1**), as well as, the optical path length of the light beam through the sample d_{UV} and the concentration c of the absorbing molecule in the solution can be determined. To account for deviations in mixing and pipetting, a dilution series of 1:500, 1:250, and 1:200 samples is prepared, and the average value is defined as the final stock protein concentration. For all measurements, a quartz cuvette with a path length of 1 cm and a volume of 1 ml is used. For UV-Vis spectroscopy measurements, the Cary 50 UV-Vis spectrometer from Varian Technologies (USA) is used, which is operated with the software Cary WinUV.

4.5 Fourier Transform Infrared Spectroscopy (FTIR)

Fourier transform infrared spectroscopy (FTIR) allows the determination of molecule structures [363]. It measures how much infrared light is absorbed by the sample at each wavenumber. This depends on the possible molecular vibration and rotation modes. The dipole moment of bonds changes, if the bond length or angle in a certain vibration mode changes, which leads to the adsorption of IR light and an infrared-active mode. Depending on the composition of the molecule, the infrared-active modes and their contributions differ from each other. These translate to a signal at a specific wavenumber ν (**Equation 4.14**) and depend on the force constant between the atoms κ and the reduced mass μ.

$$\nu = \frac{1}{2\pi}\sqrt{\frac{\kappa}{\mu}} \tag{4.14}$$

Typical infrared-active modes and their designated wavenumber in proteins can be found in **Table 4.2**.

Table 4.2*: Table of typical infrared bands of proteins and their corresponding vibrations from Ref.* [364].

Designation	Frequency (cm^{-1})	Description
Amide A	3300	NH stretching
Amide B	3100	NH stretching
Amide I	1600-1690	C=O stretching
Amide II	1480-1575	CN stretching, NH bending
Amide III	1229-1301	CN stretching, NH bending
Amide IV	625-767	OCN bending
Amide V	640-800	Out-of-plane NH bending
Amide VI	537-606	Out-of-plane C=O bending
Amide VII	200	Skeletal torsion

The core piece of FTIR is the Michelson interferometer [365]. Depending on the position of the moving mirror x, different interference patterns are created between two beams, which originate from a light source (**Figure 4.7**). The detector measures the intensity of the signal $I(x)$ in form of an interferogram and via a Fourier transform, the measured intensity is converted into a wavenumber-dependent absorbance signal $A(\nu)$ in **Equation 4.15** [366].

$$A(\nu) = \int_0^\infty I(x)\ \cos 2\pi\nu x\ \ dx \tag{4.15}$$

FTIR measurements are performed with a Vertex 70 Fourier transform infrared spectrometer by Bruker (USA) and conducted with the software OPUS.

The measurements covered a wavenumber range from 800 to 4000 cm^{-1} and are performed in transmission mode with a liquid cell. For each measurement, the integrated background subtraction tool in OPUS is used to automatically subtract the background from the sample measurement. Prior to each measurement, the sample chamber is flushed with nitrogen

for 20 min and each measurement contains 256 scans. The area of interest is the amide-I region from 1600 to 1690 cm^{-1}, which correlates with the secondary structure of proteins [364,367].

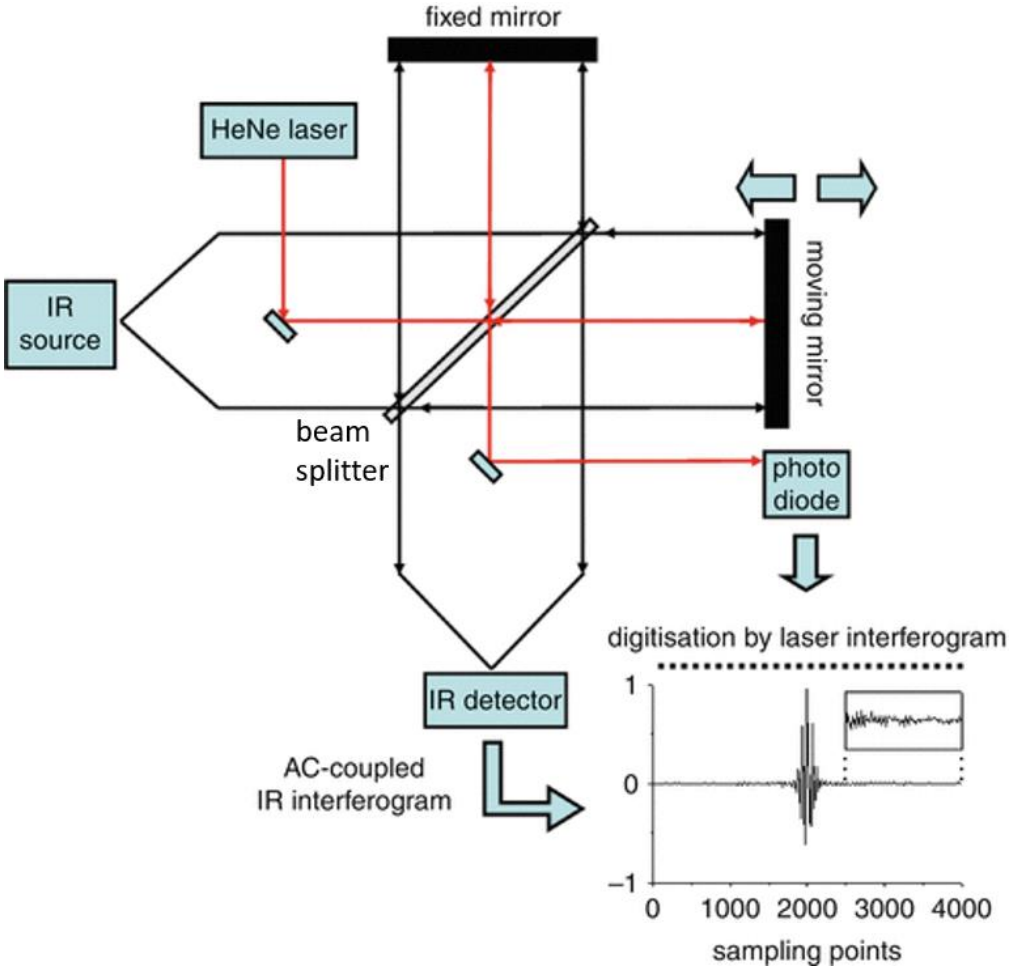

Figure 4.7: The Michelson interferometer consists of a beam splitter, a moving and fixed mirror, and a detector. The beam splitter splits the beam into two beams, which interfere with each other after reflecting on the mirrors. The moving mirror can vary its position, thus, altering the beam path length for one beam leading different interference patterns, which are recorded in the form of an interferogram by the detector. The sample is being inserted between the beam splitter and detector. A laser is included in the setup to visualise the trajectory of the IR beam and to measure the mirror position. Modified from Ref. [368].

4.6 Attenuated Total Reflection-Fourier Transform Infrared Spectroscopy

The attenuated total reflection Fourier transform infrared spectroscopy (ATR-FTIR) is a modification of the classical FTIR explained in Chapter 4.5 and allows the structure determination of molecules adsorbed to a solid interface [365]. Thus, the basic principle and main concept of a Michelson interferometer and Fourier transformation of the measured signal are identical, but the extended setup differs.

In this setup, the infrared beam enters through the solid and optically transparent substrate. At the solid-liquid or solid-air interface (depending on the sample conditions),

the beam undergoes total internal reflection due to the chosen, specific angle of incidence θ_0 illustrated in **Figure 4.8**. A photon has an electromagnetic field perpendicular to its moving direction, which extends into the optically rare medium and decays there exponentially [369]. This field is called evanescent wave [370] and is the main principle behind ATR. This evanescent wave penetrates a few microns, typically 0.5 to 2 μm [371], into the solution depending on its properties. The penetration depth d_p can be calculated by **Equation 4.16** and depends on the wavelength λ, angle of incidence θ_0, and the refractive indices of the crystal n_1 and the medium n_2.

$$d_p = \frac{\lambda}{2\pi n_1 \sqrt{\sin^2 \theta_0 - \left(\frac{n_2}{n_1}\right)^2}} \tag{4.16}$$

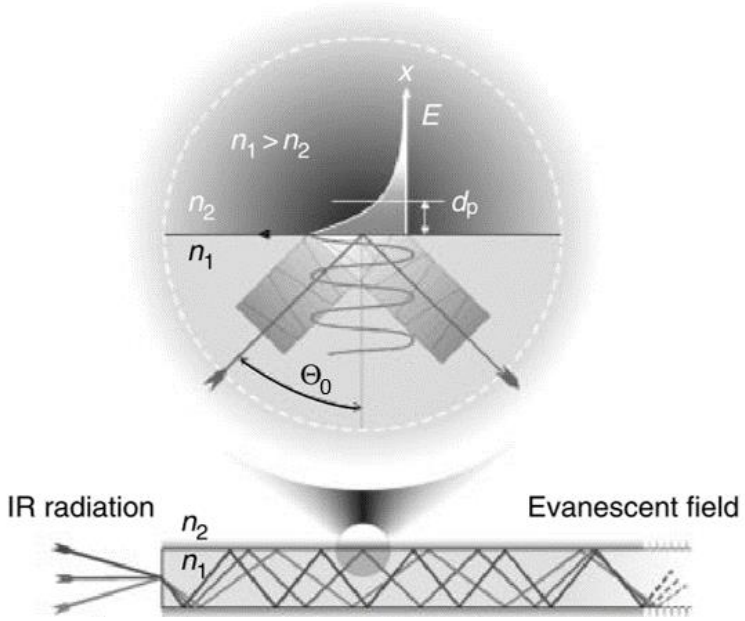

Figure 4.8: Through the total reflection of the IR beam on the substrate interface, an evanescent wave is created, which penetrates a few microns (d_p) into the bulk sample. Image is modified from Ref. [372].

The information contained in the evanescent wave sheds light on the infrared-active modes of the proteins adsorbed to an interface. For this dissertation, the structure of adsorbed proteins is investigated in real-time onto a silicon crystal submerged in water. ATR-FTIR measurements are conducted with the Thermo Nicolet iS50 with Specac Gateway ATR insert of ThermoFisher Scientific (USA) in collaboration with the Rutherford Laboratory (Didcot, UK). A solid-liquid flow cell allows quick solution exchanges and real-time structure analysis. The measurement software is Omnic and the following settings are chosen for the absorbance measurements on a Si block: gain: 1, aperture: 10, Scan No. 294, resolution: 4 cm^{-1}. The integrated background subtraction tool in Omnic is used to subtract the measured H_2O background from the sample measurement. To evaluate the influence of the bulk signal on the measured signal, after each measurement, the cell is flushed with water and the structure of the irreversibly adsorbed proteins is compared to the bulk data.

For more information on the method and literature on protein adsorption investigated with ATR-FTIR see Refs. [197,373–376].

4.7 Optical Microscopy

Optical microscopy is used to visualise and capture structures in the bulk and at interfaces, which is based on the refraction of optical light and the consequent magnification of an object [377,378]. In this dissertation, optical microscopy allows the determination of protein phases (i.e. LLPS, aggregation), as well as dynamic processes such as protein crystallisation on a microscopic level. Images and videos are taken with the Axio-Cam ICc5, usually with a magnification lens of 20x, in combination with an Axio Scope.A1 microscope by Carl Zeiss AG, which is operated with the software ZEN Lite 2012.

4.8 Atomic Force Microscopy (AFM)

Another method to visualise the surface topography and to determine surface roughness and layer formation at the air-solid interface is atomic force microscopy (AFM) [379,380]. The microscope can be operated in different modes. For the experiments, the intermittent (tapping) contact mode is applied under ambient conditions, which means that the cantilever oscillates while scanning the surface (**Figure 4.9 (A)**). In this mode compared to the direct contact mode, the contact time and force is minimised, thus reducing sample damage and lateral drag, which is ideal for loosely bound molecules, i.e. proteins [381]. The cantilever is affected by repulsive and attractive forces (**Figure 4.9 (B)**) [381].

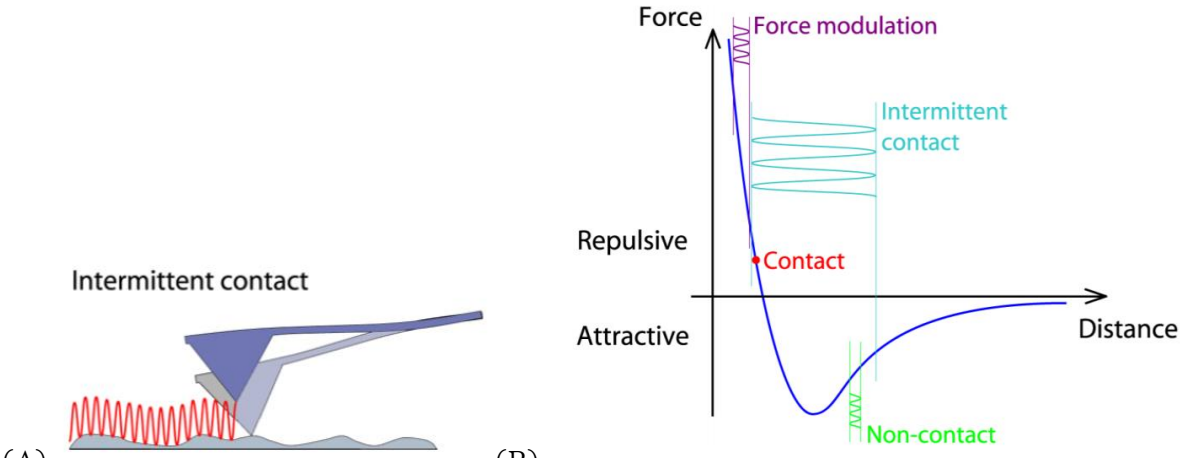

Figure 4.9: AFM imaging mode. (A) Sketch of the cantilever tip in intermittent contact mode. (B) Force-against-distance curve approaching the substrate (blue) and the interaction range of the different AFM (non-)contact modes. From Ref. [381].

At its lowest point, it experiences the strongest repulsion and can get in contact with the sample depending on the chosen set point. The deflection of the cantilever induced by the surface topography is detected via laser reflection on the backside of the cantilever to a photodiode, which translates to a height profile dependent on the cantilever's position on the sample.

For AFM measurements, the JPK NanoWizard II from JPK BioAFM/Bruker Nano GmbH (Germany) is used with the software JPK Nanowizard Control. A silicon cantilever with a tip 10 nm in diameter from AppNano (USA) is mounted on the microscope. Image analysis is performed with the software Gwyddion [382]. AFM enables the visualisation of surface-modified substrates and their qualities, which can be expressed by the surface roughness and topography.

4.9 Quartz-Crystal Microbalance with Dissipation Monitoring

The quartz-crystal microbalance with dissipation monitoring (QCM-D) is a method used for investigating the interactions and adsorption of molecules, cells, or bacteria at solid interfaces, as well as their viscoelastic properties.

The classical QCM substrate consists of a thickness-shear mode (AT-cut) quartz crystal between two metal (gold) electrodes [383,384]. By applying a voltage, mechanical deformations are induced, which lead to the oscillation of the crystal (**Figure 4.10 (A)**). This is known as the inverse piezoelectric effect meaning the transformation of electric energy into mechanical energy [385]. If the frequency of the applied voltage matches the resonance frequency F of the crystal, a standing wave within the crystal is created. F depends on the total oscillating mass including coupled water [386]. This means by the addition of mass e.g. through adsorption, a change in F (ΔF) can be detected as shown in **Figure 4.10 (B)**, which directly correlates with the mass uptake Δm according to the Sauerbrey relation (**Equation 4.17**) [387].

$$\Delta m = -\frac{C\Delta F_{\text{Sauerbrey}}}{n_f} \tag{4.17}$$

C is the mass sensitivity constant of the quartz crystal and n_f the frequency overtone. The QCM measures ΔF for different odd harmonics/overtones (3rd, 5th, 7th, 9th, 11th, and 13th) of the resonance frequency, which have different sensitivities to the mass uptake [388]. The even overtones are multiple of the eigenfrequency of the crystal, thus only resonate in the sensor and depend on the thickness of the crystal instead of the mass and are consequently not of interest. In a QCM-D setup, besides the frequency, also the dissipation D is measured. The QCM-D works in a ring-down scheme meaning the external potential is turned down intermittently and the oscillations can decay freely leading to a measurable voltage through the decaying mechanical oscillations and thus to the two measured parameters: ΔF and the dissipation (decay of voltage) ΔD [389,390]. The pulsed oscillations dissipate at a rate depending on the crystal structure, material, and adsorbed layer.

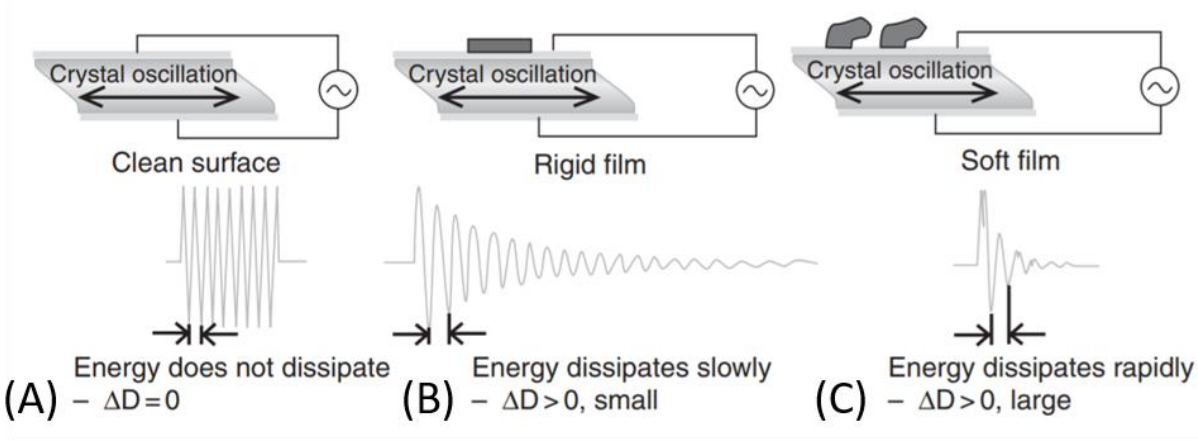

Figure 4.10: Sample-dependent QCM-D modes. (A) Bare oscillating substrate. (B) Solid-like material adsorbed to quartz leads to slow dissipation of the energy (Sauerbrey). (C) Soft material adsorbed to the substrate leads to a rapid damping/dissipation of the energy (Voigt). From Ref. [391].

Depending on the properties of the adsorbed material, it can induce strong damping of the oscillations and a high ΔD value known for viscoelastic materials [392] as illustrated in Figure 4.10 (C). The Sauerbrey relation is only valid for rigid, solid-like materials with a small ΔD ($\Delta D < 10^{-6}$) since it fails to account for this parameter [393]. Therefore, the Voigt model is introduced for viscoelastic, solid materials [392,394–396], which proteins are known to be. In this model, the change in frequency and dissipation are correlated with each other and defined in Equations 4.18 & 4.19 [395].

$$\Delta F_{\text{Voigt}} \approx -\frac{1}{2\pi\rho_0 d_0}\left\{\frac{\eta_3}{\delta_3} + d_1\rho_1\omega - 2d_1\left(\frac{\eta_3}{\delta_3}\right)^2 \frac{\eta_1\omega^2}{\mu_1^2+\omega^2\eta_1^2}\right\} \tag{4.18}$$

$$\Delta D_{\text{Voigt}} \approx \frac{1}{\pi f\rho_0 d_0}\left\{\frac{\eta_3}{\delta_3} + 2d_1\left(\frac{\eta_3}{\delta_3}\right)^2 \frac{\eta_1\omega}{\mu_1^2+\omega^2\eta_1^2}\right\} \tag{4.19}$$

The Voigt model depends on the density ρ_0 and thickness d_0 of the crystal, the viscosity η_3, penetration depth of the shear wave δ_3, and the density ρ_3 of the bulk liquid, as well as the adsorbed thickness d_1, the density ρ_1, the shear elasticity μ_1, and the viscosity η_1 of adsorbed layer. ω is the angular frequency of oscillation. Thus, with the Voigt model the thickness, density, shear elasticity, and shear viscosity of the adsorbed layer can be determined. Another model used for liquid-like viscoelastic materials is the Maxwell model (not applied in this dissertation) [392,397]. Typical ΔD values for biopolymers are between $3\text{x}10^{-6}$ and $1.1\text{x}10^{-5}$ [391]. For more information on the fundamentals of QCM-D, see Refs. [385,398–401].

For this dissertation, the QCM-D is utilised for real-time protein adsorption investigations in form of adsorbed thickness and viscoelastic properties of the adsorbed layer. The Q-Sense Analyser, as well as the Q-Sense Explorer of Biolin Scientific (Sweden) are used in combination with the standard solid-liquid flow cells in collaboration with Rutherford Laboratory (Didcot, UK). The only difference between these two devices is the number of samples, which can simultaneously be measured. The data collection is done with the QSoft

software and data analysis with the QTools software provided by Biolin Scientific. The cells are inverted to avoid sedimentation effects (i.e. substrate on top of the solution). All measurements are repeated at least three times to ensure reproducibility and to estimate real standard deviations as statistical error bars. For data analysis, the Voigt model is applied since $\Delta D > 1$ [402,403]. The used fitting parameters for the individual layers are taken from the following references for water [404,405], BSA [406–409] and BLG [410,411] (**Table 4.3**).

Table 4.3: *Material properties. Fitting constants for QCM-D data modelling from Refs.* [404–406,408,410].

Material	Density (g/L)	Viscosity (kg/(m*s))
H_2O (25 °C)	997	0.00089
H_2O (40 °C)	992	0.00065
BSA (20 mg/ml)	1003.4	0.0011
BSA (50 mg/ml)	1013.2	0.0013
BSA (powder)	1320	-
Adsorbed monolayer for BSA (1 ML)	1192.5	-
BLG (5 mg/ml) in H_2O	998	0.00101
BLG (5 mg/ml) in D_2O	1106	0.00125
Adsorbed monolayer for BLG (1 ML) in H_2O	1200	-
Adsorbed monolayer for BLG (1 ML) in D_2O	1250	-

The QCM-D cannot distinguish between adsorbed proteins and associated water. The associated water defines the water bound to the substrate, the hydration layer around the proteins, and the water trapped in the gaps of the adsorption layer [412,413]. On the one hand, this means it overestimates the adsorbed mass/thickness, on the other hand it allows the determination of the associated water through the combination with complementary methods such as ellipsometry [414], reflectometry [413], surface plasmon resonance (SPR) [415] or dual polarisation interferometry [416]. In combination with the ellipsometer, the determination of the associated water within the adsorption layer is facilitated [412,417].

4.10 pH Meter

A pH meter allows the determination of hydronium ions (H_3O^+) in solution (**Equation 4.20**) [418]. The pH scale defines solution with a pH below 7 as acidic and above pH 7 as alkaline. The pH sensor consists of two electrodes, in which the working electrode measures the diffusion of H_3O^+ (H_3O^+ gradient between the inner and outer layer of the working electrode) as shown in **Figure 4.11** and its ratio to the reference electrode (i.e. internal buffer with constant pH value) to determine the H_3O^+ concentration [418]. If a solution is acidic or alkaline, an excess of hydronium ions or hydroxyl ions (OH^-), respectively, is present [419].

$$\mathrm{pH} = -\log[\mathrm{H_3O^+}] \tag{4.20}$$

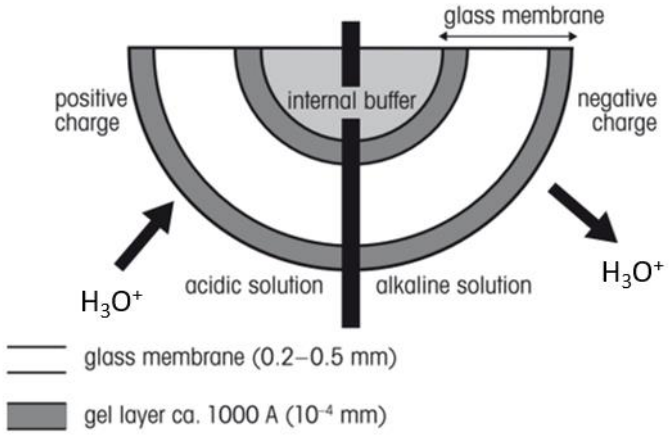

Figure 4.11: Cross-section of a pH electrode illustrating the diffusion of hydronium ions in and out of the glass membrane depending on the pH of the sample. Modified from Ref. [418].

pH measurements are performed with the pH/Ion meter S220 of the Seven Compact series from Mettler-Toledo (Switzerland). The error can be estimated to be around ±0.1 due to deviations in pipetting, concentration determination, and electrode precision. Before each measurement series, the pH meter is calibrated with buffer solutions of pH 4, 7, and 10 for maximum precision. In this dissertation, the influence of salts in protein solutions on the pH of the solutions is determined with pH meter measurements.

4.11 Contact Angle Measurements

The wettability of a surface, which is correlated to its surface energy/tension, as well as its roughness, can be determined with contact angle measurements [158,420–423]. More on the fundamentals of wetting of surfaces can be found in Chapter 2.4. To determine the contact angle, a liquid droplet is put on the interface, which is usually water, but also other solvents can be used [424]. Depending on its spreading or contracting behaviour, the droplet has a different angle with the interface for different surfaces.

$$\gamma_{\mathrm{lv}} \cos\theta_{\mathrm{Y}} = \gamma_{\mathrm{sv}} - \gamma_{\mathrm{sl}} \tag{4.21}$$

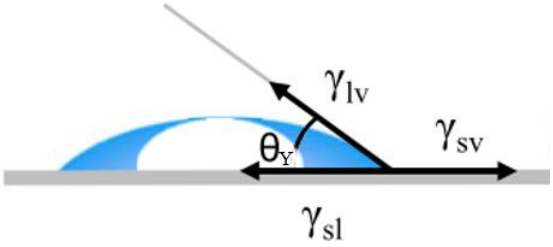

Figure 4.12: Determination of the contact angle θ_Y with a liquid droplet on a solid interface depending on three interfacial tensions. Modified from Ref. [423].

The Young equation (**Equation 4.21**) [425] describes the dependence of the contact angle θ_Y on three interfacial tensions, namely the liquid-vapor γ_{lv}, solid-vapor γ_{sv}, and

solid-liquid γ_{sl} interfacial tensions (**Figure 4.12**). Here, the solid-liquid interfacial tension γ_{sl} is of special interest, from which the substrate properties (e.g. roughness, surface energy etc.) can be determined. Contact angle measurements are utilised to check the quality of the SAM coatings and of the ozone cleaning. Ozone cleaning makes the surface (here: Si or Au) super-hydrophilic [426], thus should lead to total wetting and SAM-coated surfaces should exhibit a SAM-specific contact angle (listed in Chapter 3.3.2.3), if the SAM growth was successful. Note that the term wetting has two definitions in this dissertation. In the context of contact angle measurements and surface free energies, it describes the ability of a liquid to maintain contact with a solid substrate [157], whereas wetting discussed in the context of protein adsorption (Chapter 6) defines an excess surface adsorption of an adsorbate (e.g. proteins) due to long-range interactions [166].

II. RESULTS

5 Protein Adsorption Reflecting Bulk Re-entrant Behaviour

The following chapter is based on Ref. [427] and was conducted in collaboration with Dr. Daniel Stopper and Prof. Dr. Roland Roth of the Institute of Theoretical Physics (University of Tuebingen), who performed the theoretical calculations presented in this chapter. B_2/B_2^{HS} measurements were conducted and analysed by Dr. Michal Braun.

5.1 Background

The interactions of proteins, with their inherent heterogeneity and differently charged patches, in addition to hydrophilic and hydrophobic regions and dispersion forces, are very complex [1]. While obviously required for their biological function, this complexity of the interactions is very demanding for a quantitative physical understanding. Particularly difficult is the connection to the associated mesoscopic and macroscopic behaviour, with enormous implications for a range of rather diverse fields. These include the understanding of protein crystallisation [115,428,429], as well as various forms of aggregation [430,431], whether biologically desired [432–434] or related to diseases such as Alzheimer's [435], Huntington's, or prion diseases (e.g., Creutzfeldt-Jakob disease) [436]. A further level of complexity is added by the frequently heterogeneous environment in soft and biological systems, often with internal interfaces, at which adsorption might take place, co-existing with fluid (bulk-like) regions. While in numerous investigations the phase behaviour of proteins has been investigated [430,437,438], it remains an important challenge to understand protein-protein interactions in a microscopic picture and to predict the resulting macroscopic thermodynamic behaviour of proteins in a solution and at interfaces and how these behaviours correspond or differ.

For the manipulation of the bulk phase behaviour, different strategies have been demonstrated. On the one hand, cosolvents such as glycerol can help to avoid protein aggregation and cluster formation by stabilisation of the protein solution [439]. On the other hand, enzymatic crosslinking [440] or the use of trivalent ions such as yttrium cations can be employed to trigger bridge formation between globular proteins, which can lead to cluster formation, re-entrant condensation (RC), and liquid-liquid phase separation (**Figure 5.1**) [80,181]. An aggregation regime II occurs in between two salt concentrations c^* and c^{**} as illustrated in **Figure 5.1**. The physical mechanisms behind the observed RC behaviour are the effective inversion of protein charge (**Figure 5.1 (a)**) and a cation-mediated anisotropic attraction [80,209].

Protein adsorption at solid-liquid interfaces occurs in many natural processes, and its understanding is crucial in many fields, ranging from biotechnology, biology,

pharmacology, and medicine to environmental science and food processing with relevance in many applications [1]. In particular, it is the first step in numerous biological processes, such as the blood coagulation cascade, transmembrane signalling, and adhesion of particles bacteria or cells) [1], and therefore plays a key role in biomedical devices, including biosensors, biochips, soft contact lenses, and biomaterials for implants [53]. Bovine serum albumin (BSA) is considered as one of the model proteins for adsorption investigations [441]. In solution, BSA is a globular protein with well-characterised physicochemical properties [75]. Serum albumin is the most abundant blood protein in mammals, and its adsorption has been intensely investigated with different methods under various conditions [1,74,442]. For complementary investigations on BSA adsorption on solid surfaces without multivalent ions, the reader is referred to the following references on total internal reflection fluorescence (TIRF) [443], fluorescence recovery after pattern photo bleaching (FRAPP) [444], Förster resonance energy transfer (FRET) [445], neutron reflectivity (NR) [74,326,446], non-invasive supercritical angle fluorescence (SAFM) [215], mass spectroscopy (MS) [447], differential scanning calorimetry (DSC) [187,447], circular dichroism (CD) [187], infrared reflectivity (IR, such as FTIR-ATR [448] and GA-FTIR [449]), optical waveguide light mode spectroscopy (OWLS) [442], scanning force microscopy [450], quartz crystal microbalance (QCM) [449] and ellipsometry [316,451].

Nevertheless, controlling the interactions and connecting them to the bulk behaviour remains a challenge. In this context, the use of multivalent ions [76,77,452] offers a viable path, with the unique opportunity to tailor and even invert the charge state of proteins as well as surfaces by overcompensation [80,147,181], which has been demonstrated to be a rather universal approach [150].

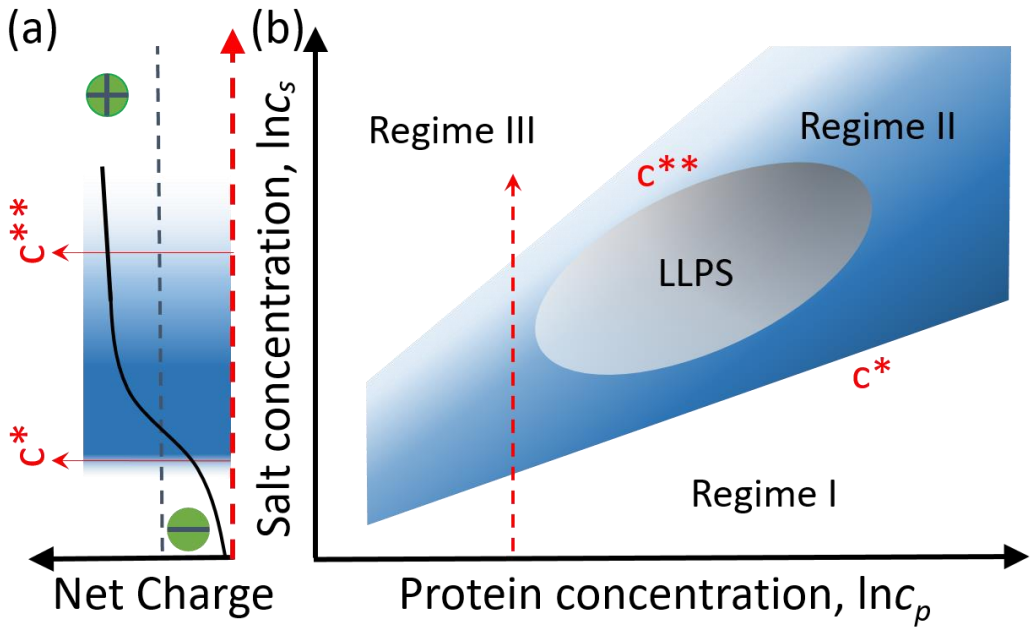

Figure 5.1: (a) Charge inversion of BSA as a consequence of adding trivalent yttrium ions. (b) Schematic of the bulk phase diagram of BSA and YCl_3 (modified from Ref. [79]) showing a liquid-liquid phase separation (LLPS) and re-entrant condensation. The dashed red arrow indicates the path taken in the experiments.

In this chapter, the use of multivalent ions (Y^{3+}) to control the interaction of BSA with SiO_2 interfaces is demonstrated. Re-entrant interface adsorption behaviour is found, reflecting in an intriguing way the bulk phase behaviour (**Figure 5.1 (b)**). Furthermore, both bulk and interface adsorption behaviour can be modelled consistently by the statistical mechanics of ion-activated patches [209].

5.2 Protein Adsorption

5.2.1 Ellipsometry Measurements

Based on real-time ellipsometry data of the adsorption kinetics, the adsorption layer thickness d is extracted in the long-time limit (saturation after ~ 60 min) and plotted in **Figure 5.2** as a function of c_s/c_p. Both BSA and SiO_2 surfaces are net negatively charged in water (no added salt). Under these conditions, the electrostatic repulsion among the proteins dominates the solution compared to the repulsion between the proteins and the solid surface leading to a minimum of the protein adsorption. An evaluation of the ellipsometry data shows that under these conditions only a d of 1.2 ± 0.25 nm is adsorbed. Upon increasing c_s to 1.3 mM (still in the clear regime I as illustrated in **Figure 5.1 (b)**), d increases to 6.29 ± 1.03 nm (solid triangles in **Figure 5.2**).

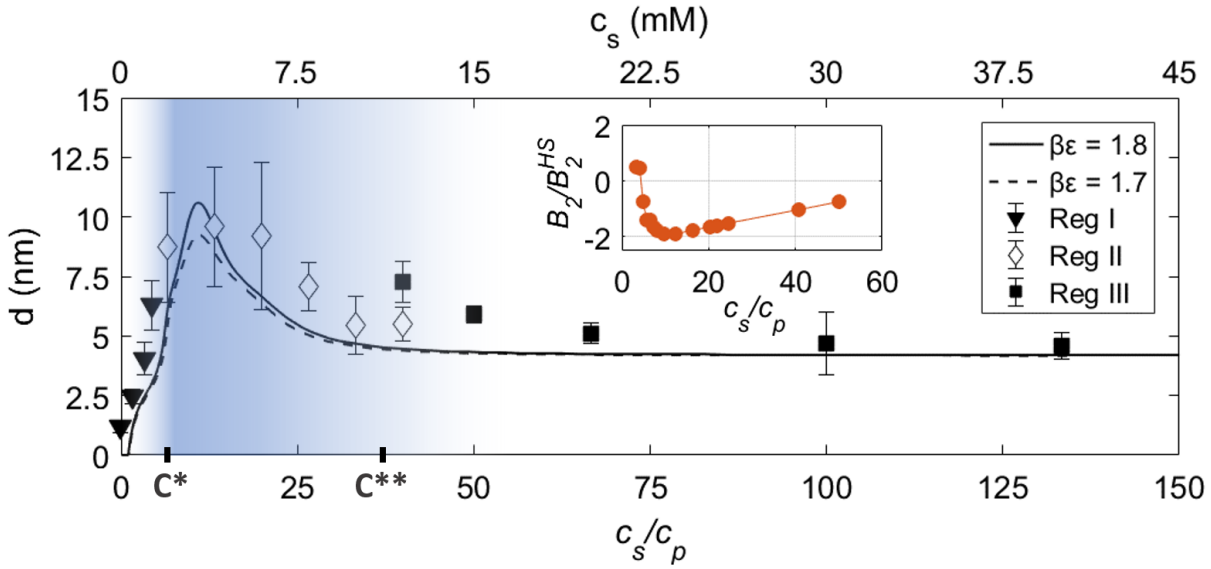

***Figure 5.2**: Individual symbols: adsorbed protein layer thickness d extracted from ellipsometry as a function of c_s/c_p. c* and c** denote the phase transitions of the bulk solution [80] (**Figure 5.1 (b)**]) Note that, around c**, there is an experimental difference between the data in regime III vs regime II. The centrifuged samples in regime II reflect the adsorption trend for overall lower adsorption values due to the removal of big clusters in bulk solution but still follow the same adsorption trend. In addition, the top c_s axis is included showing the absolute c_s in the system (at c_p = 20 mg/ml). The blue-shaded area shows the approximate range of the bulk turbidity. Solid and dashed lines: protein adsorption based on DFT calculations as bore out by the ion-activated attractive patch model, while neglecting long-range forces, as a function of c_s/c_p for two different values of βε. Inset: B_2/B_2^{HS} is the reduced second virial coefficient obtained via SAXS measurements.*

In this system, a R_p of ~3.5 nm is assumed [453] and one monolayer (ML) is defined to be equivalent to $d \approx 4$ nm, corresponding in regime I at 1.3 mM to the formation of $d > 1$ ML.

Note that depending on the experimental technique different values are reported; $R_p \sim 3.5$ nm is a reasonable number in the present context [209,453]. Here, d is defined as an effective measured layer thickness by assuming the protein density profile to be a step function. It is clear from other methods that this is not the case but the ellipsometric measurement is not sufficient to determine the full profile, which decays into the bulk. Thus, the working definition of a monolayer equivalent in this system is helpful to introduce. The single layer area per molecule measured by Su et al. was 4400 Å^2 [446]. By assuming a volume fraction of 1, a monolayer equivalent of $d \sim 4$ nm can be defined.

In regime II, d increases towards a maximum value of 9.59 ± 2.5 nm (> 1 ML) at c_s = 4 mM (open diamonds, **Figure 5.2**). At still higher c_s, d decreases down to ~6 nm, approaching the upper boundary of regime II at c^{**}. Note that in regime II (open diamonds) the bulk solution is centrifuged before the adsorption experiments, which explains the jump of d in the transition region between regimes II and III. This is done because the solution in regime II is too turbid due to extensive protein cluster formation, which causes massive bulk light scattering and a lack of sensitivity of the ellipsometer. Both data sets at c_s/c_p = 40 (centrifuged and non-centrifuged) are shown to account for the experimental difference, which, importantly, does not affect the overall adsorption trend.

In regime III close to c^{**}, d is 7.28 ± 0.87 nm at c_s = 12 mM, but with increasing c_s, d decreases down to a plateau value of 4.5 nm above 30 mM (solid squares in **Figure 5.2**). d then corresponds to slightly less than one full ML. These experimental results are supported by complementary NR and QCM-D measurements (**Table 5.1**).

***Table 5.1**: Effective adsorption layer thickness d as deduced from NR and QCM-D. Note that, while technically NR is more sensitive to thickness and density of the protein layer independently and QCM-D to the thickness-dependent surface coverage and hydration, for mutual comparability of the techniques including ellipsometry, d is normalised to a layer of pure protein. Importantly, while there are certain differences in the effective thickness, as expected from experiments using rather different methods, the overall trend of an adsorption maximum in regime II and thus a re-entrant adsorption behaviour is confirmed. Note also that data of d_{rinsed} are taken against pure water (as opposed to protein solution) which corresponds to a rinsing step. In this case, regime II still exhibits a maximum consistent with ellipsometry and QCM, but not quite as high, which implies that the 2nd ML is (partly) rinsed away and is to be considered reversibly bound.*

			QCM-D		NR
c_s (mM)	c_s/c_p	Regime	d (nm)	d_{rinsed} (nm)	d_{rinsed} (nm)
0	0	I	3.19	1.08	1.81
4	13.33	II	17.40	7.93	3.47
40	133.33	III	7.02	6.39	2.31

5.2.1 QCM-D measurements

For the QCM-D measurements as for the ellipsometry measurements, c_p is set to 20 mg/mL and T = 20 °C. c_s is varied such that regime I, II and III are entered. d is extracted by using a Voigt-Kelvin model fit (more information in Chapter 4.9) [396], which describes the adsorption of BSA on the silicon dioxide well. In terms of direct comparison (absolute

values of *d*) of the QCM-D data to the ellipsometry data, one has to bear in mind that from the QCM-D data the calculated protein thickness adsorbed to the interface also includes its hydration layer (trapped water molecules) [402] which explains why QCM-D gives slightly higher values for *d*. An additional rinsing step with H_2O (see next column in **Table 5.1**) illustrates that the first protein monolayer seems to be irreversibly attached to the surface, whereas adsorbed proteins above one ML are reversibly bound and mostly rinsed away. Even after rinsing the surface with pure water, a much weaker but still obvious re-entrant adsorption behaviour can be observed.

5.2.2 NR Measurements

Specular neutron reflectometry (NR) measurements are carried out using the INTER reflectometer at the Rutherford Appleton Laboratory (Oxfordshire, UK), using neutron wavelengths from 1.5 to 16 Å. The reflected intensity is measured at two angles of 0.7° and 2.3° as a function of the momentum transfer, $q_z = (4\pi\sin\theta_0)/\lambda$, where λ denotes the wavelength and θ_0 is the incident angle.

The measurements are performed at c_p = 20 mg/mL and T = 20 °C by varying c_s in **Table 5.1**. In terms of direct comparison (absolute values of *d*) of the NR data to the ellipsometry data (**Figure 5.2**), one has to bear in mind that the NR data shown is obtained after rinsing with pure water. Due to weak contrast, a direct extraction of *d* from the data against protein solution is not possible, thus only d_{rinsed} (i.e. measured against pure water) is presented in **Table 5.1**. The calculated effective protein thickness is the product of the thickness and volume fraction, which makes it comparable to ellipsometry data. Both QCM-D and NR data show a similar much weaker, but still detectable, re-entrant adsorption behaviour after rinsing. The slightly increased *d* obtained via QCM-D compared to NR can be explained by the QCM-D inability to distinguish between the BSA molecules adsorbed and their hydration shell, but this does not influence the overall adsorption trend or the general conclusion.

5.3 Bulk Interactions

The effective interactions $V_{eff}(r)$ between proteins are reflected in the behaviour of the reduced second virial coefficient B_2/B_2^{HS}. B_2 defines the second viral coefficient of the bulk solution. Experimental B_2/B_2^{HS} values (inset, **Figure 5.2**) are determined using small-angle X-ray scattering (SAXS) on the beamline ID02 (ESRF, France) similar to Ref. [154]. To understand the adsorption behaviour, it is important to realise that the behaviour of *d* is closely related to that of B_2/B_2^{HS} of the bulk solution (inset, **Figure 5.2**). In regime II, the value of B_2/B_2^{HS} is clearly negative, indicating a strong overall attraction between proteins compared to regimes I and III. Note that this is not the definition of the regimes nor its boundaries but rather is an important observation. The net attraction between proteins is reflected by a sharp adsorption maximum.

5.4 Theoretical Results

This observation indicates that the protein adsorption in this system is closely related to the bulk behaviour, which can successfully be accounted for by the model for ion-activated attractive patches as a mechanism for interactions in protein-salt mixtures [209]. This model is formulated within the Wertheim theory for associating fluids [208,454–461] and treats proteins as hard spheres with radius R_p and M distinct and independent binding sites (patches) [208]. These sites can be occupied by salt ions, thereby activating a given patch (ion binding). The occupation probability of a site is given by $\Theta = [1 + \exp(\beta\varepsilon_b - \beta\mu_s)]^{-1}$, where μ_s denotes the salt chemical potential, $\beta = (k_B T)^{-1}$, and ε_b the binding energy [209]. A bond between two patches of distinct proteins is possible only if an activated patch meets a deactivated one (ion bridge). As a result, c_s controls the protein-protein interactions. Note, however, that only the proteins are represented explicitly in this model. This implies that c_s as a function of μ_s cannot be predicted self-consistently within this approach. The location of the minimum of the experimentally determined B_2/B_2^{HS} is used in order to calibrate $c_s(\mu_s)$.

The resulting phase diagram of the model accounts for key features of the rather rich experimental phase diagram, such as re-entrant condensation and a closed-loop LLPS binodal schematically, which is shown in **Figure 5.1 (b)** [209]. The model also allows predictions of regions in the phase diagram, which are populated by protein clusters. A quantitative measure for this is Φ, the fraction of proteins in clusters. In the present investigation, it is assumed that in region II at least 20 % of the proteins are part of clusters, i.e., $\Phi = 0.2$ to define c^* and c^{**}. While the experimental results presented here suggest that the bulk behaviour dominates the adsorption trend, the key point is the protein adsorption at a charged planar wall, which implies breaking the translational symmetry of the system. To this end, the classical density functional theory (DFT) is employed [217], which provides a powerful and well-established framework to investigate inhomogeneous density distributions.

Within the DFT, one can show rigorously [217] that a functional

$$\Omega[\rho] = \mathcal{F}[\rho] + \int dr\, \rho(r)[V_{\mathrm{ext}}(r) - \mu] \tag{5.1}$$

of the inhomogeneous density profile $\rho(r)$ exists and takes its minimum, the grand potential, at the equilibrium density distribution. Using a DFT formulation of the Wertheim theory [462] based on the fundamental measure theory (FMT) for hard spheres [463,464], d is calculated at the SiO_2-water interface. This interface is charged and strongly attracts yttrium ions, which in turn attract proteins towards the wall (**Figure 5.3 (a)**).

Effectively, this can be described by a short-ranged external potential $V_{ext}(z)$ acting on the proteins, where z is the distance normal to the SiO_2 wall. $\beta V_{ext}(z) = 0$ is set for $z < 0$ in order to represent a steric repulsion between proteins and the substrate and $\beta V_{ext}(z) = -\beta\varepsilon M\theta\xi(z)$ for $z \geq 0$. $\xi(z)$ accounts for the rather short-ranged attraction induced by the yttrium ions condensed on the wall—which is in line with recent experimental observations [452].

Here, a Gaussian form $\xi(z) = \exp[-0.5(z/R_p)^2]$ is employed with the range of attraction being roughly one protein diameter, which effectively accounts for the range of the screened electrostatic interactions between ions and the wall and between ions and proteins.

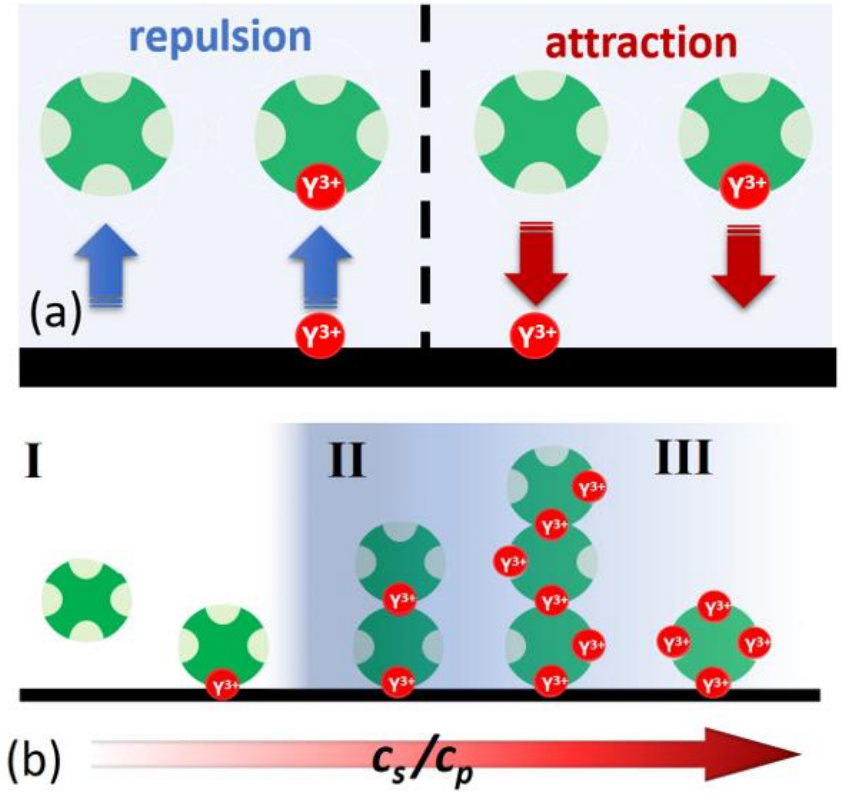

Figure 5.3 (a) Illustration of the different interaction mechanisms of the proteins, salt, and interface. (b) Sketch of protein adsorption on the attractive surface by increasing c_s/c_p.

The strength of the external potential depends on μ_s via the occupation probability Θ of the protein binding sites. This form can be motivated by the following arguments. A sketch is presented in **Figure 5.3**. At low c_s, when $\Theta \to 0$, only a few proteins are subjected to the attraction of the wall induced by the ions. As c_s increases, more ions mediate the attractions between the wall and the proteins. At the same time, the protein-protein attraction increases accordingly, which leads in turn to an increase in d. At very high c_s ($\Theta \to 1$), the mechanism for the wall attraction remains, while the protein-protein interaction becomes weak, since a majority of the binding sites are occupied so that salt ions can no longer cause a patchy attraction between the proteins. Therefore, one expects from the model ~1 ML of proteins to be adsorbed on the wall in the limit of $\Theta \to 1$.

In **Figure 5.2** (solid and dashed lines), the value of d in nanometres is shown as a function of c_s/c_p for a volume packing fraction $\eta = (4\pi/3)\rho_p R_p^3 = 0.0078$, corresponding to $c_p = 20$ mg/ml along the path indicated by the red dashed arrow in **Figure 5.1 (b)**. $M = 4$ and $\varepsilon_b = -5$ are chosen [209]. The protein adsorption is computed from the inhomogeneous density profile $\rho_p(z)$, obtained via DFT for the activated patch model.

In order to compare to experiments, d is defined as the distance from the wall where $\rho_p(z)$ is at least 50 % higher than the bulk density ρ_p. For suitable values of $\beta\varepsilon$ [1.8 (solid curve) and 1.7 (dashed curve)], very good, semiquantitative agreement between theory and experiment is found. For high values of c_s, a finite d assigned to ~1 ML is found in agreement with the experiments. Note that the fraction Φ of proteins in clusters in the bulk system is directly related to the behaviour of the layer thickness d of proteins at the wall.

The theoretical results confirm that ion binding at the protein surface drives the experimentally observed non-monotonic adsorption behaviour, thereby reflecting the underlying bulk interactions. In particular, the remarkable agreement between the experiment and theory (considering, in particular, the few parameters involved) emphasises that the presented model of ion-activated attractive patchy particles, subjected to an effective external wall potential, captures the essential effects of the protein adsorption at a charged surface in the presence of multivalent salt ions.

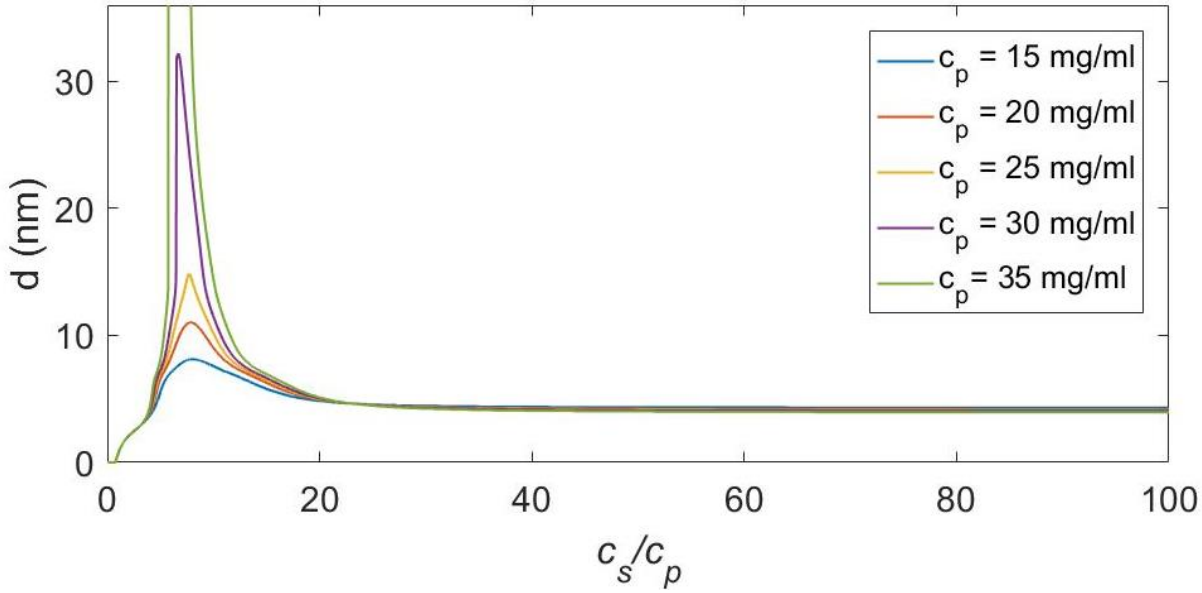

***Figure 5.4**: Theoretical calculations showing changes in d upon increasing c_p from 15 mg/ml up to 35 mg/ml. The green curve diverges to infinity due a wetting transition.*

The model is kept intentionally simple with a minimum number of parameters, which helps to identify the key mechanism responsible for the behaviour of the system, namely, the ion-activated patchy interactions of the proteins. Importantly, using this model allows the exploration of the adsorption behaviour of the system in different parts of the bulk phase diagram. Increasing the protein concentration approaching the LLPS region, the adsorbed film thickness d increases. A complete wetting regime, in which d becomes even macroscopically thick, is found (**Figure 5.4**). Qualitatively, a similar behaviour as shown in **Figure 5.2** for the experimental data is observed with a maximum for $c^* < c_s < c^{**}$.

5.5 Summary

In conclusion, it is demonstrated that multivalent ions can be employed to control not only the bulk interactions and bulk phase behaviour of proteins such as BSA, but also its adsorption behaviour at a charged interface such as water-SiO_2. Re-entrant effects at the interface are observed, which reflects the bulk behaviour, measured by B_2/B_2^{HS}, in an intriguing way. Furthermore, the experimental data can be explained and understood by theoretical calculations within the framework of classical DFT based on a model of ion-activated patchy interactions and their associated statistics. In addition to the fundamental implications of the first-time demonstration of this ion-activated patch model in the context of the symmetry break brought about by an interface, this approach may pave the way to controlled nucleation at interfaces in regime II and possibly protein crystallisation under new conditions.

6 Wetting Transition at Bulk Instability

The following chapter is based on Ref. [465] and was conducted in collaboration with Dr. Daniel Stopper and Prof. Dr. Roland Roth of the Institute of Theoretical Physics (University of Tuebingen), who performed the theoretical calculations presented in this chapter.

6.1 Background

Controlling and understanding protein adsorption is key to a number of phenomena in biomaterial science and medical devices such as biocompatibility, osseointegration, inflammation and contamination [42,165,466]. One way to systematically investigate the underlying interaction mechanisms between proteins and solid surfaces is to alter the surface chemistry and topography e.g. through the use of alloys of different composition, self-assembled monolayers (SAMs), membrane bilayers, polymer brushes, smart biomaterials or tissue engineering [53,153,163,220,466]. An interesting, and in fact efficient, alternative to modifying the surface properties would be to tune protein adsorption by exploiting suitable thermodynamic conditions, i.e. conditions that favour a certain level of adsorption driven by the underlying bulk phase behaviour.

Adsorption at solid-liquid interfaces is the result of sufficiently attractive substrate-fluid and intermolecular fluid interactions. Strongly enhanced or macroscopic adsorption may in particular result in the vicinity of bulk instability regions, a phenomenon called 'wetting' that is mostly explored in statistical physics of 'simple liquids' [467–469]. Although the bulk phase behaviour of protein solutions shares intriguing similarities with that of suspensions of spherical colloids [430,470–472], it is not clear *a priori* to what extent surface phenomena such as wetting can be transferred to solutions of proteins, in view of their significant complexity and patchy nature [209,219,428,429,437,438,473,474]. Furthermore, the tailoring of adsorption *beyond* the monolayer would be of significant importance for the understanding of e.g. heterogeneous nucleation of crystals or for improving the biocompatibility of implants by pre-adsorption, which makes this investigation not only important fundamentally, but also for applications.

Salts provide a versatile way to manipulate the interactions. Specifically, *multivalent* ions can induce novel effects at interfaces, going well beyond mean-field behaviour [156], such as strong coupling through ion-ion correlations [452,475], micelle formation at liquid-liquid interface transitions [476], elemental selectivity at interfaces [477] and charge inversion in phospholipids [478], in polyelectrolytes [479], and DNA complexes [475]. In polyelectrolyte brushes, multivalent ion bridging is found to cause diminishing lubrication properties [480] illustrating the versatile role multivalent ions can have.

For proteins, multivalent ions have proven to be a powerful tool in inducing a broad variety of interactions and associated phase behaviour [80,149]. In order to provide a basis for the adsorption investigations, first, the bulk behaviour of protein solutions is explained. The phase diagram of bovine serum albumin (BSA) and yttrium chloride (YCl_3) in water is shown in **Figure 6.1**. BSA in aqueous solution is net negatively charged at neutral pH [481]. YCl_3 is particularly suitable as a model salt since it has relatively weak effects on the pH compared to other multivalent salts. The addition of multivalent salts, such as YCl_3, to the BSA solution screens repulsive electrostatic forces due to binding of multivalent cations to the protein surfaces. At the same time, this ion-binding process induces highly directional attractive protein-protein interactions resulting in the formation of protein bridges mediated by cations [209]. At sufficiently low salt concentrations, the solution remains clear (regime I). If c_s is increased, protein clusters give rise to a transition from a clear to a turbid solution (regime II) after crossing a boundary denoted c^*. Importantly, regime II also features a (metastable) closed-loop liquid-liquid phase separation (LLPS) into a protein-poor and protein-rich phase, which is exploited here, and can also facilitate protein crystallisation [147,149,181]. Upon further increasing c_s, the system undergoes charge inversion causing the protein clusters to dissolve. This process is known as re-entrant condensation (RC), which is defined by a second transition (c^{**}) from a turbid to a clear solution (regime III) [80,150]. Note that the concept of charge inversion is not unique to BSA, but has been shown for several proteins, e.g. BLG [482,483]. The LLPS phase boundaries depend on the solution temperature T, as indicated in **Figure 6.1 (a)**.

Several aspects of the phase behaviour of proteins in solution can be understood with statistical physics of colloidal fluids [470,471]. In particular, models that treat proteins as patchy particles, interacting via highly-directional forces, turned out to be very successful [428,429,437,438,473,474,484,485]. Anisotropy in protein-protein interactions is the result of, *inter alia*, non-uniformly distributed surface charges, presence of hydrophobic and hydrophilic zones on the protein surface, or the formation of hydrogen bonds. The behaviour of proteins in the presence of multivalent salt can be successfully modelled as patchy colloids, where the patches are activated by cations [209]: in addition to a hard-sphere-like core repulsion, a patch-patch interaction is mediated by ions which can activate the sites by chemically binding to the protein surface; a bond between two distinct proteins is then only possible if an activated patch meets a deactivated one. The resulting phase diagrams, which can be obtained from Wertheim's perturbation theory for associating particles [454,456–459], are in excellent qualitative agreement with the experiments considering the coarse-grained nature of the model. This includes RC in terms of protein clusters and a closed-loop LLPS region. In line with experiments [181], critical protein volume fractions are predicted to occur at values below 10 %, and volume fractions of the high-density protein phase around 20 %. This is indeed a prominent feature of patchy fluids [206] and cannot be understood with fluids interacting via isotropic forces where liquid densities often reach volume fractions of 40 % or beyond [469].

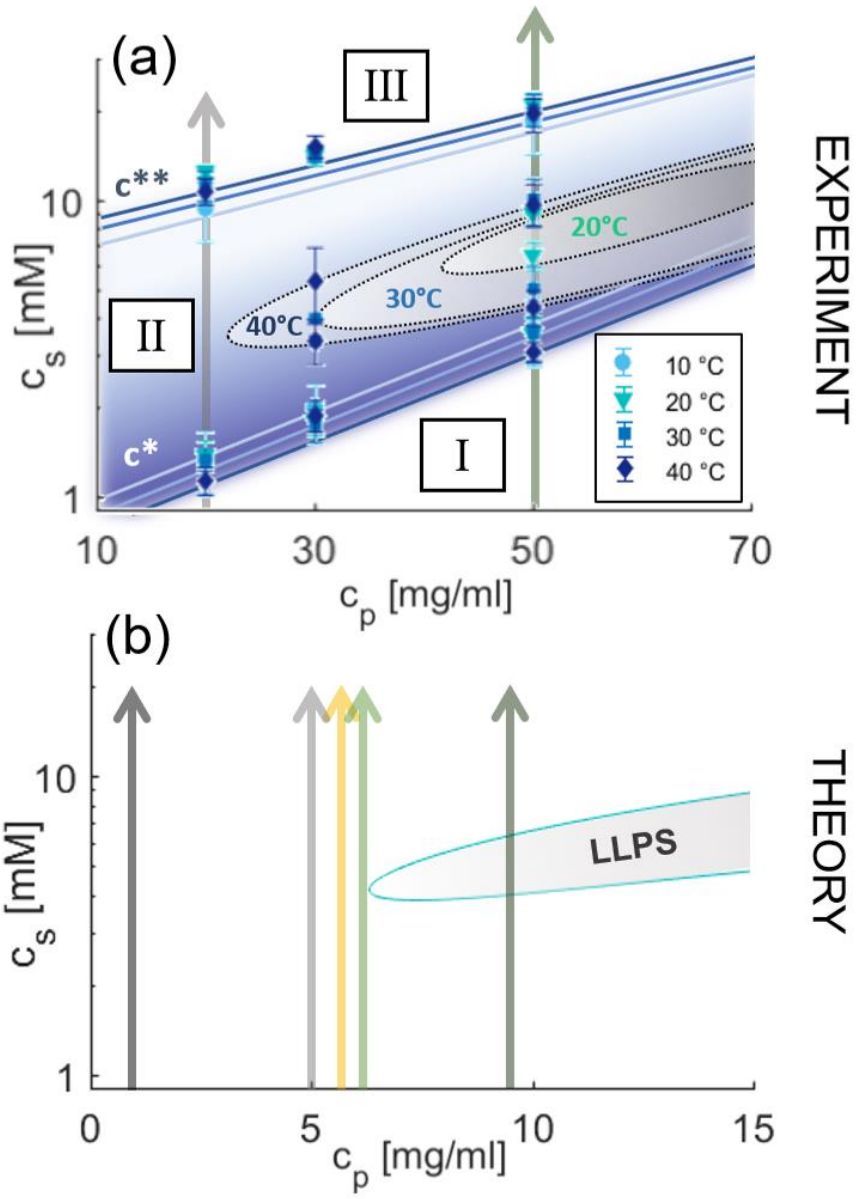

Figure 6.1: *Phase diagram. (a) Experimental phase diagram of BSA (c_p) and YCl_3 (c_s) for various temperatures T. The lines c* and c** determine the boundaries of the region where the solution is turbid and dominated by large protein clusters (blue area, regime II). It broadens slightly with increasing T. The vertical arrows indicate the paths taken in the adsorption experiments. The LLPS region (grey-shaded areas) starts to occur at 20 °C and quickly broadens with increasing temperature. Note that the grey-shaded areas do not display the coexisting densities but the regions at which LLPS is observed. The experimentally measured values of the phase boundaries can be found in* ***Table 6.1****. (b) Theoretical phase diagram of BSA (c_p) and YCl_3 (c_s) based on theoretical DFT calculations in Ref. [209]. The obtained phase diagram does not contain an explicit temperature dependence but can be compared to the experimental 20 °C data. The vertical arrows indicate the paths taken in the calculations for* ***Figure 6.6****. Note that due to the intentionally simplified nature of the model with only few parameters the agreement with experiment is only semi-quantitative.*

In this chapter, the control of enhanced adsorption beyond a monolayer is demonstrated and it is explored if the wetting phenomena, known from simple fluids, can also be exploited in the rather complex system of a protein solution exhibiting LLPS in the presence of multivalent salts in order to induce enhanced protein adsorption at a planar interface.

Wetting is driven by a combination of underlying bulk thermodynamics and sufficiently strong salt-induced wall-protein attractions. The experimental and theoretical implications and potential applications are discussed in a broader context of wetting by patchy particles, for which the present system is an interesting realisation.

6.2 Bulk Behaviour

The general bulk behaviour of globular proteins and multivalent ions has been extensively investigated over the past decade [80,149,150,153,241,486]. As a first step, the bulk phase behaviour of this specific system and its temperature dependence is determined. This is an essential key in order to draw meaningful conclusions regarding the connection between adsorption and bulk thermodynamics. The temperature-dependent phase diagram shown in **Figure 6.1 (a)** is generated with the Thermostat C from Eppendorf for a stable temperature control. The experimental results are summarised in **Figure 6.1 (a),** while the theoretical phase diagram calculated within the model of ion-activated patchy particles [209] is shown in **Figure 6.1 (b)**. Based on the Wertheim perturbation theory for fluids of patchy particles [454–459], the present model considers proteins as hard spheres with radius R_p and M distinct and independent binding sites (patches). These sites can be occupied by salt ions (Y^{3+}), thereby activating a given patch (ion binding). The occupation probability of a site reads [209]

$$\Theta(\mu_s) = (1 + \exp(\beta\varepsilon_b - \beta\mu_s)^{-1}, \tag{6.1}$$

where μ_s denotes the salt chemical potential, $\beta = (k_B T)^{-1}$ the inverse thermal energy, and ε_b the binding energy between the site and the ion. A bond between two patches of distinct proteins is possible only if an activated patch meets a de-activated one (and thus forms an ion bridge). The energy of a protein-protein bond is given by [209]

$$\beta\varepsilon_{pp}(\mu_s) = \beta\varepsilon_{uo}\Theta(\mu_s)\big(1 - \Theta(\mu_s)\big) \tag{6.2}$$

in which ε_{uo} defines an energy scale for the interaction between the occupied and unoccupied site. The longer-ranged electrostatic repulsion which dominates in the system without salt (regime I) and very high salt concentrations (regime III) is effectively described via the hard-sphere repulsion between proteins. Note that the model accounts for the salt ions implicitly via the chemical potential μ_s, which implies that the total salt concentration c_s as a function of μ_s cannot be predicted self-consistently within this approach. Therefore, the location of the minimum of the experimentally determined second virial coefficient B_2/B_2^{HS} at c_p = 20 mg/ml is used in order to calibrate c_s (μ_s) [427] and consequently generate the theoretical phase diagram (**Figure 6.1 (b)**).

In the experimental phase diagram, regime II is defined by cluster formation, thus its physical appearance changes from a clear to turbid solution. This transition from clear to turbid and turbid to clear can be detected by eye in **Figure 6.2**, if the protein concentration c_p is high enough.

Hereby, c^* has an abrupt change, whereas c^{**} is smeared out and thus is determined through taking the median of the last turbid to the first clear solution. LLPS is also detectable by eye since over time a dense yellowish liquid is separating from the dilute phase (clear) [80].

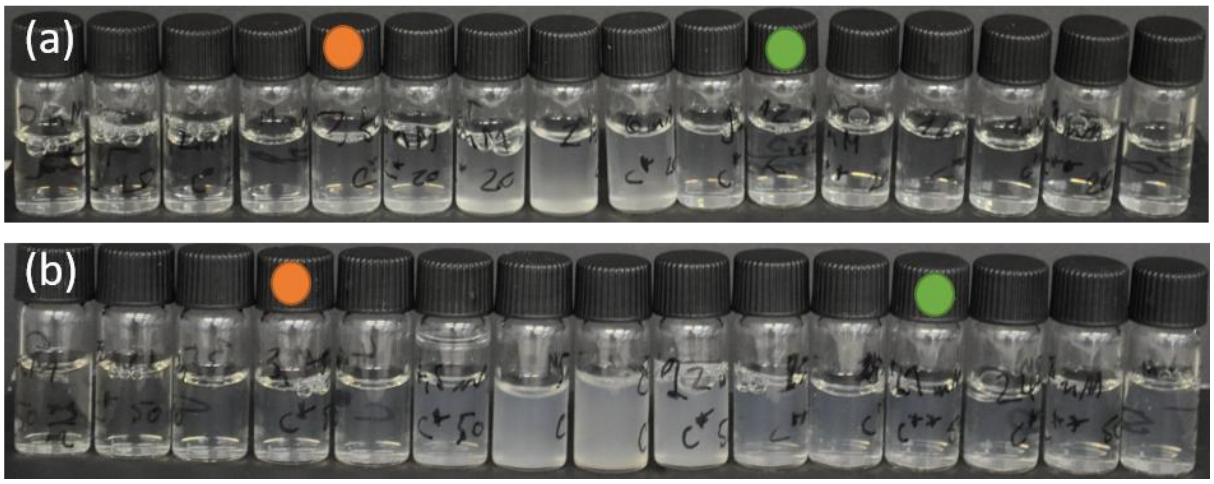

Figure 6.2: *Dilution series. Images of BSA/YCl_3 solutions at 20 °C and at different c_p of (a) 20 mg/ml and (b) 50 mg/ml BSA at varying c_s of 0-30 mM. The orange circles mark c* and the green ones c**, respectively.*

In the case of c_p = 5 mg/ml, c^* and c^{**} are determined via UV-Vis spectroscopy transmittance measurements for more quantitative results. Here, c^* and c^{**} are defined by the drop and rise in transmittance and an example is given in **Figure 6.3**. The absolute numbers to those transitions can be found in **Table 6.1** and **Figure 6.1**.

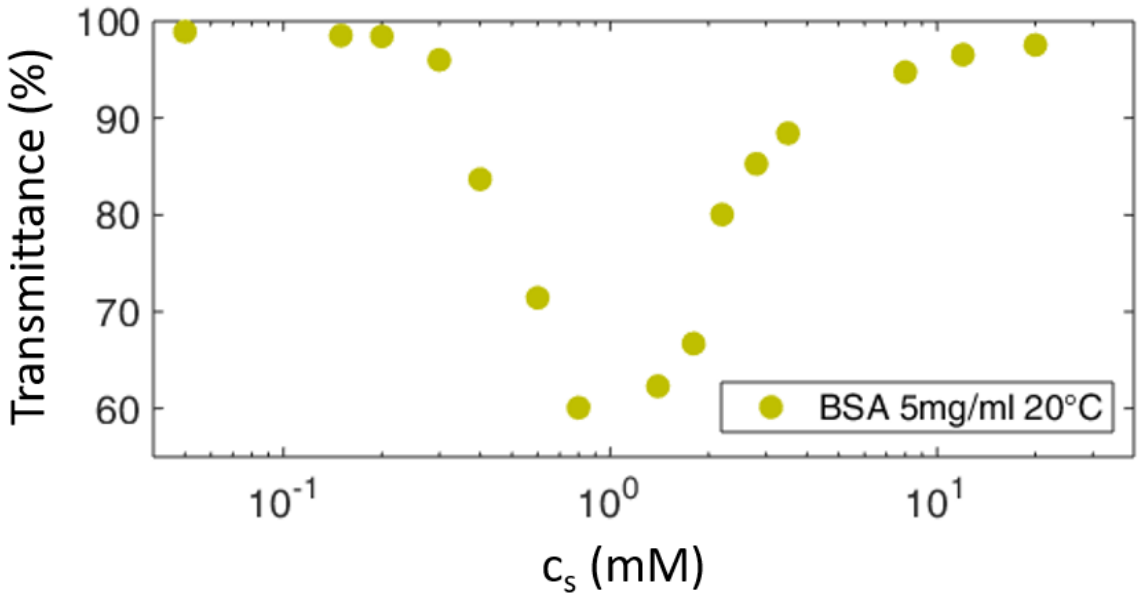

Figure 6.3: *Phase transition at low c_p. UV-Vis transmittance measurement at 5 mg/ml c_p (BSA) in the presence of YCl_3 at 20 °C. The phase transition c* and c** are defined by the decrease and increase in transmittance.*

Table 6.1: *Phase behaviour of BSA and YCl_3. Phase transition c*, c**, and LLPS salt concentrations (in mM) at different protein concentrations and temperatures.*

Temperature	10 °C		20 °C				30 °C				40 °C			
c_p [mg/ml]	c^*	c^{**}	c^*	c^{**}	lower LLPS	upper LLPS	c^*	c^{**}	lower LLPS	upper LLPS	c^*	c^{**}	lower LLPS	upper LLPS
20	1.33	9.33	1.37	12.5	-	-	1.33	11.17	-	-	1.13	10.67	-	-
30	2	14	1.8	14.7	-	-	1.73	14.17	3.33	4	1.87	15.17	3.33	5.33
50	3.67	18.5	3.53	21	6.5	9	3.53	20.17	5	10	3.07	19.5	4.33	9.67

For 10 °C, which is below the lower solution critical temperature (LCST), no coexistence of protein-poor and protein-rich phase is found (**Figure 6.1**). At higher temperatures (20 °C, 30 °C, and 40 °C), the LLPS region (grey areas) broadens strongly. Interestingly, the lines c^* and c^{**}, defining regime II, do not show such a strong temperature dependency. While there are also pH-related effects (see **Figure 6.4**), pH is not driving the rich phase behaviour for the salts employed here since the trends found do not match the pH changes in solution. This is consistent with previous results [481].

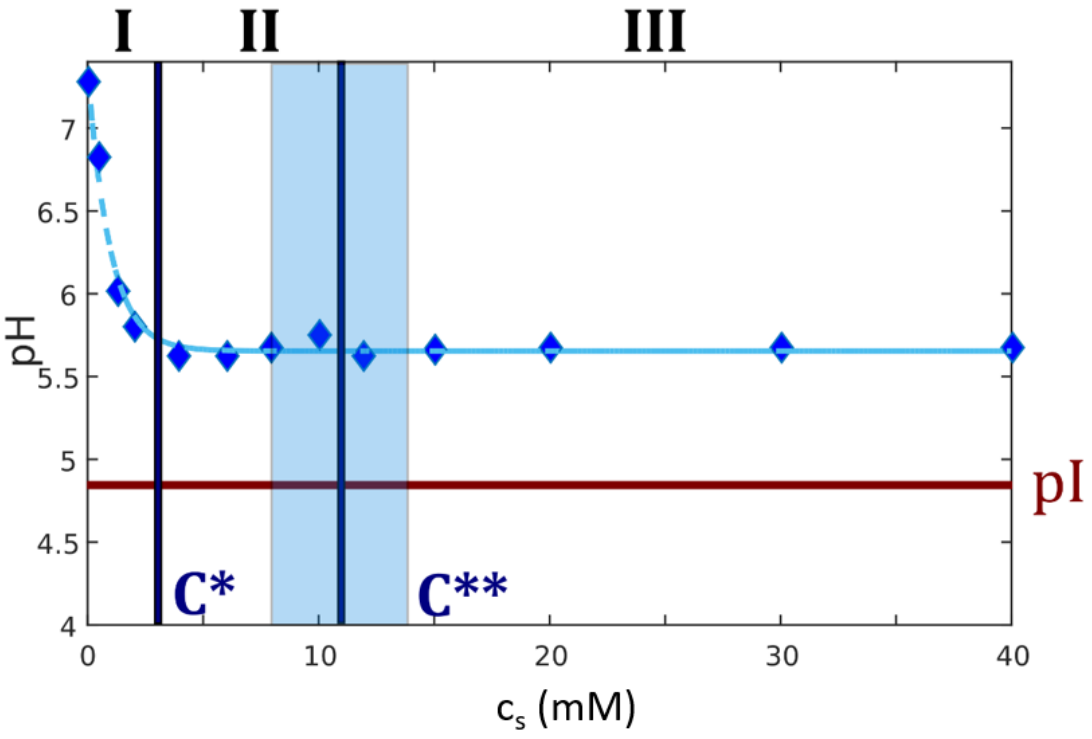

Figure 6.4: *Bulk properties. pH-meter measurements of the bulk protein solution of 20 mg/ml BSA at 20 °C by varying YCl_3 concentration.*

In the following sections, the adsorption of an aqueous BSA solution to a silicon dioxide (SiO_2) interface is presented in the presence of YCl_3 [427] as a function of c_s experimentally by means of ellipsometry and quartz-crystal microbalance with dissipation (QCM-D) and theoretically within the framework of classical density functional theory (DFT). In the adsorption experiment, the LLPS region can be approached from low protein

concentrations c_p by either increasing c_p, or increasing T. The latter procedure is achievable as the LLPS region for the present system is bounded by LCST and broadens with increasing T [155]. By comparing the experimental data with the theoretical predictions in a simplified model system, a clearer insight into the behaviour of the complex protein system is obtained.

6.3 Adsorption upon Approaching LLPS by Varying C_P

The most intuitive way to approach the LLPS region experimentally is to change c_p. The adsorption behaviour is investigated at three different values of c_p, namely 5 mg/ml, 20 mg/ml and 50 mg/ml at fixed T = 20 °C, while varying c_s as indicated by the arrows in **Figure 6.1 (a)** (the path for c_p = 5 mg/ml is far below the LLPS and not shown). The resulting effective adsorbed protein layer thickness d in nm is displayed in **Figure 6.5 (a)** as a function of c_s/c_p. The turbid regime II is indicated by the shaded area. The normalised abscissas show the adsorption profiles for different values of c_p in one figure, although c^* and c^{**} increase with increasing c_p (see **Figure 6.1 (a)**).

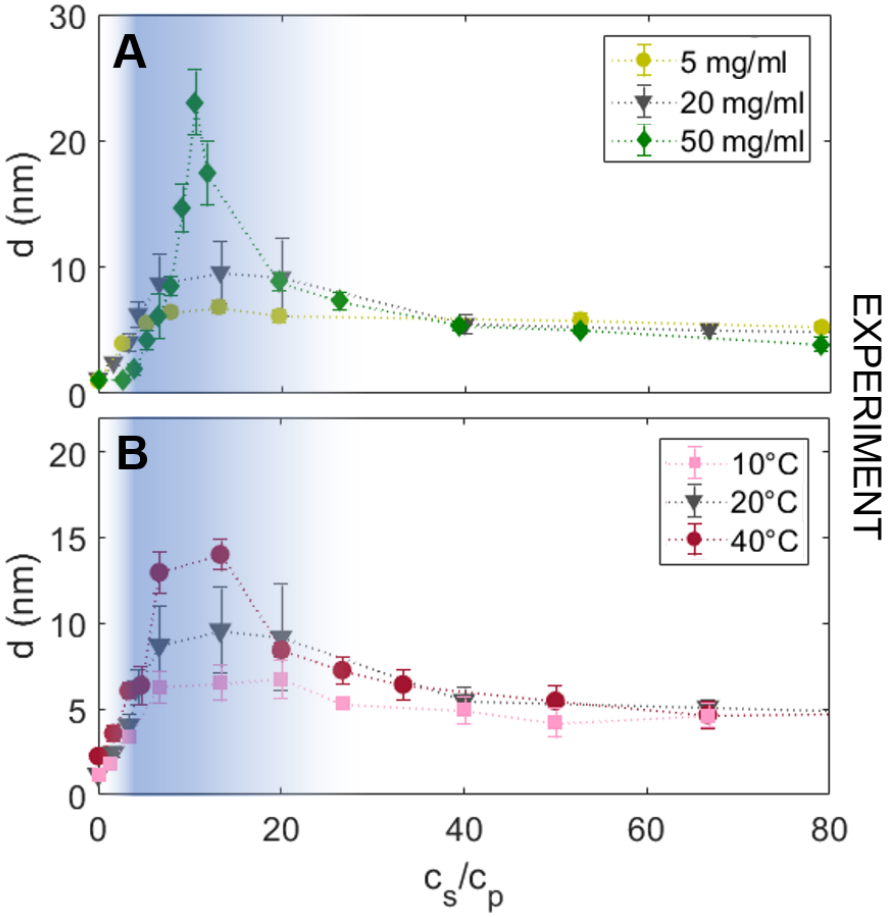

Figure 6.5: Ellipsometric protein adsorption measurements. (a) Protein layer thickness d versus c_s/c_p upon approaching the LLPS by changing the protein concentration (c_p = 5 mg/ml, 20 mg/ml and 50 mg/ml) obtained from ellipsometry measurements at 20 °C. (b) Protein adsorption as function of c_s/c_p upon approaching the LLPS by changing T (10 °C, 20 °C and 40 °C) via ellipsometry at 20 mg/ml c_p. The adsorption curves show an increase in d by increasing c_p or T in regime II (blue-shaded). Regimes I and III are essentially unaffected by the change in c_p or T.

SiO_2 in contact with water is negatively charged. Therefore, without added salt, only few proteins are adsorbed at the interface due to dominating repulsive electrostatic forces between the negatively charged surface, and the net negatively charged BSA molecules at neutral pH [225,487,488]. This results in adsorption limited to sub-monolayers [446]. Ellipsometry measurements show a fitted effective thickness of $d \approx 1$ nm (BSA has an effective sphere radius of $R_p \approx 3.5$ nm, i.e. the coverage is below 1 full monolayer).

When increasing c_s, the repulsive electrostatic forces are screened, and attractive interactions dominate in regime II. The ions adsorbed at the interface exert a strongly attractive force on the proteins [427]. The attractive protein-protein interaction in addition to the attractive substrate causes d to exhibit a prominent maximum at $c_s/c_p \approx 10$. For higher c_s entering regime III, $c_s > c^{**}$, the adsorption curves feature a re-entrant effect for all c_p. Here, the dominating protein-protein interactions become again more repulsive [80], while the interaction of proteins to the substrate remains attractive. As a consequence, d decreases down to a plateau with a value of ~5 nm corresponding to roughly 1 ML of proteins that remain adsorbed at the wall (1 ML: $d = 4$ nm). Remarkably, this appears to be insensitive to c_p.

Importantly, the maximum adsorption layer thickness d_{max} increases strongly from $d = 6.8 \pm 0.51$ nm at $c_p = 5$ mg/ml, to $d = 9.6 \pm 2.5$ nm at 20 mg/ml, and to $d = 23.5 \pm 2.55$ nm at $c_p = 50$ mg/ml. Note that for $c_p = 50$ mg/ml the system is already phase-separated, and only the dilute (protein-poor) phase is used for the adsorption measurement, to avoid interfacial effects between the dilute and dense protein phase, or density gradients influencing the measurement. The non-linear increase of d_{max} indicates that this is not simply the result of more proteins being present in the system, but rather is related to the bulk phase behaviour. Therefore, the strong adsorption peak at $c_p = 50$ mg/ml may be the precursor of a 'wetting' transition.

Using the model of activated patchy particles, the re-entrant adsorption trend can be explained within the framework of DFT [216,217], where the re-entrant behaviour is shown to be a direct consequence of the underlying bulk interactions of the proteins [427]. The classical density functional theory (DFT) [217] provides a powerful and well-established framework to investigate inhomogeneous density distributions in any external potential. The key statement of DFT is the theorem that a functional

$$\Omega[\rho] = \mathcal{F}[\rho] + \int dr\, \rho(r)[V_{\mathrm{ext}}(r) - \mu] \tag{6.3}$$

of the inhomogeneous density profile $\rho(r)$ exists and takes its minimum, the grand potential, at the equilibrium density distribution [217]. A DFT formulation of the Wertheim theory [462] based on fundamental measure theory (FMT) for hard spheres is employed [216,464], to calculate d at the SiO_2-water interface. Effectively, this is described by a salt-dependent short-ranged wall-protein potential $V_{wp}(z)$ where z is the distance normal to the substrate. The model predicts a non-monotonic, re-entrant adsorption layer at the substrate depending on c_s in excellent accordance with experiments [154,427].

For more details on the underlying bulk model and the ion-activated attractive protein adsorption model, the reader is referred to Refs. [209,427].

This model is employed to investigate the behaviour of protein adsorption upon approaching the LLPS region. The theoretical predictions for d, as a function of c_s/c_p, are displayed in **Figure 6.6** for several fixed c_p (corresponding to the arrows in **Figure 6.1 (b)**). In excellent agreement with the experimental results, the model predicts that the adsorption in regime II is enhanced strongly upon approaching the LLPS region. For the path crossing the LLPS region (dark green arrow), the attractive substrate becomes covered by a macroscopic film of the coexisting high-density protein phases, i.e. d diverges. The corresponding protein density profiles $\rho(z)$ at the maxima of d obtained from DFT shown in the inset of **Figure 6.6** are evidence for the divergence of the dark green curve ($\rho = \rho_{\text{liquid}}$ for $z \rightarrow \infty$). Note that the curves are normalised with respect to the bulk value of the protein-poor phase. For the path that misses the LLPS region slightly, the maximum of d corresponds to a film with the density of the protein-rich phase that is a few protein diameters thick. When the chosen path crosses the LLPS region at the protein-poor phase, wetting theory of simple liquids [467] would predict that if the substrate is sufficiently attractive, d can diverge, i.e. a macroscopically thick film of the coexisting protein-rich phase can be adsorbed at the substrate. This DFT model treating proteins as ion-activated patchy particles predicts a wetting behaviour which, interestingly, does not differ significantly from results for wetting of fluids with isotropic potentials despite the much higher complexity and the fundamentally different interactions.

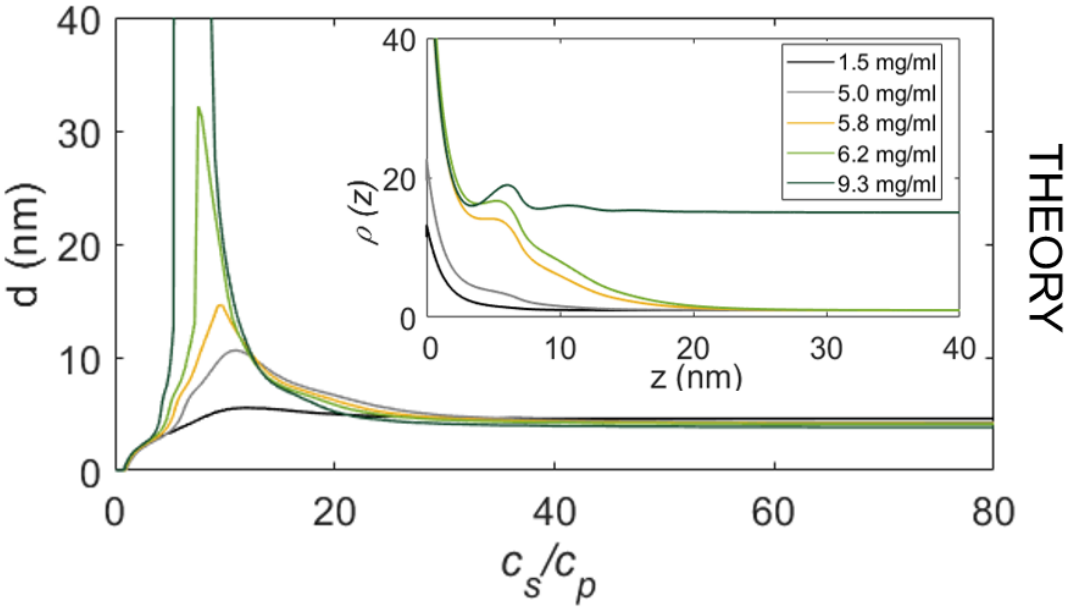

Figure 6.6: *DFT calculations. Protein layer thickness d versus c_s/c_p as obtained within DFT for different paths through the theoretically calculated phase diagram (**Figure 6.1 (b)**). The theoretical predictions of d agree qualitatively very well with those from experiments shown in **Figure 6.5 (a)**, except for the path crossing the LLPS region. The divergence in the theory is due to the grand canonical ensemble. Note that due to the complexity of the system the canonical ensemble does not quantitatively describe the experiment. (inset) Protein density ρ(z) normalised to its value for $z \rightarrow \infty$ corresponding to the adsorption maxima. When the LLPS region is crossed on the protein poor side, a macroscopically thick film of the protein rich phase adsorbed at the attractive substrate can be found (dark green line, c_p = 9.3 mg/ml).*

6.4 Adsorption upon Approaching LLPS by Varying *T*

This system offers an interesting, independent way to experimentally demonstrate the increase of *d* and relate this to the onset of a wetting transition: the LLPS regime can be entered at constant c_p by changing *T* [155]. Due to the LCST behaviour, increasing *T* up to 40 °C leads to a significant expansion of the region where LLPS is found (cf. **Figure 6.1 (a)**). Ellipsometric measurements of the adsorption layer are performed at 10 °C, 20 °C and 40 °C at c_p = 20 mg/ml. The resulting adsorption profiles shown in **Figure 6.5 (b)** exhibit a similar behaviour as those in **Figure 6.5 (a)**: by increasing *T*, *d* clearly increases in regime II. Note that the increase is not as strong as for the previous path varying c_p, which most likely is related to the fact that for *T* = 40 °C the path at c_p = 20 mg/ml is still located far from the LLPS boundary. Nevertheless, these results strongly suggest that the observed protein adsorption is connected to the underlying bulk phase diagram. This is further supported by considering the adsorption behaviour in regime I and III relative to that in regime II. Here, the values of *d* are virtually unaffected when changing *T*, even on an absolute scale. In regime I (up to $c_s/c_p \approx 5$), the data is nearly indistinguishable, and in regime III, all curves simultaneously converge to a plateau of $d \approx 5$ nm (as in the previous measurements where c_p is varied). Thus, the adsorption behaviour in regime I and III seems to be mainly guided by surface properties and is independent of (temperature-dependent) bulk conditions. In contrast, in regime II, adsorption is enhanced due to the combination of the ion-activated-attractive interface and the bulk instability.

6.5 Complementary Measurements and Properties of Adsorbed Layer

The adsorption investigation is extended with complementary QCM-D. The measured raw data consists of two parameters: frequency *F* and dissipation *D*. An example is plotted in **Figure 6.7**. The microbalance is calibrated in water prior to the adsorption measurement. Afterwards, the cell is exchanged with the prepared protein/salt solution and the adsorption process is measured for one hour. Then, the cell is flushed with water to check for the reversibility of the adsorption process. Already from those two parameters, one can obtain information about the properties of the adsorbed layer. The higher *F*, the more proteins are adsorbed at the interface. The higher *D*, the more diffuse and viscoelastic is the adsorbed layer. *D* values below 2E-6 Hz are assumed to belong to a rather stiff layer and above to a more diffuse layer [402]. During adsorption, a more diffuse layer is formed in regime II than in the other regimes. Thus, the thicker the adsorbed layer, the more diffuse it is. After rinsing with H_2O, all adsorbed films lose all their mass up to a critical value, as well as decrease in dissipation. A stiffer and much thinner layer is left at the interface. This observation can also be visualised by plotting the absolute values of *D* and *F* in **Figure 6.8**.

Through the fitting of the data with a viscoelastic model, the thickness of the adsorbed proteins, as well as its viscosity and elasticity can be extracted. In **Figure 6.10**, $d_{QCM\text{-}D}$ for T = 40 °C and in **Figure 6.9** $d_{QCM\text{-}D}$ for 20 °C are illustrated. The trends mentioned above

are also reflected in the extracted viscosity parameter in **Figure 6.9**. While the viscosity parameter is not very reliable on an absolute scale, it is an interesting and useful quantity to compare on a relative scale. Diffuse layers are accompanied by a higher viscosity.

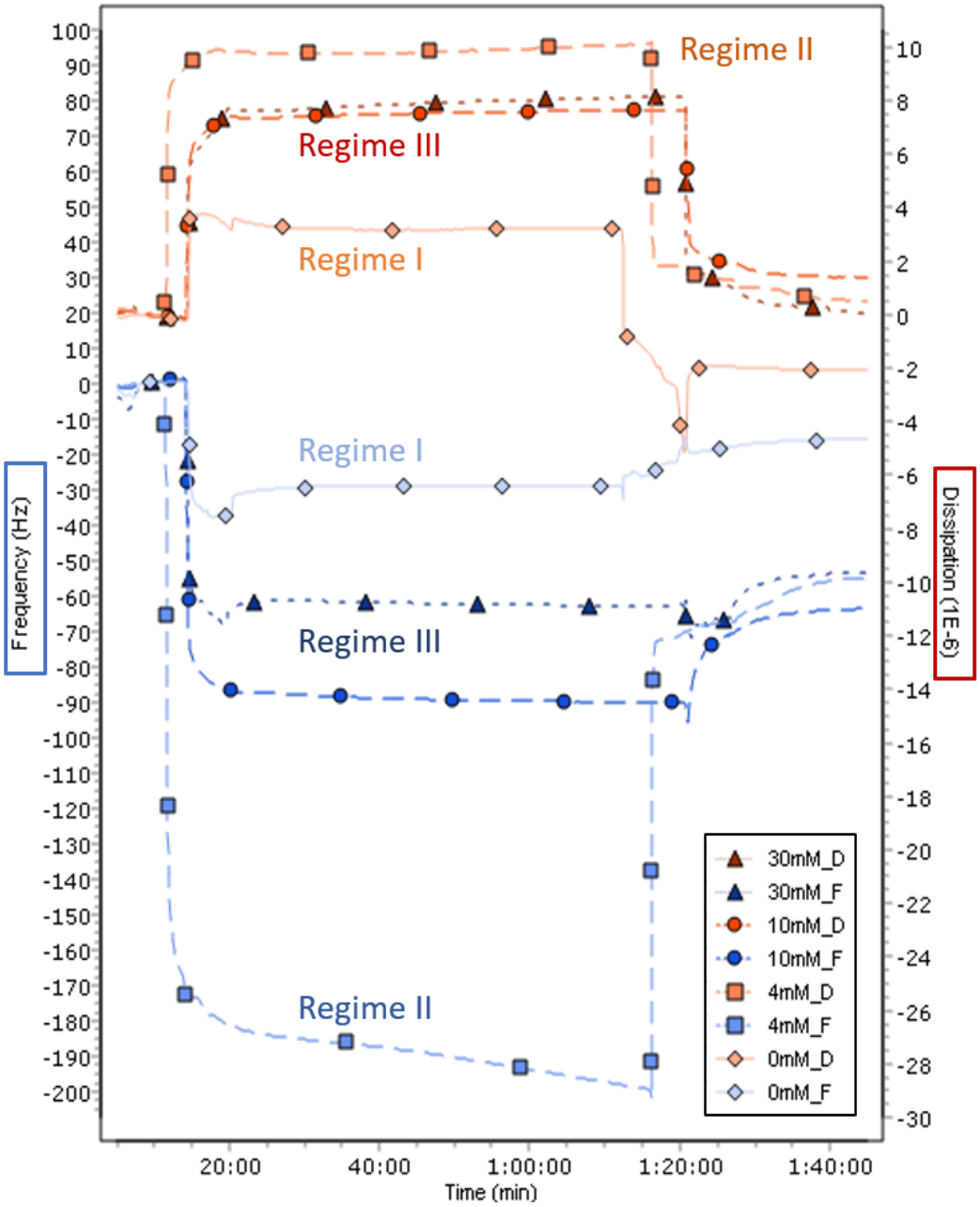

Figure 6.7: *Real-time protein adsorption. 9th overtone of the raw QCM-D data showing the change in frequency (blue) and dissipation (red) upon (step 1) the addition of protein/salt solution and (step 2) rinsing with water at different salt concentrations at 20 mg/ml c_p and 40 °C. Note: during solution exchanges the pump creates spikes in the data during turning-on and switching off.*

Importantly, the QCM-D data exhibits the same trend as the previous results: the adsorption maximum in regime II increases with increasing temperature and the curves approach a plateau value in regime III. The difference in absolute values of d_{QCM-D} obtained from QCM-D relative to that of ellipsometry arises since the QCM-D measures in addition

to the protein in a relatively open (sponge-like) morphology, also the water directly associated to the adsorbed proteins. Ellipsometry however measures an effective thickness d resulting from a step function included in the fitting model for the protein density profile with a volume fraction of 1, which is laterally averaged over the measured surface. This associated water includes the hydration layer, hydro-dynamically bound water, and trapped water in a presumably sponge-like morphology of the adsorbed protein layer. Through the subtraction of d_{EM} from d_{QCM-D}, the amount of associated water d_{assoc} within d_{QCM-D} surrounding the proteins can be calculated in **Figure 6.10 (d)**.

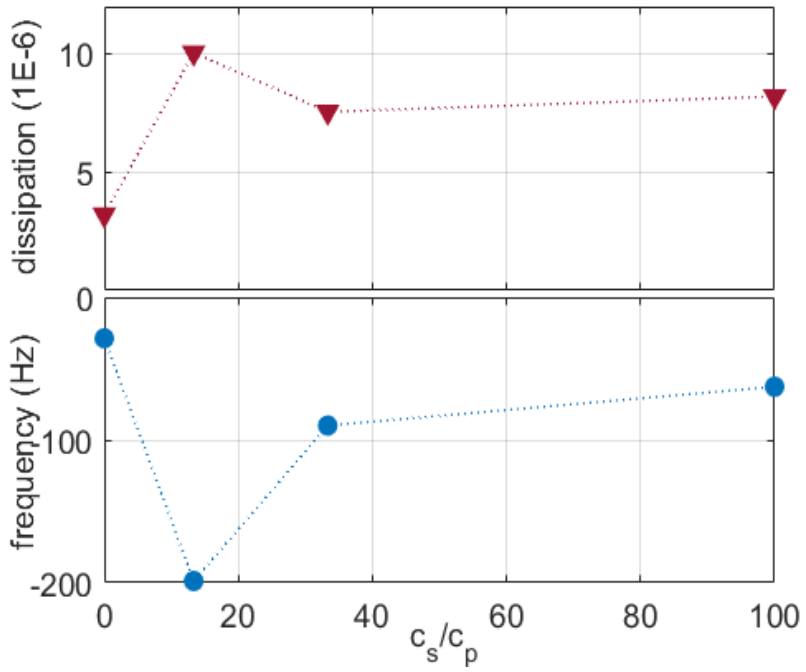

Figure 6.8: *Absolute values of frequency (blue) and dissipation (red) of the 9th overtone of BSA/YCl3 at 40 °C.*

This provides valuable insight into the density and the structure of the formed layer. It turns out that in regime II the amount of water contained in the layers is roughly two times higher at T = 20 °C (**Figure 6.9**), and four times higher at 40 °C, respectively compared to regimes I and III indicating the formation of a diffuse layer in the dense-liquid regime II. This information extends the picture of enhanced adsorption. In regime II, there are indeed more proteins adsorbed, thus "enhanced adsorption", but at the same time this layer has significantly more water associated to it. This means that this enhanced protein layer is more diffuse than a "normal" (densely packed) adsorption layer due to the water uptake, while also having more proteins incorporated leading to a different layer morphology. The different configuration of the adsorption layer vs. wetting layer is illustrated in **Figure 6.10 (a & b)**. Interestingly, this is consistent with the trend of the dissipation parameter D (see **Figure 6.7** and **Figure 6.8**) obtained from the QCM-D measurements. D is a measure for the viscoelastic properties of the adsorbed layer, where a higher value of D means that the layer is 'softer' and more diffuse [402] and a small value of D assumes a solid-like, rather stiff adsorbed layer.

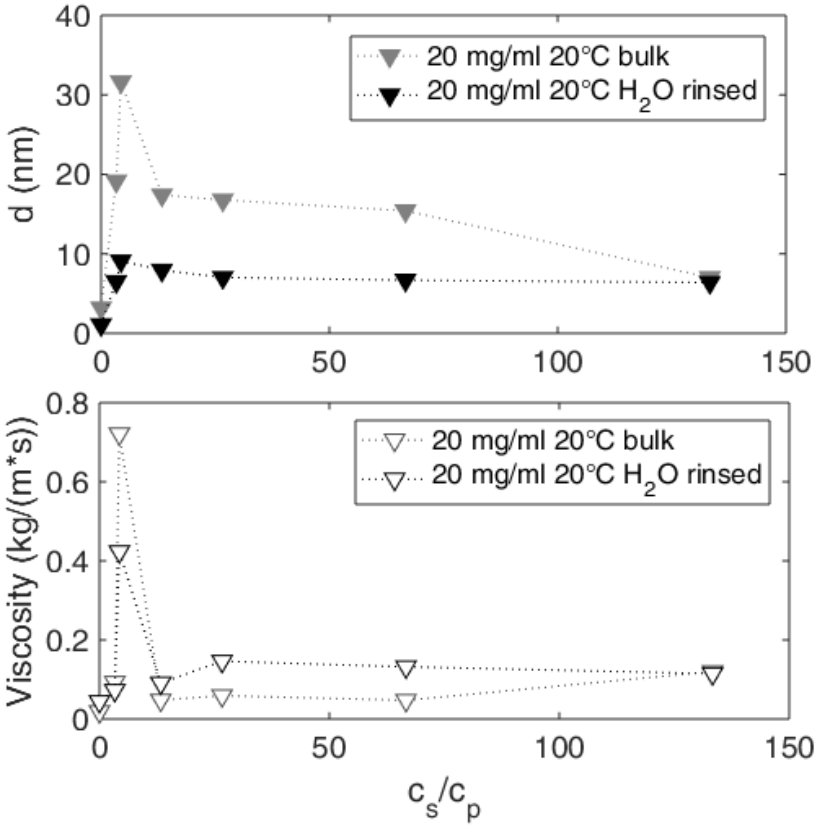

Figure 6.9: Temperature-dependent adsorption behaviour. QCM-D measurements of the adsorbed amount of proteins at the solid liquid interface at 20 mg/ml and 20 °C. The top image illustrates the adsorption behaviour and its dependence on c_s. The black data points show d after flushing the cell with H_2O, thus, the irreversibly bound proteins, which show no re-entrant adsorption. The correlated viscosity is plotted in the bottom image.

The reversibility of the adsorption process can be investigated from the QCM-D results. When the system is rinsed with water after the adsorption measurements, roughly 1 ML (≈12 nm *including* its coupled water for QCM-D) remains adsorbed at the substrate (black solid data points in **Figure 6.10**). In addition, a decrease of the value of D is observed, corresponding to a 'stiff' layer [402]. Furthermore, for c_s corresponding to regime II, no increase in adsorption is observed anymore. This observation indicates that a layer of proteins is irreversibly bound at the substrate with stronger interaction than the excess proteins above with the substrate.

6.6 Summary

The experimental and theoretical results suggest that the enhanced protein adsorption upon approaching LLPS features the onset of a 'wetting' transition (i.e. the formation of a macroscopically thick protein layer) caused by dominatingly attractive protein-protein and protein-substrate interactions mediated by the multivalent ions. In experiments with independent complementary methods (ellipsometry and QCM-D), it is demonstrated that this effect can be achieved via two independent pathways, namely approaching the LLPS region by varying c_p and by varying T.

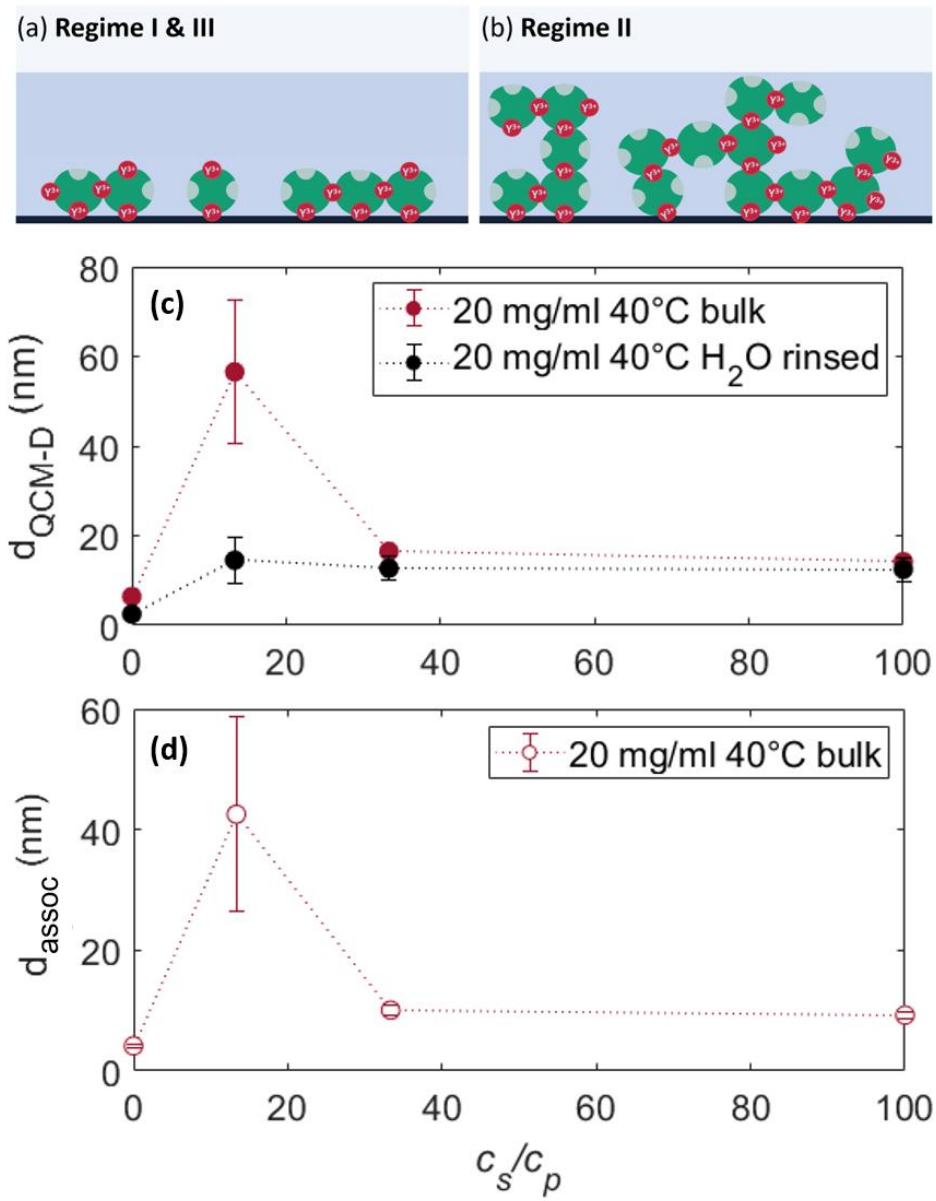

Figure 6.10: Properties of differently adsorbed layers. (Top) Sketch illustrating the different layer formation of (a) a (monolayer) adsorption layer compared to (b) a thicker (wetting) layer. (c) QCM-D measurements of the amount of adsorbed proteins at the solid-liquid interface at c_p = 20 mg/ml and 40 °C. It illustrates the adsorption behaviour and its dependence on c_s. The black data points (d_{rinsed}) show d_{QCM-D} after flushing the cell with H_2O, thus, the irreversibly bound proteins. (d) Associated water (d_{assoc}). Since the QCM-D detects the adsorbed proteins plus its associated water, whereas ellipsometry fits the data to a volume fraction of 1, which is laterally averaged over the measured surface. Through the subtraction of d_{EM} from d_{QCM-D}, the associated water surrounding the proteins can be determined (usually this is rather illustrated with the difference in mass than thickness).

The observation of strongly enhanced adsorption is particularly striking, since it underlines that interfacial phenomena such as wetting, which are known from the statistical physics of simple liquids, may also be found in rather complex solutions of proteins. This provides promising new perspectives for controlling protein adsorption at interfaces. In fact, exploiting the underlying bulk phase behaviour and thermodynamic conditions offers a particularly efficient tool for tailoring a desired protein density at substrates in a controlled

manner (not limited to BSA), which is relevant for many biological or medical applications such as biosensors or better biocompatibility in dental implants, lenses and joints [42,272] and might be extended to other biological systems such as DNA nano-stars used in hydrogels [489]. The consequences are important for the control and tailoring of protein adsorption and possibly at some stage (heterogeneous) nucleation of protein crystals or other high-density phases at the solid-liquid interface. In particular the use of multivalent ions represents a versatile tool for experimentally tuning substrate-protein interactions to achieve a desired level of protein adsorption. Moreover, adsorption phenomena only rarely seem to be investigated from the perspective of patchy colloids [490] for which proteins are a promising experimental realisation.

7 Bulk Phase Behaviour vs Interface Adsorption: Specific Multivalent Cation and Anion Effects on BSA Interactions

The following chapter is based on Ref. [491]. Additional complementary measurements collected with neutron reflectivity and X-ray reflectivity are discussed in Appendix A.

7.1 Background

Salts are essential for life as we know it. Humans need to ingest adequate amounts of salts via their diet [492] in order to maintain biological and physiological functions in the body [493]. The absence or excess of salts can ensue diseases such as renal oedema, Addison's disease, congestive heart failure [493], Parkinson's disease [494], Alzheimer's [495] or hypertension [492]. For certain bacteria - called halo bacteria - a high salt concentration is required for survival [496], while in plants it can induce cell death due to abiotic stress [497].

Salts consist of cations and anions, which have different properties and promote ion-specific interactions, thus facilitating different functions in biomolecules, such as proteins, e.g. via ion-protein interactions [156]. To decode their role and more specifically their binding mechanisms to proteins, numerous investigations were conducted in the past decades [129,237,498]. Nevertheless, there are still contradictory opinions and open questions concerning the interplay of electrostatic, hydrophobic, van der Waals, and entropic interactions between proteins and salts in bulk and at solid interfaces.

The chloride anion (Cl^-) plays a central role in the human body as its principal anion and the second main contributor to blood plasma tonicity [499] and has a key role in the regulation of body fluids, the preservation of electrical neutrality, acid-base balance [500], muscular activity and osmotic pressure [499]. In the human body, a chloride imbalance can induce diseases such as dystrophia myotonica, cystic fibrosis, chronic pancreatitis, epilepsy, cataract or Barter's disease [499,501]. In addition, it is used to diagnose other diseases and deficiencies [502]. In biopharmaceutical drugs, chloride is, e.g., added to liquid antibody solutions for long-term stability [503] or used to investigate alcohol degradation in the liver [504].

Another essential anion, which is primarily ingested through fish and dairy products, is iodide (I^-) [505]. I^- is, amongst others such as I_2, I_3, IO^-, HIO, and HI_2O^-, one form of iodine

(potentially) present in the human body [506]. Here, the focus is on I^-. It is most prominently known due to its role in thyroid hormone production [507], but is also found in saliva, stomach, intestines, kidneys, ovaries and in the blood stream [506]. An iodide deficiency can lead to goitre and hypothyroidism [506]. Especially during pregnancy, an adequate level of iodide is crucial to prevent mental retardation and cretinism in new-borns [506]. In medicine, the antioxidant nature of iodide is used to combat free radicals and peroxides. While it is known for its disinfection/antimicrobial properties [508], another important aspect is its positive effect in the treatment of cardio-vascular diseases [509], respiratory disorders [510], inflammatory skin diseases, and especially degenerative eye diseases [505].

All of these aspects illustrate the importance of investigating protein-ion interactions. Some important aspects of these interactions are summarised in the so-called Hofmeister series [126,128,511]. Anions are hereby ordered according to their propensity from salting-in (stabilising) to salting-out (destabilising) the protein:

$$SO_4^{2-} > PO_4H^{2-} > F^- > CH_3COO^- > Cl^- > Br^- \approx NO_3^- > I^- > ClO_4^- > SCN^-$$

For cations, the corresponding series reads [511]:

$$Na^+ > K^+ > Rb^{2+} > Ca^{2+} > Ni^{2+} > Mg^{2+} > Fe^{2+} > Zn^{2+} > Al^{3+} > Fe^{3+}, Cr^{3+} > NH^{4+}$$

Typical physiologically relevant cations are mostly metal ions and have valences from monovalent (e.g. Na^+) to trivalent (e.g. Al^{3+}) [512]. The trivalent lanthanum cation (La^{3+}), which is less known in the physiological context, can be used on the one hand as a model cation due to its similar size to calcium to investigate e.g. muscle contraction [513]. On the other hand, it can block unwanted bindings of physiological cations with similar size. For example, La^{3+} is found to inhibit the growth of cancerous cells in colon cancer [514], leukaemia [515] and skin cancer [516] and is thus a component in anticancer drugs already tested in vivo and in vitro [514]. In the same sense, it can act either as a neurotoxin [517] or trigger the release of neurotransmitters [518]. In plants, La^{3+} acts as a chemical fertiliser [519] and relieves the plant of salinity-induced oxidative stress [520].

Yttrium (Y) belongs to the group of transition metals, but its chemistry is similar to that of lanthanides [349]. Y^{3+} is used in chemotherapy as a treatment for liver cancer [521] and in radioimmunotherapy as part of yttrium-labelled antibodies [522]. In dentistry, elementary yttrium is incorporated into dental implants for better osteoblast adhesion [523]. For a further discussion of selected properties and application of multivalent ions, see Ref. [156].

Due to the interaction between opposite charges, cations can bind to negatively charged molecules. Under certain conditions, cations can thereby induce attractive forces e.g. between macro-anions [524] and bridge particles of equal charge, such as polyelectrolytes [480], surfactants [525] or actin filaments [526]. Cations can induce charge inversion in biological membranes [527], anionic liposomes [528] and globular proteins [80].

A complex phase behaviour for globular proteins (human and bovine serum albumins, beta-lactoglobulin, ovalbumin) in the presence of multivalent cations such as Cd^{2+}, Zn^{2+}, La^{3+}, Al^{3+}, Y^{3+}, Ho^{3+} and Fe^{3+} is observed [79,147,150,151,241,349]. The phase diagram features phenomena such as liquid-liquid phase separation (LLPS), protein crystallisation, and re-entrant condensation (RC) due to cation-induced charge inversion [79,147,150,151,241,349].

In this chapter, the focus is on the effect of anions (Cl^- vs I^-) and cations (La^{3+} vs Y^{3+}) on the bulk behaviour of bovine serum albumin (BSA), as well as on its adsorption behaviour on a negatively charged, hydrophilic surface (SiO_2). Serum albumin is often the first protein to adsorb to a solid interface [42] in contact with blood serum. It is the most abundant blood protein and has a well-known structure [232] making it an ideal and important protein to investigate. In terms of substrate properties, hydrophilic surfaces are highly hemocompatible [60,61]. Negatively charged surfaces are important for initiating blood clotting [46] by inducing protein adsorption and platelet adhesion [60], besides activating further proteolytic systems in the blood plasma [63,64]. Thus, SiO_2 is a good model surface to investigate protein adsorption in addition due to its well-defined properties and smooth surface.

In the following, insight into the dominant interactions guiding protein cluster formation and protein adsorption is given and the influence of multivalent salts on these behaviours. The aim is to obtain a comprehensive picture of the underlying mechanisms and interactions driving these phase behaviours via UV-Vis spectroscopy, optical microscopy, FTIR, and pH measurements. Depending on the ion type, composition, and valency, different protein behaviours are observed due to varying type and strength of interactions. Second, protein adsorption is investigated by ATR-FTIR, ellipsometry, and QCM-D measurements.

7.2 Phase Behaviour

The phase behaviour of BSA in the presence of YCl_3, $LaCl_3$, YI_3 and LaI_3 is presented, which differs depending on the anion and cation type in the bulk solution. The phase diagrams in the presence of chloride salts were already established in previous publications by Matsarskaia et al. [349] and Braun et al. [152] and are used as a reference for the protein adsorption measurements.

First, the focus is on the anion iodide and its influence on the protein bulk phase behaviour. The phase behaviour of BSA with YI_3 and LaI_3 at room temperature is established (**Figure 7.3 (a & b)**). The phase transitions in the phase diagrams shown in **Figure 7.3** are determined by eye, UV-Vis measurements and optical microscopy [80]. For low c_p, due to faint visual turbidity determination via UV-Vis transmittance measurements is necessary. Previous investigations have shown that the determination by eye is sufficient and comparable to laser transmittance measurements [80].

The first phase transition from regime I to II at the specific salt concentration c^* is defined by the onset of turbidity (**Figure 7.1**). Examples are given in **Figure 7.1 (a & b)** for each salt. At 1, 2, and 5 mg/ml c_p, additional UV-Vis measurements are performed to determine c^*, when detection by eye is not possible due to only faint changes in turbidity. The corresponding transmittance measurements for BSA with LaI_3 and YI_3 are given in **Figure 7.2** and the respective values of c^* are listed in **Table 7.1**. In the transmittance measurements, c^* is defined by the first drop in the transmittance signal. The method of choice to investigate LLPS formation is optical microscopy to see the droplet and network formations with examples given in **Figure 7.1 (c)**.

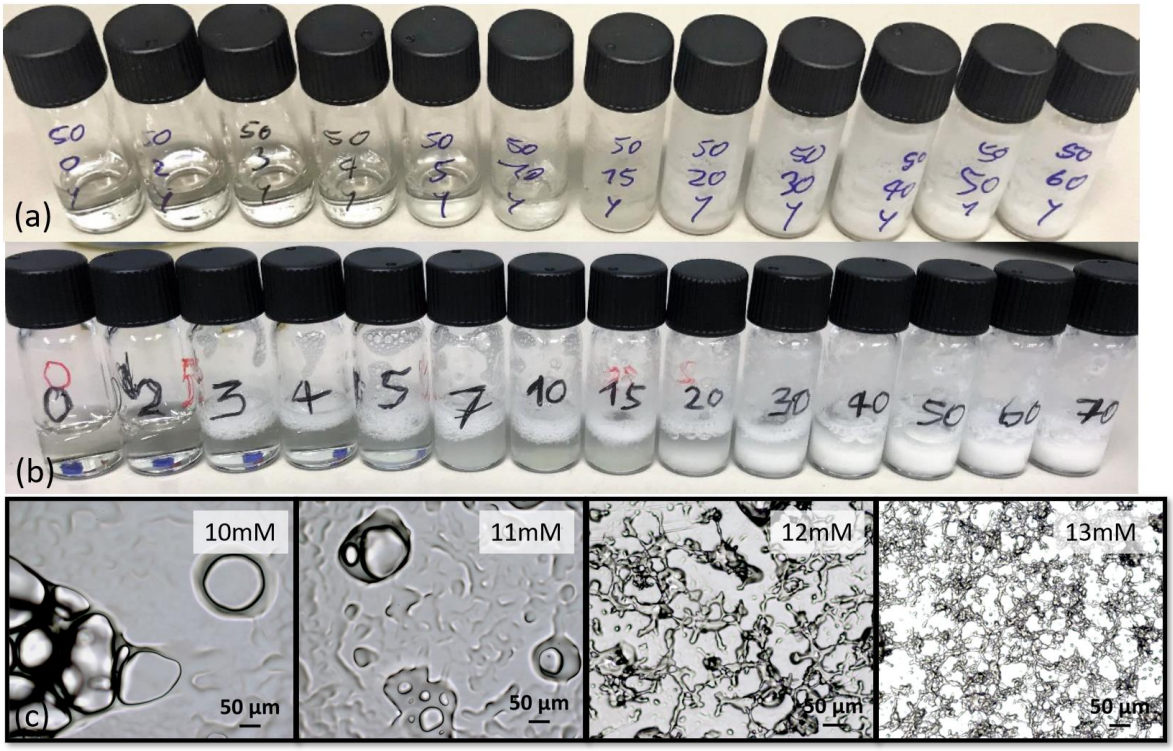

Figure 7.1: *Phase transitions. Determination of phase transition by eye at 50 mg/ml BSA and room temperature of (a) YI_3 and (b) LaI_3 one day after preparation. The bottles are labelled with the respective c_s and with the respective c_p (only in (a)). The occurrence of LLPS is determined by optical microscopy. An example is given for 50 mg/ml BSA and LaI_3 with c_s between 10 to 13 mM in (c).*

Both phase diagrams show a first phase transition from regime I (transparent) into regime II (turbid) at a given salt concentration c^* and a metastable liquid-liquid phase separation (LLPS) region (square symbols in **Figure 7.3**), which starts to occur at $c_p \sim 5$ mg/ml, i.e., within regime II. This phase behaviour of globular proteins mixed with multivalent ions has been first established by Zhang et al. [80] and can be rationalised as follows. The initially net negative charge of the proteins is neutralised by the addition of salt in regime I [79,80]. At a specific salt concentration c^*, the dominant force changes from repulsive to attractive due to the binding of trivalent cations to negatively charged patches of the protein. The cations can even bridge proteins, thus promoting protein aggregation (regime II) [209]. The binding mechanism between cations and proteins can be rationalised by electrostatic interactions.

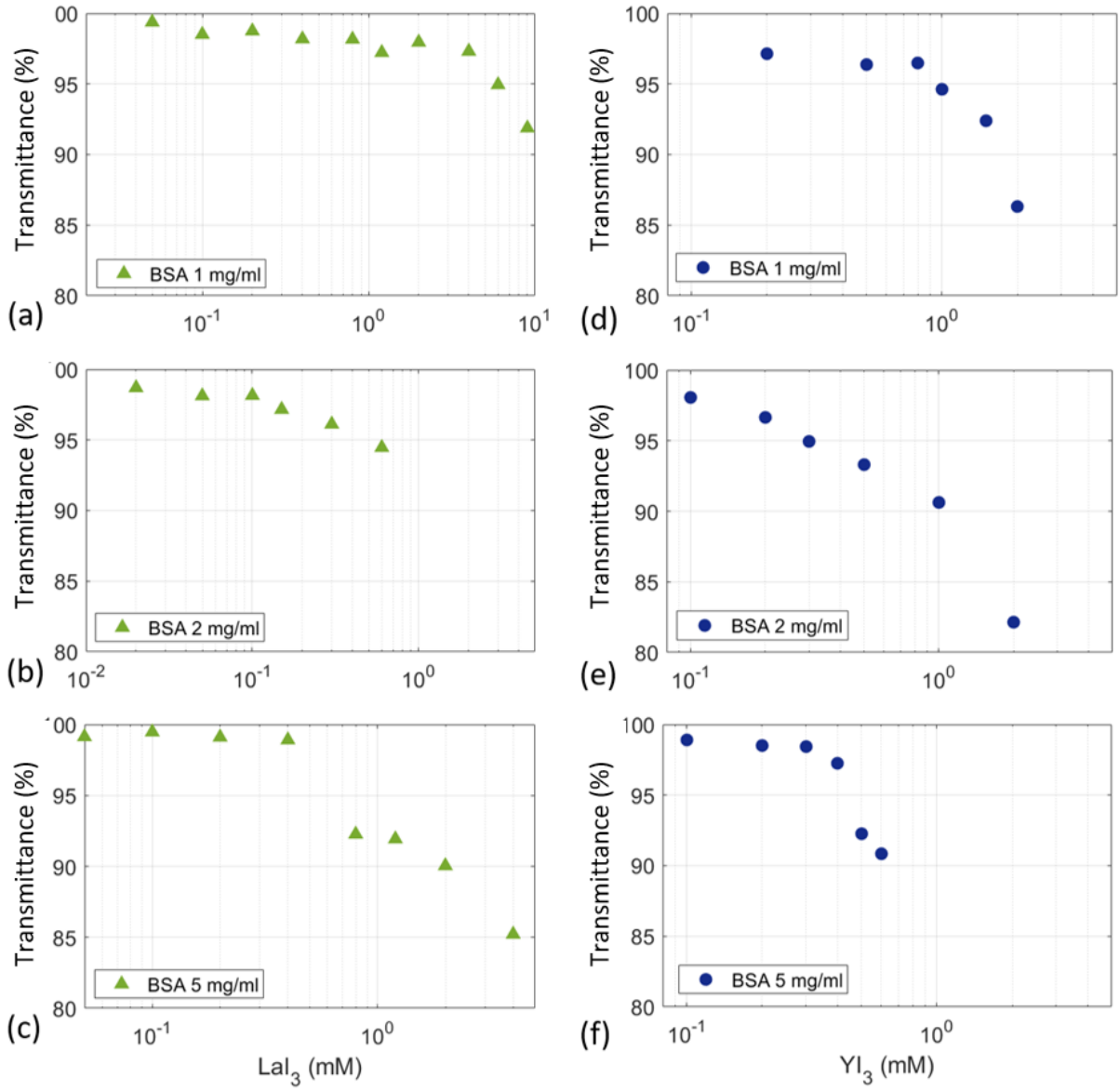

Figure 7.2: *Transmittance measurements. UV-Vis measurements of (a-c) YI_3 at 1, 2, and 5 mg/ml BSA and (d-f) for LaI_3 at 1, 2, and 5 mg/ml BSA. The values of c* determined from the UV-Vis transmittance measurements are listed in* ***Table 7.1***.

Table 7.1: *Phase transitions. c* values determined from UV-Vis transmittance measurement shown in* ***Figure 7.2***.

c_p (mg/ml)	c_s (YI_3) (mM)	c_s (LaI_3) (mM)
1	1	5
2	0.2	0.3
5	0.4	0.5

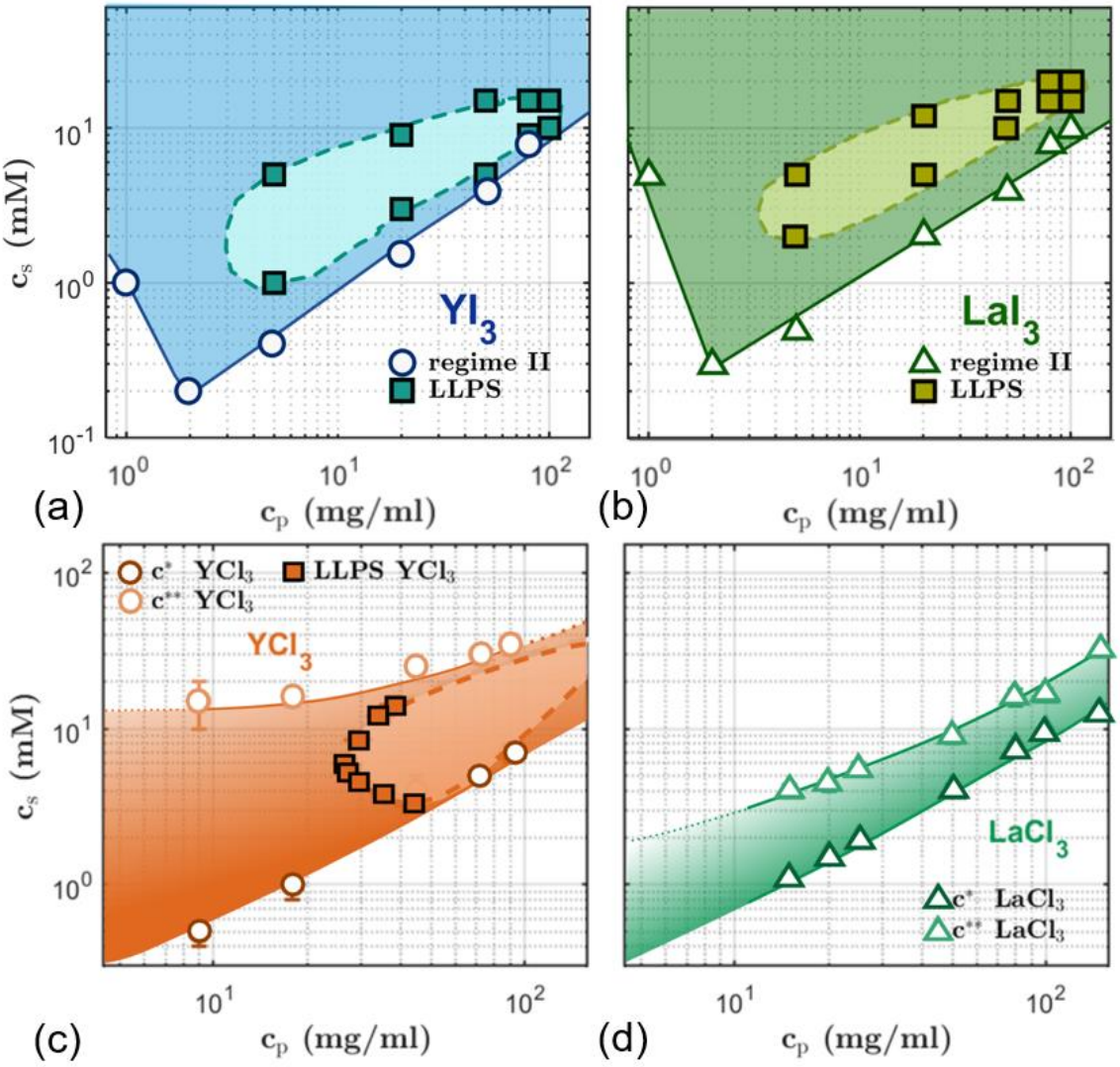

***Figure 7.3**: Phase diagrams. BSA phase diagrams at room temperature with (a) YI_3, (b) LaI_3, (c) YCl_3, and (d) $LaCl_3$. The data in (c) & (d) are modified from Ref.* [152]. *Depending on the salt type, BSA undergoes different phase transitions. All salts, except $LaCl_3$, induce LLPS (square markers). Only the chloride salts lead to re-entrant condensation, whereas BSA in the presence of iodide salts remains in regime II even at high c_s. Note that c* deviates from a linear slope at very low c_p (1 mg/ml). At low c_p, the intermolecular distances between proteins become very large, thus prohibiting cluster formation until an excessive amount of salt is added.*

In colloid-like systems, including protein solutions, LLPS can occur depending on the interaction strength between particles. One parameter to determine the interaction strength and type is the reduced second virial coefficient B_2/B_2^{HS}, where B_2^{HS} is the second virial coefficient of hard spheres [529]. A threshold value of B_2/B_2^{HS} determined for LLPS formation in colloid theory is -1.5 [154,529]. LLPS forms at lower c_s and extends to higher c_s for BSA with YI_3 than with LaI_3. In addition, c^* is lower in the presence of YI_3 than LaI_3.

These differences in BSA phase behaviour induced by Y^{3+} and La^{3+} can be rationalised by weaker protein-protein interactions and cation-protein binding properties of La^{3+}. The cation radius [530,531] and hydration effects [532,533] contribute to the effective protein-protein interactions. While other mechanisms may also play a role, it is reasonable

to assume that the bigger the cation (lower charge density), the weaker are the attractive interactions it can induce. A detailed investigation on the role of cations on the BSA phase behaviour has been performed by Matsarskaia et al. [349]. These findings are consistent with the previous results on chloride salts illustrated in **Figure 7.3 (c & d)**.

Interestingly, no re-entrant condensation occurs with either iodide salt. Thus, no transition into regime III is observed and at high c_s, the protein-salt solution remains in regime II. Additionally, in the case of the iodide salts, LLPS begins at lower c_p compared to BSA in the presence of chloride salts (**Figure 7.3 (c & d)**). This indicates much stronger BSA-BSA attractive forces in the presence of iodide salts, for which protein-protein interactions are attractive even at very high c_s. The behaviour found is in good agreement with the behaviour found for BSA with nitrate salts. Braun et al. [152] has already observed attractive interactions of BSA at very high c_s, in their case with nitrate salts ($La(NO_3)_3$ & $Y(NO_3)_3$), indicated by the phase diagram and measured B_2/B_2^{HS} values. A systematic change in phase behaviour of BSA with Cl^-, NO_3^- and I^- can be observed: c^* shifts to higher c_s, LLPS occurs at lower c_p and RC vanishes. Thus, ranking the anions from inducing strong attractive interactions from weakest to strongest: $Cl^- < NO_3^- < I^-$. Multiple factors contribute to this behaviour, which are explained in the following sections and supported by relevant anion properties in **Table 3.2**.

7.2.1 Hydration and Protein Stability

According to the Hofmeister series, iodide is more prone to cause destabilisation of the protein (denaturation) than chloride [127], which could prevent re-entrant condensation (c^{**}). Yet, at low and moderate ionic strengths (< 0.1 M), weakly hydrated anions such as iodide neutralise the electrostatic repulsive forces and thermostabilise BSA more efficiently than strongly hydrated anions and are thus more effective stabilisers leading to the reverse Hofmeister series [134,534,535]:

$$SCN^- > I^- > NO_3^- > Br^- > Cl^- > SO_4^{2-}$$

This order is based on the hydration of an ion, which is linked to its ion radius, heat capacity $C_{p,\,str}$, ionic B coefficient, and structural entropy S_{str} listed in **Table 3.2**. These properties also determine whether the ion is making or breaking the water structure around itself according to Marcus [250,254,255] and can be expressed with the water structure parameter ΔG_{HB} [257]. Thus, in this c_s range (<0.1 M), iodide stabilises the BSA structure better than nitrate and nitrate does so better than chloride. In fact, Cl^- is known to have little effect on the water structure or protein stability [133,536] and thus has a passive role in this context.

In order to assess the influence of iodide on the secondary structure of BSA, FTIR measurements are performed (see **Figure 7.4**). The measurements are performed in D_2O due to the overlapping absorbance peaks of H_2O with the amide-I band, which are an indicator of the integrity of the secondary structure of proteins. Although Braun et al. have found different phase behaviours for protein/salt systems in D_2O vs H_2O [154], in the

present context D_2O is an appropriate solvent to use since it strengthens protein-protein interactions meaning that since no structural changes in D_2O are observed, the weaker interactions in H_2O do not induce changes either. The slight difference between pD and pH values of 0.41 does not influence the overall trend of the results found [537].

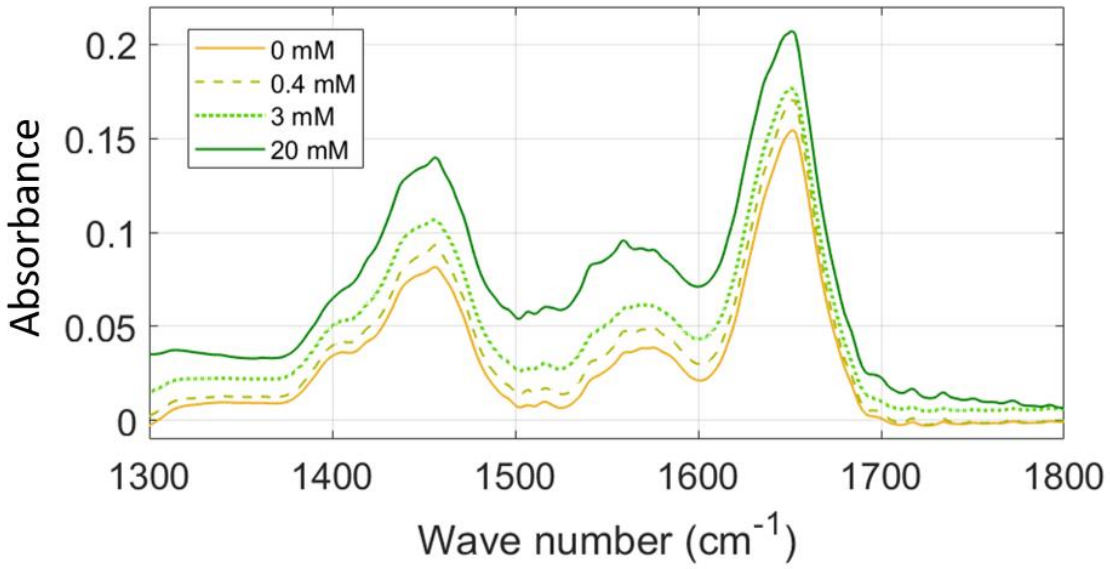

***Figure 7.4**: Secondary structure of BSA. FTIR measurements of the BSA/LaI_3 system at c_p = 20 mg/ml and 20 °C in D_2O. The measurements cover all regimes showing no significant changes in the amide-I band (1600 to 1700 cm^{-1}) at c_s of 0, 0.4, 3, and 20 mM salt. Note that the slight differences in peak intensity and position in amide-II are due to incomplete D_2O subtraction from the measurements.*

The secondary structure of BSA is stable over a LaI_3 concentration range of 0 to 20 mM with a prominent peak around 1650 nm^{-1} in D_2O (amide-I). This peak is associated with α-helices, which make up roughly 66 % of BSA in its native shape [245] and indicates an intact globular structure. Performing multiple measurements at different c_s of 0, 0.4, 3, and 20 mM does not show any significant structural changes in the amide-I band due to salt type or concentration. Thus, denaturation or strong structural changes in the protein structure can be excluded to be the cause for the suppression of re-entrant condensation, i.e. the absence of regime III.

7.2.2 pH Changes

The addition of salt and subsequent salt-induced water hydrolysis and ionisation of hydrophilic protein residues [481] can change pH and thus, in principle, protein behaviour. Importantly, though, previous findings have shown that the trivalent cations used here do not induce significant pH changes [481]. To determine the effect of anions on the pH, pH of BSA-LaI_3 samples is measured after preparing the protein/salt mixtures (**Figure 7.5**). The pH decreases slightly with increasing salt concentration, yet the drop in pH does not correlate with the phase transitions seen in the bulk. The pH does not change significantly with time or c_p either. This pH trend of LaI_3 is similar to that found for YCl_3 in our previous publication [465], as well as similar to the pH variations of pH-neutral salts [481]. Subsequently, while pH effects may contribute to the protein phase behaviour in some

form, they do not qualitatively change the bulk behaviour and are not primarily responsible for the absence of regime III observed with iodide salts as opposed to the chloride salts.

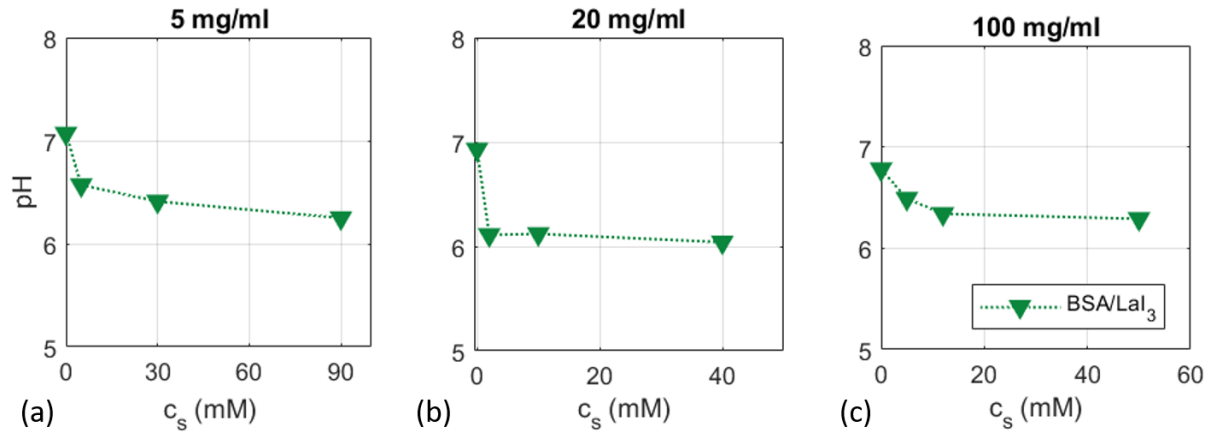

Figure 7.5: Bulk pH measurements of the BSA/LaI_3 system. Measurements are performed at c_p = (a) 5, (b) 20, and (c) 100 mg/ml with varying c_s. The precision of this method can be estimated around pH ± 0.1.

7.2.3 Number of Anions Bound to BSA

Literature consistently reports that more iodide anions are bound to BSA per molecule than nitrate ions and even less chloride anions (see **Table 3.2**) [256,538]. If the number of anions bound depend on the anion type, it can explain why a certain anion type has a stronger influence on the protein phase diagram than another, which results e.g. in the disappearance of re-entrant condensation. The number of anions bound increases from Cl^- < NO_3^- < I^-, which reflects the order of ion-induced attractive interactions in the phase diagram. Thus, it is reasonable to assume that iodide has a stronger influence on protein-protein interactions, which again emphasises the general weak effect of Cl^- on the protein stability or water structure [133,536]. The binding affinity of anions to BSA depends on the properties described in the following Chapters 7.2.4 to 7.2.6.

7.2.4 Strength of Protein-Ion Interaction

Weakly hydrated anions bind directly to proteins causing the protein to maximise its solvent accessible surface area and the bulk solution to become a better solvent [135]. In turn, strongly hydrated anions interact indirectly through bound water molecules with the protein, thus reducing the proteins surface area by making it more compact and the bulk solution to become a bad solvent [135]. Anions with a lower charge density bind more tightly to the protein. This implies that iodide binds more tightly to BSA than nitrate and nitrate stronger than chloride (see **Table 3.2** for anion radius and surface charge) [135]. In other (positively charged) proteins, it is found that iodide can bridge proteins, thus promoting anion-induced cluster formation [539,540]. One indicator for iodide-mediated protein-protein bridging, as well as cation bridging of BSA molecules in solution, is that at high c_s for both LaI_3 and YI_3, the protein cluster sizes increase until they start to sediment at $c_s > c_{s,LLPS}$. This is also inversely reflected in the c_p values of the 'dilute' (upper) phase,

which decreases with increasing c_p (**Figure 7.6**). c_p of the dilute phases of all samples at 20 mg/ml BSA with LaI_3 and YI_3 are determined via UV-Vis spectroscopy by applying the Beer-Lambert law and are plotted in **Figure 7.6**. This method is used because c_p of the dense phase is difficult to determine due to its high viscosity making its extraction impossible. Since a specific protein concentration is used and because of mass conservation, the lower c_p is in the dilute phase, the more aggregates are formed in the dense phase. The combination of increased c_p and volume of the sedimented dense phase shown in **Figure 7.1 (a & b)** indicates consistently attractive interactions between proteins even at high c_s preventing re-entrant condensation. This is consistent with results by Braun et al. [152] for BSA/$La(NO_3)_3$, which found stable B_2/B_2^{HS} values at -2.25 for high c_s and c_p, at which re-entrant condensation vanished. In systems, in which re-entrant condensation is always present (i.e. $LaCl_3$ and YCl_3), the B_2/B_2^{HS} values start to increase at high c_s illustrating the decreasing attractive force due to cation-induced overcharging effects of the proteins. The decreased c_p of the dilute phase of YI_3 compared to LaI_3 further supports the finding of stronger BSA-BSA interactions in the presence of Y^{3+}.

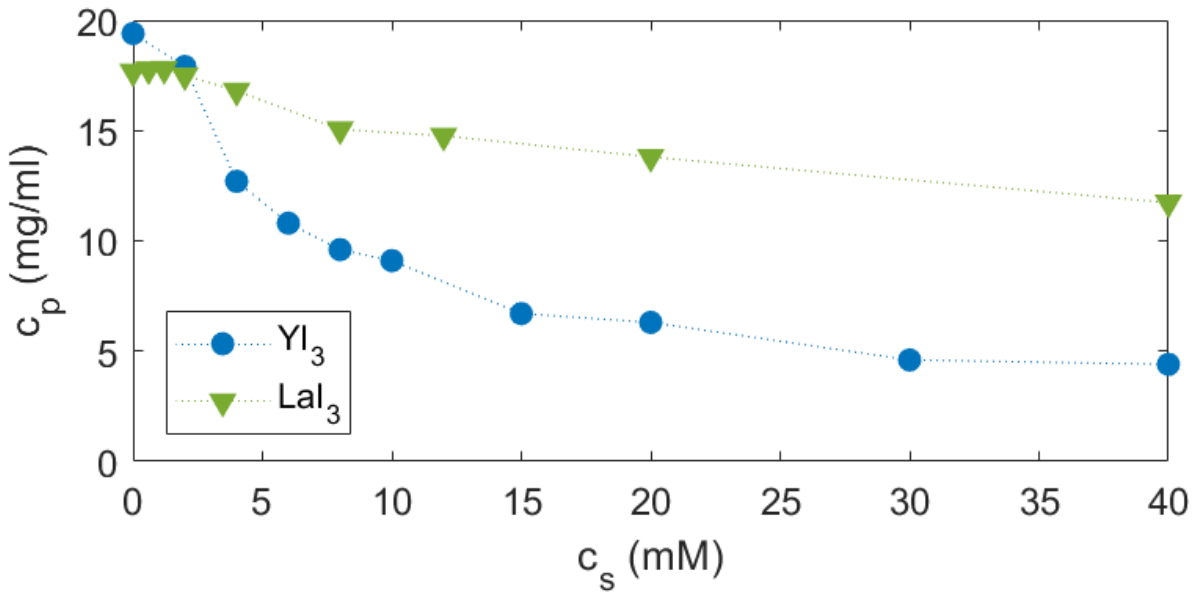

***Figure 7.6**: Dilute phase protein concentration. The samples are prepared at a BSA concentration of 20 mg/ml and only the dilute phase is measured by UV-vis spectroscopy. For YI_3, c_p decreases faster with increasing c_s, which illustrates stronger protein aggregate formation in the dense phase compared to LaI_3.*

7.2.5 Binding Sites

Literature distinguishes between specific and non-specific, high and low affinity, polar and non-polar ion-binding sites on proteins. It appears to be established that chloride binds to cationic/basic binding sites of BSA [534,541] and HSA [141,542,543], which are specific and high-affinity binding sites, whereas there are numerous and contradictory opinions on the binding of iodide. Some investigations do not discriminate between anion type and thus assume the same binding mechanism for iodide to positively charged protein groups of BSA [534,541], while others find a different (non-specific) binding mechanism for iodide to non-polar groups of HSA [141], lysozyme [539,544,545], human carbonic anhydrase II

[259] and peptide [546]. The same applies to the binding of other anions such as anionic dyes [547], anionic amphiphiles [548] or anionic ligands [549] to BSA, all of which bind preferentially to hydrophobic groups. In some cases, an interplay of electrostatic and hydrophobic interactions is needed, in which the proximity of positive and non-polar groups has a favourable effect on anion binding [141,548,550]. BSA has numerous binding sites with different binding affinities due to specific and non-specific binding mechanisms. In any case, the binding mechanism of iodide is much more complex than the binding of chloride [542]. Chloride binds only to positively charged sites, whereas, depending on the bulk properties (i.e. charge and polarity of protein), iodide binds specifically to positively charge sites and/or non-specific to hydrophobic sites with different affinities [259,541,551].

7.2.6 Competing Interactions

Beside the properties of the anion, the trivalent cations have to be considered as well. Anion-cation chloro-complex formation can be excluded since those start to form at 0.2 M for yttrium salts and 0.4 M for lanthanum salts, respectively [552–555], as well as nitrato-complexes start to form at 0.12 M for lanthanum salts and 0.18 M for yttrium salts [555]. Iodo-complexes start to form at lower c_s than chloro-complexes yet should not influence the measurements [556]. Thus, anion-cation complexes do almost certainly not contribute to the effects investigated. However, anions could assist and amplify the effect of cations on protein-protein interactions [546,557]. Depending on the cation type and charge of the protein in system, the anion can support the destabilising or stabilising role of the cation on the protein structure [546,557].

Overall, electrostatic (and hydrophobic) ion-protein and protein-protein interactions and the special role of multivalent ions are key for the understanding of the observed (bulk) behaviour. The increasing role and effect of anions from $Cl^- < NO_3^- < I^-$ on the phase diagram can be explained with the combination of an increasing number of ions bound to BSA, stronger binding, increasing protein-stabilising role of ions, potentially anion bridge formation and increasing role of non-specific protein-protein interactions, as well as cation bridges. These properties appear to be responsible for preventing the system from undergoing re-entrant condensation triggered by trivalent cations, which means that it remains in regime II with dominant attractive forces between protein molecules, for the iodide salts and partially for nitrate salts.

7.3 Protein Adsorption

In this section, it is discussed how the presence of different salts ($LaCl_3$, YCl_3, LaI_3, YI_3) in BSA solutions (c_p = 20 mg/ml) influences the adsorption behaviour of BSA to a net negatively charged, hydrophilic substrate and to which extent this is related to the bulk protein phase behaviour.

7.3.1 Salt-dependent Protein Adsorption (Ellipsometry)

The thickness of the adsorbed amount of BSA on SiO_2, d, is plotted as a function of ratio of salt/protein concentration (c_s/c_p) in **Figure 7.7**. The effective measured d with ellipsometry assumes a volume fraction of 1, which is laterally averaged over the measured surface. Different aspects need to be considered when comparing the different adsorption trends. These include the position of the adsorption maximum, the amount of protein adsorbed, and the overall shape of the curve. Without salt, adsorption of $d \sim 1$ nm can be observed. This can be attributed to positively charged side chains of the protein interacting with the negatively charged substrate, as well as contributing hydrophobic and hydrogen bond interactions [225], leading to sparse adsorption at the interface.

The initial increase of adsorption can be ordered according to $LaI_3 < LaCl_3 < YI_3 < YCl_3$ shown in the inset of **Figure 7.7** meaning that the smallest amount of YCl_3 is needed to achieve the thickest adsorption layer at low c_s. This behaviour reflects the bulk phase transition c^* from regime I to regime II at $2 > 1.5 \approx 1.5 > 1.3$ mM salt, respectively, which occurs at lower c_s for the yttrium salts than for the lanthanum salts due to the stronger attractive intermolecular forces induced by Y^{3+} (see Fig. 1).

For iodide salts, more salt has to be added to the protein solution to observe the transition from regime I to II at c^* than for chloride salts. This is due to the fact that iodide has a dominant role in the protein behaviour hindering 'simple' charge screening through multivalent cations in bulk and at the interface.

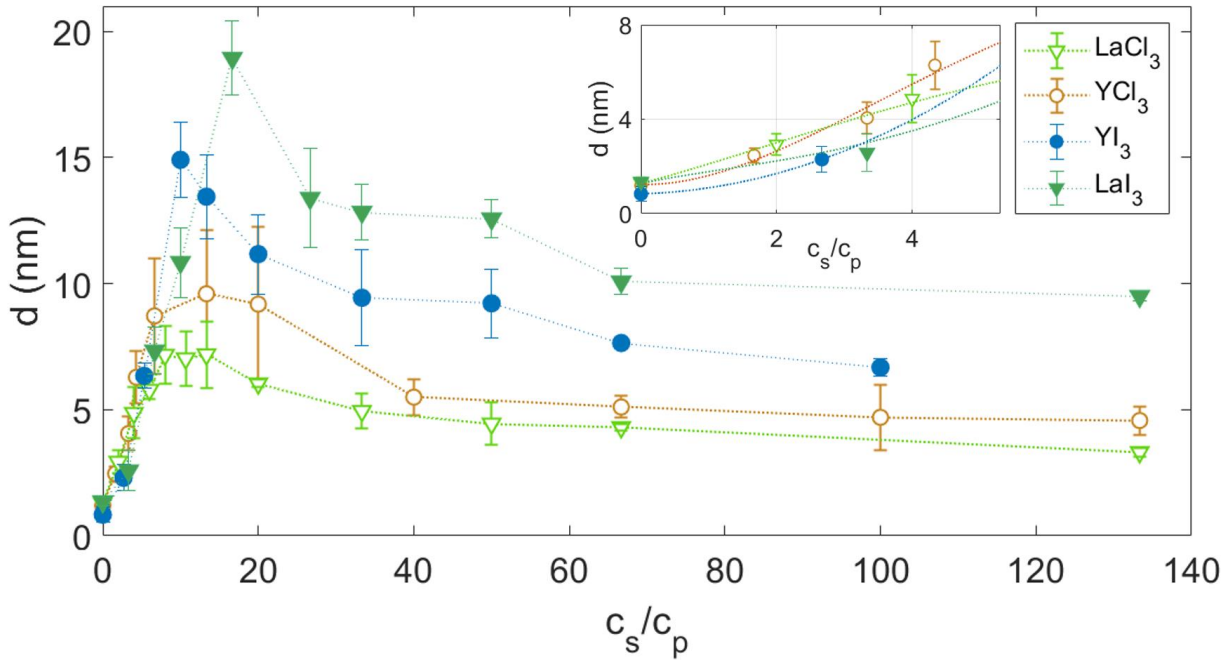

***Figure 7.7**: Ion effect on protein adsorption. Ellipsometric measurements of the adsorbed protein layer thickness d as a function of c_s/c_p at 20 mg/ml BSA and room temperature for $LaCl_3$ (light green), YCl_3 (orange), YI_3 (blue), and LaI_3 (dark green). The data for YCl_3 is taken from Ref.* [427]. *The absolute value of d increases as $LaCl_3 < YCl_3 < YI_3 < LaI_3$. For better visibility, the inset shows a magnification of the initial adsorption increase from 0 to 5 c_s/c_p together with a guide to the eye.*

The shape of the adsorption curve maximum is similar to the bulk interactions. In bulk, regime II of the BSA-$LaCl_3$ system is very narrow compared to YCl_3 (**Figure 7.3 (c)**), which is reflected in the width of the maximum. For the iodide salts, the LLPS regime starts at lower c_s (3 mM) for YI_3 than for LaI_3 (5 mM) (**Figure 7.3 (a & b)**). This bulk instability induces stronger adsorption explaining the position of the curve maximum (**Figure 7.7**).

Another interesting observable is the maximum adsorbed amount, which follows the order $LaCl_3 < YCl_3 < YI_3 < LaI_3$. The weaker adsorption for $LaCl_3$ in comparison with YCl_3 is due to weaker attractive protein-protein and subsequently protein-substrate interactions, which can be explained using the ion-activated attractive adsorption model [427]. It assumes negatively charged patches on the protein and the substrate to which cations can bind and also form ion bridges between protein molecules and between protein and substrate. In this model, the chloride anions are neglected since they have no strong impact on the overall bulk [209,481] or adsorption behaviour (as explained in Chapter 7.2). Adsorption is guided by the number of multivalent cations bound to the proteins and the substrate and an attractive wall potential experienced by the proteins [427]. This obviously applies for both $LaCl_3$ and YCl_3.

The iodide salts show higher maximum adsorption in comparison to the chloride salts. It is important to bear in mind that the iodide salts induce strong LLPS in regime II in the bulk solution (**Figure 7.3**). In Chapter 6, the correlation of metastable LLPS formation (bulk instability) in bulk with enhanced protein adsorption [465] is investigated and a wetting transition induced by LLPS at the solid interface for BSA with YCl_3 is found. These results are in good agreement with the findings in this section and further support the wetting layer transition at bulk instability also for iodide salts. Here, LaI_3 leads to more pronounced adsorption compared to YI_3, which appears counter-intuitive at first. Even though yttrium induces stronger interprotein attraction, it appears that this trend is reversed if the counterion is iodide. This shows that the ion-activated adsorption model cannot be applied to the iodide salts since the iodide anions compared to chloride ions have a strong impact on the phase behaviour, as well as on adsorption, and the model does not account for the anions in solution. Note that in regime II only the dilute phase can be used for ellipsometry measurements. The dilute phase shows a c_s -dependent decrease in c_p (see **Figure 7.6**). This effect may contribute in some form to the smaller amount of adsorbed protein in the presence of YI_3 compared to LaI_3 but does not alter the dominant interaction and interaction strength of the bulk solution. It seems that a 'stronger' cation such as Y^{3+} induces interactions, which interfere with and diminish the effect of iodide. However, with a 'weaker' cation such as La^{3+}, iodide has a more prominent effect on the amount of protein adsorbed, indicating a pronounced formation of anion bridges and non-specific protein-protein binding.

At high c_s, re-entrant adsorption is observed for all salts. For the chloride salts, this is expected since these salts undergo re-entrant condensation at c^{**} from regime II to regime III in bulk, which is defined by charge inversion of the proteins due to trivalent cation binding [150] and thus a decrease in attractive forces leading to smaller clusters and

to a decrease in adsorption. These results are consistent with previous findings in polyelectrolytes [558] and proteins [465] and can be explained with the ion-activated adsorption model [427]. For the iodide salts, re-entrant condensation in the bulk is not observed. Re-entrant adsorption on a solid interface, however, is observed. For a hypothesis rationalising this behaviour, it helps to consider the possible protein-protein vs protein-surface interactions. Due to the surface being negatively charged and hydrophilic, anions are not likely to bind to the substrate with high surface excess since iodide prefers to adsorb to non-polar and/or positively charged surfaces [141,534,539,541,545]. This means that in the vicinity of the substrate with restricted properties, charge inversion mediated by trivalent cations can and does occur. In the bulk, in contrast, this is not the case due to the complex protein surface of BSA containing nonpolar, polar, negatively and positively charged areas. Consequently, the variety of possible protein-protein and protein-salt interactions hinder re-entrant condensation.

7.3.2 Global Protein Structure on Substrate (ATR-FTIR)

To exclude denaturation at the interface as the primary source for re-entrant adsorption at high c_s, ATR-FTIR measurements with BSA are performed in the presence of $LaCl_3$ and LaI_3 on a Si block (**Figure 7.8**), which showed essentially intact secondary protein structures. To determine the influence of the bulk proteins on the absorbance data, the cell is flushed and checked if the signal of the reversibly adsorbed proteins in water is changing compared to the adsorption layer in bulk. The intensity might change, yet the overall shape of the curve is the same (***Figure* 7.9**). Thus, the difference between protein structure in bulk and at the interface is non-existent.

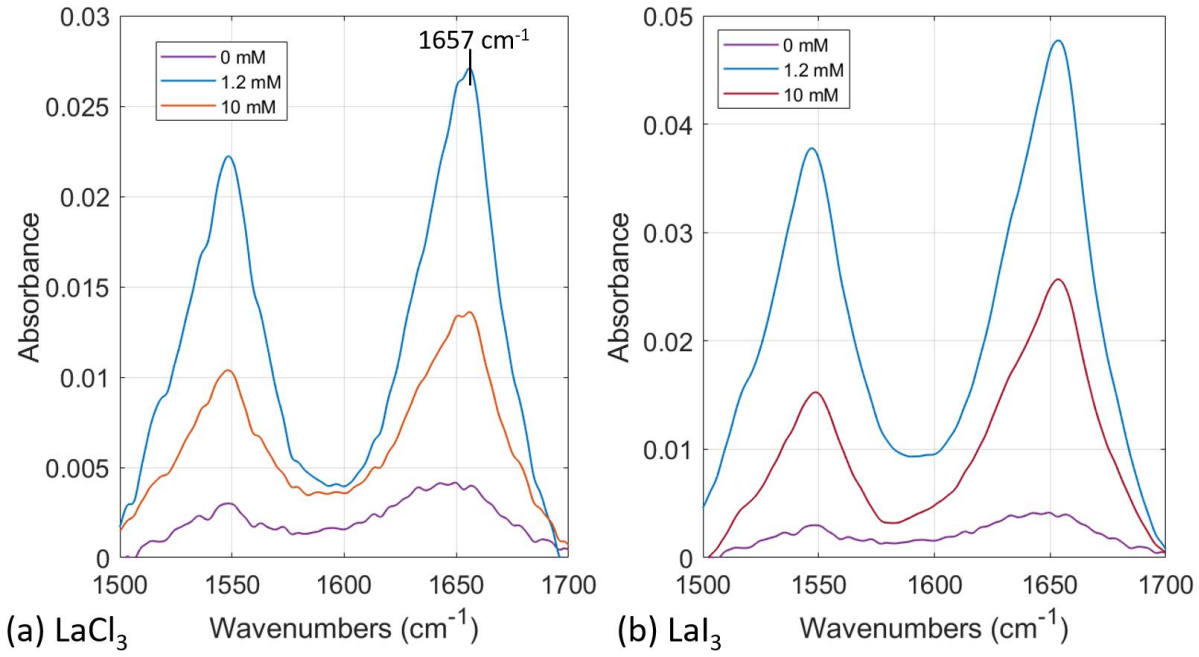

***Figure 7.8**: Structure of adsorption layer. ATR-FTIR measurements of 5 mg/ml BSA in H_2O on SiO_2 substrates for (a) $LaCl_3$ and (b) LaI_3 at no salt, 1.2, and 10 mM, respectively.*

The ATR-FTIR spectra in protein solution can be used for analysis and interpretation. The measurements are conducted in H_2O, but checks are made in D_2O (data not shown), to ensure the background subtraction is sufficient even though the H_2O and amide-I signals are overlapping. The data are corrected for the background, but not for the baseline, which explains the small offset at 0 absorbance of the individual curves (**Figure 7.8**).

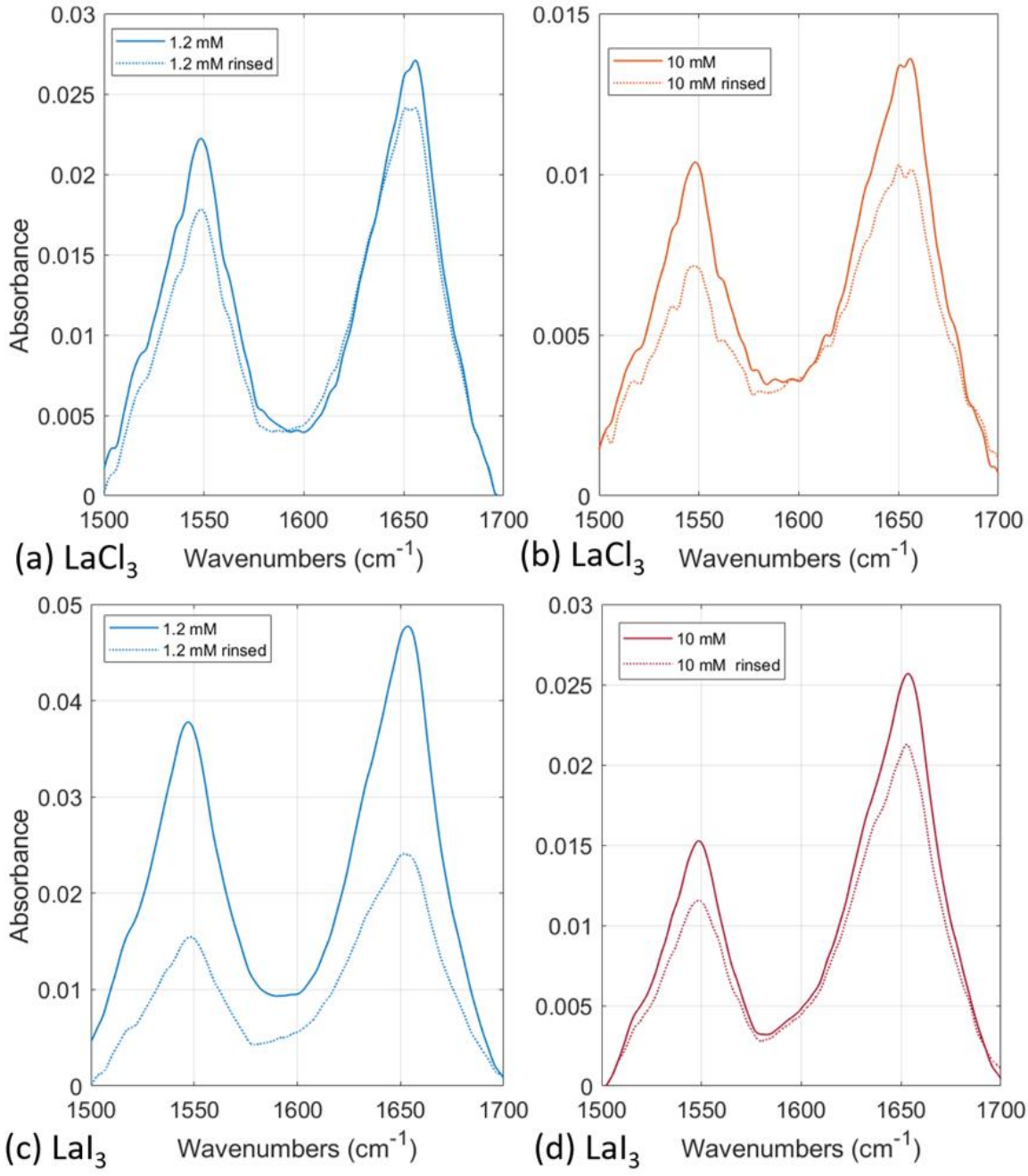

Figure 7.9: Protein interface signal vs bulk signal. Protein adsorption measurements are investigated by ATR-FTIR at RT for 5 mg/ml BSA and $LaCl_3$ at (a) 1.2 mM, (b) 10 mM, and LaI_3 at (c) 1.2 mM and (d) 10 mM. The solid lines depict the measured absorbance signal in the protein solution containing bulk and interface signal. The dotted lines show the sample rinsed with water, thus, only depict the signal of the irreversibly adsorbed proteins.

7.3.3 Protein Layer Structure and Kinetics (QCM-D)

Complementary measurements are conducted with QCM-D, which on the one hand confirm the results of the presented ellipsometry data, and on the other hand provide additional insights into the structure and properties of the adsorption layer [559,560]. For data analysis, the Voigt viscoelastic model [392,394–396] is used to calculate the thickness of the adsorbed layer from the measured frequency and dissipation changes (for examples of raw data see **Figure 7.10** & **Figure 7.11**). Already from the raw data, the difference between $LaCl_3$ and LaI_3 is obvious. For all samples in the presence of the respective salt, the frequency drop is lower in the presence of LaI_3.

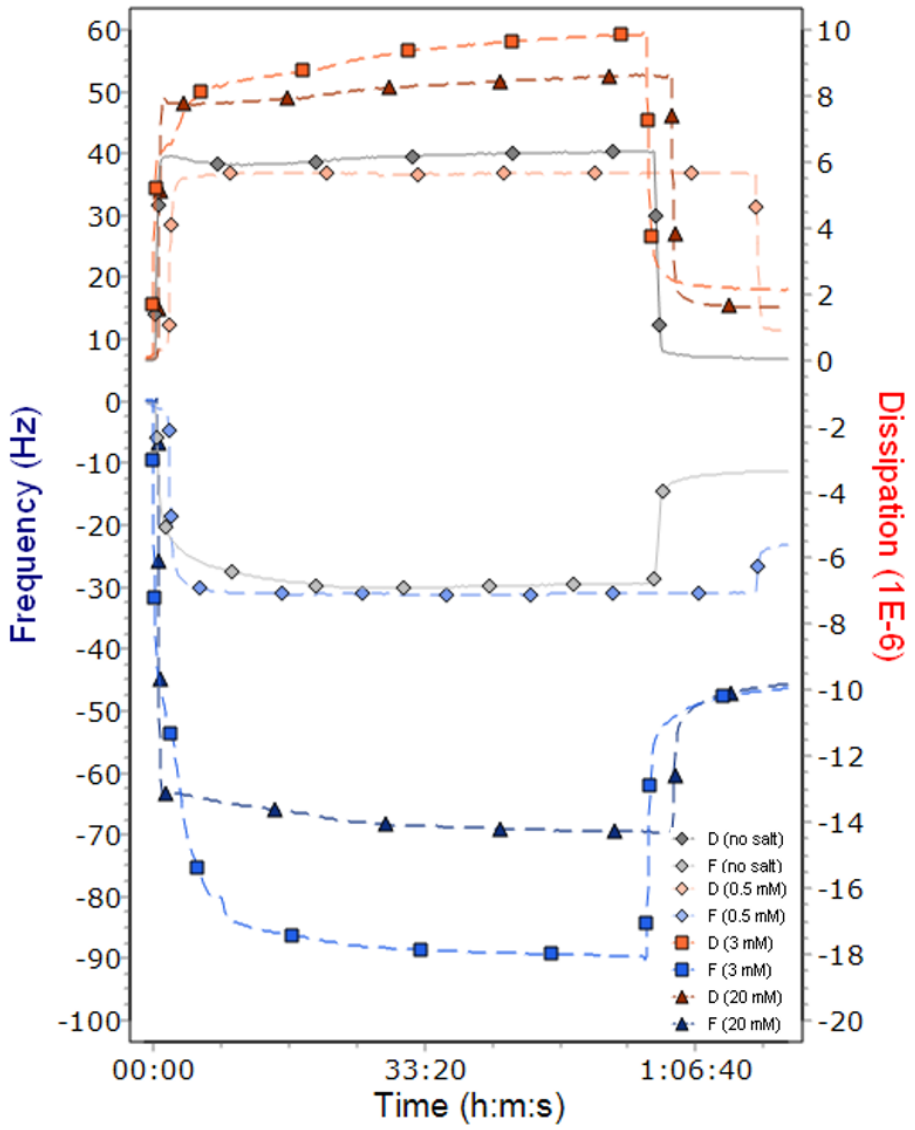

Figure 7.10: Real-time adsorption data. QCM-D frequency and dissipation changes during protein adsorption of 20 mg/ml BSA at room temperature with $LaCl_3$ at different c_s reflecting the adsorption behaviour in the different regimes. Note that only the 9th overtone of each measurement is shown for better clarity. Initially, the cell is filled with water, then the protein/salt solution is pumped in and measured for 1h, after which the cell is flushed with water to check for irreversible protein adsorption.

This means that more proteins are adsorbed to the substrate leading to a stronger damping of the oscillating substrate compared to the same c_s of $LaCl_3$. In addition, the dissipation is higher in the LLPS regime indicating a more diffuse layer formation. Similar to the ellipsometry data (**Figure 7.7**), re-entrant adsorption is observed for both data sets. The calculated adsorbed protein layer thickness $d_{QCM\text{-}D}$ is plotted in **Figure 7.12 (a)**. The overall adsorbed $d_{QCM\text{-}D}$ of BSA/LaI_3 is enhanced compared to $LaCl_3$, which is in good agreement with the results shown in **Figure 7.7**. By rinsing the QCM-D cell with water, the amount of irreversibly adsorbed proteins is determined (**Figure 7.12**, black symbols). These make up only a small portion of the full adsorption layer of roughly 10 nm and can be assumed to be the first monolayer of proteins directly in contact with the substrate.

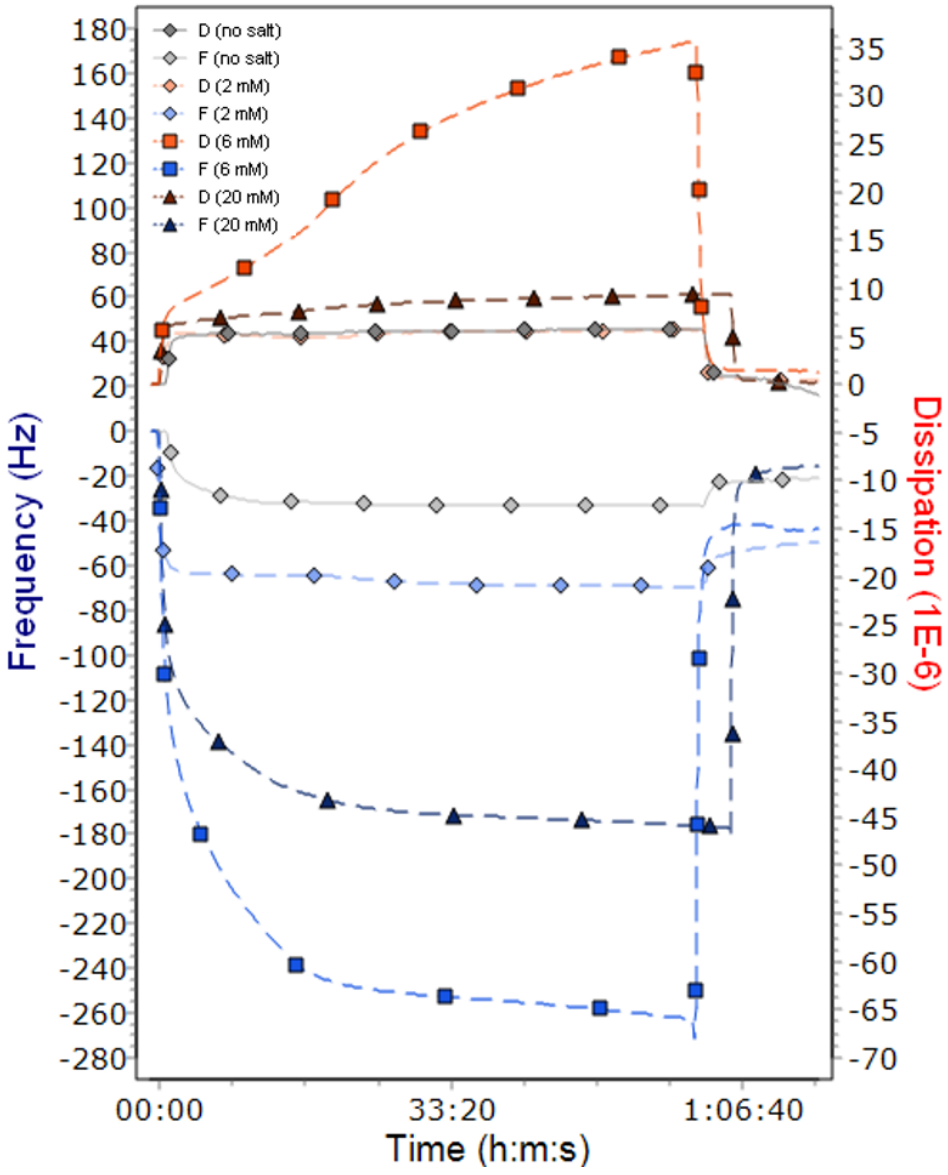

Figure 7.11: Real-time adsorption data. QCM-D frequency and dissipation changes during protein adsorption of 20 mg/ml BSA at room temperature with LaI_3 at different c_s reflecting the adsorption behaviour in the different regimes. Note that only the 9th overtone of each measurement is shown for better clarity. Initially, the cell is filled with water, then the protein/salt solution is pumped in and measured for 1h, after which the cell is flushed with water to check for irreversible protein adsorption.

A big advantage of QCM-D in combination with ellipsometry is that the associated water d_{assoc} within the adsorption model can be determined (**Figure 7.12 (b)**) [412,417]. The associated water consists of a hydration layer around the proteins, hydro-dynamically bound water to the substrate and water trapped within the adsorption layer [413]. With the information on the water content in the adsorption layer, the layer morphology can be better understood. In Chapter 6 (based on Ref. [465]), experimentally and theoretically the correlation between the formation of a wetting layer at the bulk instability induced by LLPS is established, which exceeded simple 'stronger adsorption'. Here, only LaI_3 leads to LLPS in regime II and thus induces enhanced adsorption. The calculated associated water content is massively enhanced at c_s/c_p = 20, which reflects the onset of enhanced adsorption (wetting transition) compared to a 'normal' adsorption layer in regime I and III and therefore is consistent with previous findings of BSA/YCl_3 [465].

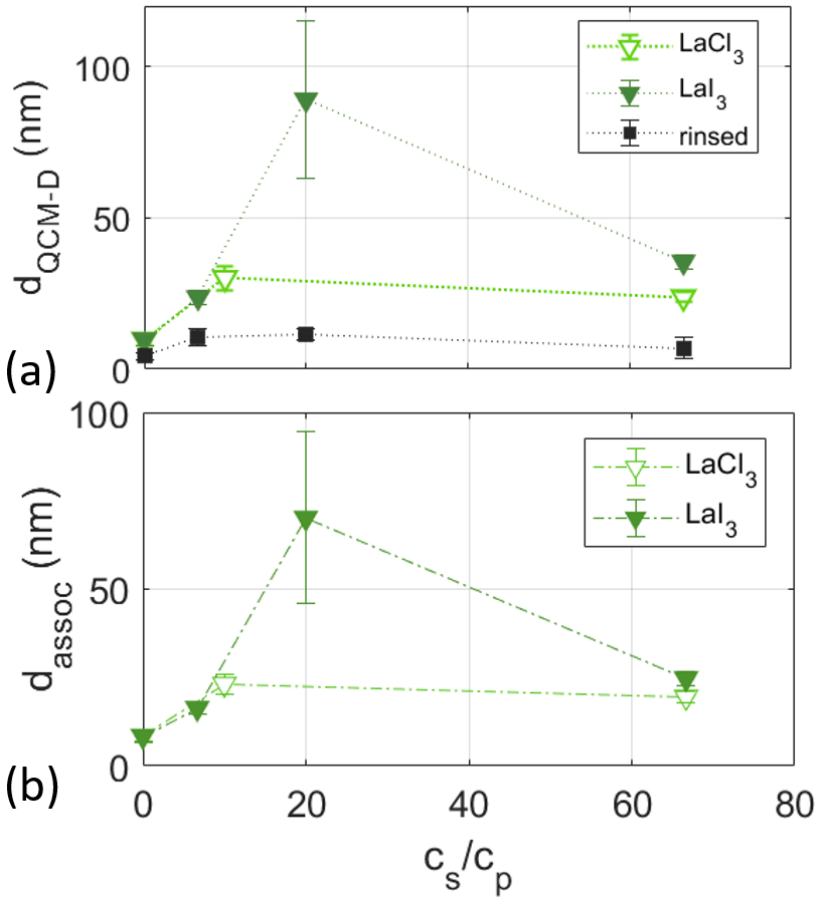

Figure 7.12: BSA adsorption with associated water content. (a) d_{QCM-D} as a function of salt concentration at 20 mg/ml BSA and room temperature for $LaCl_3$ (light green), LaI_3 (dark green), and rinsed LaI_3 with water (black). (b) Associated water d_{assoc} reflects the water content within the adsorption layer, which is calculated by subtracting the ellipsometer data from the QCM-D data. The enhanced adsorption of LaI_3 is due to a bulk instability (LLPS) and the subsequent formation of a wetting layer. Note that the offset between the two maxima is due to the different positions of regime II in the bulk.

This is also reflected in the changed viscoelastic properties and higher water content in the adsorbed protein layer in regime II. Besides this concentration, the water content in the

adsorbed layer is comparable between these two salts assuming the same layer morphologies and only enhanced adsorption in the presence of iodide salts.

7.4 Summary

In this chapter, the focus is on the effect of anions and cations on the protein bulk behaviour and adsorption behaviour of BSA. Interestingly, it is revealed that the co-ion (anion) changes the balance and weakens the effect of trivalent cations in the bulk, making re-entrant condensation disappear and liquid-liquid phase separation appear. Chloride does not appear to significantly affect the phase diagram of BSA with either cation, whereas iodide promotes stronger attractive protein-protein interactions. This illustrates a dominant role of anions on the phase behaviour of globular proteins in the presence of multivalent cations.

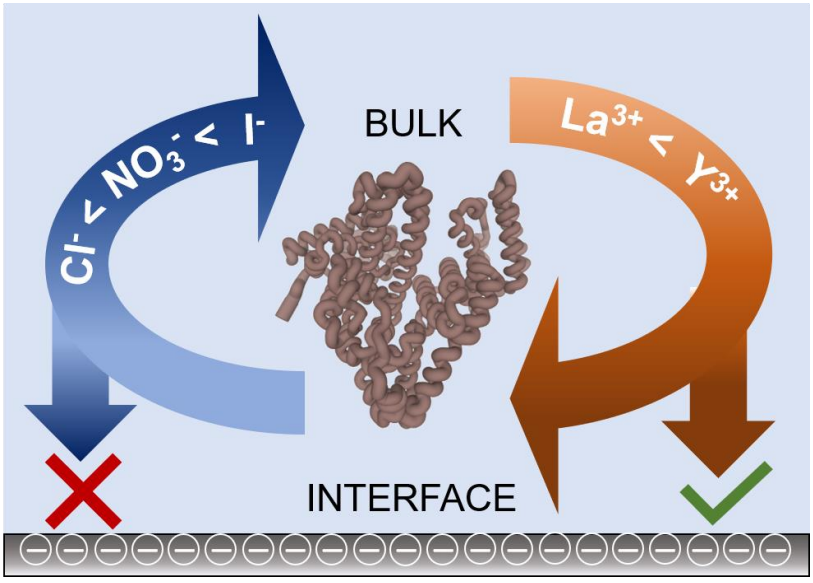

Figure 7.13: Graphic illustration of the results found. The cations can bind to the interface and to the protein, whereas the anions are bound by the protein, but not to the interface due to the specific interface properties. This leads to different interface behaviour and bulk behaviour depending on the salt used. The induced protein-protein and protein-substrate interactions increase from $Cl^- < NO_3^- < I^-$ *and* $La^{3+} < Y^{3+}$.

By choosing specific substrate properties (here: imitating the bulk properties), the influence of ions on protein adsorption can be controlled. In the BSA-YCl_3 system investigated in Ref. [427], the bulk and adsorption behaviour are highly similar due to the negative charge of the proteins, as well as the substrate, and the passive role of chloride. By extending this investigation to salts with different cations and anions, it is shown that the adsorption behaviour is not solely guided by the dominant electrostatic bulk interactions but can also be triggered by surface parameters (**Figure 7.13**). This explains the observations presented here: re-entrant adsorption in the absence of re-entrant condensation in bulk. The higher adsorbed amount supports the dominant role of iodide and the hypothesis of anion bridging and non-specific binding in bulk.

Through the use of suitable anions and cations, the dominant interactions in bulk can be tuned, while in the adsorption process substrate properties can effectively reduce or even uncouple those interactions. The regulation of interactions on a molecular level opens up new avenues for drug design and biomaterials. In addition to its medical relevance, the use of iodide is potentially very useful for investigations of these kind of systems using X-rays due to its high scattering power and contrast with light elements (i.e. water and proteins).

8 Bulk Phase Behaviour vs Interface Adsorption: Effects of Anions and Isotopes on BLG Interactions

The following chapter is based on Ref. [561] and was conducted in collaboration with Dr. Maximilian W. A. Skoda from ISIS (Rutherford Appleton Laboratory, UK), who analysed the neutron data presented in this chapter. Additional complementary neutron and X-ray measurements are discussed in Appendix A and complementary measurements of BLG in the presence of YCl_3 in Appendix B.

8.1 Background

The human body is composed of roughly 16% of proteins [19] and has to ingest ideally 180 g per day of dietary proteins to allow proper body function [562,563]. In Central European countries, these dietary proteins originate to 28% from meat and meat products, 28% from milk and dairy products, 3% from fish, 3% from eggs and the rest are of plant origin [564,565].

The major protein component of bovine whey is beta-lactoglobulin (BLG) [82]. The physiological concentration of BLG in cow milk varies between 4 to 20 mg/ml [246]. The (main) function of BLG is (not yet) fully established, but it is found to transport and bind small hydrophobic ligands e.g. vitamin D, cholesterol, retinol and fatty acids [82,233,246,247,566]. Consequently, it contributes to the milk fatty acid metabolism [246], enzyme regulation, and neonatal acquisition of passive immunity [82]. Its antioxidant properties are a health benefit especially for milk consumers [567].

On the one hand BLG does not occur in human milk [568] and as a consequence it is the most common source for food allergies and (milk) intolerances in humans [569]. On the other it can be used as a natural carrier for e.g. nutraceuticals due to its naturally abundance, biodegradability, and biocompatibility [570]. It allows the enrichment of food with nutrients through protein encapsulation, protein-based emulsions, or cross-linked hydrogels [411,570,571].

Due to its resistance to acid proteases [572] and gastric digestion in vivo [573], BLG stays intact after passing the stomach. This property is not only utilised for incorporation and delivery of nutraceuticals [411], but also for drug delivery [570,574]. Protein-based drug delivery systems enable lipophilic drugs to be absorbed more rapidly and to transport otherwise poorly water-soluble drugs such as Fenofibrate, Theophylline or Sulfamethoxazole [571,575]. Importantly in this context, BLG can crystallise under certain

conditions [576]. This facilitates new possibilities for drug production in terms of purification and stabilisation of drugs through proteins [577]. One approach to control protein crystallisation is through the addition of salt [78,147,148,482].

In food processing, salt is an important ingredient for preservation, stabilisation, and flavour enhancement [258,578]. BLG is known to naturally bind calcium (Ca^{2+}) [579], which can induce a variety of phase behaviours e.g. salt-induced gelation of BLG based on hydrophobic interactions [579], which finds application in cosmetics [571]. Other multivalent salts such as YCl_3, $NdCl_3$, $CdCl_2$ and $ZnCl_2$ are found to induce a rich phase behaviour for BLG featuring re-entrant condensation, liquid-liquid phase separation and protein crystallisation [78,147–149,482,580]. This illustrates the complexity and variety of interactions guiding the BLG bulk phase behaviour of competing (electrostatic and hydrophobic) interactions.

Yet not only the bulk interactions have to be considered, but also possible interactions with interfaces. The interactions of proteins such as BLG with the steel containers and other 'milk' components must be understood to allow sterile and contamination-free food processing. The cleaning and processing of these products are based on the idea of desorption of proteins and anti-fouling surfaces [581,582]. Certain interface properties can be favoured e.g. charged membranes in filtration systems allow better separation of proteins [14]. In this context, the interplay of bulk and adsorption properties is important to understand and to control.

In this chapter, the focus is on the behaviour of BLG and the influence of different salts ($LaCl_3$, LaI_3) and solvents (H_2O, D_2O) on its bulk phase via UV-Vis spectroscopy measurements, pH measurements and optical microscopy and adsorption behaviour on a solid, net negatively charged, hydrophilic surface (SiO_2) with NR, QCM-D, and ATR-FTIR. Thus, insight is obtained into the adsorbed layer thickness (d), hydration, roughness, and secondary structure. In addition, through the use of lanthanum (La^{3+}) as a multivalent cation, new phase diagrams of BLG are established. This chapter focuses on the primary stage of protein crystallisation, namely nucleation at interfaces or protein adsorption.

8.2 Bulk Phase Behaviour

The focus is on two different salts, namely lanthanum chloride ($LaCl_3$) and lanthanum iodide (LaI_3), and their influences on the BLG phase behaviour in H_2O as shown in **Figure 8.1 (a & b)**. The respective phase diagrams in D_2O can be found in **Figure 8.5**. Both salts in either solvent exhibit the same general trend showing two phase transitions, c^* and c^{**}, as well as protein crystals.

8.2.1 Phase Diagrams

BLG is net negatively charged (10 e^-) at neutral pH [78,195]. This means repulsive forces dominate and the samples of regime I are clear (see **Figure 8.2**).

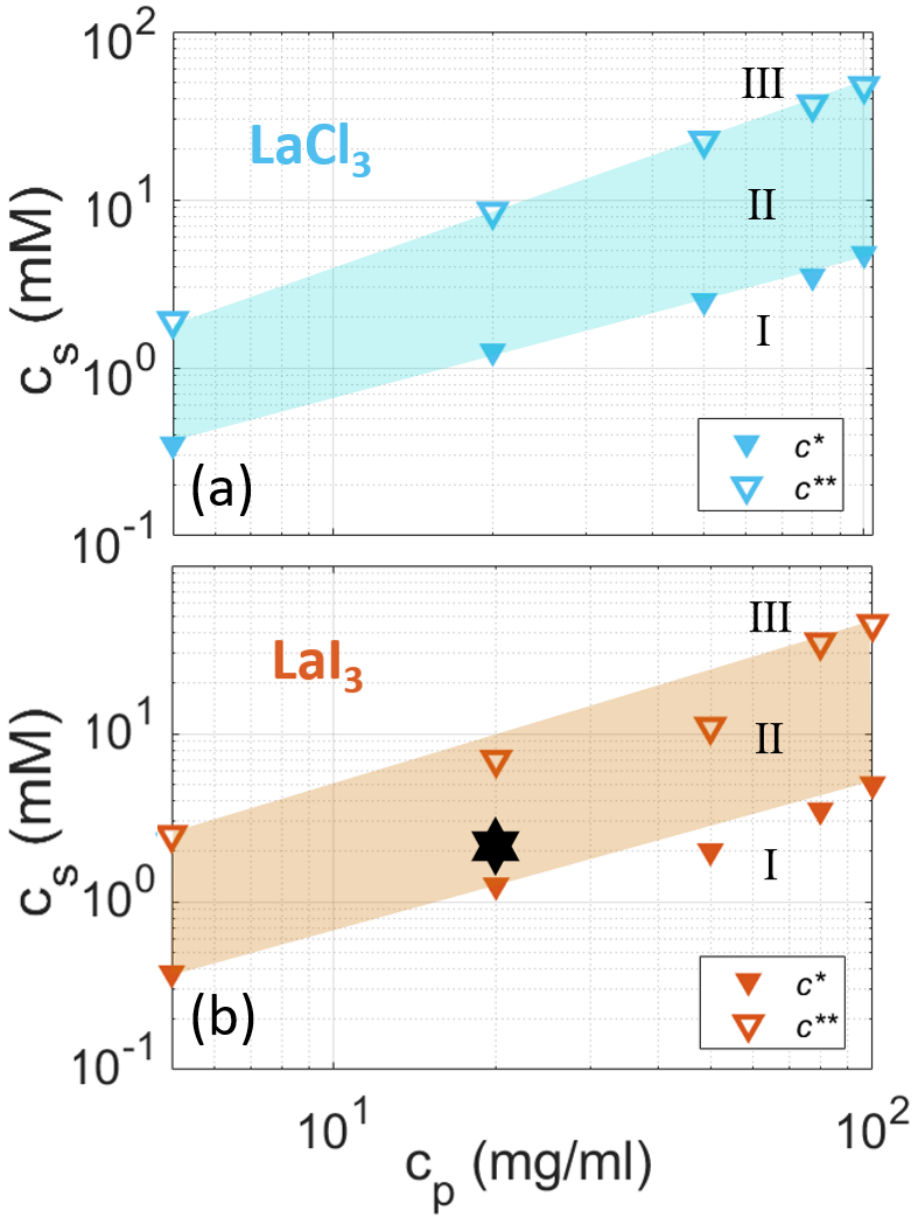

Figure 8.1: Phase diagrams. BLG in H_2O (a) with $LaCl_3$ and (b) with LaI_3. The solid triangles define c, which separates regime I from regime II. The hollow triangles define c**, which separates regime II from regime III. The phase diagrams are nearly identical when comparing the different lanthanum salts. All samples in regime II and around c*/c** crystallise over time. Note that the black star refers to the sample condition shown in Figure 8.3.*

The first phase transition, defined by the specific salt concentration *c**, is reached, if the dominant interactions convert from repulsive to attractive due to multivalent cation binding and bridging [148,155,209]. Through the addition and increase in salt concentration (c_S), protein aggregates start to form in regime II, which can be confirmed by the turbidity of the solution [80]. If c_S is further increased, the proteins undergo charge inversion from net negatively to net positively charged resulting in a decrease in attractive forces and the break-up of protein aggregates (clear solution in regime III, **Figure 8.2**).

Figure 8.2: Phase transitions. Dilution series at 5 mg/ml BLG and room temperature with (a) $LaCl_3$ and (b) LaI_3 in H_2O. The bottles are labelled with the respective c_s in mM.

This behaviour is called re-entrant condensation (RC) and defined by another transition point c^{**}. Certain samples in regime II and around the phase transitions initially form aggregates and undergo a (two-step) liquid-liquid phase separation in a dilute and dense liquid phase over time (Figure 8.3 (b)), if the dominant attractive forces are sufficiently strong. This behaviour is similar to the phase behaviour found for other multivalent salts such as YCl_3 with BLG [148].

In comparison with the phase diagram of BLG/YCl_3, the lanthanum salts show a narrower regime II, which indicates weaker attractive forces induced by lanthanum (La^{3+}), which is consistent with trends found for other globular proteins such as BSA and can be explained with differences in surface charge density and polarisation of the individual cations [152,349].

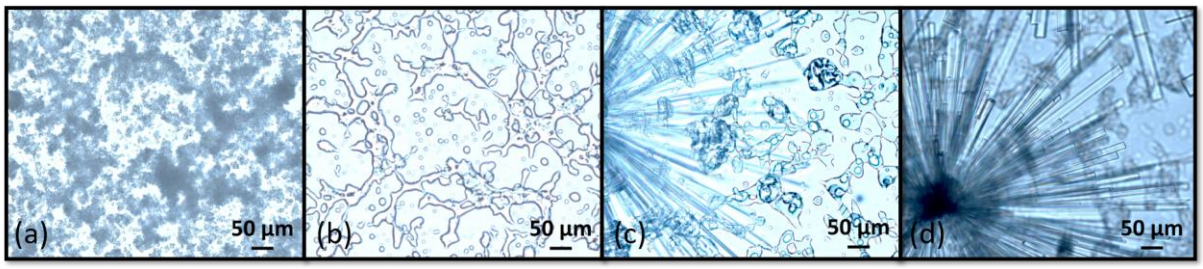

Figure 8.3: Crystallisation pathway. Microscopy images of a sample containing 20 mg/ml BLG and 2 mM LaI_3 in H_2O. (a) Aggregation. (b) Liquid-liquid phase separation (LLPS) into dilute and dense phase after 1h. (c) Nucleation and crystal growth after 8 hours consuming the dense phase. (d) Crystalline sample with sea-urchin-like structure after 2 days.

8.2.2 Protein Crystallisation

The samples in regime II and around the phase transitions are of special interest since those can crystallise over time. Initially, due to the attractive forces in the system, protein aggregates are formed (**Figure 8.3 (a)**). Those aggregates undergo liquid-liquid phase separation (LLPS) resulting in a dilute and dense liquid phase (**Figure 8.3 (b)**). Over time, nuclei start to form, and protein crystallisation begins forming sea-urchin-like structures and consuming the dense liquid phase shown by gas/bubble formation in **Figure 8.3** (**c & d**), which is typical for a two-step crystallisation pathway. Interestingly, BLG (PDB: 3PH6) [148] shows the same crystal structure/space groups with different trivalent salts, namely $P2_12_12_1$, even though the crystallisation pathways may differ [148,482]. From the protein crystal, the binding sites of the multivalent cations could be determined, which are exclusively negatively charged protein domains [148] meaning electrostatic interactions guide the binding of cations, which is consistent with the established theoretical ion-activated attractive patchy model describing the bulk phase behaviour [209]. Yet, no bound anions are found within the crystal structure, which could explain the anion-independent phase behaviour of BLG. The crystallisation time is significantly longer in D_2O than H_2O (days vs hours), which could be due to stronger solvent-solvent interactions in D_2O than in H_2O, which stabilise the protein in its cluster formation [154], as well as hinder protein flexibility [583] and thus slow down the crystallisation process.

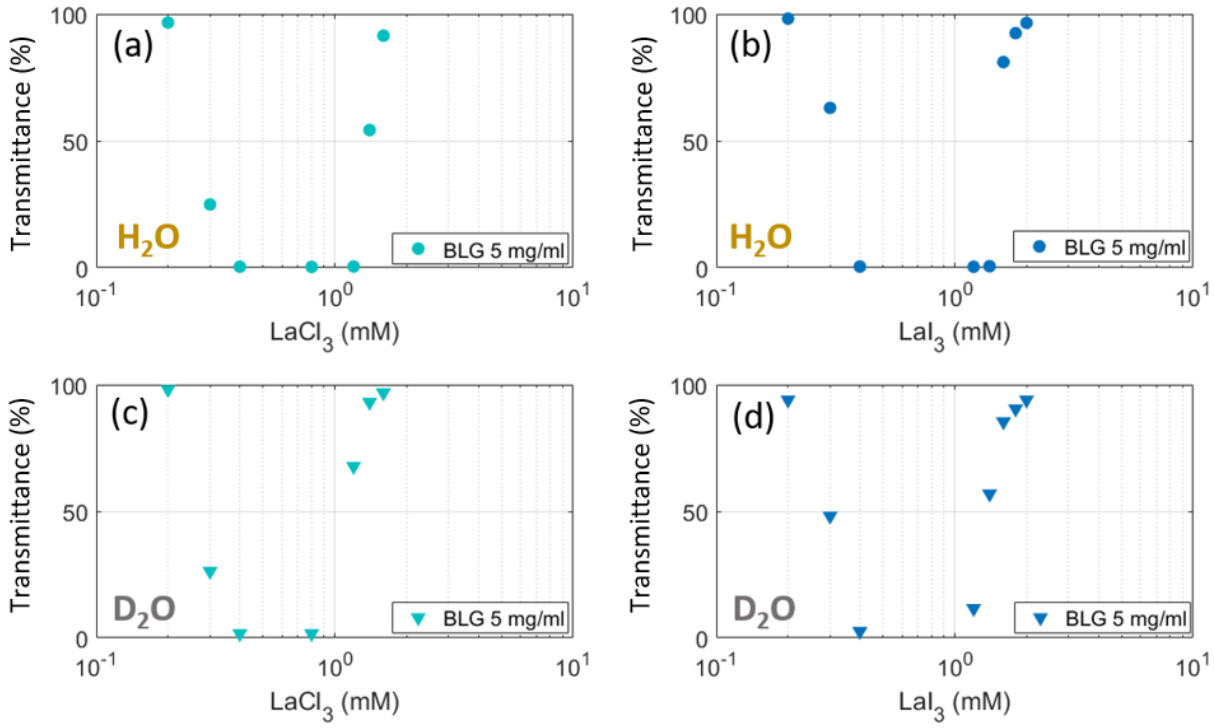

***Figure 8.4**: UV-Vis transmittance measurements. The phase transitions at 5 mg/ml BLG with $LaCl_3$ (a) in H_2O, (c) in D_2O, and BLG with LaI_3 (b) in H_2O, (d) in D_2O are depicted dependent on its transmittance (λ = 400 to 800 nm). c* is defined as the c_s, at which transmittance starts to decrease. c** is defined as c_s at which 50 % of transmittance is restored. The absolute numbers are listed in **Table 8.1**.*

Table 8.1: Phase transitions. This list contains the determined phase transitions, c and c**, of BLG at 5 mg/ml with $LaCl_3$ and LaI_3 in H_2O and D_2O from Figure 8.4.*

	$LaCl_3$		LaI_3	
Solvent	c^* [mM]	c^{**} [mM]	c^* [mM]	c^{**} [mM]
H_2O	0.25	1.4	0.3	1.5
D_2O	0.25	1.2	0.3	1.4

8.2.3 Bulk Behaviour for Adsorption Measurements

The protein concentration of interest for the adsorption investigation is set to 5 mg/ml, which is high enough to observe the complete rich phase behaviour and to be physiologically relevant, but low enough to minimise the bulk signal, and thus, bulk scattering in the neutron reflectivity measurements. The phase behaviour at $c_p = 5$ mg/ml is illustrated in **Figure 8.4** which shows the measured transmittance runs via UV-Vis spectroscopy since detecting by eye at this concentration is not precise enough. The determined values of c^* and c^{**} from **Figure 8.4** are listed in **Table 8.1**.

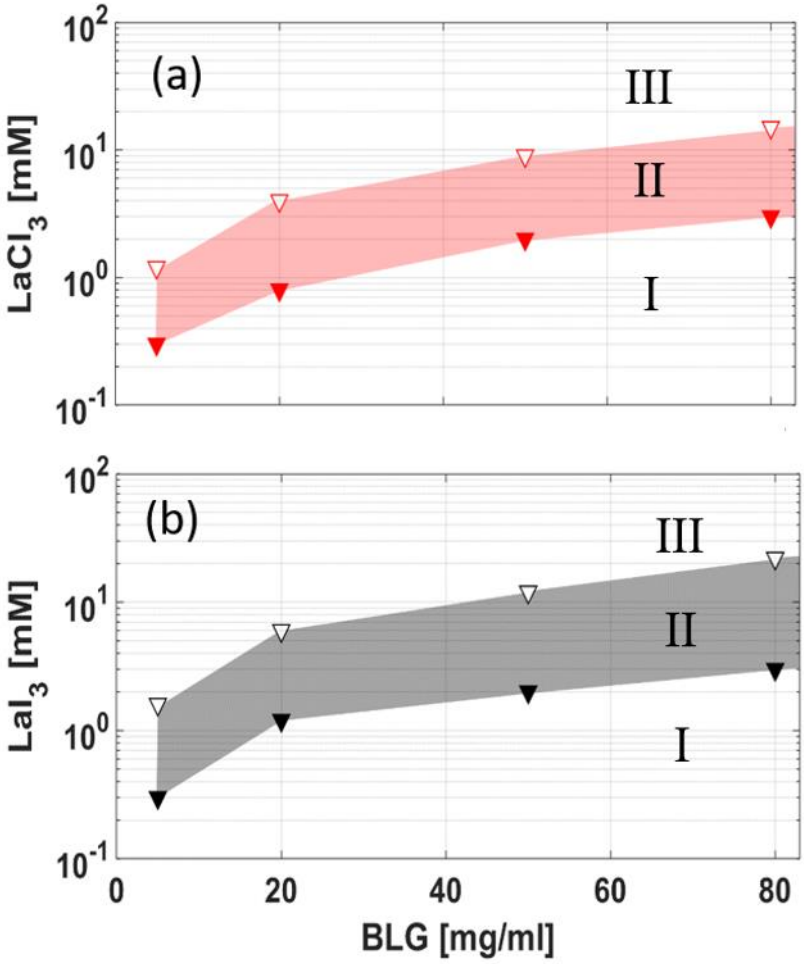

Figure 8.5: Phase diagrams in D_2O. The phase behaviour of BLG in D_2O in presence of (a) $LaCl_3$ and (b) LaI_3 at room temperature is determined via dilution series and UV-Vis transmittance measurements.

The phase diagrams of BLG, as well as the transmittance measurements, with the individual salts and solvents in **Figure 8.1**, **Figure 8.4** and **Figure 8.5** are quite similar to each other, yet small differences in trends can be seen. For LaI_3, the phase transitions occur at slightly higher c_s compared to $LaCl_3$, as well as in H_2O compared to D_2O. These differences are within the statistical error of the measurements at 5 mg/ml but become more pronounced at higher c_p.

In order to assess and estimate the change in pH induced by the addition of multivalent salts, pH measurements are conducted and presented in **Figure 8.6**. Initially for both systems, the pH slightly decreases due to the salt-induced water hydrolysis upon the addition of salts [481], yet these changes do not correlate with the phase behaviour and cannot explain phenomena such as re-entrant condensation at high c_s. Consequently, pH can be excluded as the dominant force driving the bulk phase behaviour. This is in good agreement with past pH measurements with BLG and other globular, net negatively charged proteins [481,491].

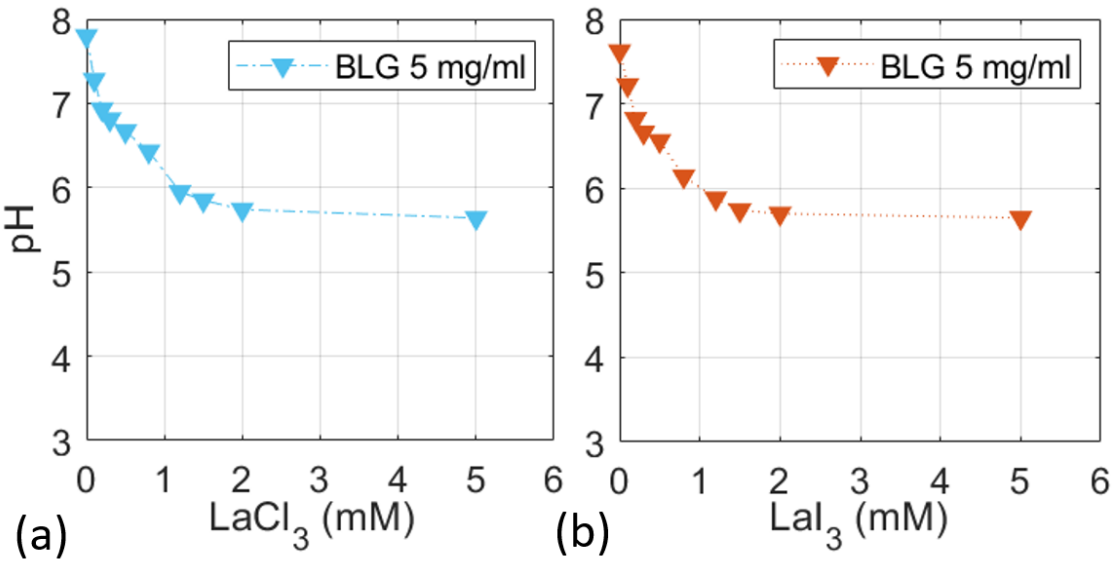

Figure 8.6: Bulk pH measurements at 5 mg/ml BLG with (a) $LaCl_3$ and (b) LaI_3 in H_2O and room temperature. No salt-type-dependent differences in pH can be observed.

Importantly, the known isotope effect of BSA [154], meaning significantly stronger attractive forces in D_2O compared to H_2O and thus a strong shift in phase transitions, cannot be observed for BLG, if even, slightly the opposite effect can be detected. This is important to mention since this means there are more fundamental differences between BSA and BLG, both belonging to the group of net negatively charged globular proteins, as initially obvious. In addition, in the case of BLG, the use of the solvent contrast for the neutron reflectivity measurements is feasible since the differences in phase behaviour are marginal between the two solvents (more details can be found in the neutron reflectivity section).

8.2.4 Isotope Effect in the Bulk

The absence of the isotope effect in BLG may be rationalised by its secondary structure and amino acid sequence. It is found that β-sheets show little to no isotope substitution, thus affect, whereas α-helices contribute to the isotope effect [584]. BSA mainly consists of α-helices showing a strong isotope effect and BLG having dominantly β-sheets (54 %) [244] showing no isotope effect. The helix formation substantially benefits if the side chain hydrophobic surface buried against the side of the helix since it facilitates stability [585] explaining the dominant hydrophobic amino acids contribution to α-helix formation and the correlation between hydrophobic interactions and secondary structure (formation). With the Gibbs free energy ΔG of transfer from water, the hydrophobicity of a molecular can be expressed and defines BSA (ΔG = -5.1 kcal/mol) to be more hydrophobic than BLG (ΔG = -1.7 kcal/mol) [238]. It is found that hydrophobic interactions are enhanced in D_2O due to stronger solvent-solvent hydrogen bonds [154,583,586,587], consequently BSA feels a stronger impact of D_2O. Hence, the combination of less α-helices and less hydrophobic interactions could explain the absence of the isotope effect for BLG.

8.2.5 Anion Effect in the Bulk

At last, the absence of an anion effect on the BLG phase diagrams is discussed. Literature shows consistently that BLG binds only a few to none small anions e.g. chloride [588,589]. The ability to bind small anions can be expressed in form of the binding index $'\sum(NH^+)/|\sum(COO^-) - \sum(OH)|'$, which is 4.6 for BLG, but 29 for BSA in comparison [237]. This is supported by Longsworth et al. [538], who found lower anion binding by a factor of 2 for chloride and iodide to BLG, yet the number of bound anions increases from Cl^- to I^-. In this context, it is useful to have a look at the conformation and structure of BLG. The amount of free cationic vs anionic side chains in BLG is 48 (12,9 %) to 64 (17,9 %), which illustrates the protein's stronger tendency to bind cations e.g. Ca^{2+}. In fact, BLG binds twice as many Ca^{2+} as BSA [590]. In addition, BLG tends to bind hydrophobic molecules via hydrophobic interactions [233,591–593]. This is further supported by the absence of fixed anions in the protein crystal structure [148].

8.3 Protein Adsorption

In this section, the focus is on the adsorption behaviour of BLG (c_p = 5 mg/ml) at the solid-liquid interface. For the characterisation of the adsorption layer, QCM-D, ATR-FTIR and NR is used. Through the use of complementary methods, information of the thickness, density and hydration of the adsorption layer, as well as general trends introduced by the different bulk regimes are gathered. SiO_2 is used as the substrate material, which is net negatively charged and hydrophilic in contact with H_2O and D_2O [264,265].

8.3.1 Layer Morphology and Adsorption Kinetics

Protein adsorption at the solid-liquid interface (SiO_2) is measured in real-time in a flow cell with a quartz-crystal microbalance with dissipation (QCM-D). QCM-D allows to get insight into the adsorbed thickness d including the trapped water within in the layer and

its viscoelastic properties [387,398,399,594]. In addition, neutron reflectivity (NR) measurements are performed in-situ at POLREF (ISIS, Rutherford Laboratory, UK) on large Si/SiO_2 substrates to provide information about the thickness, density, roughness, hydration, and morphology of the adsorption layer. In **Figure 8.11**, an overview of the reflectivity curves of BLG with different salt concentrations and types in D_2O is given.

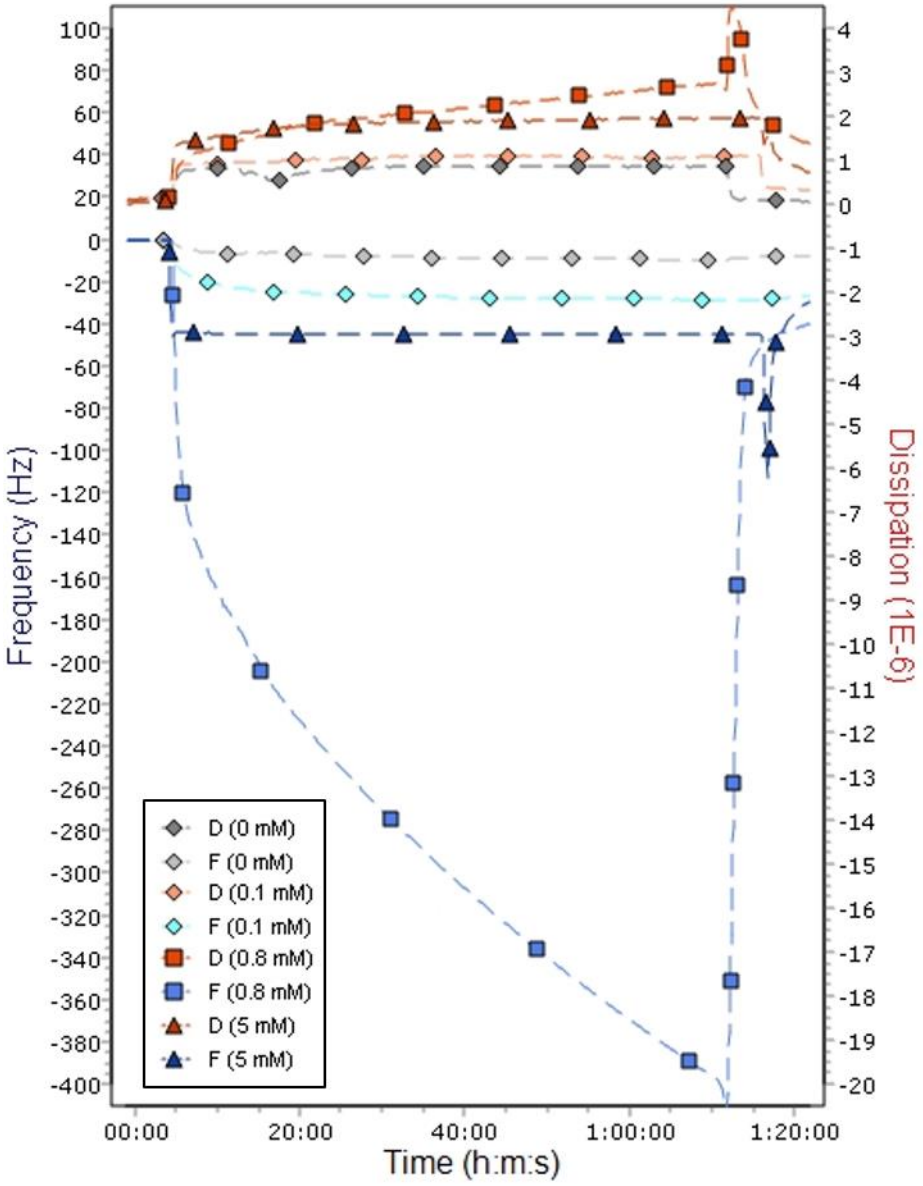

Figure 8.7: Raw QCM-D adsorption data. Frequency (blue) and dissipation (red) of the 9th overtone of BLG at 5 mg/ml in H_2O with $LaCl_3$ at 0, 0.1, 0.8 and 5 mM c_s adsorbed on SiO_2 quartz sensor. These c_s cover the whole phase diagrams and the individual regimes. The measurements start in H_2O and after a few minutes the salt/water mixtures is pump into the cell inducing protein adsorption. After roughly 1 h, the cell is flushed with H_2O to check for the reversibility of protein adsorption. Note that spikes in the raw data are induced by turning the pump on and off for solution exchange.

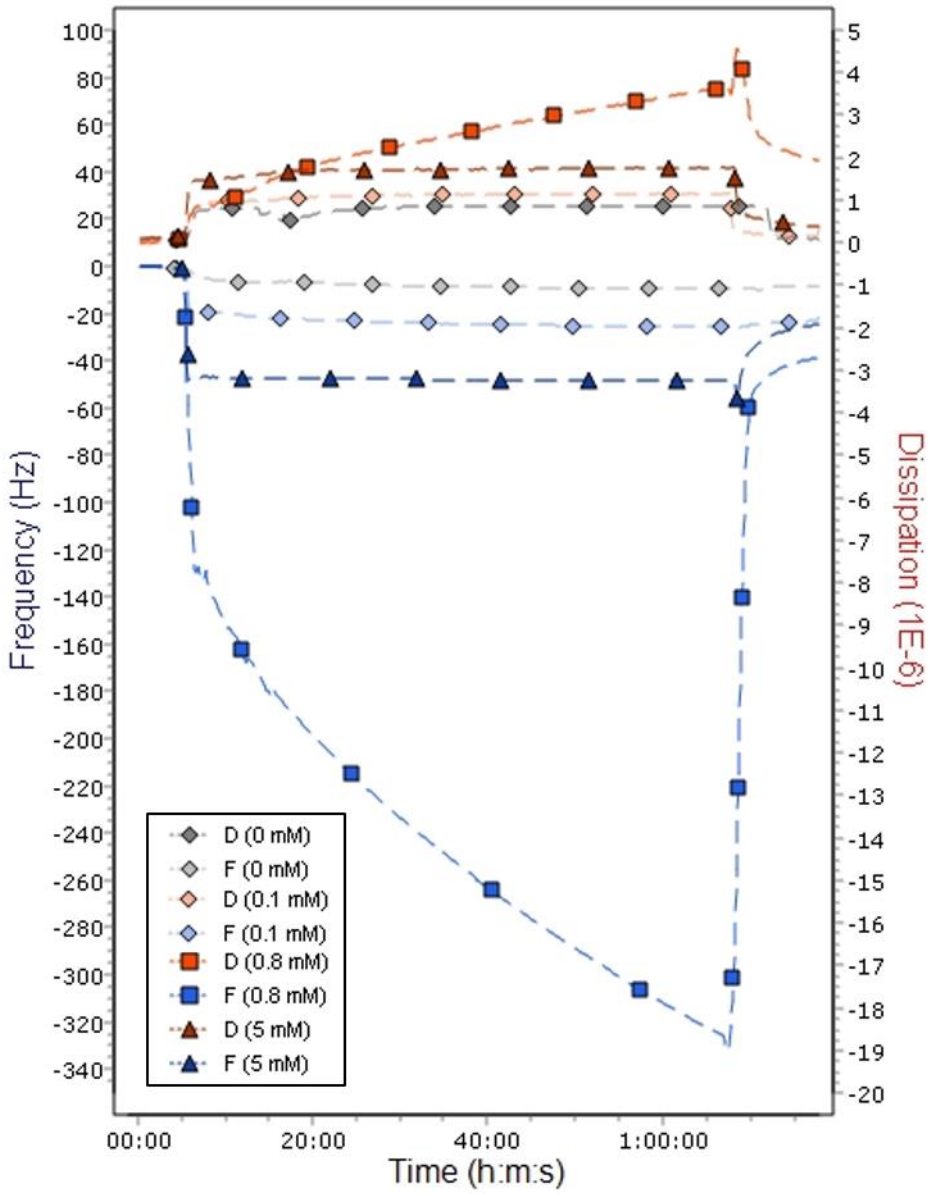

***Figure 8.8**: Raw QCM-D adsorption data. Frequency (blue) and dissipation (red) of the 9th overtone of BLG at 5 mg/ml in H_2O with LaI_3 at 0, 0.1, 0.8 and 5 mM c_s adsorbed on SiO_2 quartz sensor. These c_s cover the whole phase diagrams and the individual regimes. The measurements start in H_2O and after a few minutes the salt/water mixtures is pump into the cell inducing protein adsorption. After roughly 1 h, the cell is flushed with H_2O to check for the reversibility of protein adsorption. Note that spikes in the raw data are induced by turning the pump on and off for solution exchange.*

From the raw QCM-D data, which consists of the measured frequency F and dissipation D, one can deduce general trends and behaviours. Examples are given in **Figure 8.7**, **Figure 8.8** and **Figure 8.9** for BLG with $LaCl_3$ and LaI_3 in H_2O and D_2O, respectively. The weakest adsorption (smallest ΔF) is measured without salt and the strongest adsorption in regime II (strongest ΔF) at 0.8 mM for both salts and solvents. The change in D varies from 1 to $4x10^{-6}$. For $D \approx 0$, the adsorbate behaves solid-like and stiff. Since D is a measure for the viscoelastic properties, one can conclude that the protein layer formation is rather dense and stiff compared to e.g. free BSA in solution [427,465]. In the rinsing step only in regime II, a significant amount of proteins is flushed from the surface. Under all other conditions,

most of the adsorbed proteins are irreversibly adsorbed, which implies strong protein-surface interactions. The adsorption process happens on a time scale of seconds (which is not measurable in this system by NR), except in regime II, where the layer continues to grow even after 1 h.

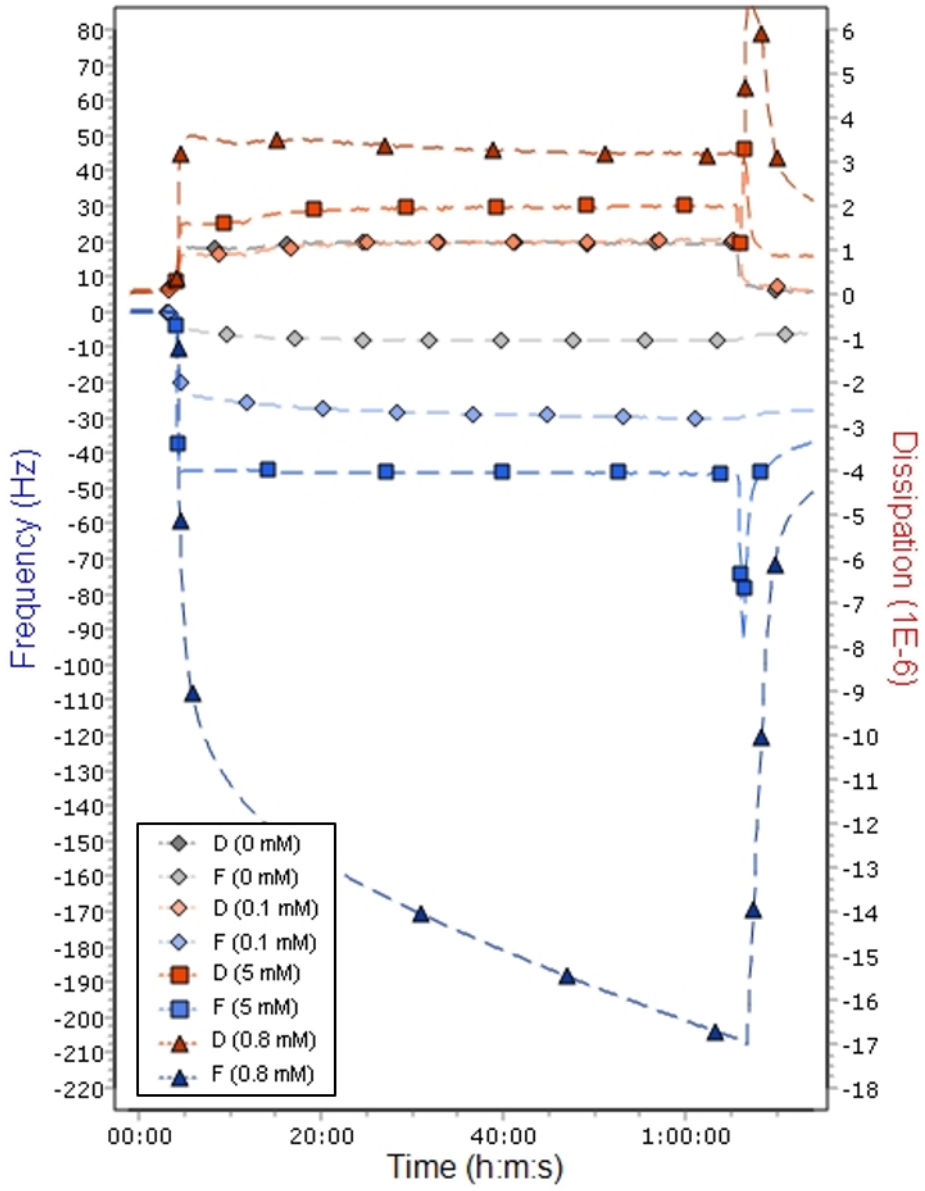

***Figure 8.9**: Raw QCM-D data. Frequency (blue) and dissipation (red) of the 9th overtone of BLG at 5 mg/ml with $LaCl_3$ in D_2O at 0, 0.1, 0.8, and 5 mM c_s. These c_s cover the whole phase diagrams and the individual regimes. The measurements start with the substrate being submerged in D_2O. After a few minutes, the salt/solvent mixture is pumped into the cell inducing protein adsorption. After roughly 1 h, the cell is flushed with D_2O, to check for the reversibility of protein adsorption. Note that spikes in the raw data are induced by turning the pump on and off for solution exchange.*

By applying a viscoelastic Kelvin-Voigt model [394,395,595] in **Figure 8.10**, the averaged adsorbed protein layer thickness d over a cross-section of the substrate can be measured and calculated. Without salt, there is very little adsorption observable (d_{LaCl_3} = 1.8 ± 0.9 nm) in **Figure 8.10** (blue). Adding trivalent salt causes an enhancement

in adsorption. At c_S = 0.1 mM (regime I), a slight increase of d_{LaCl_3} = 6.9 ± 2.6 nm can be seen, then, by further increasing c_S to 0.8 mM (regime II), thus crossing the first bulk phase transition, strongly enhanced adsorption of d_{LaCl_3}= 60.1 ± 11.2 nm. This is in good agreement with enhanced adsorption found for BSA with multivalent ions, which is correlated with bulk instability due to LLPS formation [465]. From the bulk phase behaviour, it is known that also BLG undergoes LLPS formation, which gives rise to strongly increased adsorption (wetting transition). This can be theoretically explained with the ion-activated-attractive protein adsorption model established in this context [427]. At high c_S of 5 mM (regime III), d_{LaCl_3}decreases to 11.6 ± 3.3 nm showing re-entrant adsorption caused by an overcharging effect of the substrate at high c_S.

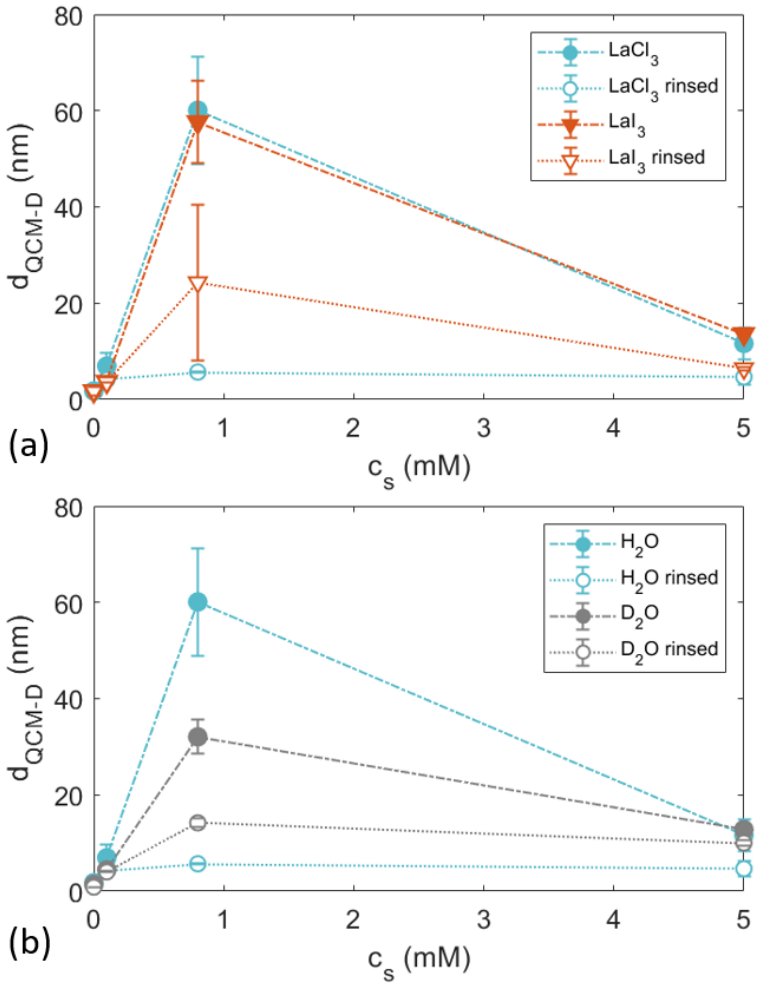

Figure 8.10: Solid-liquid BLG adsorption. Adsorbed layer thickness d calculated with a viscoelastic model from QCM-D data for 5 mg/ml BLG on SiO_2 at room temperature. (a) Anion comparison of $LaCl_3$ (blue) and LaI_3 (orange) in H_2O. (b) Solvent comparison of $LaCl_3$ in D_2O (grey) and H_2O (blue). The solid markers are samples with the salt/protein mixtures and the hollow markers label the samples after flushing the cell with H_2O to check the reversibility of the adsorption process.

For both salts in **Figure 8.10 (a)**, the found adsorption curves lie within the error bars of each other meaning there is no salt-induced (anion-induced) adsorption change. In other words, both have exactly the same adsorption behaviour, which is in accordance with their

similar protein bulk phase behaviour. No anion-induced bulk or adsorption effect could be found. Concerning the isotope effect (solvent exchange), the raw data can be found in **Figure 8.7** and **Figure 8.9** and the analysed data is shown in **Figure 8.10 (b)**. The D_2O data of $LaCl_3$ follows the same trend as the H_2O data with little adsorption in regime I, enhanced adsorption in regime II and re-entrant adsorption in regime III. Yet in regime II, it deviates from the identical behaviour. Here, adsorption is decreased by a factor of 0.5. In regime II, the dominant interactions are attractive. One explanation could be the stronger solvent-solvent interactions in D_2O [257], which diminish/compete with the attractive protein-protein interactions. In addition, the protein stability and rigidity in bulk in D_2O [584] may hinder excessive adsorption and rather keeps the proteins stable in the bulk solution. Nevertheless, the differences in regime I and III are marginal and the solvent contrast can be used for NR measurements.

The NR measurements are in good agreement with the QCM-D and ATR-FTIR data (cf. next section) and reveal additional structural features of the adsorbed layer. By applying a one-layer model, the scattering length density (SLD) of the sample used in **Figure 8.11** could be fitted, from which one can extract the adsorbed protein layer thickness d_{NR}, the adsorption layer roughness σ and the hydration of the adsorbed layer in **Table 8.2**. BLG is a rather small protein (R_p = 2.35 nm) and has a high charge density, which leads to strong repulsive forces, thus the NR fits show a highly hydrated protein layer with thickness of 28.2 Å and hydration of 91 %. At low c_s, a small bump is measured at q_z = 0.1 Å^{-1}, indicating the formation of a distinct and denser layer of 38.0 Å with a hydration of 49 %. In both cases (no salt and 0.1 mM), a two-layer model is also tested, but it is discarded, since the error analysis does not support the presence of two layers. Thus, in regime I, BLG forms a single monolayer, the density (or volume fraction) of which increases, when salt is added. The roughness of the layer at 0.1 mM salt concentration is 12.1 Å, which indicates a rather ordered layer.

***Table 8.2**: NR adsorption. Fitting results of NR reflectivity data of BLG at 5 mg/ml with $LaCl_3$ and LaI_3. d_{NR} defines the adsorbed protein layer thickness, σ defines the layer roughness. Sub- and superscript values are parameter limits at the 95 % confidence interval (CI). Examples for data and fits are shown in the insets of **Figure 8.11** .*

	$LaCl_3$ (±95 % CI)			LaI_3 (±95 % CI)		
c_s	d_{NR} (Å)	σ (Å)	Hydr. (%)	d_{NR} (Å)	σ (Å)	Hydr. (%)
No salt	$28.2^{44.9}_{1.4}$	$14.0^{21.5}_{8.8}$	91^{99}_{79}	$28.2^{44.9}_{1.4}$	$14.0^{21.5}_{8.8}$	91^{99}_{79}
Regime I (0.1 mM)	$38.0^{45.0}_{31.2}$	$8.9^{13.5}_{3.1}$	49^{70}_{35}	$39.2^{47.8}_{30.5}$	$12.2^{18.0}_{3.2}$	51^{70}_{37}
Regime II (0.8 mM)	$280.8^{311.5}_{254.2}$	$78.7^{97.9}_{58.3}$	47^{53}_{40}	$256.7^{287.8}_{233.8}$	$74.1^{90.9}_{40.9}$	53^{59}_{46}
Regime III (5 mM)	$60.6^{68.7}_{52.1}$	$15.7^{10.4}_{25.0}$	36^{59}_{16}	$64.6^{71.5}_{57.8}$	$16.1^{24.7}_{11.0}$	35^{56}_{14}

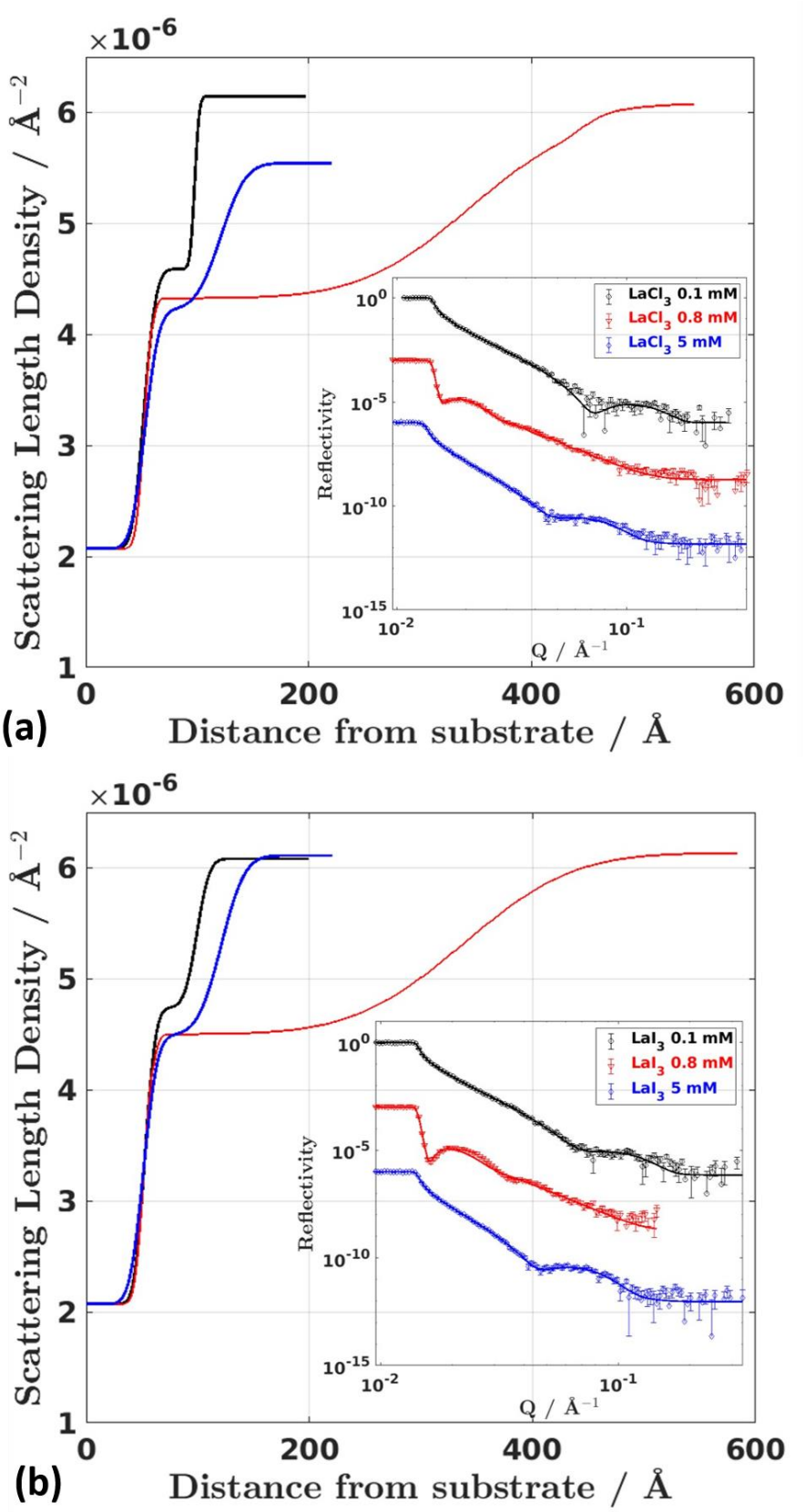

Figure 8.11: *NR reflectivity and SLD data. Neutron reflectivity data (insets) and derived scattering length density (real space) profiles of 5 mg/ml BLG adsorbed to SiO_2 in the presence of (a) $LaCl_3$ and (b) LaI_3 in D_2O.*

In regime II, enhanced adsorption is observable (see **Figure 8.11** and **Figure 8.13**). For regime II, the NR best fits yield a two-layer configuration, with the first layer being 280.8 Å at a lower hydration of 47 %, and a second, much sparser layer having a thickness of 98.1 Å with a hydration of 92 %. The roughness of the first layer is rather high (46.7 Å) suggesting a much more disordered layer, possibly caused by the adsorption of aggregates from solution, rather than growth arising from adsorption of individual proteins. It is interesting to note, that the hydration of the first layer does not suggest any significant denaturation of protein at the interface, which is also in agreement with the ATR-FTIR analysis. In agreement with ellipsometry and ATR-FTIR, re-entrant adsorption and diverging thickness is detected in regime II. In absolute numbers, the overall trend is very clear. There is nearly no difference between protein adsorption in the presence of $LaCl_3$ and LaI_3 and their behaviour can be described as identical. The thicker the adsorption layer gets, the rougher (and more diffuse) it becomes, while the hydration is around 50 % for regimes I and II, but drops to about 35 % in regime III (although the error bars a quite large). This reduced hydration is below that of a minimally solvated protein layer and suggests some potential denaturation. This however is a small effect and could not be confirmed in the ATR measurements.

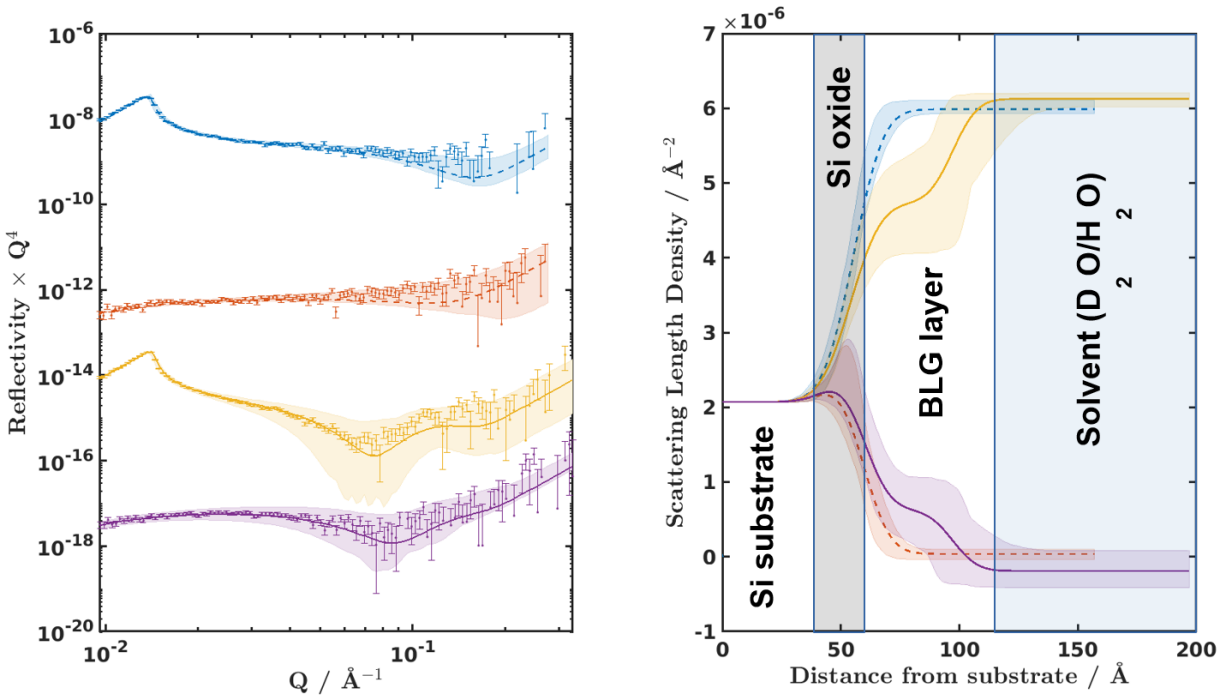

Figure 8.12: Bayesian error analysis. Fit quality of model showing 95 % confidence intervals (shaded regions). Data shown is the bare substrate (blue and red, dashed) and another sample of 5 mg/ml BLG with 0.1 mM LaI_3 (yellow and purple, solid), in D_2O and H_2O, respectively.

A hydration of around 50 % means that the protein layer is densely packed. This can be explained with BLG naturally occurring as a dimer [236], as well as, its ability to crystallise. Sufficiently close proximity between proteins might be needed to start the nucleation process.

In order to assess the accuracy and precision of the created fitting model, Bayesian error analysis is performed. The error intervals given in **Table 8.2** are obtained from this analysis and denote 95 % confidence intervals. An example is shown in **Figure 8.12** of 5 mg/ml BLG with no salt and 5 mM $LaCl_3$ (further plots are presented in Appendix C). The shaded areas depict the possible fit and real space profile ranges within the 95 % confidence interval. Although the 95 % confidence interval is broader than usual, the adsorption trend and structural changes can be clearly determined.

Here, one can see the benefit of using the solvent contrast of D_2O and H_2O due to the different shape in reflectivity curve and D_2O having a critical edge. This is based on their different scattering length densities (SLD) and allows tailored data analysis. Note that the QCM-D data showed reduced protein adsorption in regime II with D_2O, which should be kept in mind, yet, due to the strongly enhanced adsorption compared to the other regimes does not falsify the overall adsorption trend. In **Figure 8.13**, the $LaCl_3$ sample in regime II is measured for more than 2 h in order to observe the kinetics of the enhanced adsorption layer (wetting layer) in order to get insight into the morphology changes occurring. As can be seen, the data in D_2O shows a fringe and peak at relatively low q, corresponding to a layer thickness of 200 Å. After 2 h, the layer thickness increases up to approximately 300 Å.

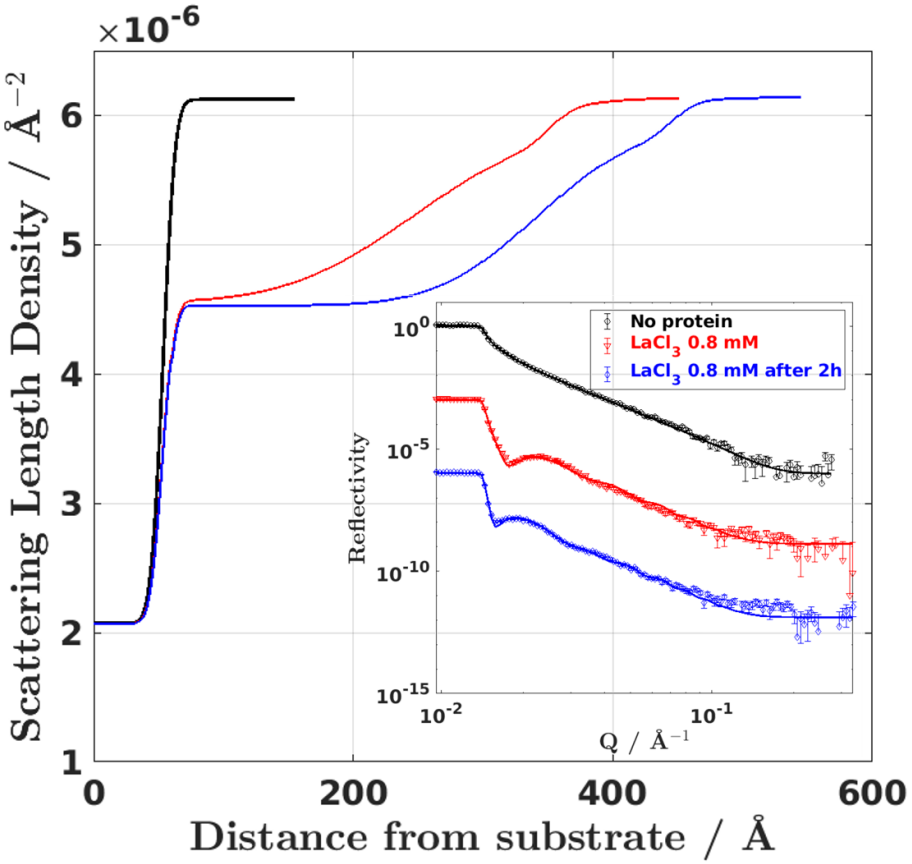

Figure 8.13: Wetting layer growth in regime II. Time-dependent reflectivity curves of BLG 5 mg/ml at 0.8 mM $LaCl_3$ in D_2O. The adsorption layer continuously keeps on growing (red after injection, blue after 2h).

8.3.2 Layer stability via ATR-FTIR

ATR-FTIR is used to investigate the layer stability and structural arrangement after protein adsorption on the solid-liquid SiO_2 interface. One concern is that iodide due to its protein-destabilising properties may cause denaturation [596]. Thus, infrared absorbance measurements are able to provide insight into the secondary structure, which can be extracted from the amide-I band at 1600 to 1700 cm^{-1}. In **Figure 8.14**, the ATR-FTIR spectra of BLG with $LaCl_3$ and LaI_3 are plotted in H_2O. The peak maxima correlate with the formation of β-sheets at 1632 cm^{-1}, which make up 54 % of the BLG structure [244,597]. Thus, it can be concluded that the main protein structure seems to be intact and is not affected by the addition of multivalent salts or adsorption to a solid interface.

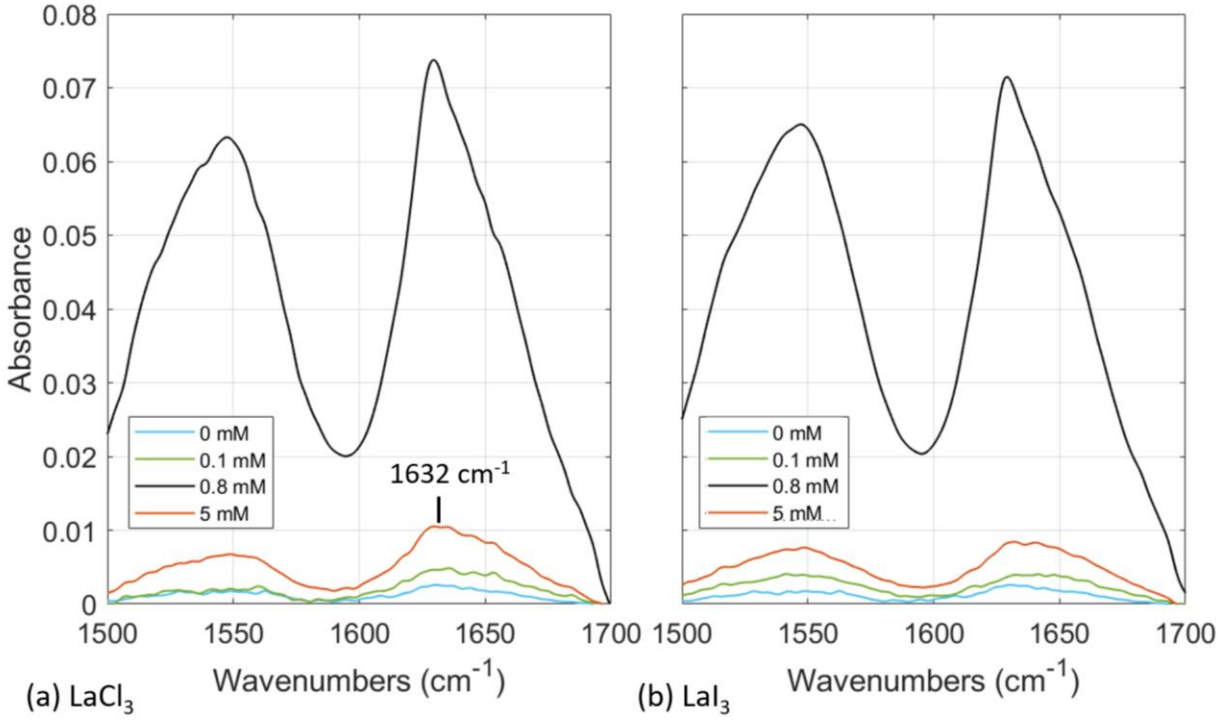

Figure 8.14: Secondary BLG structure. ATR-FTIR absorbance measurements of BLG at 5 mg/ml in H_2O with (a) $LaCl_3$ and (b) LaI_3 at different c_s adsorbed on SiO_2. The shapes of the curves are similar to each other under all conditions meaning the same intact protein structure can be assumed.

Comparing the $LaCl_3$ to LaI_3 data in **Figure 8.14** show the same intensities in absorbance and curve shapes in the individual regimes. No salt-dependent structural changes could be found. Another interesting observation is the change in absorbance over the different regimes, which does directly correlate with the amount of proteins adsorbed to the interface. Again, re-entrant adsorption (red curve) and enhanced adsorption (black curve) in regime II can be observed, which reflect the findings of the QCM-D data in **Figure 8.10 (a)**.

8.4 Summary

In this chapter, the focus is on the role of anions and isotopes on the BLG phase behaviour in bulk and at interfaces. BLG is found to be less influenced by anion type or solvent than BSA, which can be explained with its secondary structure (mainly β-sheets) and the properties of its amino acids. All established phase diagrams show re-entrant condensation and LLPS formation, which is induced by the binding and bridging of multivalent cations. Through the addition of multivalent salts to the protein solution, protein adsorption increases at the interface up to a critical c_s, after which re-entrant adsorption occurs. The enhanced adsorption in regime II has been previously established for BSA [465] and illustrates the universality of the "wetting" transition at bulk instability induced by LLPS formation. In the future, the combination of neutron and X-ray reflectivity may pave the way to investigate the transition from adsorption to crystallisation, i.e. nucleation at interfaces.

9 Effect of Surface Properties on Protein Adsorption

This chapter is devoted to surface properties and their effect on protein adsorption. There are still open questions on the influence of the substrate properties, such as surface charge, hydrophobicity, and roughness, on protein adsorption. Compared to the previous chapters, the results presented in this chapter are rather complementary studies testing the influence of specific surface parameters on protein adsorption and should be viewed as a point of contact and outlook for future research giving first impressions on underlying mechanisms. For a systematic investigation on the role of certain surface properties on protein adsorption, different approaches are discussed, which include coating of the substrate with a self-assembled monolayer, electrochemical manipulation of the surface charge, and the use of possible implant materials to establish ties to more application-oriented systems.

9.1 Protein Adsorption on a Hydrophobic Surface

This section focuses on the influence of a hydrophobic surface on protein adsorption. In the scope of this dissertation, so far, only silicon wafers were used as a substrate, which are hydrophilic and negatively charged. Self-assembled monolayers are one option to modify surface properties and are offered in a variety of chemical terminations and chain lengths (for more information on SAMs, see Chapter 3.3.2.3). In this section, Si wafers are coated with trichloro(octadecyl)silane (OTS), which changes the surface properties of a Si wafer to a neutral and hydrophobic interface (**Figure 9.1**). The OTS samples are prepared according to the description in Chapter 3.3.2.3. The quality of the OTS samples is first checked via contact angle measurements, which should be around 98° for a successful monolayer formation (**Figure 9.1**) [293]. Via AFM, a visual image of the OTS coating is obtained and the quality of the monolayer is further evaluated, which shows monolayer and cluster formation (white spots in **Figure 9.2 (a)**). The surface roughness extracted is on average 0.72 ± 0.5 nm and after masking the clusters 0.35 ± 0.11 nm (**Figure 9.2 (b)**), which is consistent with literature values [279].

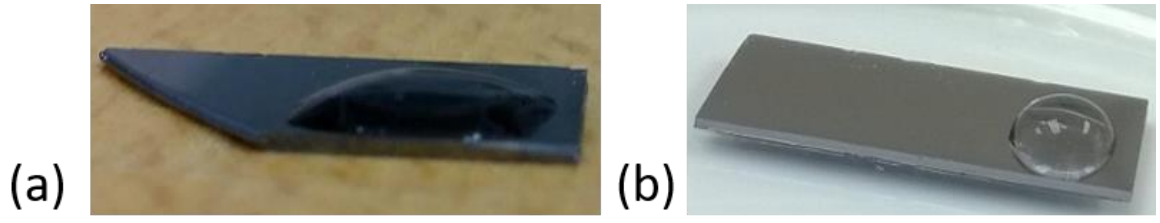

***Figure 9.1**: Image illustrating the surface tension of a water droplet on (a) a bare Si substrate (θ_y < 10°) and (b) a silane-coated (OTS) substrate (θ_y = 98°).*

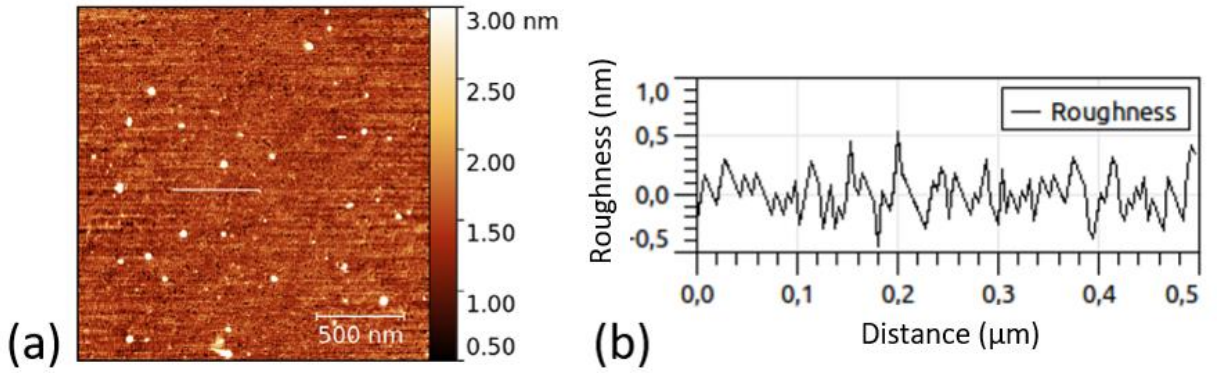

Figure 9.2: *AFM measurements of an OTS-coated silicon wafer. (a) Image of an OTS-coated substrate with visible (white) clusters. (b) Height profile of the surface giving an indication on the topography of the sample. The roughness determined for this sample is 0.52 nm, and after masking the clusters 0.27 nm. Image is provided by Christian Exner.*

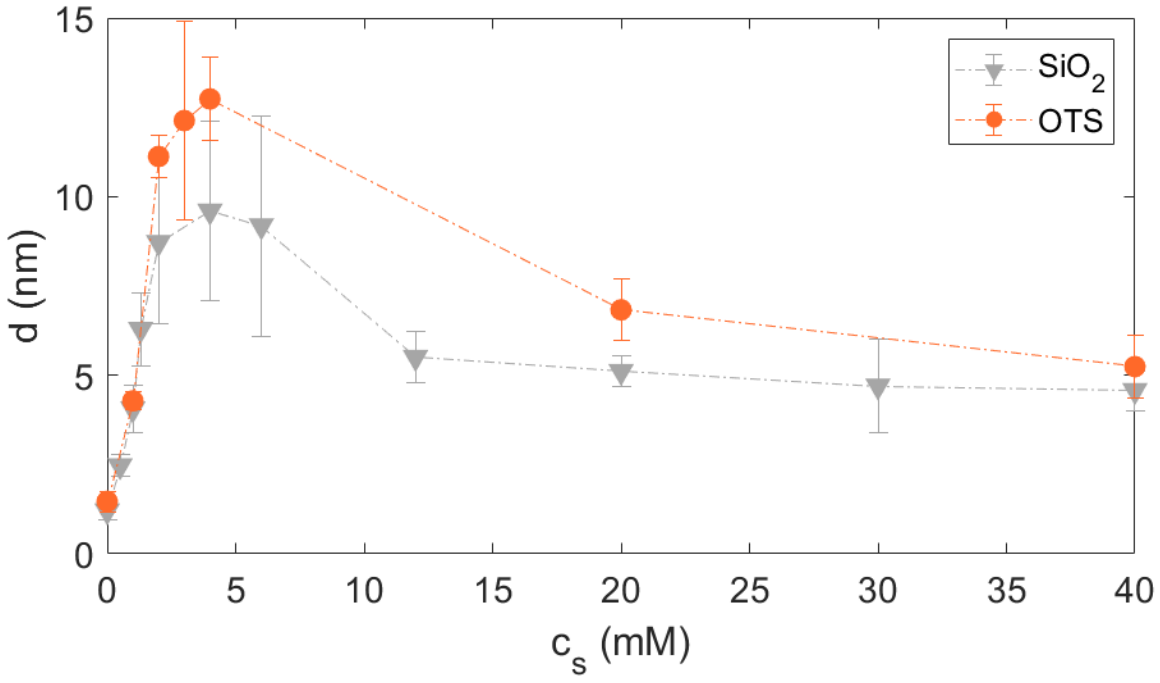

Figure 9.3: *Ellipsometry measurements of protein adsorption of 20 mg/ml BSA in the presence of YCl_3 at different molar concentrations on SiO_2 (grey) and OTS-coated substrate (orange).*

In addition, the thickness of the OTS layer is determined by ellipsometry and on average 2.6 nm, which is slightly higher than the literature value of 2.33 nm, but can be rationalised by considering the cluster formation on top of the monolayer [279]. Only samples with an appropriate roughness and OTS layer thickness are used for the adsorption measurements to minimise sources of error and to guarantee a certain sample quality. In **Figure 9.3**, the ellipsometry results of BSA adsorption are presented and compared to the adsorbed layer thickness on SiO_2. The adsorption curve follows the same trend as on SiO_2, yet the overall adsorbed amount is slightly larger on OTS. Subsequently, it seems as if the overall adsorption trend is affected by the salt concentration of YCl_3, yet the adsorbed amount is influenced by the surface properties. The adsorbed BSA layer thickness without salt on OTS

leads to an adsorbed layer of roughly 1 nm, which is comparable with findings by Hähl et al. [598]. These findings support on one hand the successful substrate preparation and on the other hand can also be used as a comparison system to the results presented. Hähl et al. [598] found that hydrophobic interfaces promote denaturation of proteins upon adsorption, especially of soft proteins such as BSA, and lead to a denser packing of proteins at the interface compared to the adsorbed layer on SiO_2. The effective measured d assumes a volume fraction of 1, which is laterally averaged over the measured surface. Thus, ellipsometry cannot distinguish between layer density and thickness, instead it accounts for the amount of adsorbed protein to the interface. At this juncture, it cannot be said if the increased adsorption on OTS is hence due to denser protein packing and/or a thicker adsorbed protein layer. Complementary methods such as neutron reflectivity could be used to shed light onto this question.

The hydrophobicity of proteins can be expressed with its surface hydrophobicity S_0 [599]. BSA ($S_0 = 2322$) is compared to other proteins, e.g. lysozyme ($S_0 = 25$), highly hydrophobic [599]. Due to the strongly hydrophobic nature of BSA, one could assume even stronger adsorption on OTS compared to SiO_2, which is not found in the present results. Nevertheless, the addition of multivalent salts increases adsorption significantly and can be used to control protein adsorption.

9.2 Protein Adsorption on Protein-Repellent Surface

Protein resistance of surfaces is highly relevant in biocompatible materials, e.g. for biosensors or stents, to prevent blood clotting [53,164,600,601]. Depending on the application, the regulation of the adsorbing amount can be useful. SAMs with oligoethylene glycol (OEG) groups are unique in the sense that they not only allow the tuning of substrate properties in the classical sense, but also directly influence protein adsorption due to their protein-repellent property. Protein-repellent SAMs are usually hydrophilic, contain groups that are hydrogen bond acceptors, but not hydrogen bond donors, and are overall electrically neutral [285].

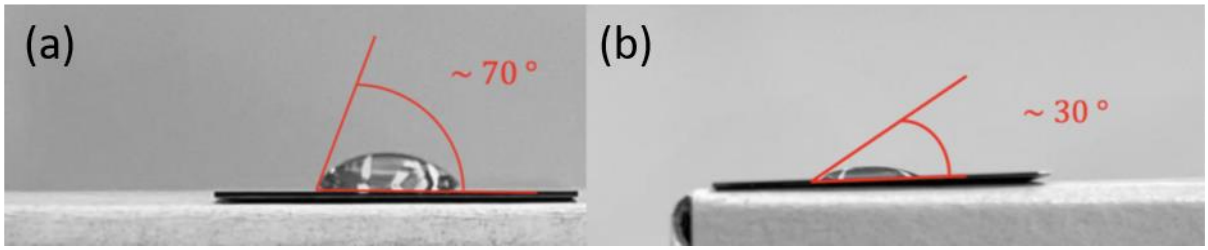

Figure 9.4: Contact angle measurement of (a) a bare gold substrate and (b) of a thiol-coated (TEG) substrate. Image is provided by Lara Reichart.

The mechanism behind the protein resistance is not completely understood, but it is found that the resistance of these surfaces increases with the increasing number of OEGs in the functional group [285]. Harder et al. [602] speculated that the protein resistance is connected to the molecular conformation of the OEG units. If the OEG has a helical structure, interfacial water is strongly bonded and creates a stable solvation shell.

The direct contact between the surface and the protein is prevented by forming a stable solid-liquid interphase involving tightly bound water [602,603].

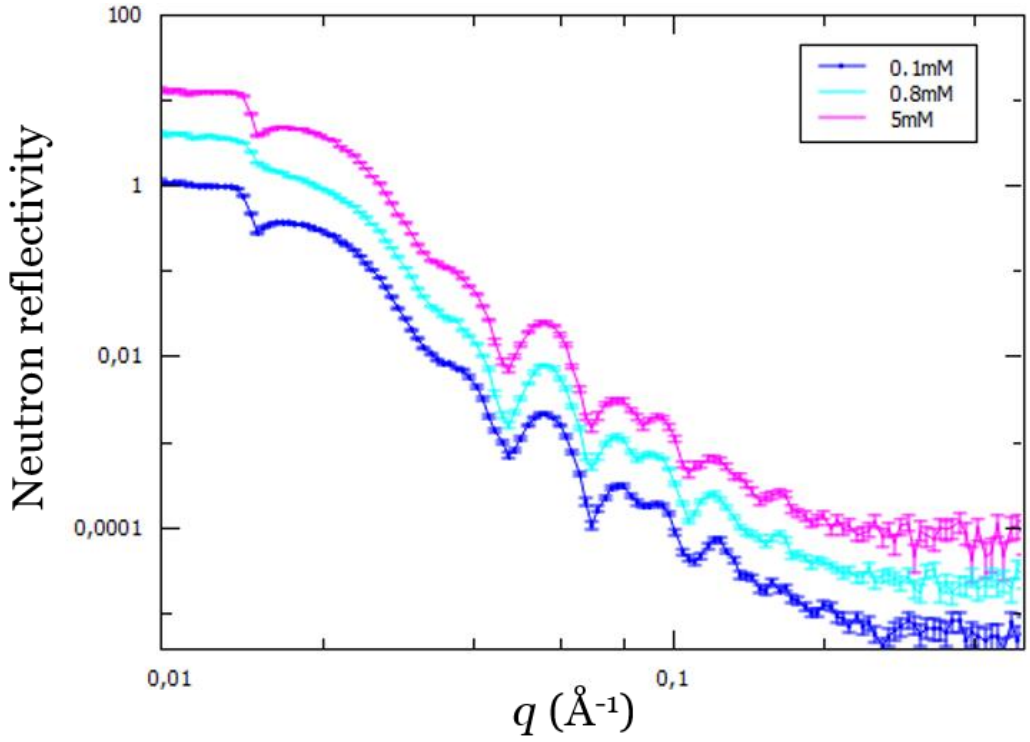

Figure 9.5: Neutron reflectivity data on protein adsorption of 5 mg/ml BLG on a protein-repellent TEG-coated gold block tuned by $LaCl_3$ at 0.1 mM (blue), 0.8 mM (light blue), and 5 mM (pink) in D_2O. At 0.8 mM, the strongest change in the reflectivity curve and fringes can be observed.

In this section, triethylene glycol mono-11-mercaptoundecyl ether (TEG) is used to create a protein-repellent interface. Since thiol formation can be difficult and prone to defects [604,605], the samples prepared are tested for their quality before use. A first estimate of the quality of the thiol formation is provided by contact angle measurements (**Figure 9.4**). The contact angle should be around 31 ± 2° [284]. Complementary methods are AFM and polarisation-modulation infrared reflection-absorption spectroscopy (PMIRRAS) measurements (data not shown) to evaluate the film topography, roughness, and chemical composition.

The TEG-coated substrates are used to investigate BLG adsorption in the presence of multivalent salts ($LaCl_3$) as shown in **Figure 9.5** and **Figure 9.7** via NR and QCM-D. The measurements without salt (**Figure 9.7**) show that the protein-repellent property is present for the samples investigated and no adsorption is detected. With the addition of multivalent salts, this property can be overturned. After a critical amount of multivalent salt added (0.8 mM $LaCl_3$) to the protein solution, protein adsorption starts to massively increase (**Figure 9.5** and **Figure 9.7**). Salt concentrations of 0.1 mM are not sufficient to induce a change (i.e. induce protein adsorption). Interestingly, increasing c_S further up to 5 mM leads to a decrease in adsorption (known as re-entrant adsorption), which correlates with the dominant bulk interactions in regime III (see bulk phase transitions in **Figure 8.4**).

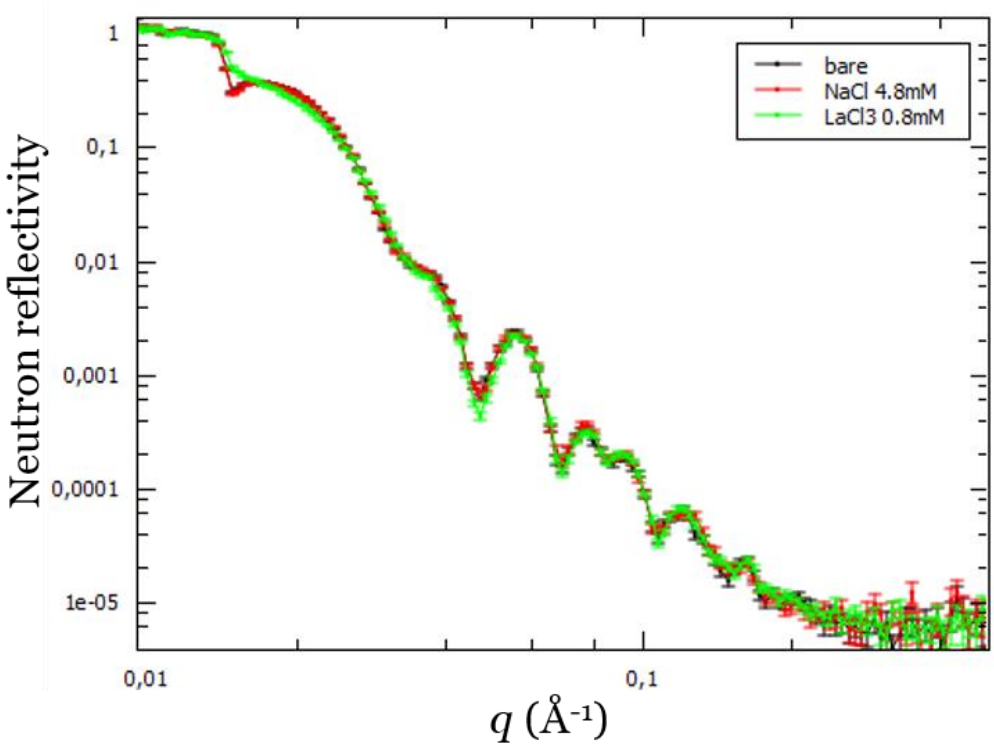

Figure 9.6: Neutron reflectivity data on protein adsorption of 5 mg/ml BLG on a protein-repellent TEG-coated gold block tuned by $LaCl_3$ at 0.8 mM (green) and by NaCl at 4.8 mM (red) in D_2O. The measurement with a monovalent salt is performed to prove that the trends found are solely induced by the valency of the ion.

Since for QCM-D measurements a flow cell is used, the reversibility of the protein adsorption can be investigated by flushing the cell with water (rinsing step after 1:10 h in **Figure 9.7**). In the initial measurements presented in **Figure 9.7**, it seems that the addition of a critical concentration of multivalent ions changes the surface properties irreversibly, since the protein-repellent properties are lost and proteins bind irreversibly. As a control measurement, the equivalent in ionic strength of a monovalent salt (here: 4.8 mM NaCl) compared to the multivalent salt (0.8 mM $LaCl_3$) is added to the BLG solution (**Figure 9.6**). The monovalent salt has no effect on the protein resistance of TEG (green curve in **Figure 9.6**). Thus, the disruption of the protein-repellent property is caused by a unique property of the multivalent ions. More measurements must be performed to prove the results found and their reproducibility. In this context, questions arise on the reversibility of this process, which might be of relevance for hydrogel formation, as well as on the role of multivalent ions on the interfacial water stability within the TEG layer or the orientation of the TEG molecules, which seem to facilitate the protein resistance of the TEG layer.

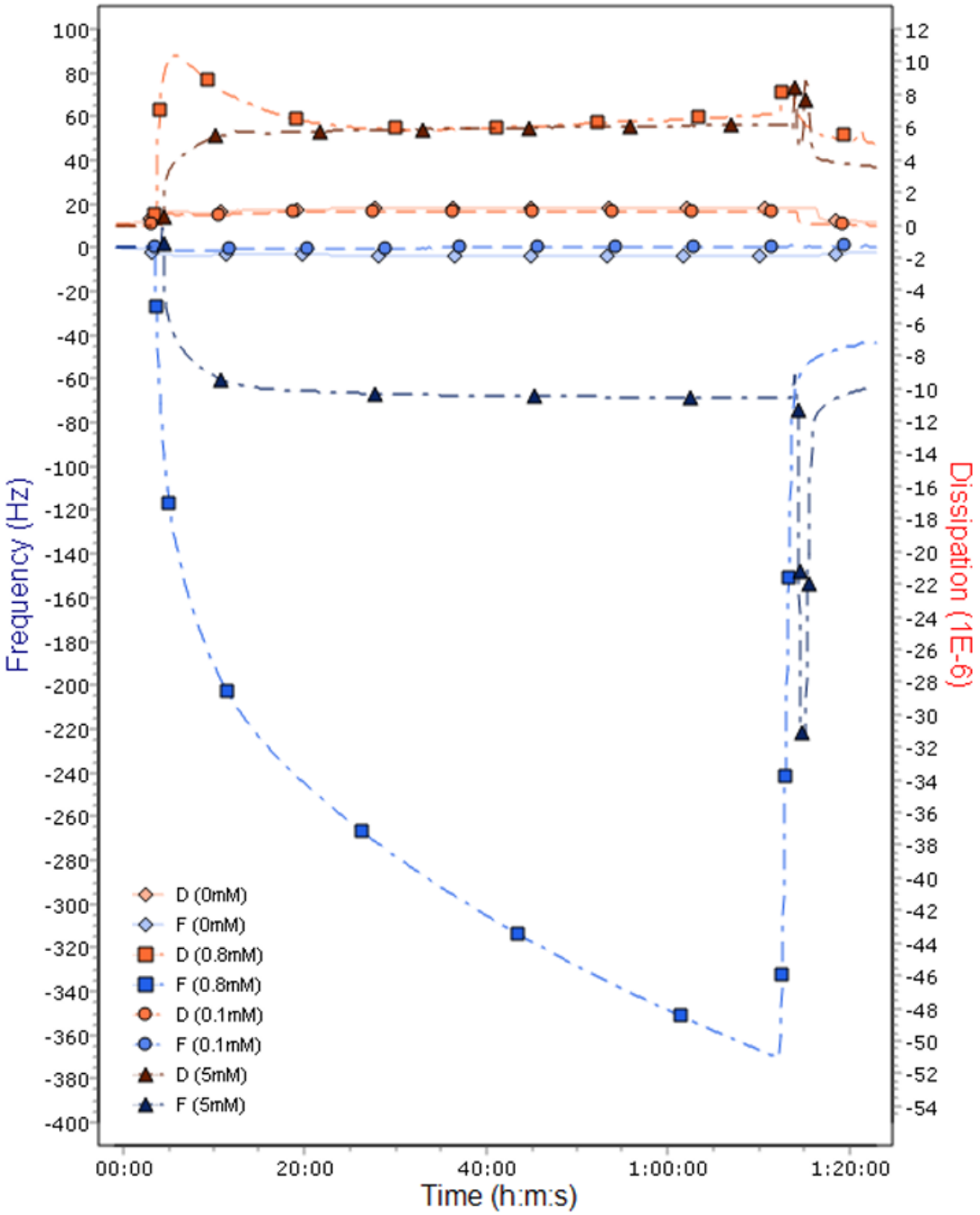

Figure 9.7: Initial QCM-D measurements. Protein adsorption of 5 mg/ml BLG in the presence of $LaCl_3$ (0, 0.1, 0.8 and 5 mM) in H_2O to a TEG-coated substrate. The protein solution is pumped into the cell after 5 min and is rinsed with water after roughly 1:10 h.

9.3 Protein Adsorption on Charge-modified Surface

All of the results presented in Chapters 5, 6, 7 and 8 are dependent on a net negatively charged, hydrophilic surface. The adsorption model introduced in Chapter 5 is based on the concept of a charged interface inducing an attractive wall potential, which promotes protein adsorption. These mechanisms are mainly dominated by electrostatic forces. If the surface charge within the same system is changed, it might lead to other dominating forces.

Thus, the question on the role of surface charge on protein adsorption (in the presence of multivalent salts) must be understood to obtain a universal understanding of the underlying forces.

One approach, which facilitates the manipulation of charges within a system over time and without additional sources of interference, is electrochemical manipulation of the surface charge. Electrochemical surface manipulation on BSA adsorption has already been investigated with ellipsometry, QCM-D, and electrochemical impedance spectroscopy on different surfaces, mostly gold due to its high conductivity [307,606–609]. For the measurements presented in this section, a three-electrode cell is used to perform NR measurements. All samples in **Figure 9.8** are measured at the same conditions of 5 mg/ml BLG with 0.8 mM $LaCl_3$ in D_2O adsorbed on p-doped SiO_2. Without the potential applied, these conditions show the strongest adsorption (regime II), hence the conclusion is that the strongest impact of potential applied is detected at this concentration. The neutron reflectivity measurements in **Figure 9.8** show that only the application of a negative potential (-0.5 V) induces a change (decrease) in adsorption behaviour compared to the system without applied potential.

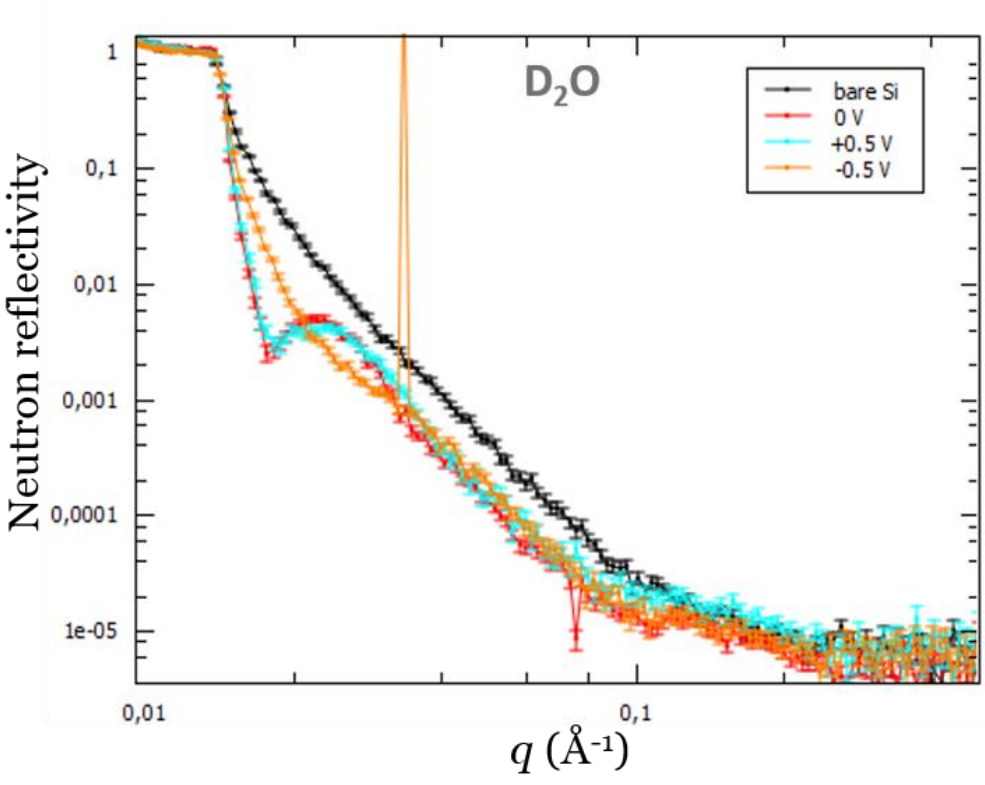

***Figure 9.8**: Surface charge modification in a three-electrode NR cell investigating protein adsorption of 5 mg/ml BLG with 0.8 mM $LaCl_3$ in D_2O without any applied voltage (red), with +0.5 V (blue) and -0.5 V (orange) on SiO_2. The application of a negative potential decreases adsorption massively.*

These results are at first glance counterintuitive. This observation could be rationalised as follows: the surface is negatively charged, and the proteins are also net negatively charged (without salt) at neutral pH. Under the conditions investigated (at 0.8 mM $LaCl_3$), the

proteins experience now short-ranged attractive interactions and might be close to charge neutrality or even positively charged due to cation binding. The substrate also might have bound cations changing its surface charge. Through the application of a negative potential, repulsive forces might be introduced, which would lead to reduced adsorption. A positive potential, however, does not change anything since 0.8 mM is close to the point of charge neutrality, at which the attractive forces between proteins and the interface are the strongest (i.e. repulsive forces are at their weakest) and a further increase in adsorption might not be possible since it is already at maximum adsorption.

This hypothesis is in good agreement with Beykal et al. [609], who have demonstrated increased adsorption for increasing magnitude of applied potential, if the protein and the surface carry opposite charges. The potential-dependent adsorption trends in **Figure 9.8** perfectly match their found potential-dependent BSA adsorption on gold. The only difference is that no salt is added to their system. Since no difference between a positive applied potential and multivalent salt (regime II) can be detected in NR measurements, this might indicate that multivalent salts induce the same effect in proteins than a positive potential does in the sense of 'increased adsorption'. To assess and understand the adsorption mechanism, measurements must be repeated under further conditions e.g. without salt, to estimate the salt's contribution and role, as well as extend it to other complementary methods.

Benavidez et al. [607] found that the applied potential polarised the layer and induced dipole-dipole interactions between the adsorbed and incoming proteins, thus interfering protein-proteins interactions have to be kept in mind and considered for the adsorption process.

9.4 Protein Adsorption on Implant Surfaces

Up to the present chapter, the system investigated are model-like and simplified to understand specific correlations and mechanisms. In this chapter, the focus is on a first approach to establish a connection between fundamental research and application. The substrate of interest is anatase, which is crystalline TiO_2, and used in dental implants for better osseointegration [165]. Anatase has a valuable property of decomposing organic material upon UVA treatment by photocatalysis, which decreases the risk of bacterial infections after implantation [271]. Due to the UV treatment, the surface also becomes super-hydrophilic [271].

First, the quality of substrates is determined, which were provided by the group of Prof. Dr. Jürgen Geis-Gerstorfer (University Hospital Tübingen) (for more information see Chapter 3.3.2.1). The surface roughness is determined by AFM (data not shown), the layer thickness is determined by ellipsometry and listed with other typical surface properties of anatase in comparison to SiO_2 in **Table 9.1**. Due to the production of the anatase via heat treatment, the anatase layer is rather thick and rough compared to standard Si wafers.

Table 9.1: Overview of surface properties of SiO_2 and anatase (TiO_2) obtained from Refs. [264,293,610,611]. The surface roughness is determined from AFM images (not shown).

Properties	SiO_2 (amorphous)	TiO_2 (anatase)
Crystal structure	Si [111]	[101]
Surface tension (mN/m)	143.5	210
Contact angle (°)	<10°	24°
Surface roughness (nm)	<1	~7
Thickness (nm)	~ 1.5	~ 400
Charge density (mC/m^2)	-0.5	-50

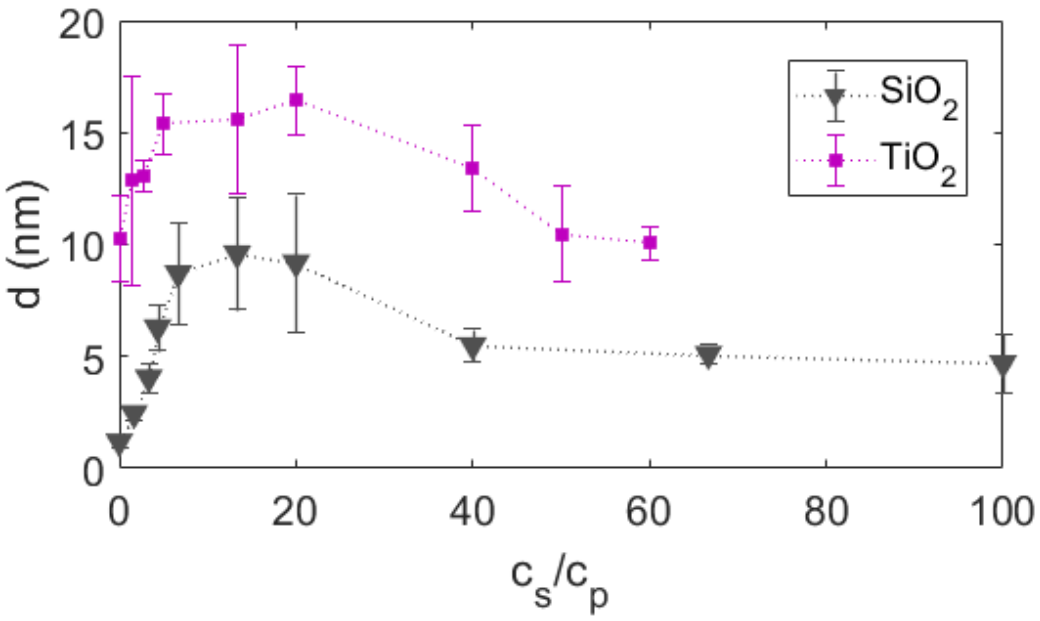

Figure 9.9: Thickness of adsorbed protein layer of 20 mg/ml BSA in the presence of YCl_3 in H_2O adsorbed to SiO_2 (grey) and anatase TiO_2 (purple). Adsorption is significantly increased for anatase.

The adsorption investigation with BSA and YCl_3 on anatase illustrated in **Figure 9.9** shows an overall increased adsorption compared to SiO_2, while the adsorption trend itself is mirrored. Anatase is negatively charged in water. This indicates (again) that the general adsorption trend seems to be guided by the electrostatic protein-protein and protein-interface interactions (also seen for hydrophobicity in Chapter 9.1), whereas the absolute adsorbed amount is solely guided by changes in the interface-protein interactions. So far, it cannot be said whether the increase in adsorption is due to the different surface properties of anatase (itself) compared to SiO_2 or the higher surface roughness of the substrate. In literature, an increase in surface roughness usually correlates with an increase in protein adsorption [412,414]. Thus, one challenge present is the control of the surface roughness. Either a rougher SiO_2 substrate or a smoother anatase substrate is needed to estimate the contribution of surface roughness to protein adsorption and to obtain a clearer picture of the real material-specific effect of anatase on adsorption. Furthermore, anatase will allow the investigation of the effect of super-hydrophilicity on the adsorption process.

10 Discussion and Conclusions

The aim of this dissertation is to gain a deeper understanding on protein-protein and protein-surface interactions with the focus on the role of multivalent ions. In the following, a comparison between BSA and BLG is given illustrating fundamental similarities and differences between the two proteins and how those affect their behaviours in bulk and at solid interfaces. This highlights the main results established and discussed individually in the result chapters in this dissertation (Refs. [427,465,491,561]) and relate them to prior results and literature. This overview is based on Ref. [561] and is summarised in Table 10.1.

Table 10.1: Protein phase and adsorption behaviour. Collection of protein-specific properties and effects of BLG and BSA established in this dissertation and previous investigations.

Protein behaviour	BLG	BSA
LLPS	Two-step	One-step
Re-entrant condensation	√	X
Crystallisation	√	X
Temperature dependency [183]	UCST (LCST)	LCST (UCST)
Isotope effect	X	√
Anion effect	X	√
Cation effect	√	√
Adsorption amount	low	high
Re-entrant adsorption	√	√
Wetting transition	√	√

First, similarities and differences in *bulk* phase behaviour of BSA and BLG are discussed:

- Role of cations. Here, the focus is on two multivalent cations, La^{3+} and Y^{3+}, and their role in the BSA and BLG phase behaviour. In previous publications, Matsarskaia et al. [349] have established the influence of La^{3+}, Y^{3+}, and Ho^{3+} on the BSA phase behaviour and Zhang et al. [148] the phase behaviour of BLG with YCl_3. Based on the results presented in this dissertation and the previous publications, a universal trend can be observed. Depending on the cation size, thus surface charge density, and polarisibility, their influence on the dominant bulk interactions can be estimated. The higher the surface charge density of the cation, the stronger protein-protein forces are expected, but there are also non-trivalent entropic contributions, which are difficult to estimate. Cation binding and bridging are electrostatically driven [155] and their respective protein binding sites are solely negatively charged [148,612].

- **Liquid-liquid phase separation.** LLPS is formed for BSA in one step and for BLG within two steps (first aggregates in **Figure 8.3 (a)**). LLPS formation is temperature-driven. The different behaviours are influenced by the entropy and enthalpy of mixing and de-mixing [613], which is guided by a lower critical solution temperature (LCST) in BSA [155] and a upper critical solution temperature (UCST) in BLG [148] depending on the position in the phase diagram [183]. The only exception is BSA with $LaCl_3$, in which no LLPS occurs at the conditions investigated. Here, the attractive forces are the weakest compared to the other systems and do not become strong enough to form LLPS meaning B_2/B_2^{HS} does not reach values below -1.5 [152].

- **Role of solvent (isotope).** A strong isotope effect is observed for BSA, which is also the conclusion of a previous publication by Braun et al. [154], whereas, for BLG, the isotope effect is absent as shown in **Figure 8.4**. Due to the exchange of solvent, the strength of solvent-solvent hydrogen bonds with D_2O is increased compared to H_2O [257], which lead to enhanced hydrophobic interactions within the protein, which stabilises and stiffens the protein structure [584,586,587,614]. The hydrophobicity of a protein can be determined and expressed in multiple ways [615,616]. One way is the Gibbs free energy ΔG of transfer from water, which is a direct method and was determined by Pérez-Fuentes et al. [238] for BSA and BLG (see **Table 3.1**). Thereby, BSA is more hydrophobic than BLG [592,599,617,618] meaning BSA feels a stronger impact by D_2O. Furthermore, the hydrophobicity of a protein depends on its amino acid sequence, as well as its secondary structure. It was found that for α-helix formation hydrophobic amino acids are essential since those provide stabilisation to the structure [585].

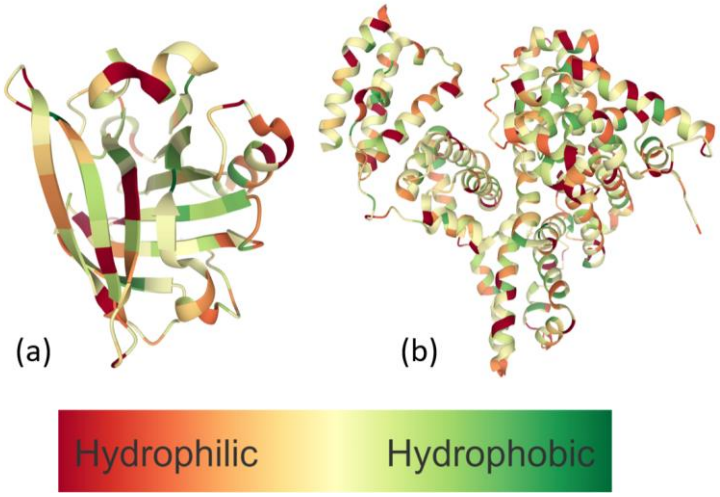

***Figure 10.1**: Hydrophobicity and 3D structure of proteins. These protein images of (a) BLG (PDB ID: 3PH6)* [148] *and (b) BSA (PDB ID: 4F5S)* [234] *were created with Mol** [619] *on the RCSB PDB website (rcsb.org). The differences in secondary structure (α-helices and β-sheets) are prominent (see also **Table 3.1**) and the colour code illustrates the hydrophobicity of different amino acids based on the work of Wimley & White* [620].

Thus, the nature of α-helices contributes strongly to the hydrophobicity of a protein and consequently to the amide isotope effect, whereas no isotope substitution occurs within β-sheets, which mainly define the BLG structure (**Figure 10.1**) [583]. BLG belonging to the protein class of all-β, therefore, does not undergo D/H isotope substitution for most of its structure compared to BSA belonging to the class of all-α (see **Table 3.1**) [230]. Thus, the discrepancy between a strong isotope effect in BSA and the absence in BLG systems can be explained based on their secondary structure/amino acid sequence and hydrophobicity illustrated in **Figure 10.1**.

- **Role of anion.** There seems to be a fundamental difference in BSA and BLG ability to bind anions. For BSA, the anion effect on its bulk behaviour increases from $Cl^- < NO_3^- < I^-$ [491], whereas for BLG all anions induce the same behaviour (**Figure 8.1** & **Figure 8.5**). The behaviour for BSA is in good agreement with literature from Carr et al. [256] and Longsworth et al. [538], which found that the amount of anions bound increases from $Cl^- < Br^- < NO_3^- < I^- = CNS^-$. Carr et al. [590] determined that 8 Cl^- anions are bound to BSA at pH 5, but 12 I^- ions. For BLG, this anion-type-specific binding to the protein is similar to BSA (i.e. more iodide is bound than chloride), but the absolute number of anions bound are reduced by a factor of 2 according to Longsworth et al. [538]. Klotz et al. [237] coined the parameter 'anion binding index' illustrating the proteins' affinity to bind anions, which is 29 for serum albumin and 4.6 for beta-lactoglobulin (**Table 3.1**). This is further supported by Tanford et al. [589] and the amount of chloride bound by each protein. Chloride, in general, has a passive role [536,585,589] and is also not traceable in the BLG crystal structure [148,612]. A recent publication by Maier et al. [612] evaluated the surface coverage of cations on proteins after cation binding (here: Y^{3+}). In BLG, 30 % of its surface is covered with cations in comparison to only 15 % coverage for BSA meaning less space is available for anions to bind to BLG. Another explanation might be the difference in binding mechanisms. BSA has a high affinity for anionic binding [548], whereas BLG prefers binding of hydrophobic molecules via hydrophobic interactions [591].

- **Re-entrant condensation.** Re-entrant condensation is driven by protein charge inversion and the consequently decreasing attractive protein-protein interactions, which cause the cation-bridged protein cluster to break apart [241]. In the presence of chloride salts, both BSA and BLG undergo re-entrant condensation (**Figure 6.1**), as well as in the presence of iodide salts for BLG (**Figure 8.1**). For BSA with iodide salts, the samples stay in regime II showing no re-entrant condensation (i.e. absence of regime III) (**Figure 7.3 (a & b)**). Chloride has a passive role [536] and thus cations dominate and determine the phase behaviour in those systems. Since BLG has in general a low anion binding affinity (for both chloride and iodide) [237,538], the phase behaviour is unaffected by any anion and the occurrence of re-entrant condensation can be explained by the binding of multivalent cations. This behaviour changes for BSA with iodide salts. Iodide has a prominent role due to its protein

stabilising properties [534,535], stronger binding to BSA [135] and higher quantity bound to BSA [256,538] than chloride. Additionally, an interplay between hydrophobic and charged amino acids improve anion binding to BSA [547,548]. Thus, iodide induces stronger attractive interactions and might facilitate anion-mediated and non-specific protein cluster formation, which hinder re-entrant condensation and stabilise BSA in bulk.

In the next section, similarities and differences in protein *adsorption* of BSA and BLG at a solid-liquid, net negatively charged, and hydrophilic interface is discussed:

- **Role of cations and anions.** The role of ions on the protein adsorption behaviour is reflected by its bulk properties. The stronger interactions an ion induces in bulk (**Figure 7.3**), the stronger is its effect on protein adsorption, in the sense that it enhances adsorption (**Figure 7.7**). One exception is BSA/YI_3, in which the combination of a strong cation with a strong anion seems to diminish each other.

- **Role of protein**. Adsorption is also regulated by the protein type. BLG is smaller in size than BSA (**Table 3.1**), which is reflected in its overall reduced adsorption (**Figure B.1**, Appendix B). In addition, BLG also forms denser packed adsorption layer reflected in the strong difference in dissipation measured by QCM-D (**Figure 7.10** & **Figure 7.11** & **Figure 8.7** & **Figure 8.8**). The adsorption trend (meaning its increase and decrease) is connected to the bulk phase transitions of the respective protein, which are reflected at the interface due to their similar properties.

- **Adsorption without salt.** Numerous investigations have shown that adsorption for BLG is reduced compared to BSA without salt [239,242,621], which is consistent with the presented findings in **Table 8.2**. BLG has a smaller size (**Table 3.1**) and a higher surface charge density, which could induce stronger repulsion in a system with negatively charged surfaces (of the proteins and the substrate) and thus limiting surface adsorption.

- **Re-entrant adsorption.** The non-linear behaviour in adsorption at high c_S can be observed with both proteins and all salts and either solvent as illustrated in **Figure 7.7** and **Figure 8.10**. Thus, it can be concluded that re-entrant adsorption is related to the surface properties and not the bulk re-entrant condensation behaviour (which is absent for BSA/iodide system). Due to surface properties being hydrophilic and net negatively charged, anion binding is hindered and solely the cations and solvent molecules are interacting with the interface. In the vicinity of the substrate (here: substrate and proteins are negatively charged), local charge inversion due to multivalent cation binding can be induced leading to re-entrant adsorption independent of the bulk properties.

- **Enhanced adsorption / wetting transition.** In regime II, attractive interactions dominate the system, which induces enhanced adsorption compared to regime I and III in all systems investigated (see **Figure 7.7** and **Figure 8.13**). The maximum adsorbed amount *d* is limited by the strength of the cations and anions in the system and subsequently LLPS formation. In systems with LLPS formation, continuous adsorption of proteins is observed and the formation of a wetting layer at the bulk instability [465]. The general mechanism is explained in Chapter 6. This wetting transition appears to be general, yet, the morphology differs for BSA and BLG. In BSA, the wetting layer is diffuse with a high portion of associated water trapped within [465] In BLG, a densely packed layer formation can be observed (50 % hydration in **Table 8.2**). This difference could be the determining factor for nucleation of protein crystals at interfaces for BLG and the absence of those in BSA, as well one has to bear in mind that BLG in its natural state forms dimers at neutral pH [236].

An *external* parameter, which influence the adsorption and bulk behaviour as well, is e.g. temperature. Depending on the formation of LLPS via LCST or UCST, the attractive interactions increase or decrease in bulk upon increase in temperature. Through the external manipulation of the phase behaviour, the bulk phase transitions and consequently the adsorption behaviour can be controlled e.g. though the introduction of a bulk instability (i.e. LLPS formation in bulk) and wetting transition at the interface (**Figure 6.5**).

All in all, comprehensive understanding of the relevant protein-protein, protein-salt, und protein-surface interactions and consequential protein behaviour connecting bulk and adsorption phenomena is developed in this dissertation. In the following chapter, possible next steps, open questions, and implications for application are discussed.

11 Outlook and Open Questions

There are still open questions, which need to be addressed and answered, especially in the context of surface modifications, which are summarised in this chapter.

The presence and absence of an anion-type dependence on BSA and BLG, respectively, can be understood and supported by literature, yet the investigation of these mechanisms on a molecular level, e.g. via molecular dynamic simulations, could provide information on if and where those anions bind or interact with the protein to prove the proposed hypotheses.

Furthermore, it might be of interest to see if the temperature-dependent adsorption behaviour found for BSA in Chapter 5 (LCST-LLPS) is also reflected in BLG since BLG and BSA show a different temperature dependency (UCST vs LCST) in different areas of the phase diagram [183].

The use of QCM-D and NR on systems showing LLPS formation and protein crystallisation in bulk might be a first step in solving the question on the location of nucleation origin in protein crystals. This is still unknown and highly relevant e.g. in drug production. If the nucleation starts at the interface, these methods should be able to detect the change in density and mass of the adsorbed protein layer.

First implications and starting points for future research topics in the context of surface modifications are given in Chapter 9. There are different aspects, which are of interest. To understand the effect of hydrophobicity on protein adsorption, NR could provide the required insight into the protein layer morphology and possibly denaturation of systems suitable for H/D.

To investigate the effect of surface charge on adsorption, SAMs with different terminations could be employed, especially positively charged SAMs. In this context, questions arise on which interactions guide the adsorption behaviour and if the ion-activated model can also be applied to a positively charged interface. Another possibility to investigate the role of surface charges on protein adsorption is through an applied potential, which would have the benefit of investigating the same sample under different conditions.

Preliminary measurements show that protein-resistant surfaces can be manipulated through the application of multivalent ions. Here, questions arise on the reversibility of this process, which might be of relevance for hydrogel formation, as well as on the role of multivalent ions on the interfacial water stability within the TEG layer.

Implant coatings could be a viable tool to establish ties between (so far) more fundamentally oriented research to application-oriented research. One challenge currently is the control of the surface roughness and the unknown role of super-hydrophilicity on protein adsorption.

These results could pave the way for the manipulation of biomaterials and hydrogels for controlled protein adsorption and consequently regulated foreign body response and better biocompatibility, as well extend the comprehensive understanding of protein adsorption.

APPENDICES

APPENDIX A: COMPLEMENTARY NEUTRON AND X-RAY REFLECTIVITY DATA

In this section, additional information to Chapter 7 and Chapter 8 is provided. Over the PhD period, several beam times were granted to perform X-ray and neutron reflectivity measurements. An overview of the beam times executed is given in **Table A.1**.

Table A.1: *Overview of allotted and carried out beam times at different facilities and beamlines.*

Facility	Beamline	Method	Experimental No.
ISIS	INTER	NR	RB1700010
ISIS	INTER	NR	RB1900001
ISIS	INTER	NR	RB1820534
ISIS	POLREF	NR	RB1910571
ILL	D17	NR	9-13-686
Diamond	I07	XRR	SI19032-1

An example for successful data collection is given in Chapter 8 (**Figure 8.11** & **Figure 8.12**). Before identifying the ideal measurements conditions, a substantial amount of troubleshooting had to be conducted, which is discussed in the following. The protein used first for neutron reflectivity (NR) measurements was BSA. BSA is used as a model protein, yet it formed rather diffuse adsorption layers, which lead to strong scattering and featureless reflectivity curves (**Figure A.1 (b) inset**). Consequently, data analysis is rather difficult.

In addition, the solvent used (H_2O) has no critical edge since it is outside of the detection limit. The critical edge can also be used as a feature to check the sample alignment, solution exchange, and fitting feature. Its absence further complicates the analysis. Another disadvantage of BSA is that it does not allow the use of solvent contrast since the phase transitions in H_2O compared to D_2O are at different salt concentrations. The isotope-dependent phase behaviour is known as the isotope effect in BSA and was investigated by Braun et al. [154]. Using different contrasts for the same system can usually compensate for the lack of features in the reflectivity curve and increase the chances to find an appropriate model, which is not applicable for BSA. Nevertheless, the Gompertz model [622] is found to describe the measured reflectivity curves well leading to density and adsorption profiles depending on the salt concentration in solution (**Figure A.1**).

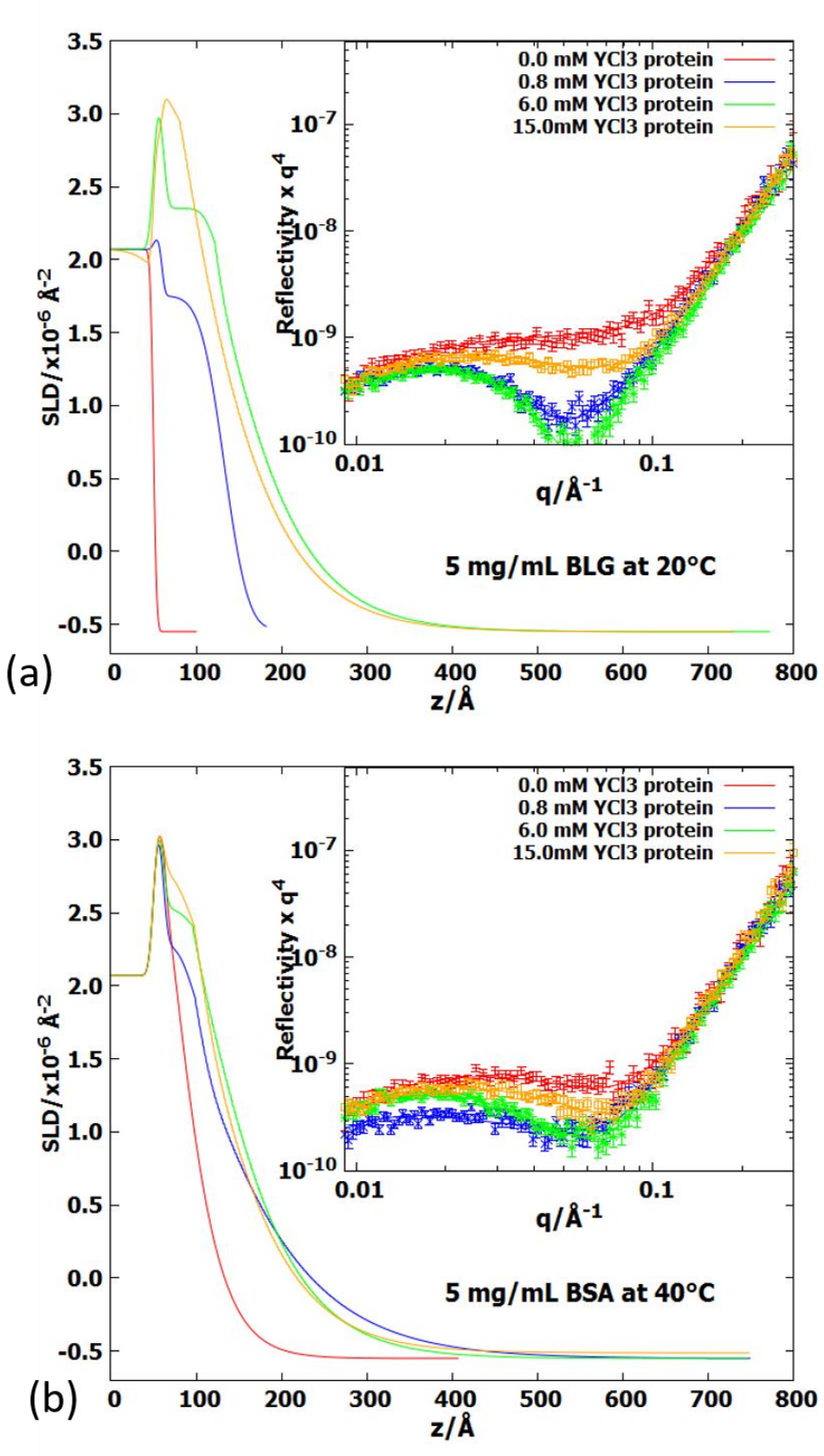

Figure A.1: Density profiles of (a) 5 mg/ml BLG at 20 °C and (b) 5 mg/ml BSA at 40 °C in the presence of YCl_3 (at 0, 0.8, 6, 15 mM) in H_2O analysed with the Gompertz model. The insets show the neutron reflectivity curves normalised by q^4measurd at D17 (ILL). Plots are provided by Maximilian Skoda.

However, Bayesian error analysis with a confidence interval of 95 % (**Figure A.2**) illustrated that the precision of the model applied is not enough since all found trends fall within the confidence interval (**Figure A.2 (b)**). Variations in salt type and temperature also do not lead to sufficiently strong changes in the obtained data to improve data analysis (**Figure A.3**), thus BSA is categorised as not analysable under the given circumstances.

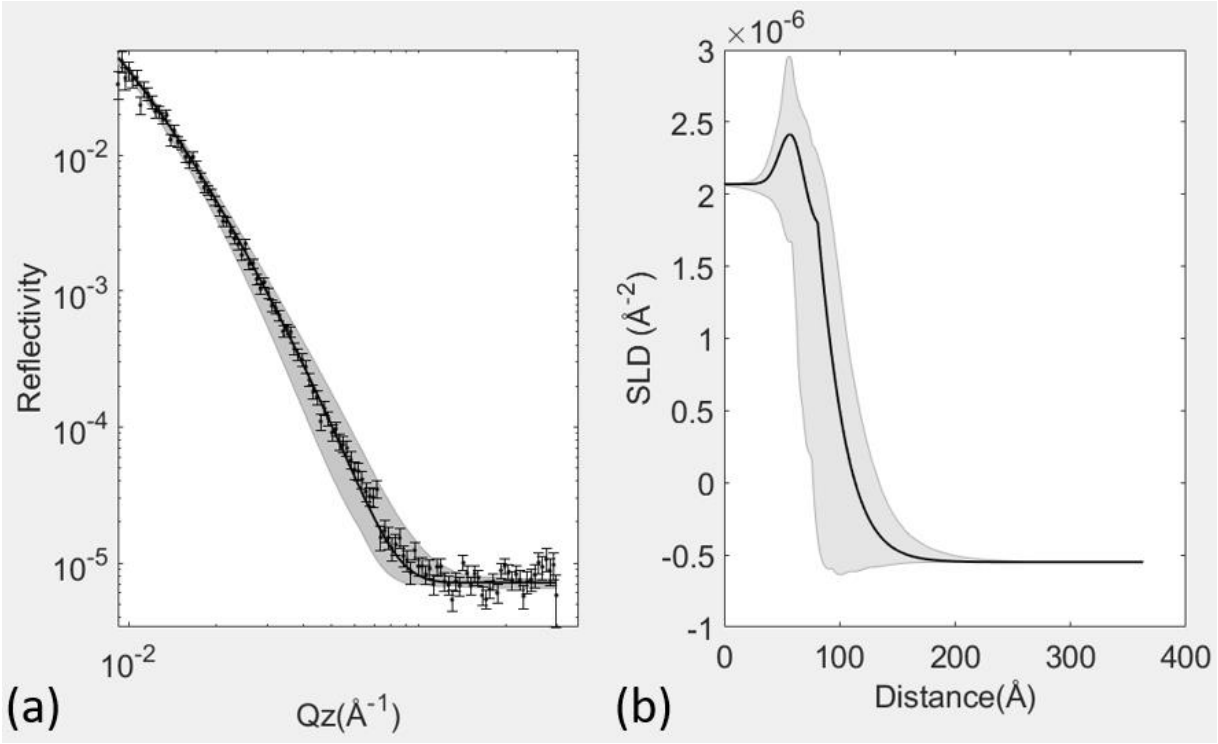

Figure A.2: *Bayesian error analysis (grey-shaded area) of the fitted curve (solid line) via the Gompertz model to (a) the neutron reflectivity data and (b) SLD of BSA 5 mg/ml at 40 °C no salt adsorbed to SiO_2 with a confidence interval of 95 %. Plots are provided by Maximilian Skoda.*

In another attempt, the protein used is changed to BLG, which is smaller in size and packs denser since it naturally occurs as a dimer [572]. This leads to a more defined adsorption layer and thus to a stronger change in the reflectivity data (**Figure A.1 (a) inset**) compared to BSA (**Figure A.1 (b) inset**). However, the use of only one solvent is also not sufficient for BLG (**Figure A.1 (a)**). Only with a second contrast, data analysis is distinct. The results are shown and discussed in Chapter 8.

Another method used to investigate protein adsorption is X-ray reflectivity (XRR). In combination with NR, it should provide the needed contrast to analyse the NR and XRR data. However, the measured signals are very noisy, and the experimental setup needed to be optimised several times (**Figure A.4**). In addition, X-rays can lead to beam damage in organic materials, which relates to denaturation of proteins [346]. The amount of beam damage in the samples cannot be accounted for. The changes for BLG (**Figure A.4 (b)**) compared to BSA (**Figure A.4 (a)**) are again more pronounced, yet not enough to allow successful data analysis.

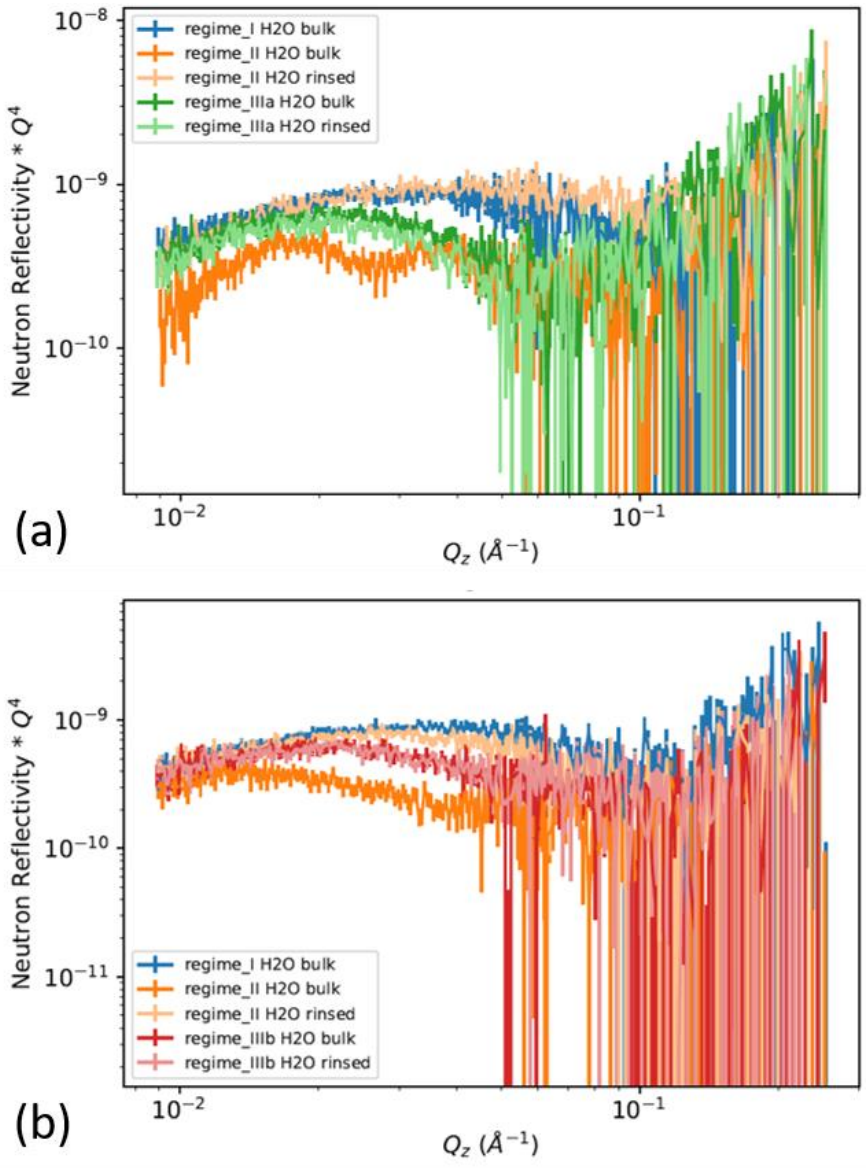

Figure A.3: *Neutron reflectivity curves of 5 mg/ml BSA (a) with YCl_3 (0, 0.8, and 6 mM) at 40 °C and (b) with $LaCl_3$ (0, 0.8, and 15 mM) at 20 °C in H_2O normalised by q^4measurd at D17 (ILL). Plots are provided by Simon Schönberg.*

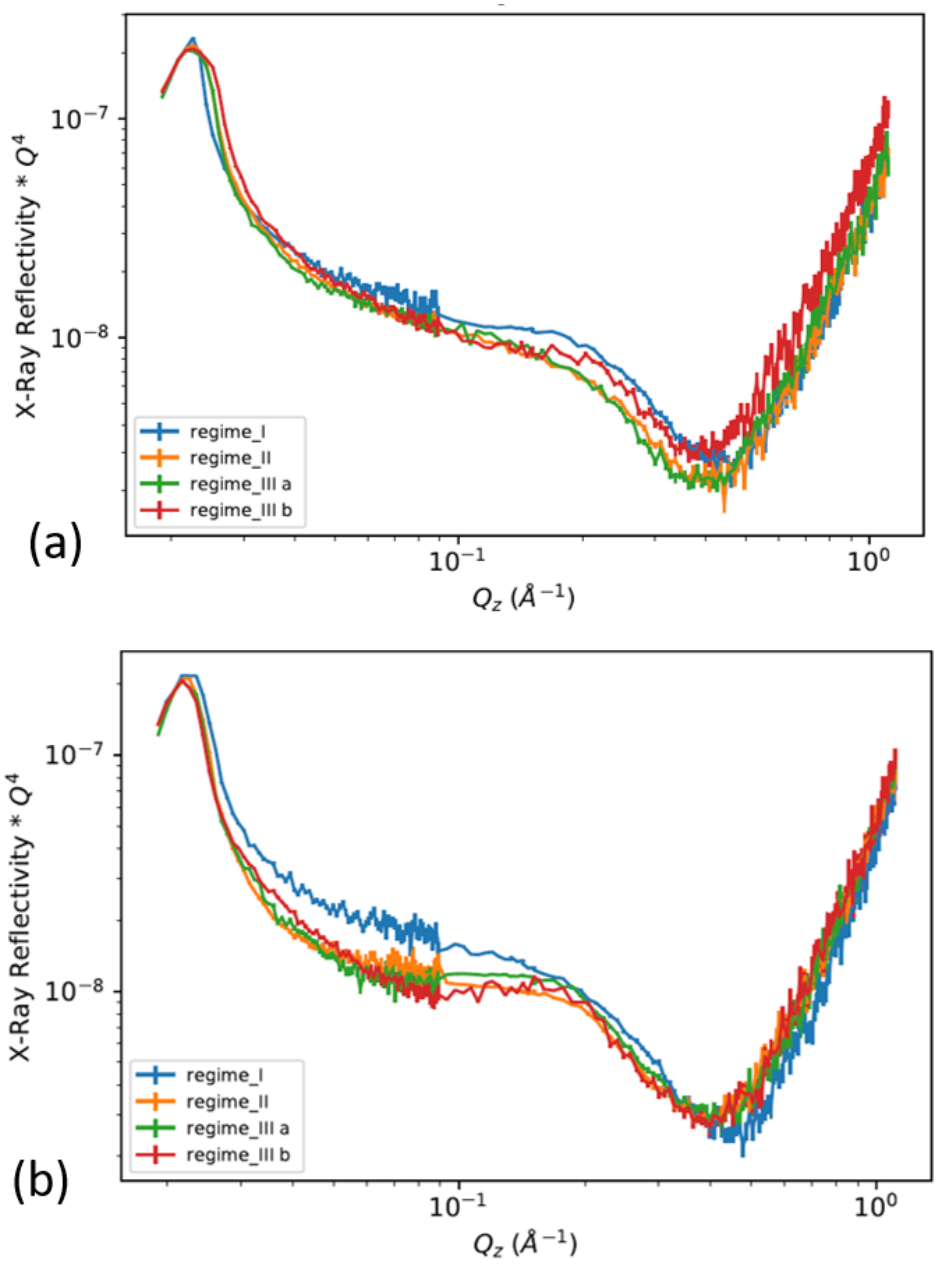

***Figure A.4**: X-ray reflectivity curves normalised by q^4. (a) 5 mg/ml BSA with YCl_3 at 40 °C and (b) with 5 mg/ml BLG with YCl_3 at 40 °C in H_2O measured at I07 (Diamond). The salt concentrations are set to 0, 0.8, 6, and 15 mM, which correlate with the increase in regimes e.g. regime I relates to 0 mM. Plots are provided by Simon Schönberg.*

Appendix B: Complementary BLG Adsorption Measurements

In addition to the BLG data presented in Chapter 8, additional ellipsometry measurements of BLG at 20 mg/ml in the presence of YCl_3 at 20 °C adsorbed to SiO_2 are conducted. The protein concentration used is four times higher than the concentration used in Chapter 8, thus a direct comparison with this data is not possible, instead a comparison between BSA and BLG can be done. The BLG adsorption behaviour initially increases and reaches a maximum value around $c_s/c_p = 5$, after which it starts to decrease until it stagnates around d = 4 nm at high c_s, known as re-entrant adsorption (**Figure B.1**, red triangle). In comparison to BSA adsorption (grey triangles in **Figure B.1**), maximum adsorption is reached at lower c_s/c_p values and can be described as a "quenched" version of the BSA data, as well adsorption in overall reduced compared to BSA. The reduced adsorption could be explained with the smaller size of BLG (R_p = 2.35 nm) compared to BSA (R_p = 3.5 nm).

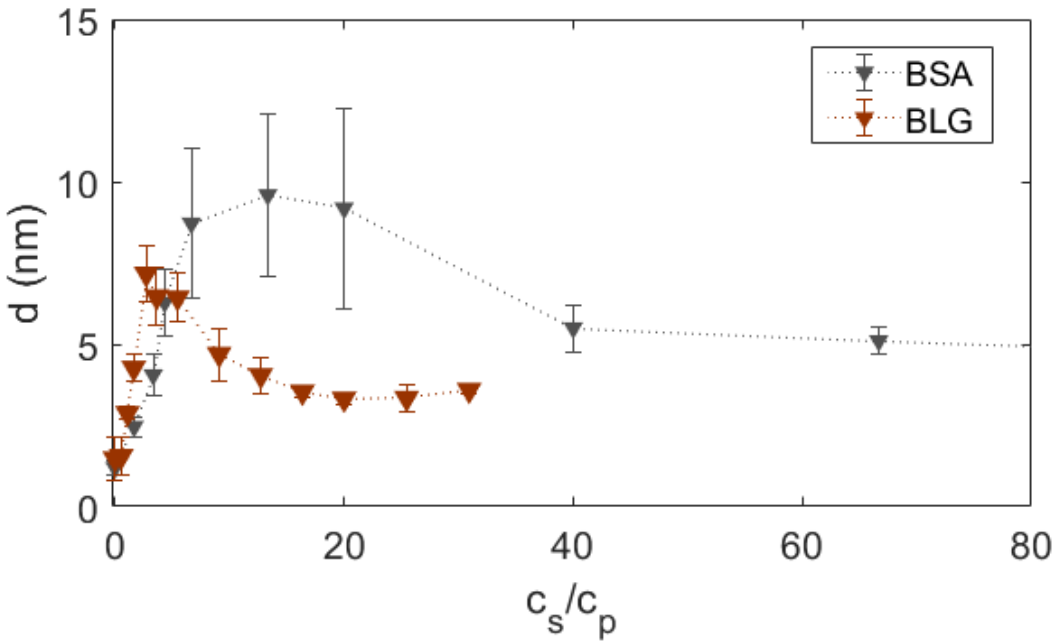

Figure B.1: *Protein adsorption of BSA (grey) and BLG (red) at c_p = 20 mg/ml plotted against c_s/c_p in the presence of YCl_3 on SiO_2 at 20 °C. Adsorption of BLG is overall much smaller than BSA under the same conditions.*

The salt-concentration-dependent adsorption trend of BLG seems to correlate with the dominant bulk interactions reflected in the bulk phase behaviour (**Figure B.2**). As explained in Chapter 5, the adsorption trend (for BSA) can be described through ion-activated attractive patchy interactions between proteins and proteins with the interface. In a system with chloride anions, only the cations influence the bulk behaviour and adsorption behaviour. If the surface properties mirror the bulk properties (here: net negatively charged and hydrophilic), the cations bind and bridge proteins to proteins in the same manner as proteins to the interface. The adsorption behaviour consequently not only depends on the bulk properties, but also on the substrate properties.

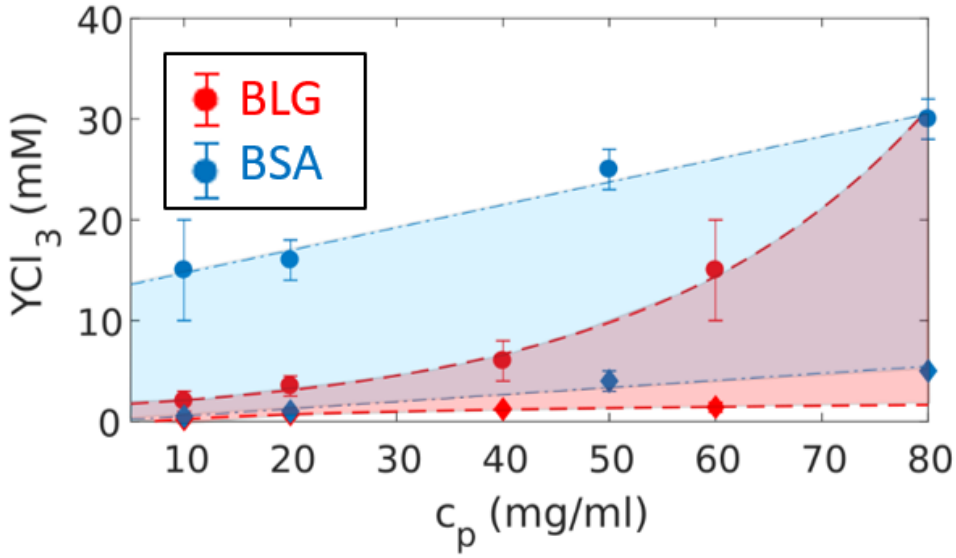

Figure B.2: Protein phase behaviour of BSA (blue) and BLG (red) in the presence of YCl_3. The shaded area illustrates samples, which are turbid and in regime II. Below this area, the samples are clear and in regime I and above, the samples are clear and in regime III.

Appendix C: Further Bayesian Error Analysis Plots of BLG Neutron Data

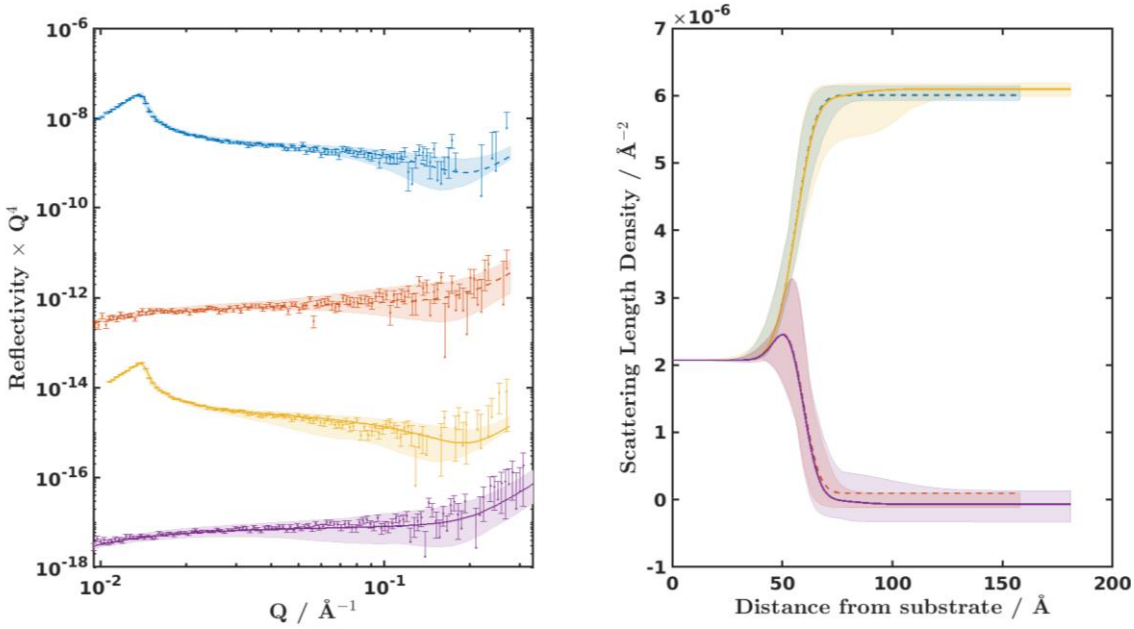

Figure C.1: Bayesian error analysis. Fit quality of model showing 95 % confidence intervals (shaded regions). Data shown is the bare sample (blue and red, dashed) and another sample of 5 mg/ml BLG in no salt (yellow and purple, solid), in D_2O and H_2O, respectively. Plots are provided by Maximilian Skoda.

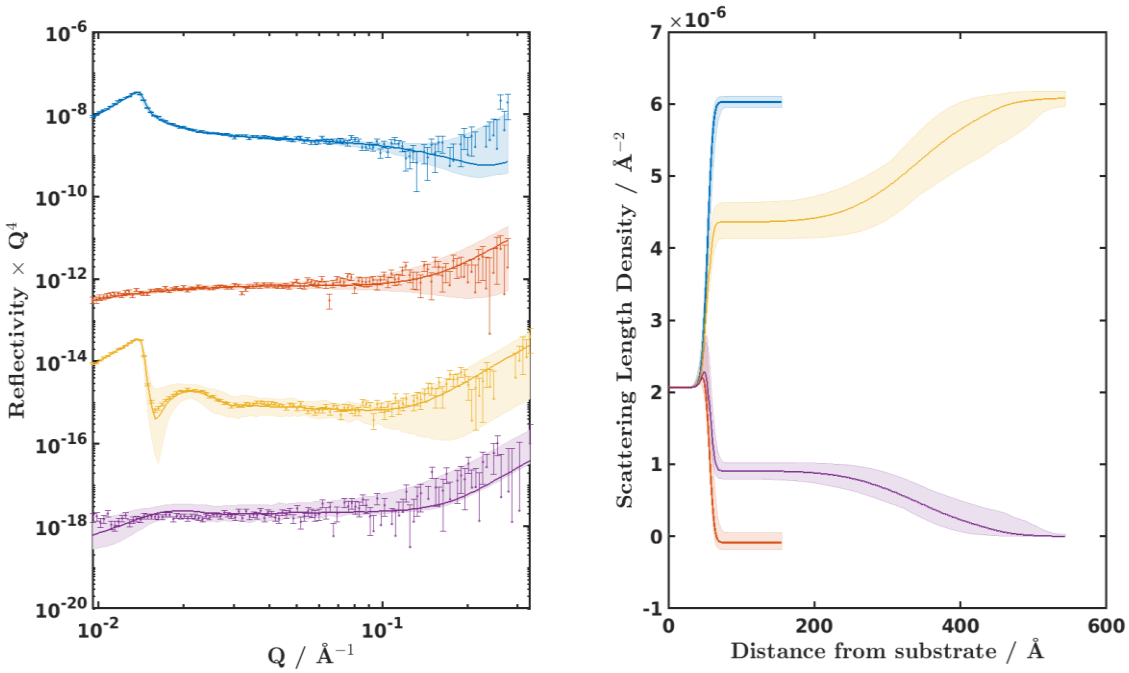

Figure C.2: Bayesian error analysis. Fit quality of model showing 95 % confidence intervals (shaded regions). Data shown is the bare substrate (blue and red, dashed) and another sample of 5 mg/ml BLG with 0.8 mM $LaCl_3$ (yellow and purple, solid), in D_2O and H_2O, respectively. Plots are provided by Maximilian Skoda.

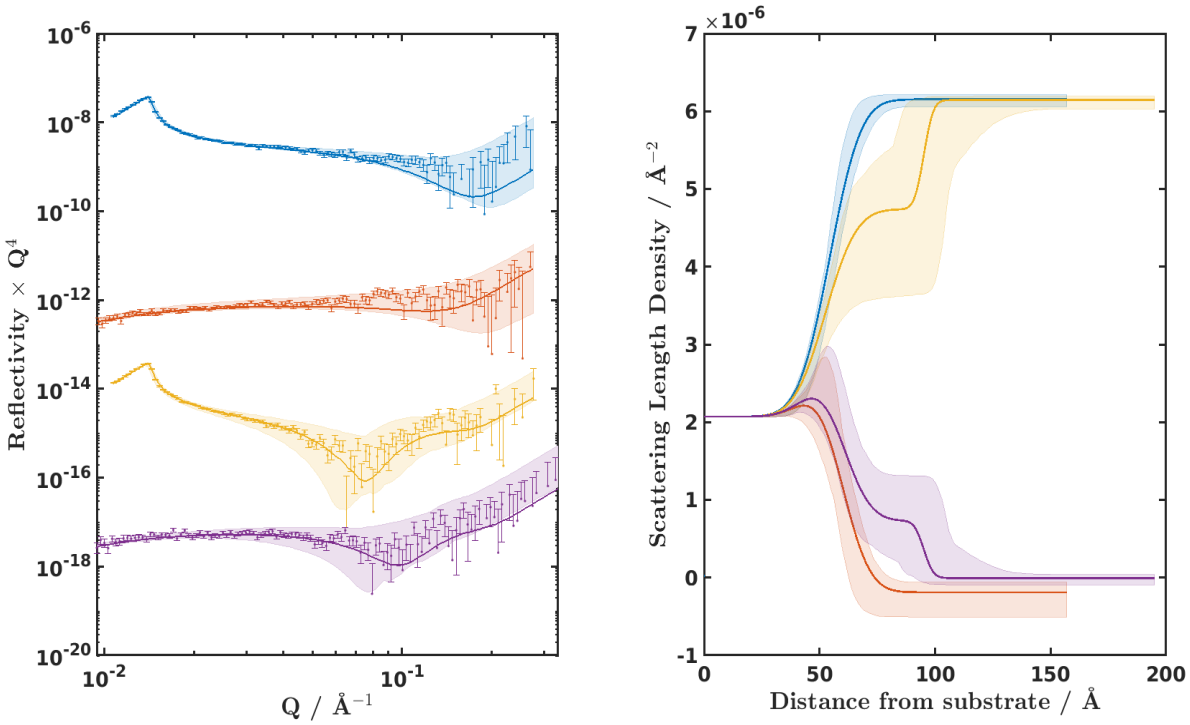

Figure C.3: Bayesian error analysis. Fit quality of model showing 95 % confidence intervals (shaded regions). Data shown is the bare substrate (blue and red, dashed) and another sample of 5 mg/ml BLG with 5 mM $LaCl_3$ (yellow and purple, solid), in D_2O and H_2O, respectively. Plots are provided by Maximilian Skoda.

List of Abbreviations

List of Latin Abbreviations

A	Absorbance
$AlCl_3$	Aluminium chloride
AFM	Atomic force microscopy
ATR-FTIR	Attenuated total reflectance Fourier transform infrared spectroscopy
Au	Gold
B	Jones-Dole ionic B coefficient
B_2	Second virial coefficient of bulk solution
B_2/B_2^{HS}	Reduced second virial coefficient
B_2^{HS}	Second virial coefficient of hard spheres
BLG	Beta lactoglobulin (engl.) / β-Lactoglobulin (dt.)
BSA	Bovine serum albumin (engl.) / Rinderserumalbumin (dt.)
c	concentration
C	Mass sensitivity constant
c^*	First phase transition from regime I to regime II
c^{**}	Second phase transition from regime II to regime III
$CdCl_2$	Cadmium chloride
$CeCl_3$	Caesium chloride
CI	Confidence interval
CNT	Classical nucleation theory
c_p	Protein concentration
$C_{p,str}$	Heat capacity
c_s	Salt concentration
$c_{s,LLPS}$	Salt concentration, at which LLPS occurs
d *or* $d(c_s)$	Thickness of adsorbed protein layer
D	Dissipation
d_0	Thickness of crystal
d_1	Thickness of adsorbed layer; equivalent to $d_{QMC\text{-}D}$
d_{assoc}	Thickness/amount of associated water within protein layer
d_{EM}	Equivalent to d; thickness of adsorbed proteins determined with ellipsometry
d_p	Penetration depth
D_{pp}	Protein-protein distance
$d_{QMC\text{-}D}$	Thickness of adsorbed proteins with associated water

d_{rinsed}	Thickness of irreversibly bound proteins
d_{uv}	Optical path length
DFT	Classical density functional theory
DLVO	Derjaguin-Landau-Verwey-Overbeek theory
E_{yx}	Electric field of two variable components (x,y)
F	Resonance frequency
$FeCl_3$	Iron chloride
FFPT	Flüssig-Flüssig-Phasentrennung
FMT	Fundamental measure theory
$F(q)$	Form factor
FTIR	Fourier transform infrared spectroscopy
G	Surface free energy
H_3O^+	Hydronium ions
$HoCl_3$	Holmium chloride
I	Transmitted intensity
I_0	Incident intensity
$I(q)$	Scattering intensity
$I(x)$	Intensity of measured signal (interferogram)
$k_{i,r}$	Magnitude of the wavevector of incident or reflected beam
$LaCl_3$	Lanthanum chloride
LaI_3	Lanthanum iodide
$La(NO_3)_3$	Lanthanum nitrate
LCST	Lower critical solution temperature
LLPS	Liquid-liquid phase separation
M	Number of patches on hard sphere
MC	Monte Carlo simulations
MD	Molecular dynamics simulations
ML	Monolayer
M_W	Molecular weight
NaCl	Sodium chloride
n	Refractive index
$\tilde{n}$	Complex refractive index
n_f	Frequency overtone
n_{ion}	Number of bound ions
NR	Neutron reflectivity
O_3	Ozone
OTS	Trichloro(octadecyl)silane
PEG	Polyethylene glycol
pH	Lat. *potentia Hydrogenii*
pI	Isoelectric point
PME	Phase-modulated ellipsometry

q	Momentum transfer/ scattering vector
q_c	Critical scattering vector
QCM-D	Quartz crystal microbalance with dissipation monitoring
q_x	Momentum transfer in x-direction
q_z	Momentum transfer in z-direction
r	Distance of interactions
RC	Re-entrant condensation
r_{ion}	Effective (an)ion radius
r_p	Fresnel reflection coefficient of p-component of polarised light
R_p	Radius of protein (hard sphere)
$R(q)$	Reflectivity
r_s	Fresnel reflection coefficient of s-component of polarised light
S	Spreading parameter
S_0	Surface hydrophobicity
S_{str}	Structural entropy
SAM	Self-assembled monolayer
SAXS	Small-angle X-ray scattering
SI	Supporting/supplementary information
SiO_2	Silicon dioxide
SLD	Scattering length density
SM	Supporting material
$S(q)$	Structure factor
T	Temperature
TEG	Triethylene glycol mono-11-mercaptoundecyl ether
T_{UV}	Transmittance
UCST	Upper critical solution temperature
$U(r)$	Interaction pair potential
UV-Vis	Ultraviolet-visible spectroscopy
VASE	Variable-angle spectroscopic ellipsometry
vdW	Van der Waals interactions
$V(D_{pp})$	Interaction potential between two macromolecules (proteins)
$V_{Particle}$	Volume of the particle
$V_{ext}(r)$	Arbitrary external potential
$V_{eff}(r)$	Effective bulk interactions
$V_{wp}(z)$	Short-ranged wall-potential potential
x	Mirror position
XRR	X-ray reflectivity
YCl_3	Yttrium chloride
YI_3	Yttrium iodide
z	Distance normal to the wall/ height of adsorbed layer
$ZnCl_2$	Zinc chloride

List of Greek Abbreviations

$A(\nu)$	Wavenumber-dependent absorbance signal
δ_3	Penetration depth of shear wave of bulk liquid
Δ	Relative phase shift between the s-and p-component of polarised light
ΔD	Change in dissipation
ΔF	Change in resonance frequency
ΔG_{HB}	Water structure parameter
Δm	Mass uptake
$\Delta\rho$	Scattering cross section between particle and solvent
$d\gamma/dc_i$	Ionic aqueous surface tension
ε	Extinction coefficient
$\varepsilon = \varepsilon_{0.1\,\%}^{279nm}$	Extinction coefficient of proteins
ε_b	Binding energy between patch and ion
ε_{PP}	Binding energy between protein/patch and protein/patch
ε_{uo}	Binding energy between occupied patch and unoccupied patch
$\mathcal{F}[\rho]$	Functional of the intrinsic free energy
γ	Interfacial surface tension between liquid and air (vapor)
γ_{SL}	Interfacial surface tension between solid and liquid
γ_{SV}	Interfacial surface tension between solid and air (vapor)
κ	Force constant between atoms
λ	Wavelength
μ	Reduced mass
μ_1	Shear elasticity of adsorbed layer
μ_s	Salt chemical potential
η	Volume packing fraction
η_1	Viscosity of adsorbed layer
η_3	Viscosity of bulk liquid
ν	Specific wavenumber
ω	Angular frequency of oscillation
$\Omega[\rho]$	Functional of the grand potential
Φ	Fraction of proteins in cluster
Φ_V	Volume fraction of the particle in solution
Ψ	Relative amplitude change between the s-and p-component of polarised light
ρ	Polarisation
ρ_0	Density of crystal
ρ_1	Density of bulk liquid
ρ_3	Density of adsorbed protein
$\rho(r)$	Inhomogeneous density profile
ρ_p	Bulk/protein density profile
$\rho_p(z)$	Computed inhomogeneous density profile

ρ_{SLD}	Scattering length density
σ	Surface roughness
Θ	Occupation probability of a patch
θ_0	Incident angle
θ_c	Critical angle
θ_Y	Young contact angle
$\xi(z)$	Short-ranged attraction induced by the yttrium ions condensed on the wall

Bibliography

[1] M. Rabe, D. Verdes, and S. Seeger, Adv. Colloid Interface Sci. **162**, 87–106 (2011): *Understanding protein adsorption phenomena at solid surfaces*.

[2] E. Dickinson, Food Hydrocoll. **1**, 3–23 (1986): *Mixed proteinaceous emulsifiers: review of competitive protein adsorption and the relationship to food colloid stabilization*.

[3] T. Nicolai, M. Britten, and C. Schmitt, Food Hydrocoll. **25**, 1945–1962 (2011): *β-Lactoglobulin and WPI aggregates: Formation, structure and applications*.

[4] S. Assenza, and R. Mezzenga, Nat. Rev. Phys. **1**, 551–566 (2019): *Soft condensed matter physics of foods and macronutrients*.

[5] A.E. Ince Coskun, and S. Otles, Integr. Food, Nutr. Metab. **6**, 1–5 (2019): *Preparation, properties and behaviour of protein microparticles in salt containing dispersions*.

[6] T.Ö. Yilsay, L. Yilmaz, and A.A. Bayizit, Eur. Food Res. Technol. **222**, 171–175 (2006): *The effect of using a whey protein fat replacer on textural and sensory characteristics of low-fat vanilla ice cream*.

[7] D.J. McMahon, M.C. Alleyne, R.L. Fife, and C.J. Oberg, J. Dairy Sci. **79**, 1911–1921 (1996): *Use of fat replacers in low fat mozzarella cheese*.

[8] N. Ron, P. Zimet, J. Bargarum, and Y.D. Livney, Int. Dairy J. **20**, 686–693 (2010): *Beta-lactoglobulin-polysaccharide complexes as nanovehicles for hydrophobic nutraceuticals in non-fat foods and clear beverages*.

[9] C. Le Tien, C. Vachon, M.-A. Mateescu, and M. Lacroix, J. Food Sci. **66**, 512–516 (2001): *Milk protein coatings prevent oxidative browning of apples and potatoes*.

[10] S.Y. Lin, and J.M. Krochta, J. Food Process Eng. **29**, 532–546 (2006): *Fluidized-bed system for whey protein film coating of peanuts*.

[11] J. Osés, I. Fernández-Pan, K. Ziani, and J.I. Maté, Eur. Food Res. Technol. **227**, 623–628 (2008): *Use of edible films based on whey protein isolate to protect foods rich in polyunsaturated fatty acids*.

[12] A. Addesso, and D.B. Lund, J. Food Process. Preserv. **21**, 319–333 (1997): *Influence of solid surface energy on protein adsorption*.

[13] J.L. Nilsson, J. Memb. Sci. **52**, 121–142 (1990): *Protein fouling of UF membranes: Causes and consequences*.

[14] A.W. Mohammad, C.Y. Ng, Y.P. Lim, and G.H. Ng, Food Bioprocess Technol. **5**, 1143–1156 (2012): *Ultrafiltration in food processing industry: Review on application, membrane fouling, and fouling control*.

[15] R. Atra, G. Vatai, E. Bekassy-Molnar, and A. Balint, J. Food Eng. **67**, 325–332 (2005): *Investigation of ultra- and nanofiltration for utilization of whey protein and lactose*.

[16] E.A. Zottola, and K.C. Sasahara, Int. J. Food Microbiol. **23**, 125–148 (1994): *Microbial biofilms in the food processing industry-should they be a concern?*

[17] R. Wüstneck, J. Krägel, R. Miller, P.J. Wilde, and D.C. Clark, Colloid. Surf. A . **114**, 255–265 (1996): *The adsorption of surface-active complexes between β-casein, β-lactoglobulin and ionic surfactants and their shear rheological behaviour*.

[18] R.M. Forbes, A.R. Cooper, and H.H. Mitchell, J. Biol. Chem. **203**, 359–366 (1953): *The composition of the adult human body as determined by chemical analysis*.

[19] P.J. Moughan, Digestion and absorption of proteins and peptides, in: Des. Funct. Foods, Elsevier Ltd., (2009): pp. 148–170.

[20] B.Y. Shekunov, and P. York, J. Cryst. Growth. **211**, 122–136 (2000): *Crystallization processes in pharmaceutical technology and drug delivery design*.

[21] L. Stewart, R. Clark, and C. Behnke, Drug Discov. Today. **7**, 187–196 (2002): *High-throughput crystallization and structure determination in drug discovery*.

[22] K.E. Goodwill, M.G. Tennant, and R.C. Stevens, Drug Discov. Today. **6**, 113–118 (2001): *High-throughput X-ray crystallography for structure-based drug design*.

[23] J. Liu, Y. Huang, A. Kumar, A. Tan, S. Jin, A. Mozhi, and X.J. Liang, Biotechnol. Adv. **32**, 693–710 (2014): *pH-sensitive nano-systems for drug delivery in cancer therapy*.

[24] V. Hasirci, and N. Hasirci, Controlled Release Systems, in: Fundam. Biomater., Springer New York, (2018): pp. 257–279.

[25] C. Du, J. Tian, S. Wan, J. Cao, X. Chi, and Y. Gu, Synthesis and evaluation of a folate-linked anti-cancer prodrug, in: Int. Conf. Biomed. Eng. Biotechnol., IEEE, (2012): pp. 1089–1092.

[26] C. Du, D. Deng, L. Shan, S. Wan, J. Cao, J. Tian, S. Achilefu, and Y. Gu, Biomaterials. **34**, 3087–3097 (2013): *A pH-sensitive doxorubicin prodrug based on folate-conjugated BSA for tumor-targeted drug delivery*.

[27] H. Thakkar, R.K. Sharma, A.K. Mishra, K. Chuttani, and R.R. Murthy, AAPS PharmSciTech. **6**, 65–73 (2005): *Albumin microspheres as carriers for the antiarthritic drug celecoxib*.

[28] U. Krach-Hansen, V.T.G. Chuang, and M. Otagiri, Biol. Pharm. Bull. **25**, 695–704 (2002): *Practical aspects of the ligand-binding and enzymatic properties of human serum albumin*.

[29] J. Stange, S.R. Mitzner, T. Risler, C.M. Erley, W. Lauchart, H. Goehl, S. Klammt, P. Peszynski, J. Freytag, H. Hickstein, M. Löhr, S. Liebe, W. Schareck, U.T. Hopt, and R. Schmidt, Artif. Organs. **23**, 319–330 (1999): *Molecular adsorbent recycling system (MARS): Clinical results of a new membrane-based blood purification system for bioartificial liver support*.

[30] E.S. Place, N.D. Evans, and M.M. Stevens, Nat. Mater. **8**, 457–470 (2009): *Complexity in biomaterials for tissue engineering*.

[31] T.J. Sill, and H.A. von Recum, Biomaterials. **29**, 1989–2006 (2008): *Electrospinning: Applications in drug delivery and tissue engineering*.

[32] H. Jiang, Y. Hu, P. Zhao, Y. Li, and K. Zhu, J. Biomed. Mater. Res. - Part B Appl. Biomater. **79**, 50–57 (2006): *Modulation of protein release from biodegradable core-shell structured fibers prepared by coaxial electrospinning*.

[33] H. Jiang, Y. Hu, Y. Li, P. Zhao, K. Zhu, and W. Chen, J. Control. Release. **108**, 237–243 (2005): *A facile technique to prepare biodegradable coaxial electrospun nanofibers for controlled release of bioactive agents*.

[34] S.Y. Chew, J. Wen, E.K.F. Yim, and K.W. Leong, Biomacromolecules. **6**, 2017–2024 (2005): *Sustained release of proteins from electrospun biodegradable fibers*.

[35] H. Jiang, D. Fang, B.S. Hsiao, B. Chu, and W. Chen, Biomacromolecules. **5**, 326–333 (2004): *Optimization and characterization of dextran membranes prepared by electrospinning*.

[36] H. Qi, P. Hu, J. Xu, and A. Wang, Biomacromolecules. **7**, 2327–2330 (2006): *Encapsulation of drug reservoirs in fibers by emulsion electrospinning: Morphology characterization and preliminary release assessment*.

[37] Y.Z. Zhang, X. Wang, Y. Feng, J. Li, C.T. Lim, and S. Ramakrishna, Biomacromolecules. **7**, 1049–1057 (2006): *Coaxial electrospinning of (fluorescein isothiocyanate-conjugated bovine serum albumin)-encapsulated poly(ε-caprolactone) nanofibers for sustained release*.

[38] V. Hasirci, and N. Hasirci, Biomaterials and devices in soft tissue augmentation, in: Fundam. Biomater., Springer New York, (2018): pp. 199–218.

[39] C.M. Bhamidipati, J.S. Coselli, and S.A. LeMaire, J. Extra. Corpor. Technol. **44**, 6–12 (2012): *BioGlue® in 2011: What is its role in cardiac surgery?*

[40] K.J. Zehr, Ann. Thorac. Surg. **84**, 1048–1052 (2007): *Use of bovine albumin-glutaraldehyde glue in cardiovascular surgery*.

[41] J.G. Torres-Rendon, T. Femmer, L. De Laporte, T. Tigges, K. Rahimi, F. Gremse, S. Zafarnia, W. Lederle, S. Ifuku, M. Wessling, J.G. Hardy, and A. Walther, Adv. Mater. **27**, 2989–2995 (2015): *Bioactive gyroid scaffolds formed by sacrificial templating of nanocellulose and nanochitin hydrogels as instructive platforms for biomimetic tissue engineering*.

[42] J.D. Andrade, and V. Hlady, Protein adsorption and materials biocompatibility: a tutorial review and suggested hypotheses, in: Adv. Polym. Sci. Vol. 79, Springer, (1986): pp. 1–63.

[43] V. Hasirci, and N. Hasirci, Hemocompatibility, in: Fundam. Biomater., Springer New York, (2018): pp. 173–186.

[44] C.J. Nonckreman, S. Fleith, P.G. Rouxhet, and C.C. Dupont-Gillain, Colloid Surf. B. **77**, 139–149 (2010): *Competitive adsorption of fibrinogen and albumin and blood platelet adhesion on surfaces modified with nanoparticles and/or PEO*.

[45] M. Rahmati, E.A. Silva, J.E. Reseland, C. A Heyward, and H.J. Haugen, Chem. Soc. Rev. **49**, 5178–5224 (2020): *Biological responses to physicochemical properties of biomaterial surface*.

[46] C. Werner, M.F. Maitz, and C. Sperling, J. Mater. Chem. **17**, 3376–3384 (2007): *Current strategies towards hemocompatible coatings*.

[47] G. Janvier, C. Baquey, C. Roth, N. Benillan, S. Bélisle, and J.-F. Hardy, Ann. Thorac. Surg. **62**, 1926–1934 (1996): *Extracorporeal circulation, hemocompatibility, and biomaterials*.

[48] J.L. Brash, T.A. Horbett, R.A. Latour, and P. Tengvall, Acta Biomater. **94**, 11–24 (2019): *The blood compatibility challenge. Part 2: Protein adsorption phenomena governing blood reactivity*.

[49] K. Kottke-Marchant, J.M. Anderson, Y. Umemura, and R.E. Marchant, Biomaterials. **10**, 147–155 (1989): *Effect of albumin coating on the in vitro blood compatibility of Dacron® arterial prostheses*.

[50] C.D. Mc Farland, C. De Filippis, M. Jenkins, A. Tunstell, N.P. Rhodes, D.F. Williams, and J.G. Steele, J. Biomater. Sci. Polym. Ed. **9**, 1227–1239 (1998): *Albumin-binding surfaces: in vitro activity*.

[51] K.R. Kamath, and K. Park, J. Appl. Biomater. **5**, 163–173 (1994): *Surface modification of polymeric biomaterials by albumin grafting using γ-irradiation*.

[52] C. Zhang, J. Jin, J. Zhao, W. Jiang, and J. Yin, Colloid Surf. B. **102**, 45–52 (2013): *Functionalized polypropylene non-woven fabric membrane with bovine serum albumin and its hemocompatibility enhancement*.

[53] D.G. Castner, Biointerphases. **12**, 02C301 (2017): *Biomedical surface analysis: Evolution and future directions (Review)*.

[54] M.G. Baines, F. Cai, and H.A. Backman, Optom. Vis. Sci. **67**, 807–810 (1990): *Adsorption and removal of protein bound to hydrogel contact lenses*.

[55] M.F. Refojo, and F.J. Holly, Contact Intraocul. Lens Med. J. **3**, 23–36 (1977): *Tear protein adsorption on hydrogels: a possible cause of contact lens allergy*.

[56] S. V. Murphy, and A. Atala, Nat. Biotechnol. **32**, 773–785 (2014): *3D bioprinting of tissues and organs*.

[57] A.S. Lynch, and G.T. Robertson, Annu. Rev. Med. **59**, 415–428 (2008): *Bacterial and fungal biofilm infections*.

[58] B. Kasemo, Surf. Sci. **500**, 656–677 (2002): *Biological surface science*.

[59] J.M. Anderson, A. Rodriguez, and D.T. Chang, Semin. Immunol. **20**, 86–100 (2008): *Foreign body reaction to biomaterials*.

[60] C. Sperling, R.B. Schweiss, U. Streller, and C. Werner, Biomaterials. **26**, 6547–6557 (2005): *In vitro hemocompatibility of self-assembled monolayers displaying various functional groups*.

[61] J. Jin, C. Zhang, W. Jiang, S. Luan, H. Yang, J. Yin, and P. Stagnaro, Colloid. Surf. A . **407**, 141–149 (2012): *Melting grafting polypropylene with hydrophilic monomers for improving hemocompatibility*.

[62] R.K. Roy, H.W. Choi, J.W. Yi, M.-W. Moon, K.-R. Lee, D.K. Han, J.H. Shin, A. Kamijo, and T. Hasebe, Acta Biomater. **5**, 249–256 (2009): *Hemocompatibility of surface-modified, silicon-incorporated, diamond-like carbon films*.

[63] R.W. Colman, and A.H. Schmaier, Blood. **90**, 3819–3843 (1997): *Contact system: A vascular biology modulator with anticoagulant, profibrinolytic, antiadhesive, and proinflammatory attributes*.

[64] R.W. Colman, J. Clin. Invest. **73**, 1249–1253 (1984): *Surface-mediated defense reactions. The plasma contact activation system*.

[65] G.A. Yarovaya, T.B. Blokhina, and E.A. Neshkova, Biochemistry. (Mosc). **67**, 13–24 (2002): *Contact system. New concepts on activation mechanisms and bioregulatory functions*.

[66] V. Hasirci, and N. Hasirci, Ceramics, in: Fundam. Biomater., Springer New York, (2018): pp. 51–64.

[67] K.A. Mosiewicz, L. Kolb, A.J. Van Der Vlies, M.M. Martino, P.S. Lienemann, J.A. Hubbell, M. Ehrbar, and M.P. Lutolf, Nat. Mater. **12**, 1072–1078 (2013): *In situ cell manipulation through enzymatic hydrogel photopatterning*.

[68] P.H.J. Kouwer, M. Koepf, V.A.A. Le Sage, M. Jaspers, A.M. Van Buul, Z.H. Eksteen-Akeroyd, T. Woltinge, E. Schwartz, H.J. Kitto, R. Hoogenboom, S.J. Picken, R.J.M. Nolte, E. Mendes, and A.E. Rowan, Nature. **493**, 651–655 (2013): *Responsive biomimetic networks from polyisocyanopeptide hydrogels*.

[69] T.A. Horbett, and J.L. Brash, Proteins at interfaces: Current issues and future prospects, in: Proteins at Interfaces, 1st ed., American Chemical Society, (1987): pp. 1–33.

[70] T.A. Horbett, Protein Adsorption on Biomaterials, in: S.L. Cooper, N.A. Peppas, A.S. Hoffman, B.D. Ratner (Eds.), Biomater. Interfacial Phenom. Appl., American Chemical Society, (1982): pp. 233–244.

[71] J.D. Andrade, and V. Hlady, Ann. N. Y. Acad. Sci. **516**, 158–172 (1987): *Plasma protein adsorption: the big twelve*.

[72] D.R. Schmidt, H. Waldeck, and W.J. Kao, Protein Adsorption to Biomaterials, in: Biol. Interact. Mater. Surfaces, Springer New York, (2009): pp. 1–18.

[73] L. Vroman, and A.L. Adams, Why plasma proteins interact at interfaces, in: Proteins at Interfaces, 1st ed., American Chemical Society, (1987): pp. 154–164.

[74] J.R. Lu, X. Zhao, and M. Yaseen, Curr. Opin. Colloid Interface Sci. **12**, 9–16 (2007): *Protein adsorption studied by neutron reflection*.

[75] T.J. Su, J.R. Lu, R.K. Thomas, and Z.F. Cui, J. Phys. Chem. B. **103**, 3727–3736 (1999): *Effect of pH on the adsorption of bovine serum albumin at the silica/water interface studied by neutron reflection*.

[76] E. Anbazhagan, A. Rajendran, D. Natarajan, M.S. Kiran, and D.K. Pattanayak, Colloids Surf. B. **143**, 213–223 (2016): *Divalent ion encapsulated nano titania on Ti metal as a bioactive surface with enhanced protein adsorption*.

[77] K. Kandori, S. Toshima, M. Wakamura, M. Fukusumi, and Y. Morisada, J. Phys. Chem. B. **114**, 2399–2404 (2010): *Effects of modification of calcium hydroxyapatites by trivalent metal ions on the protein adsorption behavior*.

[78] A. Sauter, M. Oelker, G. Zocher, F. Zhang, T. Stehle, and F. Schreiber, Cryst. Growth Des. **14**, 6357–6366 (2014): *Nonclassical pathways of protein crystallization in the presence of multivalent metal ions*.

[79] F. Zhang, F. Roosen-Runge, A. Sauter, M. Wolf, R.M.J. Jacobs, and F. Schreiber, Pure Appl. Chem. **86**, 191–202 (2014): *Reentrant condensation, liquid–liquid phase separation and crystallization in protein solutions induced by multivalent metal ions*.

[80] F. Zhang, M.W.A. Skoda, R.M.J. Jacobs, S. Zorn, R.A. Martin, C.M. Martin, G.F. Clark, S. Weggler, A. Hildebrandt, O. Kohlbacher, and F. Schreiber, Phys. Rev. Lett. **101**, 148101 (2008): *Reentrant condensation of proteins in solution induced by multivalent counterions*.

[81] D.C. Carter, and J.X. Ho, Structure of serum albumin, in: C.B. Anfinsen, J.T. Edsall, F.M. Richards, D.S. Eisenberg (Eds.), Adv. Protein Chem., Academic Press, (1994): pp. 153–203.

[82] G. Kontopidis, C. Holt, and L. Sawyer, J. Dairy Sci. **87**, 785–796 (2004): *Invited review: β-lactoglobulin: Binding properties, structure, and function*.

[83] V. Hasirci, and N. Hasirci, Building blocks of the human body, in: Fundam. Biomater., Springer New York, (2018): pp. 95–115.

[84] H. Lodish, A. Berk, S.L. Zipursky, P. Matsudaira, D. Baltimore, and J. Darnell, Covalent bonds, in: Mol. Cell Biol., 4th ed., W. H. Freeman, New York (2000): pp. 1–12.

[85] G. Vogt, S. Woell, and P. Argos, J. Mol. Biol. **269**, 631–643 (1997): *Protein thermal stability, hydrogen bonds, and ion pairs*.

[86] J.N. Israelachvili, 3rd ed. Academic Press, (2011): *Intermolecular and surface forces*.

[87] K. Timberlake, and M. Orgill, 12th ed. Pearson, Harlow, UK (2017): *Chemistry: an introduction to general, organic, and biological*.

[88] C. Tanford, J. Am. Chem. Soc. **84**, 4240–4247 (1962): *Contribution of hydrophobic interactions to the stability of the globular conformation of proteins*.

[89] J.N. Israelachvili, Strong intermolecular forces: Covalent and coulomb interactions, in: Intermol. Surf. Forces, 3rd ed., Academic Press, (2011): pp. 53–70.

[90] A. Blanco, and G. Blanco, Proteins, in: Med. Biochem., 1st ed., Academic Press, (2017): pp. 21–71.

[91] A. Tkatchenko, M. Rossi, V. Blum, J. Ireta, and M. Scheffler, Phys. Rev. Lett. **106**, 118102 (2011): *Unraveling the stability of polypeptide helices: critical role of van der Waals interactions*.

[92] E.C. Donaldson, and W. Alam, Surface forces, in: Wettability, 1st ed., Gulf Publishing Company, Houston (2008): pp. 57–119.

[93] E. Dil, and T. Yumak, Phys. Scr. **94**, 085002 (2019): *On the entropic nature of unified interactions*.

[94] I.N. Berezovsky, W.W. Chen, P.J. Choi, and E.I. Shakhnovich, PLoS Comput. Biol. **1**, e47 (2005): *Entropic stabilization of proteins and its proteomic consequences*.

[95] A.J. Doig, and M.J.E. Sternberg, Protein Sci. **4**, 2247–2251 (1995): *Side-chain conformational entropy in protein folding*.

[96] S.R. Tzeng, and C.G. Kalodimos, Nature. **488**, 236–240 (2012): *Protein activity regulation by conformational entropy*.

[97] R.R. Knowles, and E.N. Jacobsen, Proc. Natl. Acad. Sci. U.S.A. **107**, 20678–20685 (2010): *Attractive noncovalent interactions in asymmetric catalysis: Links between enzymes and small molecule catalysts*.

[98] B.W. Ninham, Adv. Colloid Interface Sci. **83**, 1–17 (1999): *On progress in forces since the DLVO theory*.

[99] D. Horinek, DLVO theory, in: G. Kreysa, K. Ota, R.F. Savinell (Eds.), Encycl. Appl. Electrochem., 1st ed., Springer New York, (2014): pp. 343–346.

[100] W.G. McMillan Jr., and J.E. Mayer, J. Chem. Phys. **13**, 276–305 (1945): *The statistical thermodynamics of multicomponent systems*.

[101] B. Guo, S. Kao, H. McDonald, A. Asanov, L.L. Combs, and W.W. Wilson, J. Cryst. Growth. **196**, 424–433 (1999): *Correlation of second virial coefficients and solubilities useful in protein crystal growth*.

[102] R.A. Curtis, and L. Lue, Chem. Eng. Sci. **61**, 907–923 (2006): *A molecular approach to bioseparations: protein-protein and protein-salt interactions*.

[103] F. Platten, J. Hansen, D. Wagner, and S.U. Egelhaaf, J. Phys. Chem. Lett. **7**, 4008–4014 (2016): *Second virial coefficient as determined from protein phase behavior*.

[104] T.H. Zhang, and X.Y. Liu, Chem. Soc. Rev. **43**, 2324–2347 (2014): *Experimental modelling of single-particle dynamic processes in crystallization by controlled colloidal assembly*.

[105] J.B. Rowe, R.A. Cancel, T.D. Evangelous, R.P. Flynn, S. Pechenov, J.A. Subramony, J. Zhang, and Y. Wang, Biophys. J. **113**, 1750–1756 (2017): *Metastability gap in the phase diagram of monoclonal IgG antibody*.

[106] G. Foffi, G.D. McCullagh, A. Lawlor, E. Zaccarelli, K.A. Dawson, F. Sciortino, P. Tartaglia, D. Pini, and G. Stell, Phys. Rev. E. **65**, 031407 (2002): *Phase equilibria and glass transition in colloidal systems with short-ranged attractive interactions: Application to protein crystallization*.

[107] S. Alberti, and D. Dormann, Annu. Rev. Genet. **53**, 171–194 (2019): *Liquid-liquid phase separation in disease*.

[108] F. Cardinaux, T. Gibaud, A. Stradner, and P. Schurtenberger, Phys. Rev. Lett. **99**, 118301 (2007): *Interplay between spinodal decomposition and glass formation in proteins exhibiting short-range attractions*.

[109] T. Gibaud, and P. Schurtenberger, J. Phys. Condens. Matter. **21**, 322201 (2009): *A closer look at arrested spinodal decomposition in protein solutions*.

[110] S. Bucciarelli, L. Casal-Dujat, C. De Michele, F. Sciortino, J. Dhont, J. Bergenholtz, B. Farago, P. Schurtenberger, and A. Stradner, J. Phys. Chem. Lett. **6**, 4470–4474 (2015): *Unusual dynamics of concentration cluctuations in solutions of weakly attractive globular proteins*.

[111] P.J. Lu, E. Zaccarelli, F. Ciulla, A.B. Schofield, F. Sciortino, and D.A. Weitz, Nature. **453**, 499–503 (2008): *Gelation of particles with short-range attraction*.

[112] P.G. Vekilov, Cryst. Growth Des. **4**, 671–685 (2004): *Dense liquid precursor for the nucleation of ordered solid phases from solution*.

[113] C. Haas, and J. Drenth, J. Cryst. Growth. **196**, 388–394 (1999): *Understanding protein crystallization on the basis of the phase diagram*.

[114] J. Wedekind, L. Xu, S. V Buldyrev, H.E. Stanley, D. Reguera, and G. Franzese, Sci. Rep. **5**, 11260 (2015): *Optimization of crystal nucleation close to a metastable fluid-fluid phase transition*.

[115] P.R. ten Wolde, and D. Frenkel, Science. **277**, 1975–1978 (1997): *Enhancement of protein crystal nucleation by critical density fluctuations*.

[116] M. Sleutel, J. Lutsko, A.E.S. Van Driessche, M.A. Durán-Olivencia, and D. Maes, Nat. Commun. **5**, 1–8 (2014): *Observing classical nucleation theory at work by monitoring phase transitions with molecular precision*.

[117] M. Sleutel, and A.E.S. Van Driessche, Proc. Natl. Acad. Sci. U.S.A. **111**, E546–E553 (2014): *Role of clusters in nonclassical nucleation and growth of protein crystals*.

[118] F. Zhang, J. Phys. Condens. Matter. **29**, 443002 (2017): *Nonclassical nucleation pathways in protein crystallization*.

[119] A. McPherson, Methods. **34**, 254–265 (2004): *Introduction to protein crystallization*.

[120] M. Sleutel, Vrije Universiteit Brussel (Belgium), Dissertation (2008): *Growth kinetics and mass transport phenomena during protein crystallization*.

[121] M. Herz, and P. Knabner, ArXiv. 1605.08602 (2016): *Modeling and simulation of coagulation according to DLVO-theory in a continuum model for electrolyte solutions*.

[122] P.M. Tessier, S.D. Vandrey, B.W. Berger, R. Pazhianur, S.I. Sandler, and A.M. Lenhoff, Acta Crystallogr. Sect. D. **58**, 1531–1535 (2002): *Self-interaction chromatography: A novel screening method for rational protein crystallization*.

[123] V.L. Vilker, C.K. Colton, and K.A. Smith, J. Colloid Interface Sci. **79**, 548–566 (1981): *The osmotic pressure of concentrated protein solutions: Effect of concentration and pH in saline solutions of bovine serum albumin*.

[124] R. Glaser, 2nd ed. Springer-Verlag Berlin Heidelberg, (2012): *Biophysics: An introduction*.

[125] R.A. Curtis, J.M. Prausnitz, and H.W. Blanch, Biotechnol. Bioeng. **57**, 11–21 (1998): *Protein-protein and protein-salt interactions in aqueous protein solutions containing concentrated electrolytes*.

[126] F. Hofmeister, Arch. Für Exp. Pathol. Und Pharmakologie. **25**, 1–30 (1888): *Zur Lehre von der Wirkung der Salze*.

[127] Y. Zhang, and P.S. Cremer, Curr. Opin. Chem. Biol. **10**, 658–663 (2006): *Interactions between macromolecules and ions: the Hofmeister series*.

[128] L.A. Moreira, M. Boström, B.W. Ninham, E.C. Biscaia, and F.W. Tavares, Colloid. Surf. A . **282–283**, 457–463 (2006): *Hofmeister effects: Why protein charge, pH titration and protein precipitation depend on the choice of background salt solution*.

[129] M. Lund, Colloids Surf. B. **137**, 17–21 (2016): *Anisotropic protein-protein interactions due to ion binding*.

[130] J. Zhang, Protein-protein interactions in salt solutions, in: W. Cai, H. Hong (Eds.), Protein-Protein Interact. - Comput. Exp. Tools, 1st ed., InTech, Rijeka, Croatia (2012): pp. 359–376.

[131] Y.R. Dahal, and J.D. Schmit, Biophys. J. **114**, 76–87 (2018): *Ion specificity and nonmonotonic protein solubility from salt entropy*.

[132] V. Mazzini, and V.S.J. Craig, Chem. Sci. **8**, 7052–7065 (2017): *What is the fundamental ion-specific series for anions and cations? Ion specificity in standard partial molar volumes of electrolytes and electrostriction in water and non-aqueous solvents*.

[133] K.D. Collins, and M.W. Washabaugh, Q. Rev. Biophys. **18**, 323–422 (1985): *The Hofmeister effect and the behaviour of water at interfaces*.

[134] M.G. Cacace, E.M. Landau, and J.J. Ramsden, Q. Rev. Biophys. **30**, 241–277 (1997): *The Hofmeister series: Salt and solvent effects on interfacial phenomena*.

[135] K.D. Collins, Methods. **34**, 300–311 (2004): *Ions from the Hofmeister series and osmolytes: Effects on proteins in solution and in the crystallization process*.

[136] J. Lyklema, Chem. Phys. Lett. **467**, 217–222 (2009): *Simple Hofmeister series*.

[137] N. Schwierz, D. Horinek, U. Sivan, and R.R. Netz, Curr. Opin. Colloid Interface Sci. **23**, 10–18 (2016): *Reversed Hofmeister series—the rule rather than the exception*.

[138] N. Schwierz, D. Horinek, and R.R. Netz, Langmuir. **26**, 7370–7379 (2010): *Reversed anionic Hofmeister series: the interplay of surface charge and surface polarity*.

[139] I. Fridovich, J. Biol. Chem. **238**, 592–598 (1963): *Inhibition of acetoacetic decarboxylase by anions. The Hofmeister lyotropic series*.

[140] S. Damodaran, Int. J. Biol. Macromol. **11**, 2–8 (1989): *Influence of protein conformation on its adaptability under chaotropic conditions*.

[141] J.E. Norne, S.G. Hjalmarsson, B. Lindman, and M. Zeppezauer, Biochemistry. **14**, 3401–3408 (1975): *Anion binding properties of human serum albumin from halide ion quadrupole relaxation*.

[142] M. McSwiney, H. Singh, and O.H. Campanella, Top. Catal. **8**, 441–453 (1994): *Thermal aggregation and gelation of bovine β-lactoglobulin*.

[143] K. Ako, T. Nicolai, D. Durand, and G. Brotons, Soft Matter. **5**, 4033–4041 (2009): *Micro-phase separation explains the abrupt structural change of denatured globular protein gels on varying the ionic strength or the pH*.

[144] S.P.F.M. Roefs, and H.A. Peppelman, Aggregation and gelation of whey proteins: Specific effect of divalent cations?, in: E. Dickinson, R. Miller (Eds.), Food Colloids Fundam. Formul., Royal Society of Chemistry, Cambridge, UK (2007): pp. 358–368.

[145] K.R. Kuhn, Â.L.F. Cavallieri, and R.L. da Cunha, Int. J. Food Sci. Technol. **45**, 348–357 (2010): *Cold-set whey protein gels induced by calcium or sodium salt addition*.

[146] H. Zhang, Z. Zhu, Y. Wang, Z. Fei, and J. Cao, Appl. Surf. Sci. **427**, 1019–1029 (2018): *Changing the activities and structures of bovine serum albumin bound to graphene oxide*.

[147] A. Sauter, F. Roosen-Runge, F. Zhang, G. Lotze, R.M.J. Jacobs, and F. Schreiber, J. Am. Chem. Soc. **137**, 1485–1491 (2015): *Real-time observation of nonclassical protein crystallization kinetics*.

[148] F. Zhang, G. Zocher, A. Sauter, T. Stehle, and F. Schreiber, J. Appl. Crystallogr. **44**, 755–762 (2011): *Novel approach to controlled protein crystallization through ligandation of yttrium cations*.

[149] F. Zhang, F. Roosen-Runge, A. Sauter, R. Roth, M.W.A. Skoda, R.M.J. Jacobs, M. Sztucki, and F. Schreiber, Faraday Discuss. **159**, 313–325 (2012): *The role of cluster formation and metastable liquid-liquid phase separation in protein crystallization*.

[150] F. Zhang, S. Weggler, M.J. Ziller, L. Ianeselli, B.S. Heck, A. Hildebrandt, O. Kohlbacher, M.W.A. Skoda, R.M.J. Jacobs, and F. Schreiber, Proteins. **78**, 3450–3457 (2010): *Universality of protein reentrant condensation in solution induced by multivalent metal ions*.

[151] L. Ianeselli, F. Zhang, M.W.A. Skoda, R.M.J. Jacobs, R.A. Martin, S. Callow, S. Prévost, and F. Schreiber, J. Phys. Chem. B. **114**, 3776–3783 (2010): *Protein-protein interactions in ovalbumin solutions studied by small-angle scattering: Effect of ionic strength and the chemical nature of cations*.

[152] M.K. Braun, A. Sauter, O. Matsarskaia, M. Wolf, F. Roosen-Runge, M. Sztucki, R. Roth, F. Zhang, and F. Schreiber, J. Phys. Chem. B. **122**, 11978–11985 (2018): *Reentrant phase behavior in protein solutions induced by multivalent salts: strong effect of anions Cl^- versus NO_3^-*.

[153] T. Narayanan, H. Wacklin, O. Konovalov, and R. Lund, Crystallogr. Rev. **23**, 160–226 (2017): *Recent applications of synchrotron radiation and neutrons in the study of soft matter*.

[154] M.K. Braun, M. Wolf, O. Matsarskaia, S. Da Vela, F. Roosen-Runge, M. Sztucki, R. Roth, F. Zhang, and F. Schreiber, J. Phys. Chem. B. **121**, 1731–1739 (2017): *Strong isotope effects on effective interactions and phase behavior in protein solutions in the presence of multivalent ions*.

[155] O. Matsarskaia, M.K. Braun, F. Roosen-Runge, M. Wolf, F. Zhang, R. Roth, and F. Schreiber, J. Phys. Chem. B. **120**, 7731–7736 (2016): *Cation-induced hydration effects cause lower critical solution temperature behavior in protein solutions*.

[156] O. Matsarskaia, F. Roosen-Runge, and F. Schreiber, ChemPhysChem. **21**, 1–27 (2020): *Multivalent ions and biomolecules: attempting a comprehensive perspective*.

[157] E.Y. Bormashenko, 2nd ed. De Gruyter, (2018): *Wetting of Real Surfaces*.

[158] P.-G. de Gennes, F. Brochard-Wyart, and D. Quéré, Springer-Verlag New York, (2004): *Capillarity and wetting phenomena*.

[159] A.J. Kinloch, 1st ed. Springer, Dodrecht, Netherlands (1987): *Adhesion and adhesives: Science and technology*.

[160] S.A. Mirji, Surf. Interface Anal. **38**, 158–165 (2006): *Octadecyltrichlorosilane adsorption kinetics on Si(100)/SiO_2 surface: contact angle, AFM, FTIR and XPS analysis*.

[161] A.J. Kinloch, J. Mater. Sci. **15**, 2141–2166 (1980): *The science of adhesion - part 1: surface and interfacial aspects*.

[162] D. Bonn, J. Eggers, J. Indekeu, J. Meunier, and E. Rolley, Rev. Mod. Phys. **81**, 739–805 (2009): *Wetting and spreading*.

[163] B.D. Ratner, and S.J. Bryant, Annu. Rev. Biomed. Eng. **6**, 41–75 (2004): *Biomaterials: Where we have been and where we are going*.

[164] D. Rana, and T. Matsuura, Chem. Rev. **110**, 2448–2471 (2010): *Surface modifications for antifouling membranes*.

[165] F. Rupp, L. Liang, J. Geis-Gerstorfer, L. Scheideler, and F. Hüttig, Dent. Mater. **34**, 40–57 (2018): *Surface characteristics of dental implants: a review*.

[166] S. Dietrich, and M. Schick, Phys. Rev. B. **31**, 4718–4720 (1985): *Critical wetting of surfaces in systems with long-range forces*.

[167] C.A. Haynes, and W. Norde, Colloids Surf. B. **2**, 517–566 (1994): *Globular proteins at solid/liquid interfaces*.

[168] P. Ying, G. Jin, and Z. Tao, Colloids Surf. B. **33**, 259–263 (2004): *Competitive adsorption of collagen and bovine serum albumin - effect of the surface wettability*.

[169] Y. Arima, and H. Iwata, Biomaterials. **28**, 3074–3082 (2007): *Effect of wettability and surface functional groups on protein adsorption and cell adhesion using well-defined mixed self-assembled monolayers*.

[170] J.H. Lee, and H.B. Lee, J. Biomed. Mater. Res. **41**, 304–311 (1998): *Platelet adhesion onto wettability gradient surfaces in the absence and presence of plasma proteins*.

[171] M. Miyamoto, S. Sasakawa, T. Ozawa, H. Kawaguchi, and Y. Ohtsuka, Biomaterials. **11**, 385–388 (1990): *Mechanisms of blood coagulation induced by latex particles and the roles of blood cells*.

[172] S. Sagnella, and K. Mai-Ngam, Colloids Surf. B. **42**, 147–155 (2005): *Chitosan based surfactant polymers designed to improve blood compatibility on biomaterials*.

[173] D.K. Han, S.Y. Jeong, Y.H. Kim, B.G. Min, and H.I. Cho, J. Biomed. Mater. Res. **25**, 561–575 (1991): *Negative cilia concept for thromboresistance: synergistic effect of PEO and sulfonate groups grafted onto polyurethanes*.

[174] J.H. Lee, Y.M. Ju, W.K. Lee, K.D. Park, and Y.H. Kim, J. Biomed. Mater. Res. **40**, 314–323 (1998): *Platelet adhesion onto segmented polyurethane surfaces modified by PEO- and sulfonated PEO-containing block copolymer additives*.

[175] G.B. Sigal, M. Mrksich, and G.M. Whitesides, J. Am. Chem. Soc. **120**, 3464–3473 (1998): *Effect of surface wettability on the adsorption of proteins and detergents*.

[176] M.M. Ouberai, K. Xu, and M.E. Welland, Biomaterials. **35**, 6157–6163 (2014): *Effect of the interplay between protein and surface on the properties of adsorbed protein layers*.

[177] S.J. Attwood, R. Kershaw, S. Uddin, S.M. Bishop, and M.E. Welland, J. Mater. Chem. B. **7**, 2349–2361 (2019): *Understanding how charge and hydrophobicity influence globular protein adsorption to alkanethiol and material surfaces*.

[178] Y.F. Yano, J. Phys. Condens. Matter. **24**, 503101 (2012): *Kinetics of protein unfolding at interfaces*.

[179] S.L. Hirsh, D.R. McKenzie, N.J. Nosworthy, J.A. Denman, O.U. Sezerman, and M.M.M. Bilek, Colloids Surf. B. **103**, 395–404 (2013): *The Vroman effect: competitive protein exchange with dynamic multilayer protein aggregates*.

[180] M. Rabe, Universität Zürich (Switzerland), Dissertation (2009): *Understanding protein adsorption phenomena on solid surfaces*.

[181] F. Zhang, R. Roth, M. Wolf, F. Roosen-Runge, M.W.A. Skoda, R.M.J. Jacobs, M. Stzucki, and F. Schreiber, Soft Matter. **8**, 1313–1316 (2012): *Charge-controlled metastable liquid-liquid phase separation in protein solutions as a universal pathway towards crystallization*.

[182] S. Da Vela, C. Exner, R.S. Schäufele, J. Möller, Z. Fu, F. Zhang, and F. Schreiber, Soft Matter. **13**, 8756–8765 (2017): *Arrested and temporarily arrested states in a protein-polymer mixture studied by USAXS and VSANS*.

[183] N. Begam, O. Matsarskaia, M. Sztucki, F. Zhang, and F. Schreiber, Soft Matter. **16**, 2128–2134 (2020): *Unification of lower and upper critical solution temperature phase behavior of globular protein solutions in the presence of multivalent cations*.

[184] K.M. Poluri, and K. Gulati, World of proteins: Structure-function relationships and engineering techniques, in: Protein Eng. Tech., 1st ed., Springer, Singapore (2017): pp. 1–25.

[185] J.A. Seo, A. Hédoux, Y. Guinet, L. Paccou, F. Affouard, A. Lerbret, and M. Descamps, J. Phys. Chem. B. **114**, 6675–6684 (2010): *Thermal denaturation of beta-lactoglobulin and stabilization mechanism by trehalose analyzed from Raman spectroscopy investigations*.

[186] B.T. O'Kennedy, and J.S. Mounsey, Int. Dairy J. **19**, 123–128 (2009): *The dominating effect of ionic strength on the heat-induced denaturation and aggregation of β-lactoglobulin in simulated milk ultrafiltrate*.

[187] C.E. Giacomelli, and W. Norde, J. Colloid Interface Sci. **233**, 234–240 (2001): *The adsorption-desorption cycle. Reversibility of the BSA-silica system*.

[188] C. Tanford, Protein Denaturation, in: C.B. Anfinsen Jr., M.L. Anson, J.T. Edsall, F.M. Richards (Eds.), Adv. Protein Chem., Academic Press, (1968): pp. 121–282.

[189] G. Hummer, S. Garde, A.E. García, M.E. Paulaitis, and L.R. Pratt, Proc. Natl. Acad. Sci. U.S.A. **95**, 1552–1555 (1998): *The pressure dependence of hydrophobic interactions is consistent with the observed pressure denaturation of proteins*.

[190] D.E. Graham, and M.C. Phillips, J. Colloid Interface Sci. **70**, 403–414 (1979): *Proteins at liquid interfaces. I. Kinetics of adsorption and surface denaturation*.

[191] I. Kiesel, M. Paulus, J. Nase, S. Tiemeyer, C. Sternemann, K. Rüster, F.J. Wirkert, K. Mende, T. Büning, and M. Tolan, Langmuir. **30**, 2077–2083 (2014): *Temperature-driven adsorption and desorption of proteins at solid-liquid interfaces*.

[192] K. Das, S. Kundu, S. Mehan, and V.K. Aswal, Chem. Phys. Lett. **645**, 127–132 (2016): *Modified interactions among globular proteins below isoelectric point in the presence of mono-, di- and tri-valent ions: a small angle neutron scattering study*.

[193] J.F. Foster, Some aspects of the structure and conformational properties of serum albumin, in: V.M. Rosenoer, M. Oratz, M.A. Rothschild (Eds.), Albumin Struct. Funct. Uses, Pergamon Press Inc., (1977): pp. 53–84.

[194] R.D. Waniska, and J.E. Kinsella, J. Agric. Food Chem. **33**, 1143–1148 (1985): *Surface properties of β-lactoglobulin: Adsorption and rearrangement during film formation*.

[195] U.M. Elofsson, M.A. Paulsson, and T. Arnebrant, Langmuir. **13**, 1695–1700 (1997): *Adsorption of β-lactoglobulin A and B in relation to self-association: Effect of concentration and pH*.

[196] S.M. Acuña-Nelson, J.M. Bastías-Montes, F.R. Cerda-Leal, J.E. Parra-Flores, J.S. Aguirre-García, and P.G. Toledo, J. Nanomater. **2020**, 1–11 (2020): *Nanocoatings of bovine serum albumin on glass: Effects of pH and temperature*.

[197] B.E. Givens, Z. Xu, J. Fiegel, and V.H. Grassian, J. Colloid Interface Sci. **493**, 334–341 (2017): *Bovine serum albumin adsorption on SiO_2 and TiO_2 nanoparticle surfaces at circumneutral and acidic pH: a tale of two nano-bio surface interactions*.

[198] J. Koo, M. Erlkamp, S. Grobelny, R. Steitz, and C. Czeslik, Langmuir. **29**, 8025–8030 (2013): *Pressure-induced protein adsorption at aqueous-solid interfaces*.

[199] P. Szabelski, A. Cavazzini, K. Kaczmarski, X. Liu, J. Van Horn, and G. Guiochon, J. Chromatogr. A. **950**, 41–53 (2002): *Experimental studies of pressure/temperature dependence of protein adsorption equilibrium in reversed-phase high-performance liquid chromatography*.

[200] Y. Ikeuchi, K. Nakagawa, T. Endo, A. Suzuki, T. Hayashi, and T. Ito, J. Agric. Food Chem. **49**, 4052–4059 (2001): *Pressure-induced denaturation of monomer β-lactoglobulin is partially irreversible: Comparison of monomer form (highly acidic pH) with dimer form (neutral pH)*.

[201] I. Hayakawa, J. Kajihara, K. Morikawa, M. Oda, and Y. Fujio, J. Food Sci. **57**, 288–292 (1992): *Denaturation of bovine serum albumin (BSA) and ovalbumin by high pressure, heat and chemicals*.

[202] I. Hayakawa, Y.Y. Linko, and P. Linko, LWT - Food Sci. Technol. **29**, 756–762 (1996): *Mechanism of high pressure denaturation of proteins*.

[203] S. Da Vela, N. Begam, D. Dyachok, R.S. Schäufele, O. Matsarskaia, M.K. Braun, A. Girelli, A. Ragulskaya, A. Mariani, F. Zhang, and F. Schreiber, J. Phys. Chem. Lett. **11**, 7273–7278 (2020): *Interplay between glass formation and liquid–liquid phase separation revealed by the scattering invariant*.

[204] S. Kmiecik, D. Gront, M. Kolinski, L. Wieteska, A.E. Dawid, and A. Kolinski, Chem. Rev. **116**, 7898–7936 (2016): *Coarse-grained protein models and their applications*.

[205] J.M. Tavares, C.S. Dias, N.A.M. Araújo, and M.M. Telo Da Gama, J. Phys. Chem. B. **122**, 3514–3518 (2018): *Dynamics of patchy particles in and out of equilibrium*.

[206] E. Bianchi, J. Largo, P. Tartaglia, E. Zaccarelli, and F. Sciortino, Phys. Rev. Lett. **97**, 168301 (2006): *Phase diagram of patchy colloids: towards empty liquids*.

[207] E. Bianchi, B. Capone, I. Coluzza, L. Rovigatti, and P.D.J. Van Oostrum, Phys. Chem. Chem. Phys. **19**, 19847–19868 (2017): *Limiting the valence: Advancements and new perspectives on patchy colloids, soft functionalized nanoparticles and biomolecules*.

[208] A.B. Pawar, and I. Kretzschmar, Macromol. Rapid Commun. **31**, 150–168 (2010): *Fabrication, assembly, and application of patchy particles*.

[209] F. Roosen-Runge, F. Zhang, F. Schreiber, and R. Roth, Sci. Rep. **4**, 7016 (2014): *Ion-activated attractive patches as a mechanism for controlled protein interactions*.

[210] E. Runge, and E.K.U. Gross, Phys. Rev. Lett. **52**, 997–1000 (1984): *Density-functional theory for time-dependent systems*.

[211] R.A. Latour, J. Biomed. Mater. Res. A. **103**, 949–958 (2015): *The Langmuir isotherm: A commonly applied but misleading approach for the analysis of protein adsorption behavior*.

[212] S. Alaeddine, H. Andreasson, M. Larsson, and H. Nygren, Biophys. Chem. **54**, 211–218 (1995): *Discontinuous formation and desorption of clusters during particles adsorption at surfaces*.

[213] M. Wahlgren, and U. Elofsson, J. Colloid Interface Sci. **188**, 121–129 (1997): *Simple models for adsorption kinetics and their correlation to the adsorption of β-lactoglobulin A and B*.

[214] Z. Adamczyk, J. Colloid Interface Sci. **229**, 477–489 (2000): *Kinetics of diffusion-controlled adsorption of colloid particles and proteins*.

[215] M. Rabe, D. Verdes, J. Zimmermann, and S. Seeger, J. Phys. Chem. B. **112**, 13971–13980 (2008): *Surface organization and cooperativity during nonspecific protein adsorption events*.

[216] Y. Rosenfeld, Phys. Rev. Lett. **63**, 980 (1989): *Free-energy model for the inhomogeneous hard-sphere fluid mixture and density-functional theory of freezing*.

[217] R. Evans, Adv. Phys. **28**, 143–200 (1979): *The nature of liquid-vapour interface and other topics in the statistical mechanics of non-uniform, classical fluids*.

[218] E. Paquet, and H.L. Viktor, Biomed Res. Int. **2015**, 18 (2015): *Molecular dynamics, Monte Carlo simulations, and Langevin dynamics: A computational review*.

[219] A.I. Abrikosov, B. Stenqvist, and M. Lund, Soft Matter. **13**, 4591–4597 (2017): *Steering patchy particles using multivalent electrolytes*.

[220] M. Ozboyaci, D.B. Kokh, S. Corni, and R.C. Wade, Q. Rev. Biophys. **49**, e4 (2016): *Modeling and simulation of protein–surface interactions: achievements and challenges*.

[221] H.J.C. Berendsen, Molecular dynamics simulations: the limits and beyond, in: P. Deuflhard, J. Hermans, B. Leimkuhler, A.E. Mark, S. Reich, R.D. Skeel (Eds.), Comput. Mol. Dyn. Challenges, Methods, Ideas, 1st ed., Springer, Berlin Heidelberg (1999): pp. 3–36.

[222] K. Baler, O.A. Martin, M.A. Carignano, G.A. Ameer, J.A. Vila, and I. Szleifer, J. Phys. Chem. B. **118**, 921–930 (2014): *Electrostatic unfolding and interactions of albumin driven by pH changes: a molecular dynamics study*.

[223] B.A. Russell, B. Jachimska, I. Kralka, P.A. Mulheran, and Y. Chen, J. Mater. Chem. B. **4**, 6876–6882 (2016): *Human serum albumin encapsulated gold nanoclusters: Effects of cluster synthesis on natural protein characteristics*.

[224] K. Kubiak-Ossowska, B. Jachimska, and P.A. Mulheran, J. Phys. Chem. B. **120**, 10463–10468 (2016): *How negatively charged proteins adsorb to negatively charged surfaces: A molecular dynamics study of BSA adsorption on silica*.

[225] K. Kubiak-Ossowska, K. Tokarczyk, B. Jachimska, and P.A. Mulheran, J. Phys. Chem. B. **121**, 3975–3986 (2017): *Bovine serum albumin adsorption at a silica surface explored by simulation and experiment*.

[226] K. Kubiak-Ossowska, B. Jachimska, M. Al Qaraghuli, and P.A. Mulheran, Curr. Opin. Colloid Interface Sci. **41**, 104–117 (2019): *Protein interactions with negatively charged inorganic surfaces*.

[227] V.N. Uversky, Biotechnol. J. **10**, 356–366 (2015): *Proteins without unique 3D structures: biotechnological applications of intrinsically unstable/disordered proteins*.

[228] A. Andreeva, D. Howorth, C. Chothia, E. Kulesha, and A.G. Murzin, Nucleic Acid Res. **42**, D310–D314 (2014): *SCOP2 prototype: a new approach to protein structure mining*.

[229] M.M. Gromiha, and S. Selvaraj, Prog. Biophys. Mol. Biol. **86**, 235–277 (2004): *Inter-residue interactions in protein folding and stability*.

[230] A.D. Michie, C.A. Orengo, and J.M. Thornton, J. Mol. Biol. **262**, 168–185 (1996): *Analysis of domain structural class using an automated class assignment protocol*.

[231] J. Figge, T.H. Rossing, and V. Fencl, J. Lab. Clin. Med. **117**, 453–467 (1991): *The role of serum proteins in acid-base equilibria*.

[232] K.A. Majorek, P.J. Porebski, A. Dayal, M.D. Zimmerman, K. Jablonska, A.J. Stewart, M. Chruszcz, and W. Minor, Mol. Immunol. **52**, 174–182 (2012): *Structural and immunologic characterization of bovine, horse, and rabbit serum albumins*.

[233] S. Le Maux, S. Bouhallab, L. Giblin, A. Brodkorb, and T. Croguennec, Dairy Sci. Technol. **94**, 409–426 (2014): *Bovine β-lactoglobulin/fatty acid complexes: binding, structural, and biological properties*.

[234] A. Bujacz, Acta Crystallogr. Sect. D. **68**, 1278–1289 (2012): *Structures of bovine, equine and leporine serum albumin*.

[235] S. Brownlow, J.H. Morais Cabral, R. Cooper, D.R. Flower, S.J. Yewdall, I. Polikarpov, A.C.T. North, and L. Sawyer, Structure. **5**, 481–495 (1997): *Bovine β-lactoglobulin at 1.8 Å resolution - still an enigmatic lipocalin*.

[236] M.K. Braun, M. Grimaldo, F. Roosen-Runge, I. Hoffmann, O. Czakkel, M. Sztucki, F. Zhang, F. Schreiber, and T. Seydel, J. Phys. Chem. Lett. **8**, 2590–2596 (2017): *Crowding-controlled cluster size in concentrated aqueous protein solutions: Structure, self- and collective diffusion*.

[237] I.M. Klotz, and J.M. Urquhart, J. Am. Chem. Soc. **71**, 1597–1603 (1949): *The binding of organic ions by proteins. Comparison of native and of modified proteins*.

[238] L. Pérez-Fuentes, C. Drummond, J. Faraudo, and D. Bastos-González, Soft Matter. **13**, 1120–1131 (2017): *Interaction of organic ions with proteins*.

[239] B. Jachimska, S. Świątek, J.I. Loch, K. Lewiński, and T. Luxbacher, Bioelectrochemistry. **121**, 95–104 (2018): *Adsorption effectiveness of β-lactoglobulin onto gold surface determined by quartz crystal microbalance*.

[240] G. Yohannes, S.K. Wiedmer, M. Elomaa, M. Jussila, V. Aseyev, and M.L. Riekkola, Anal. Chim. Acta. **675**, 191–198 (2010): *Thermal aggregation of bovine serum albumin studied by asymmetrical flow field-flow fractionation*.

[241] F. Zhang, M.W.A. Skoda, R.M.J. Jacobs, R.A. Martin, C.M. Martin, and F. Schreiber, J. Phys. Chem. B. **111**, 251–259 (2007): *Protein interactions studied by SAXS: Effect of ionic strength and protein concentration for BSA in aqueous solutions*.

[242] L. Pérez-Fuentes, C. Drummond, J. Faraudo, and D. Bastos-González, Materials. **10**, 893 (2017): *Adsorption of milk proteins (β-casein and β-lactoglobulin) and BSA onto hydrophobic surfaces*.

[243] H.A. Sober, 2nd ed. CRC Press, Cleveland (1970): *Handbook of biochemistry. Selected data for molecular biology*.

[244] S. Ngarize, H. Herman, A. Adams, and N. Howell, J. Agric. Food Chem. **52**, 6470–6477 (2004): *Comparison of changes in the secondary structure of unheated, heated, and high-pressure-treated β-lactoglobulin and ovalbumin proteins using Fourier transform Raman spectroscopy and self-deconvolution*.

[245] T. Maruyama, S. Katoh, M. Nakajima, H. Nabetani, T.P. Abbott, A. Shono, and K. Satoh, J. Memb. Sci. **192**, 201–207 (2001): *FT-IR analysis of BSA fouled on ultrafiltration and microfiltration membranes*.

[246] M.D. Pérez, and M. Calvo, J. Dairy Sci. **78**, 978–988 (1995): *Interaction of β-lactoglobulin with retinol and fatty acids and its role as a possible biological function for this protein: a review*.

[247] Q. Wang, J.C. Allen, and H.E. Swaisgood, J. Dairy Sci. **80**, 1054–1059 (1997): *Binding of vitamin D and cholesterol to β-lactoglobulin*.

[248] X.H. Zhang, X.D. Zhang, S.T. Lou, Z.X. Zhang, J.L. Sun, and J. Hu, Langmuir. **20**, 3813–3815 (2004): *Degassing and temperature effects on the formation of nanobubbles at the mica/water interface*.

[249] J.M. Mirtallo, K. Caryer, P.J. Schneider, L. Ayers, and P.J. Fabri, Am. J. Hosp. Pharm. **38**, 1907–1910 (1981): *Growth of bacteria and fungi in parenteral nutrition solutions containing albumin*.

[250] Y. Marcus, Langmuir. **29**, 2881–2888 (2013): *Individual ionic surface tension increments in aqueous solutions*.

[251] Y. Marcus, John Wiley & Sons, Inc, Hoboken, USA (2015): *Ions in solution and their solvation*.

[252] R.D. Shannon, Acta Crystallogr. Sect. A. **32**, 751–767 (1976): *Revised effective ionic radii and systematic studies of interatomic distances in halides and chalcogenides*.

[253] J.K. Nagle, J. Am. Chem. Soc. **112**, 4741–4747 (1990): *Atomic polarizability and electronegativity*.

[254] Y. Marcus, J. Solution Chem. **23**, 831–848 (1994): *Viscosity B-coefficients, structural entropies and heat capacities, and the effects of ions on the structure of water*.

[255] Y. Marcus, Chem. Rev. **109**, 1346–1370 (2009): *Effect of ions on the structure of water: Structure making and breaking*.

[256] C.W. Carr, Arch. Biochem. Biophys. **40**, 286–294 (1952): *Studies on the binding of small ions in protein solutions with the use of membrane electrodes. I. The binding of the chloride ion and other inorganic anions in solutions of serum albumin*.

[257] Y. Marcus, Marcel Dekker Inc., New York, Basel (1997): *Ion properties*.

[258] M. Elias, M. Laranjo, A. Cristina Agulheiro-Santos, and M. Eduarda Potes, The Role of salt on food and human health, in: M. Cengiz, S. Karabulut (Eds.), Salt Earth, 1st ed., InTechOpen, (2020): pp. 19–43.

[259] J.M. Fox, K. Kang, W. Sherman, A. Héroux, G.M. Sastry, M. Baghbanzadeh, M.R. Lockett, and G.M. Whitesides, J. Am. Chem. Soc. **137**, 3859–3866 (2015): *Interactions between Hofmeister anions and the binding pocket of a protein*.

[260] R. Zangi, J. Phys. Chem. B. **114**, 643–650 (2010): *Can salting-in/salting-out ions be classified as chaotropes/kosmotropes?*

[261] A. Tilocca, J. Mater. Chem. **20**, 6848–6858 (2010): *Models of structure, dynamics and reactivity of bioglasses: a review*.

[262] M. Vallet-Regí, J. Chem. Soc. Dalt. Trans. 97–108 (2001): *Ceramics for medical applications*.

[263] L.L. Hench, and Ö. Andersson, Bioactive glasses, in: L.L. Hench, J. Wilson (Eds.), An Introd. to Bioceram., World Scientific, Singapore (1993): pp. 41–62.

[264] S.H. Behrens, and D.G. Grier, J. Chem. Phys. **115**, 6716–6721 (2001): *The charge of glass and silica surfaces*.

[265] R. Williams, and A.M. Goodman, Appl. Phys. Lett. **25**, 531–532 (1974): *Wetting of thin layers of SiO_2 by water*.

[266] J.R. Vig, UV/ozone cleaning of surfaces, in: K.L. Mittal (Ed.), Treatise Clean Surf. Technol., Springer, Boston (1987): pp. 1–26.

[267] F. Cataldo, Polym. Degrad. Stab. **82**, 105–114 (2003): *On the action of ozone on proteins*.

[268] R. Kohli, Applications of UV-ozone cleaning technique for removal of surface contaminants, in: R. Kohli, K.L. Mittal (Eds.), Dev. Surf. Contam. Clean. Appl. Clean. Tech., Elsevier, (2019): pp. 355–390.

[269] S.M. Rossnagel, and J. Hopwood, J. Vac. Sci. Technol. B . **12**, 449–453 (1994): *Metal ion deposition from ionized mangetron sputtering discharge*.

[270] F. Schreiber, J. Phys. Condens. Matter. **16**, R881 (2004): *Self-assembled monolayers: from "simple" model systems to biofunctionalized interfaces*.

[271] F. Rupp, M. Haupt, H. Klostermann, H.-S. Kim, M. Eichler, A. Peetsch, L. Scheideler, C. Doering, C. Oehr, H.P. Wendel, S. Sinn, E. Decker, C. Von Ohle, and J. Geis-Gerstorfer, Acta Biomater. **6**, 4566–4577 (2010): *Multifunctional nature of UV-irradiated nanocrystalline anatase thin films for biomedical applications*.

[272] P. Silva-Bermudez, and S.E. Rodil, Surf. Coatings Technol. **233**, 147–158 (2013): *An overview of protein adsorption on metal oxide coatings for biomedical implants*.

[273] A. Matthews, Am. Mineral. **61**, 419–424 (1976): *The crystallization of anatase and rutile from amorphous titanium dioxide under hydrothermal conditions*.

[274] G. Hass, Vacuum. **2**, 331–345 (1952): *Preparation, properties and optical applications of thin films of titanium dioxide*.

[275] C. Morterra, A. Chiorino, and F. Boccuzzi, Zeitschrift Fur Phys. Chemie. **124**, 211–222 (1981): *A spectroscopic study of anatase properties*.

[276] S. Hosseinpour, F. Tang, F. Wang, R.A. Livingstone, S.J. Schlegel, T. Ohto, M. Bonn, Y. Nagata, and E.H.G. Backus, J. Phys. Chem. Lett. **8**, 2195–2199 (2017): *Chemisorbed and physisorbed water at the TiO_2/water interface*.

[277] T. Smith, J. Colloid Interface Sci. **75**, 51–55 (1980): *The hydrophilic nature of a clean gold surface*.

[278] A.R. Bishop, and R.G. Nuzzo, Curr. Opin. Colloid Interface Sci. **1**, 127–136 (1996): *Self-assembled monolayers: recent developments and applications*.

[279] Y. Yang, A.M. Bittner, S. Baldelli, and K. Kern, Thin Solid Films. **516**, 3948–3956 (2008): *Study of self-assembled triethoxysilane thin films made by casting neat reagents in ambient atmosphere*.

[280] F. Schreiber, Prog. Surf. Sci. **65**, 151–257 (2000): *Structure and growth of self-assembling monolayers*.

[281] R. Colorado, and T.R. Lee, Thiol-based self-assembled monolayers: Formation and organization, in: K.H.J. Buschow, M.C. Flemingsürgen, E.J. Kramer, P. Veyssière, R.W. Cahn, B. Ilschner, S. Mahajan (Eds.), Encycl. Mater. Sci. Technol., Pergamon Press, Oxford, (2001): pp. 9332–9344.

[282] A. Ulman, Chem. Rev. **96**, 1533–1554 (1996): *Formation and structure of self-assembled monolayers*.

[283] E. Delamarche, B. Michel, H.A. Biebuyck, and C. Gerber, Adv. Mater. **8**, 719–729 (1996): *Golden interfaces: The surface of self-assembled monolayers*.

[284] M. Sayin, A. Nefedov, and M. Zharnikov, J. Phys. Chem. C. **122**, 10918–10928 (2018): *Spectroscopic study of water adsorption and desorption on/from oligo(ethylene glycol)-substituted alkanethiolate self-assembled monolayers*.

[285] E. Ostuni, R.G. Chapman, R.E. Holmlin, S. Takayama, and G.M. Whitesides, Langmuir. **17**, 5605–5620 (2001): *A survey of structure-property relationships of surfaces that resist the adsorption of protein*.

[286] M. Sayin, A. Nefedov, and M. Zharnikov, Phys. Chem. Chem. Phys. **22**, 8088–8095 (2020): *Interaction of water with oligo(ethylene glycol) terminated monolayers: Wetting versus hydration*.

[287] S. Herrwerth, W. Eck, S. Reinhardt, and M. Grunze, J. Am. Chem. Soc. **125**, 9359–9366 (2003): *Factors that determine the protein resistance of oligoether self-assembled monolayers– internal hydrophilicity, terminal hydrophilicity, and lateral packing density*.

[288] L.A. Clifton, N. Paracini, A. V. Hughes, J.H. Lakey, N.J. Steinke, J.F.K. Cooper, M. Gavutis, and M.W.A. Skoda, Langmuir. **35**, 13735–13744 (2019): *Self-assembled fluid phase floating membranes with tunable water interlayers*.

[289] S. Onclin, B.J. Ravoo, and D.N. Reinhoudt, Angew. Chem. Int. Ed. **44**, 6282–6304 (2005): *Engineering silicon oxide surfaces using self-assembled monolayers*.

[290] S. Li, Y. Zheng, and C. Chen, J. Chem. Phys. **144**, 244709 (2016): *AFM investigation of effect of absorbed water layer structure on growth mechanism of octadecyltrichlorosilane self-assembled monolayer on oxidized silicon*.

[291] M.-H. Jung, and H.-S. Choi, Korean J. Chem. Eng. **26**, 1778–1784 (2009): *Characterization of octadecyltrichlorosilane self-assembled monolayers on silicon (100) surface*.

[292] Y. Wang, and M. Lieberman, Langmuir. **19**, 1159–1167 (2003): *Growth of ultrasmooth octadecyltrichlorosilane self-assembled monolayers on SiO_2*.

[293] D. Janssen, R. De Palma, S. Verlaak, P. Heremans, and W. Dehaen, Thin Solid Films. **515**, 1433–1438 (2006): *Static solvent contact angle measurements, surface free energy and wettability determination of various self-assembled monolayers on silicon dioxide*.

[294] C. Carraro, O.W. Yauw, M.M. Sung, and R. Maboudian, J. Phys. Chem. B. **102**, 4441–4445 (1998): *Observation of three growth mechanisms in self-assembled monolayers*.

[295] K. Bierbaum, and M. Grunze, Langmuir. **11**, 2143–2150 (1995): *Growth of self-assembled n-alkyltrichlorosilane films on Si(100) investigated by atomic force microscopy*.

[296] N.L. Jeon, K. Finnie, K. Branshaw, and R.G. Nuzzo, Langmuir. **13**, 3382–3391 (1997): *Structure and stability of patterned self-assembled films of octadecyltrichlorosilane formed by contact printing*.

[297] F.L. McCrackin, E. Passaglia, R.R. Stromberg, and H.L. Steinberg, J. Res. Natl. Bur. Stand. - A. Phys. Chem. **67A**, 363–377 (1963): *Measurement of the thickness and refractive index of very thin films and the optical properties of surfaces by ellipsometry*.

[298] R. Pascu, and M. Dinescu, Rom. Rep. Phys. **64**, 135–142 (2012): *Spectroscopic ellipsometry*.

[299] W. Ogieglo, H. Wormeester, K.J. Eichhorn, M. Wessling, and N.E. Benes, Prog. Polym. Sci. **42**, 42–78 (2015): *In situ ellipsometry studies on swelling of thin polymer films: a review*.

[300] J.C. Maxwell, Philos. Trans. R. Soc. London. **155**, 459–512 (1865): *VIII. A dynamical theory of the electromagnetic field*.

[301] D. Gonçalves, and E.A. Irene, Quim. Nova. **25**, 794–800 (2002): *Fundamentals and applications of spectroscopic ellipsometry*.

[302] J.H.W.G. Den Boer, Technische Universiteit Eindhoven (Netherlands), Dissertation (1996): *Spectroscopic infrared ellipsometry: components, calibration, and application*.

[303] H. Fujiwara, 1st ed. John Wiley & Sons, Ltd, Chichester, UK (2007): *Spectroscopic ellipsometry: Principles and applications*.

[304] G.E. Jellison Jr., L.A. Boatner, J.D. Budai, B.S. Jeong, and D.P. Norton, J. Appl. Phys. **93**, 9537–9541 (2003): *Spectroscopic ellipsometry of thin film and bulk anatase (TiO_2)*.

[305] R. Kurrat, J.E. Prenosil, and J.J. Ramsden, J. Colloid Interface Sci. **185**, 1–8 (1997): *Kinetics of human and bovine serum albumin adsorption at silica-titania surfaces*.

[306] G. Poste, and C. Moss, Prog. Surf. Sci. **2**, 139–232 (1972): *The study of surface reactions in biological systems by ellipsometry*.

[307] B.W. Morrissey, L.E. Smith, R.R. Stromberg, and C.A. Fenstermaker, J. Colloid Interface Sci. **56**, 557–563 (1976): *Ellipsometric investigation of the effect of potential on blood protein conformation and adsorbance*.

[308] M.R. Fries, Eberhard Karls Universität Tübingen (Germany), Master thesis (2016): *Tuning protein adsorption using multivalent ions*.

[309] M.F. Mora, J.L. Wehmeyer, R. Synowicki, and C.D. Garcia, Investigating protein adsorption via spectroscopic ellipsometry, in: D.A. Puleo, R. Bizios (Eds.), Biol. Interact. Mater. Surfaces, Springer, New York (2009): pp. 19–41.

[310] P.A. Cuypers, W.T. Hermens, and H.C. Hemker, Anal. Biochem. **84**, 56–67 (1978): *Ellipsometry as a tool to study protein films at liquid-solid interfaces*.

[311] C.M. Herzinger, B. Johs, W.A. McGahan, J.A. Woollam, and W. Paulson, J. Appl. Phys. **83**, 3323–3336 (1998): *Ellipsometric determination of optical constants for silicon and thermally grown silicon dioxide via a multi-sample, multi-wavelength, multi-angle investigation*.

[312] P. Schiebener, J. Straub, J.M.H. Levelt Sengers, and J.S. Gallagher, J. Phys. Chem. Ref. Data. **19**, 677–717 (1990): *Refractive index of water and steam as function of wavelength, temperature and density*.

[313] A. Scarangella, M. Soumbo, C. Villeneuve-Faure, A. Mlayah, C. Bonafos, M.-C. Monje, C. Roques, and K. Makasheva, Nanotechnology. **29**, 115101 (2018): *Adsorption properties of BSA and DsRed proteins deposited on thin SiO_2 layers: optically non-absorbing versus absorbing proteins*.

[314] Z. Balevicius, A. Paulauskas, I. Plikusiene, L. Mikoliunaite, M. Bechelany, A. Popov, A. Ramanavicius, and A. Ramanaviciene, J. Mater. Chem. C. **6**, 8778–8783 (2018): *Towards the application of Al_2O_3/ZnO nanolaminates in immunosensors: total internal reflection spectroscopic ellipsometry based evaluation of BSA immobilization*.

[315] M.R. Nejadnik, and C.D. Garcia, Colloids Surf. B. **82**, 253–257 (2011): *Staining proteins: a simple method to increase the sensitivity of ellipsometric measurements in adsorption studies*.

[316] A. Tsargorodskaya, A. V. Nabok, and A.K. Ray, Nanotechnology. **15**, 703–709 (2004): *Ellipsometric study of the adsorption of bovine serum albumin into porous silicon*.

[317] L. Asinovski, D. Beaglehole, and M.T. Clarkson, Phys. Status Solidi A. **205**, 764–771 (2008): *Imaging ellipsometry: quantitative analysis*.

[318] B. Drévillon, Prog. Cryst. Growth Charact. Mater. **27**, 1–87 (1993): *Phase modulated ellipsometry from the ultraviolet to the infrared: in situ application to the growth of semiconductors*.

[319] O. Acher, E. Bigan, and B. Drévillon, Rev. Sci. Instrum. **60**, 65–77 (1989): *Improvements of phase-modulated ellipsometry*.

[320] L.A. Clifton, M.W.A. Skoda, E.L. Daulton, A. V Hughes, A.P. Le Brun, J.H. Lakey, and S. Holt, J. R. Soc. Interface. **10**, 20130810 (2013): *Asymmetric phospholipid: lipopolysaccharide bilayers; a Gram-negative bacterial outer membrane mimic*.

[321] G. Fragneto-Cusani, J. Phys. Condens. Matter. **13**, 4973–4989 (2001): *Neutron reflectivity at the solid/liquid interface: Examples of applications in biophysics*.

[322] J. Penfold, and R.K. Thomas, J. Phys. Condens. Matter. **2**, 1369–1412 (1990): *The application of specular neutron reflection to the study of surfaces and interfaces*.

[323] F. Cousin, and A. Menelle, EPJ Web Conf. **104**, 1005 (2015): *Neutron reflectivity*.

[324] D.S. Sivia, Oxford University Press, (2011): *Elementary scattering theory: for X-ray and neutron users*.

[325] M. Campana, S.L. Hosking, J.T. Petkov, I.M. Tucker, J.R.P. Webster, A. Zarbakhsh, and J.R. Lu, Langmuir. **31**, 5614–5622 (2015): *Adsorption of bovine serum albumin (BSA) at the oil/water interface: a neutron reflection study*.

[326] M.W.A. Skoda, F. Schreiber, R.M.J. Jacobs, J.R.P. Webster, M. Wolff, R. Dahint, D. Schwendel, and M. Grunze, Langmuir. **25**, 4056–4064 (2009): *Protein density profile at the interface of water with oligo (ethylene glycol) self-assembled monolayers*.

[327] S.A. Holt, M.J. Henderson, and J.W. White, Aust. J. Chem. **55**, 449–459 (2002): *Thermal denaturation of interfacial protein layers*.

[328] D. Schwendel, T. Hayashi, R. Dahint, A. Pertsin, M. Grunze, R. Steitz, and F. Schreiber, Langmuir. **19**, 2284–2293 (2003): *Interaction of water with self-assembled monolayers: Neutron reflectivity measurements of the water density in the interface region*.

[329] J. Penfold, Specular neutron reflectivity: application to soft matter, in: Neutron Reflectometry- a Probe Mater. Surfaces, International Atomic Energy Agency, Vienna, Austria (2004): pp. 45–58.

[330] R. Zhang, R. Itri, and M. Caffrey, Biophys. J. **74**, 1924–1936 (1998): *Membrane structure characterization using variable-period X-ray standing waves*.

[331] J. Penfold, Curr. Opin. Colloid Interface Sci. **7**, 139–147 (2002): *Neutron reflectivity and soft condensed matter*.

[332] A.S. Brown, S.A. Holt, P.M. Saville, and J.W. White, Aust. J. Phys. **50**, 391–405 (1997): *Neutron and X-ray reflectometry: solid multilayers and crumpling films*.

[333] R.K. Thomas, Annu. Rev. Phys. Chem. **55**, 391–426 (2004): *Neutron reflection from liquid interfaces*.

[334] J. Daillant, and A. Gibaud, Springer-Verlag, Berlin Heidelberg (2009): *X-ray and neutron reflectivity: Principles and applications*.

[335] N.M. Pawlowska, H. Fritzsche, C. Blaszykowski, S. Sheikh, M. Vezvaie, and M. Thompson, Langmuir. **30**, 1199–1203 (2014): *Probing the hydration of ultrathin antifouling organosilane adlayers using neutron reflectometry*.

[336] J. Webster, S. Holt, and R. Dalgliesh, Physica B Condens. Matter. **385–386**, 1164–1166 (2006): *INTER the chemical interfaces reflectometer on target station 2 at ISIS*.

[337] J.R.P. Webster, S. Langridge, R.M. Dalgliesh, and T.R. Charlton, Eur. Phys. J. Plus. **126**, 112 (2011): *Reflectometry techniques on the second target station at ISIS: Methods and science*.

[338] T.R. Charlton, R.L.S. Coleman, R.M. Dalgliesh, C.J. Kinane, C. Neylon, S. Langridge, J. Plomp, N.G.J. Webb, and J.R.P. Webster, Neutron News. **22**, 15–18 (2011): *Advances in neutron reflectometry at ISIS*.

[339] R.M. Dalgliesh, A.A. van Well, S. Boag, T.R. Charlton, C.D. Frost, V.O. de Haan, S. Parnell, and J. Plomp, Physica B Condens. Matter. **397**, 176–178 (2007): *Broad bandpass spin polarizers for the ISIS second target station*.

[340] T. Saerbeck, R. Cubitt, A. Wildes, G. Manzin, K.H. Andersen, and P. Gutfreund, J. Appl. Crystallogr. **51**, 249–256 (2018): *Recent upgrades of the neutron reflectometer D17 at ILL*.

[341] M. Born, and E. Wolf, 7th ed. Cambridge University Press, (1999): *Principles of optics: electromagnetic theory of propagation, interference and diffraction of light*.

[342] L. Névot, and P. Croce, Rev. Phys. Appliquée. **15**, 761–779 (1980): *Caractérisation des surfaces par réflexion rasante de rayons X. Application à l'étude du polissage de quelques verres silicates*.

[343] D.S. Sivia, W.A. Hamilton, and G.S. Smith, Physica B Condens. Matter. **173**, 121–138 (1991): *Analysis of neutron reflectivity data: maximum entropy, Bayesian spectral analysis and speckle holography*.

[344] C.R. Hogg, J.B. Kadane, J.S. Lee, and S.A. Majetich, Bayesian Anal. **5**, 1–34 (2010): *Error analysis for small angle neutron scattering datasets using Bayesian inference*.

[345] T.P. Russel, Mater. Sci. Reports. **5**, 171–271 (1990): *X-ray and neutron reflectivity for the investigation of polymers*.

[346] M. Weik, R.B.G. Ravelli, G. Kryger, S. McSweeney, M.L. Raves, M. Harel, P. Gros, I. Silman, J. Kroon, and J.L. Sussman, Proc. Natl. Acad. Sci. U.S.A. **97**, 623–628 (2000): *Specific chemical and structural damage to proteins produced by synchrotron radiation*.

[347] S.K. Sinha, Physica B Condens. Matter. **173**, 25–34 (1991): *Reflectivity using neutrons or X-rays? A critical comparison*.

[348] S. Skou, R.E. Gillilan, and N. Ando, Nat. Protoc. **9**, 1727–1739 (2014): *Synchrotron-based small-angle X-ray scattering of proteins in solution*.

[349] O. Matsarskaia, F. Roosen-Runge, G. Lotze, J. Möller, A. Mariani, F. Zhang, and F. Schreiber, Phys. Chem. Chem. Phys. **20**, 27214–27225 (2018): *Tuning phase transitions of aqueous protein solutions by multivalent cations*.

[350] J.S. Pedersen, Adv. Colloid Interface Sci. **70**, 171–210 (1997): *Analysis of small-angle scattering data from colloids and polymer solutions: Modeling and least-squares fitting*.

[351] F. Bonneté, and D. Vivarès, Acta Crystallogr. Sect. D. **58**, 1571–1575 (2002): *Interest of the normalized second virial coefficient and interaction potentials for crystallizing large macromolecules*.

[352] J.B. Hayter, and J. Penfold, Mol. Phys. **42**, 109–118 (1981): *An analytic structure factor for macroion solutions*.

[353] J.P. Hansen, and J.B. Hayter, Mol. Phys. **46**, 651–656 (1982): *A rescaled MSA structure factor for dilute charged colloidal dispersions*.

[354] R.J. Baxter, J. Chem. Phys. **49**, 2770–2774 (1968): *Percus–Yevick equation for hard spheres with surface adhesion*.

[355] M.G. Noro, and D. Frenkel, J. Chem. Phys. **113**, 2941–2944 (2000): *Extended corresponding-states behavior for particles with variable range attractions*.

[356] M. Wolf, F. Roosen-Runge, F. Zhang, R. Roth, M.W.A. Skoda, R.M.J. Jacobs, M. Sztucki, and F. Schreiber, J. Mol. Liq. **200**, 20–27 (2014): *Effective interactions in protein-salt solutions approaching liquid-liquid phase separation*.

[357] H. Förster, UV/Vis spectroscopy, in: H.G. Karge, J. Weitkamp (Eds.), Mol. Sieves-Vol. 7-Characterization I, Springer-Verlag, Berlin, Heidelberg (2004): pp. 337–426.

[358] C.M. Stoscheck, Quantitation of protein, in: M.P. Deutscher (Ed.), Methods Enzymol. Vol. 182, Academic Press, London (1990): pp. 50–68.

[359] J.W. Verhoeven, Pure Appl. Chem. **68**, 2223–2286 (1996): *Glossary of terms used in photochemistry*.

[360] E. Layne, Spectrophotometric and turbidimetric methods for measuring proteins, in: Methods Enzymol. Vol. 3, Academic Press Inc., London (1957): pp. 447–454.

[361] S.E. Braslavsky, Pure Appl. Chem. **79**, 296–465 (2007): *Glossary of terms used in photochemistry*.

[362] A. Beer, Ann. Phys. **162**, 78–88 (1852): *Bestimmung der Absorption des rothen Lichts in farbigen Flüssigkeiten*.

[363] J.S. Gaffney, N.A. Marley, and D.E. Jones, Fourier transform infrared (FTIR) spectroscopy, in: E.N. Kaufmann (Ed.), Charact. Mater., John Wiley & Sons, Inc., Hoboken, USA (1978): pp. 1104–1135.

[364] J. Kong, and S. Yu, Acta Biochim. Biophys. Sin. (Shanghai). **39**, 549–559 (2007): *Fourier transform infrared spectroscopic analysis of protein secondary structures*.

[365] B.C. Smith, 2nd ed. CRC Press, Boca Raton (2011): *Fundamentals of Fourier transform infrared spectroscopy*.

[366] J.L.R. Arrondo, A. Muga, J. Castresana, and F.M. Goñi, Prog. Biophys. Mol. Biol. **59**, 23–56 (1993): *Quantitative studies of the structure of proteins in solution by Fourier-transform infrared spectroscopy*.

[367] T. Lefèvre, and M. Subirade, Int. J. Food Sci. Technol. **34**, 419–428 (1999): *Structural and interaction properties of β-lactoglobulin as studied by FTIR spectroscopy*.

[368] K. Fahmy, Fourier transform infrared spectroscopy for biophysical applications: technical aspects, in: G.C.K. Roberts (Ed.), Encycl. Biophys., Springer Verlag, Berlin Heidelberg (2013): pp. 844–852.

[369] P.R. Griffiths, and J.A. De Haseth, 2nd ed. John Wiley & Sons, Hoboken, USA (2007): *Fourier transform infrared spectrometry*.

[370] M. Milosevic, Appl. Spectrosc. **67**, 126–131 (2013): *On the nature of the evanescent wave*.

[371] A. Bouhekka, and T. Bürgi, Appl. Surf. Sci. **261**, 369–374 (2012): *In situ ATR-IR spectroscopy study of adsorbed protein: Visible light denaturation of bovine serum albumin on TiO_2*.

[372] B. Mizaikoff, and B. Lendl, Sensor systems based on mid-infrared transparent fibers, in: J.M. Chalmers, P.R. Griffith (Eds.), Handb. Vib. Spectrosc., John Wiley & Sons, Ltd, Chichester, UK (2002): pp. 1–14.

[373] K.K. Chittur, Biomaterials. **19**, 357–369 (1998): *FTIR/ATR for protein adsorption to biomaterial surfaces*.

[374] R. Tantipolphan, T. Rades, A.J. McQuillan, and N.J. Medlicott, Int. J. Pharm. **337**, 40–47 (2007): *Adsorption of bovine serum albumin (BSA) onto lecithin studied by attenuated total reflectance Fourier transform infrared (ATR-FTIR) spectroscopy*.

[375] Z. Xu, and V.H. Grassian, J. Phys. Chem. C. **121**, 21763–21771 (2017): *Bovine serum albumin adsorption on TiO_2 nanoparticle surfaces: Effects of pH and coadsorption of phosphate on protein-surface interactions and protein structure*.

[376] C.C. Tsai, H.H. Huo, P. Kulkarni, and R.C. Eberhart, ASAIO Trans. **36**, M307-10 (1990): *Biocompatible coatings with high albumin affinity*.

[377] D. Lawlor, 1st ed. Springer Verlag, Cham Switzerland (2019): *Introduction to light microscopy: Tips and tricks for beginners*.

[378] R. Haynes, 1st ed. Springer US, New York (1984): *Optical microscopy of materials*.

[379] E. Meyer, Prog. Surf. Sci. **41**, 3–49 (1992): *Atomic force microscopy*.

[380] V.J. Morris, A.R. Kirby, and A.P. Gunning, 2nd ed. Imperial College Press, London (2009): *Atomic force microscopy for biologists*.

[381] JPK Instruments, (2012): *NanoWizard ® AFM Handbook Version 2.2a*.

[382] D. Nečas, and P. Klapetek, Cent. Eur. J. Phys. **10**, 181–188 (2012): *Gwyddion: an open-source software for SPM data analysis*.

[383] L. Bradshaw, RF Time Freq. **23**, 50–59 (2000): *Understanding piezoelectric quartz crystals*.

[384] F. Li, J.H.-C. Wang, and Q.-M. Wang, Sens. Actuators B Chem. **128**, 399–406 (2008): *Thickness shear mode acoustic wave sensors for characterizing the viscoelastic properties of cell monolayer*.

[385] I. Reviakine, D. Johannsmann, and R.P. Richter, Anal. Chem. **83**, 8838–8848 (2011): *Hearing what you cannot see and visualizing what you hear: Interpreting quartz crystal microbalance data from solvated interfaces*.

[386] A. Jaiswal, S. Smoukov, M. Poggi, and B. Grzybowski, NSTI-Nanotech 2008. **1**, 855–858 (2008): *Quartz crystal microbalance with dissipation monitoring (QCM-D): real-time characterization of nano-scale interactions at surfaces*.

[387] G. Sauerbrey, Zeitschrift Für Phys. **155**, 206–222 (1959): *Verwendung von Schwingquarzen zur Wägung dünner Schichten und zur Mikrowägung*.

[388] D. Johannsmann, I. Reviakine, E. Rojas, and M. Gallego, Anal. Chem. **80**, 8891–8899 (2008): *Effect of sample heterogeneity on the interpretation of QCM(-D) data: Comparison of combined quartz crystal microbalance/atomic force microscopy measurements with finite element method modeling*.

[389] G. Ohlsson, C. Langhammer, I. Zorić, and B. Kasemo, Rev. Sci. Instrum. **80**, 083905 (2009): *A nanocell for quartz crystal microbalance and quartz crystal microbalance with dissipation-monitoring sensing*.

[390] M. Rodahl, and B. Kasemo, Rev. Sci. Instrum. **67**, 3238–3241 (1996): *A simple setup to simultaneously measure the resonant frequency and the absolute dissipation factor of a quartz crystal microbalance*.

[391] B. Zhang, and Q. Wang, Quartz crystal microbalance with dissipation, in: G.W. Padua, Q. Wang (Eds.), Nanotechnol. Res. Methods Foods Bioprod., Wiley-Blackwell, Oxford, UK (2012): pp. 181–194.

[392] C. Steinem, and A. Janshoff, Springer Verlag, Berlin Heidelberg (2007): *Piezoelectric sensors*.

[393] T.P. McNamara, and C.F. Blanford, Analyst. **141**, 2911–2919 (2016): *A sensitivity metric and software to guide the analysis of soft films measured by a quartz crystal microbalance*.

[394] M. V Voinova, M. Rodahl, M. Jonson, and B. Kasemo, Phys. Scr. **59**, 391–396 (1999): *Viscoelastic acoustic response of layered polymer films at fluid-solid interfaces: continuum mechanics approach*.

[395] S.X. Liu, and J.-T. Kim, J. Lab. Autom. **14**, 213–220 (2009): *Application of Kevin—Voigt model in quantifying whey protein adsorption on polyethersulfone using QCM-D*.

[396] M. V Voinova, M. Jonson, and B. Kasemo, Biosens. Bioelectron. **17**, 835–841 (2002): *"Missing mass" effect in biosensor's QCM applications*.

[397] A. Mahdi, N. Meshkat, and S. Sullivant, PLoS One. **9**, e86411 (2014): *Structural identifiability of viscoelastic mechanical systems*.

[398] D. Johannsmann, 1st ed. Springer International, Switzerland (2015): *The quartz crystal microbalance in soft matter research: Fundamentals and modeling*.

[399] K. Sakai, Quartz crystal microbalance with dissipation monitoring (QCM-D), in: M. Abe (Ed.), Meas. Tech. Pract. Colloid Interface Phenom., Springer, Singapore (2019): pp. 45–50.

[400] Q. Chen, S. Xu, Q. Liu, J. Masliyah, and Z. Xu, Adv. Colloid Interface Sci. **233**, 94–114 (2016): *QCM-D study of nanoparticle interactions*.

[401] C. Tonda-Turo, I. Carmagnola, and G. Ciardelli, Front. Bioeng. Biotechnol. **6**, 1–7 (2018): *Quartz crystal microbalance with dissipation monitoring: A powerful method to predict the in vivo behavior of bioengineered surfaces*.

[402] A.A. Feiler, A. Sahlholm, T. Sandberg, and K.D. Caldwell, J. Colloid Interface Sci. **315**, 475–481 (2007): *Adsorption and viscoelastic properties of fractionated mucin (BSM) and bovine serum albumin (BSA) studied with quartz crystal microbalance (QCM-D)*.

[403] E. Rojas, M. Gallego, and I. Reviakine, Anal. Chem. **80**, 8982–8990 (2008): *Effect of sample heterogeneity on the interpretation of quartz crystal microbalance data: Impurity effects*.

[404] L. Korson, W. Drost-Hansen, and F.J. Millero, J. Phys. Chem. **73**, 34–39 (1969): *Viscosity of water at various temperatures*.

[405] J.C. Crittenden, R.R. Trussell, D.W. Hand, K.J. Howe, and G. Tchobanoglous, Physical properties of water, in: MWH's Water Treat. Princ. Des., 3rd ed., John Wiley & Sons, Inc., Hoboken, USA (2012): pp. 1861–1862.

[406] M. Heinen, F. Zanini, F. Roosen-Runge, D. Fedunová, F. Zhang, M. Hennig, T. Seydel, R. Schweins, M. Sztucki, M. Antalík, F. Schreiber, and G. Nägele, Soft Matter. **8**, 1404–1419 (2012): *Viscosity and diffusion: Crowding and salt effects in protein solutions*.

[407] K. Monkos, Int. J. Biol. Macromol. **18**, 61–68 (1996): *Viscosity of bovine serum albumin aqueous solutions as a function of temperature and concentration*.

[408] Rheosense, (2008): *Application Note: Viscosity measurement of a model protein solution of BSA*.

[409] S. Yadav, S.J. Shire, and D.S. Kalonia, Pharm. Res. **28**, 1973–1983 (2011): *Viscosity analysis of high concentration bovine serum albumin aqueous solutions*.

[410] J.T. Kim, N. Weber, G.H. Shin, Q. Huang, and S.X. Liu, J. Food Sci. **72**, E214–E221 (2007): *The study of β-lactoglobulin adsorption on polyethersulfone thin film surface using QCM-D and AFM*.

[411] Z. Teng, R. Xu, and Q. Wang, RSC Adv. **5**, 35138–35154 (2015): *Beta-lactoglobulin-based encapsulating systems as emerging bioavailability enhancers for nutraceuticals: a review*.

[412] L. Macakova, E. Blomberg, and P.M. Claesson, Langmuir. **23**, 12436–12444 (2007): *Effect of adsorbed layer surface roughness on the QCM-D response: Focus on trapped water*.

[413] P. Bingen, G. Wang, N.F. Steinmetz, M. Rodahl, and R.P. Richter, Anal. Chem. **80**, 8880–8890 (2008): *Solvation effects in the quartz crystal microbalance with dissipation monitoring response to biomolecular adsorption. A phenomenological approach*.

[414] K. Rechendorff, M.B. Hovgaard, M. Foss, V.P. Zhdanov, and F. Besenbacher, Langmuir. **22**, 10885–10888 (2006): *Enhancement of protein adsorption induced by surface roughness*.

[415] E. Reimhult, C. Larsson, B. Kasemo, and F. Höök, Anal. Chem. **76**, 7211–7220 (2004): *Simultaneous surface plasmon resonance and quartz crystal microbalance with dissipation monitoring measurements of biomolecular adsorption events involving structural transformations and variations in coupled water*.

[416] K. Xu, M.M. Ouberai, and M.E. Welland, Biomaterials. **34**, 1461–1470 (2013): *A comprehensive study of lysozyme adsorption using dual polarization interferometry and quartz crystal microbalance with dissipation*.

[417] K.B. Rodenhausen, and M. Schubert, Thin Solid Films. **519**, 2772–2776 (2011): *Virtual separation approach to study porous ultra-thin films by combined spectroscopic ellipsometry and quartz crystal microbalance methods*.

[418] Mettler-Toledo, Theory & Practice of Laboratory pH Applications. 1–52 (2016): *A Guide to pH Measurement*.

[419] C.C. Westcott, 1st ed. Academic Press, London (1978): *pH measurements*.

[420] D.Y. Kwok, and A.W. Neumann, Adv. Colloid Interface Sci. **81**, 167–249 (1999): *Contact angle measurement and contact angle interpretation*.

[421] F. Hejda, P. Solař, and J. Kousal, Surface free energy determination by contact angle measurements – a comparison of various approaches, in: WDS'10 Proc. Contrib. Pap., (2010): pp. 25–30.

[422] K.Y. Law, and H. Zhao, Determination of solid surface tension by contact angle, in: Surf. Wetting Charact. Contact Angle, Fundam., Springer International, Switzerland (2016): pp. 1–162.

[423] Y. Yuan, and T.R. Lee, Contact angle and wetting properties, in: G. Bracco, Y. Yuan (Eds.), Surf. Sci. Tech., Springer, Berlin Heidelberg (2013): pp. 3–34.

[424] D.Y. Kwok, and A.W. Neumann, Colloid. Surf. A . **161**, 31–48 (2000): *Contact angle interpretation in terms of solid surface tension*.

[425] T. Young, Philos. Trans. R. Soc. London. **95**, 65–87 (1805): *III. An essay on the cohesion of fluids*.

[426] H. Wang, B. Yu, S. Jiang, L. Jiang, and L. Qian, RSC Adv. **7**, 39651–39656 (2017): *UV/ozone-assisted tribochemistry-induced nanofabrication on Si(100) surfaces*.

[427] M.R. Fries, D. Stopper, M.K. Braun, A. Hinderhofer, F. Zhang, R.M.J. Jacobs, M.W.A. Skoda, H. Hansen-Goos, R. Roth, and F. Schreiber, Phys. Rev. Lett. **119**, 228001 (2017): *Multivalent-ion-activated protein adsorption reflecting bulk reentrant behavior*.

[428] S. Whitelam, Phys. Rev. Lett. **105**, 088102 (2010): *Control of pathways and yields of protein crystallization through the interplay of nonspecific and specific attractions*.

[429] D. Fusco, and P. Charbonneau, Phys. Rev. E. **88**, 012721 (2013): *Crystallization of asymmetric patchy models for globular proteins in solution*.

[430] A. Stradner, H. Sedgwick, F. Cardinaux, W.C.K. Poon, S.U. Egelhaaf, and P. Schurtenberger, Nature. **432**, 492–495 (2004): *Equilibrium cluster formation in concentrated protein solutions and colloids*.

[431] P.D. Godfrin, S.D. Hudson, K. Hong, L. Porcar, P. Falus, N.J. Wagner, and Y. Liu, Phys. Rev. Lett. **115**, 228302 (2015): *Short-time glassy dynamics in viscous protein solutions with competing interactions*.

[432] U. Schmidt, G. Guigas, and M. Weiss, Phys. Rev. Lett. **101**, 128104 (2008): *Cluster formation of transmembrane proteins due to hydrophobic mismatching*.

[433] J. Yan, M. Enge, T. Whitington, K. Dave, J. Liu, I. Sur, B. Schmierer, A. Jolma, T. Kivioja, M. Taipale, and J. Taipale, Cell. **154**, 801–813 (2013): *Transcription factor binding in human cells occurs in dense clusters formed around cohesin anchor sites*.

[434] C.R.F. Monks, B.A. Freiberg, H. Kupfer, N. Sciaky, and A. Kupfer, Nature. **395**, 82–86 (1998): *Three-dimensional segregation of supramolecular activation clusters in T cells*.

[435] A. Kakio, S.-I. Nishimoto, K. Yanagisawa, Y. Kozutsumi, and K. Matsuzaki, J. Biol. Chem. **276**, 24985–24990 (2001): *Cholesterol-dependent formation of GM1 ganglioside-bound amyloid β-protein, an endogenous seed for alzheimer amyloid*.

[436] A. Aguzzi, T.O. Connor, and T. O'Connor, Nat. Rev. Drug. Discov. **9**, 237–248 (2010): *Protein aggregation diseases: Pathogenicity and therapeutic perspectives*.

[437] R.P. Sear, J. Chem. Phys. **111**, 4800–4806 (1999): *Phase behavior of a simple model of globular proteins*.

[438] C. Gögelein, G. Nägele, R. Tuinier, T. Gibaud, A. Stradner, and P. Schurtenberger, J. Chem. Phys. **129**, 085102 (2008): *A simple patchy colloid model for the phase behavior of lysozyme dispersions*.

[439] V. Vagenende, M.G.S. Yap, and B.L. Trout, Biochemistry. **48**, 11084–11096 (2009): *Mechanisms of protein stabilization and prevention of protein aggregation by glycerol*.

[440] Y. Saricay, S.K. Dhayal, P.A. Wierenga, and R. de Vries, Faraday Discuss. **158**, 51–63 (2012): *Protein cluster formation during enzymatic cross-linking of globular proteins*.

[441] S. Schöttler, G. Becker, S. Winzen, T. Steinbach, K. Mohr, K. Landfester, V. Mailänder, and F.R. Wurm, Nat. Nanotechnol. **11**, 372–377 (2016): *Protein adsorption is required for stealth effect of poly(ethylene glycol)- and poly(phosphoester)-coated nanocarriers*.

[442] J.J. Gray, Curr. Opin. Struct. Biol. **14**, 110–115 (2004): *The interaction of proteins with solid surfaces*.

[443] V. Hlady, and J.D. Andrade, Colloids Surf. **32**, 359–369 (1988): *Fluorescence emission from adsorbed bovine serum albumin and albumin-bound 1-anilinonaphthalene-8-sulfonate studied by TIRF*.

[444] R.D. Tilton, C.R. Robertson, and A.P. Gast, J. Colloid Interface Sci. **137**, 192–203 (1990): *Lateral diffusion of bovine serum albumin adsorbed at the solid-liquid interface*.

[445] M. Rabe, D. Verdes, and S. Seeger, Soft Matter. **5**, 1039–1047 (2009): *Surface-induced spreading phenomenon of protein clusters*.

[446] T.J. Su, J.R. Lu, R.K. Thomas, Z.F. Cui, and J. Penfold, J. Phys. Chem. B. **102**, 8100–8108 (1998): *The conformational structure of bovine serum albumin layers adsorbed at the silica water interface*.

[447] H. Larsericsdotter, S. Oscarsson, and J. Buijs, J. Colloid Interface Sci. **289**, 26–35 (2005): *Structure, stability, and orientation of BSA adsorbed to silica*.

[448] Y.I. Tarasevich, and L.I. Monakhova, Colloid J. **64**, 482–487 (2002): *Interaction between globular proteins and silica surfaces*.

[449] P. Roach, D. Farrar, and C.C. Perry, J. Am. Chem. Soc. **127**, 8168–8173 (2005): *Interpretation of protein adsorption: surface-induced conformational changes*.

[450] M. Mondon, S. Berger, and C. Ziegler, Anal. Bioanal. Chem. **375**, 849–855 (2003): *Scanning-force techniques to monitor time-dependent changes in topography and adhesion force of proteins on surfaces*.

[451] H. Elwing, Biomaterials. **19**, 397–406 (1998): *Protein absorption and ellipsometry in biomaterial research*.

[452] S.S. Lee, M. Schmidt, N. Laanait, N.C. Sturchio, and P. Fenter, J. Phys. Chem. C. **117**, 23738–23749 (2013): *Investigation of structure, adsorption free energy, and overcharging behavior of trivalent yttrium adsorbed at the muscovite (001)–water interface*.

[453] G. Yohannes, S.K. Wiedmer, M. Elomaa, M. Jussila, V. Aseyev, and M.L. Riekkola, Anal. Chim. Acta. **675**, 191–198 (2010): *Thermal aggregation of bovine serum albumin studied by asymmetrical flow field-flow fractionation*.

[454] G. Jackson, W.G. Chapman, and K.E. Gubbins, Mol. Phys. **65**, 1–31 (1988): *Phase equilibria of associating fluids: spherical molecules with multiple bonding sites*.

[455] W.G. Chapman, G. Jackson, and K.E. Gubbins, Mol. Phys. **65**, 1057–1079 (1988): *Phase equilibria of associating fluids: Chain molecules with multiple bonding sites*.

[456] M.S. Wertheim, J. Stat. Phys. **35**, 19–34 (1984): *Fluids with highly directional attractive forces. I. Statistical thermodynamics*.

[457] M.S. Wertheim, J. Stat. Phys. **35**, 35–47 (1984): *Fluids with highly directional attractive forces. II. Thermodynamic perturbation theory and integral equations*.

[458] M.S. Wertheim, J. Stat. Phys. **42**, 459–476 (1986): *Fluids with highly directional attractive forces. III. Multiple attraction sites*.

[459] M.S. Wertheim, J. Stat. Phys. **42**, 477–492 (1986): *Fluids with highly directional attractive forces. IV. Equilibrium polymerization*.

[460] F. Romano, E. Sanz, and F. Sciortino, J. Chem. Phys. **132**, 184501 (2010): *Phase diagram of a tetrahedral patchy particle model for different interaction ranges*.

[461] J. Russo, J.M. Tavares, P.I.C. Teixeira, M.M.T. Da Gama, and F. Sciortino, J. Chem. Phys. **135**, 34501 (2011): *Re-entrant phase behaviour of network fluids: a patchy particle model with temperature-dependent valence*.

[462] Y.-X. Yu, and J. Wu, J. Chem. Phys. **116**, 7094–7103 (2002): *A fundamental-measure theory for inhomogeneous associating fluids*.

[463] Y. Rosenfeld, Phys. Rev. Lett. **63**, 980 (1989): *Free-energy model for the inhomogeneous hard-sphere fluid mixture and density-functional theory of freezing*.

[464] R. Roth, J. Phys. Condens. Matter. **22**, 63102 (2010): *Fundamental measure theory for hard-sphere mixtures: a review*.

[465] M.R. Fries, D. Stopper, M.W.A. Skoda, M. Blum, C. Kertzscher, A. Hinderhofer, F. Zhang, R.M.J. Jacobs, R. Roth, and F. Schreiber, Sci. Rep. **10**, 1–9 (2020): *Enhanced protein adsorption upon bulk phase separation*.

[466] L. Shen, and J. Zhu, Adv. Colloid Interface Sci. **228**, 40–54 (2016): *Heterogeneous surfaces to repel proteins*.

[467] S. Dietrich, Wetting phenomena, in: C. Domb and J. L. Lebowitz (Ed.), Phase Transit. Crit. Phenom., 12th ed., Academic Press, London (1988): pp. 2–218.

[468] M. Schick, Introduction to wetting phenomena, in: J. Zinn-Justin, J. Charvolin, J. F. Joanny (Ed.), Liq. Interfaces Vol. 48, Elsevier, Amsterdam (1990): pp. 415–497.

[469] J.P. Hansen, and I.R. McDonald, 4th ed. Academic Press, London (2013): *Theory of simple liquids: with applications to soft matter*.

[470] D. Rosenbaum, P.C. Zamora, and C.F. Zukoski, Phys. Rev. Lett. **76**, 150–153 (1996): *Phase behavior of small attractive colloidal particles*.

[471] D.F. Rosenbaum, and C.F. Zukoski, J. Cryst. Growth. **169**, 752–758 (1996): *Protein interactions and crystallization*.

[472] R. Piazza, V. Peyre, and V. Degiorgio, Phys. Rev. E. **58**, R2733–R2736 (1998): *"Sticky hard spheres" model of proteins near crystallization: a test based on the osmotic compressibility of lysozyme solutions*.

[473] N. Kern, and D. Frenkel, J. Chem. Phys. **118**, 9882–9889 (2003): *Fluid–fluid coexistence in colloidal systems with short-ranged strongly directional attraction*.

[474] J. Bleibel, M. Habiger, M. Lütje, F. Hirschmann, F. Roosen-Runge, T. Seydel, F. Zhang, F. Schreiber, and M. Oettel, Soft Matter. **14**, 8006–8016 (2018): *Two time scales for self and collective diffusion near the critical point in a simple patchy model for proteins with floating bonds*.

[475] A.Y. Grosberg, T.T. Nguyen, and B.I. Shklovskii, Rev. Mod. Phys. **74**, 329–345 (2002): *Colloquium: The physics of charge inversion in chemical and biological systems*.

[476] Z. Liang, W. Bu, K.J. Schweighofer, D.J. Walwark, J.S. Harvey, G.R. Hanlon, D. Amoanu, C. Erol, I. Benjamin, and M.L. Schlossman, Proc. Natl. Acad. Sci. U.S.A. **116**, 18227–18232 (2019): *Nanoscale view of assisted ion transport across the liquid–liquid interface*.

[477] M. Miller, Y. Liang, H. Li, M. Chu, S. Yoo, W. Bu, M. Olvera de la Cruz, and P. Dutta, Phys. Rev. Lett. **122**, 058001 (2019): *Electrostatic origin of element selectivity during rare earth adsorption*.

[478] M.M. Sartin, W. Sung, S. Nihonyanagi, and T. Tahara, J. Chem. Phys. **149**, 024703 (2018): *Molecular mechanism of charge inversion revealed by polar orientation of interfacial water molecules: a heterodyne-detected vibrational sum frequency generation study*.

[479] M. Olvera de La Cruz, L. Belloni, M. Delsanti, J.P. Dalbiez, O. Spalla, and M. Drifford, J. Chem. Phys. **103**, 5781–5791 (1995): *Precipitation of highly charged polyelectrolyte solutions in the presence of multivalent salts*.

[480] J. Yu, N.E. Jackson, X. Xu, Y. Morgenstern, Y. Kaufman, M. Ruths, J.J. de Pablo, and M. Tirrell, Science. **360**, 1434–1438 (2018): *Multivalent counterions diminish the lubricity of polyelectrolyte brushes*.

[481] F. Roosen-Runge, B.S. Heck, F. Zhang, O. Kohlbacher, and F. Schreiber, J. Phys. Chem. B. **117**, 5777–5787 (2013): *Interplay of pH and binding of multivalent metal ions: Charge inversion and reentrant condensation in protein solutions*.

[482] A. Sauter, F. Roosen-Runge, F. Zhang, G. Lotze, A. Feoktystov, R.M.J. Jacobs, and F. Schreiber, Faraday Discuss. **179**, 41–58 (2015): *On the question of two-step nucleation in protein crystallization*.

[483] A. Sauter, F. Zhang, N.K. Szekely, V. Pipich, M. Sztucki, and F. Schreiber, J. Phys. Chem. B. **120**, 5564–5571 (2016): *Structural evolution of metastable protein aggregates in the presence of trivalent salt studied by (V)SANS and SAXS*.

[484] J.J. McManus, P. Charbonneau, E. Zaccarelli, and N. Asherie, Curr. Opin. Colloid Interface Sci. **22**, 73–79 (2016): *The physics of protein self-assembly*.

[485] E. Bianchi, J. Largo, P. Tartaglia, E. Zaccarelli, and F. Sciortino, Phys. Rev. Lett. **97**, 168301 (2006): *Phase diagram of patchy colloids: towards empty liquids*.

[486] D. Soraruf, F. Roosen-Runge, M. Grimaldo, F. Zanini, R. Schweins, T. Seydel, F. Zhang, R. Roth, M. Oettel, and F. Schreiber, Soft Matter. **10**, 894–902 (2014): *Protein cluster formation in aqueous solution in the presence of multivalent metal ions-a light scattering study*.

[487] P.A. Mulheran, D. Pellenc, R.A. Bennett, R.J. Green, and M. Sperrin, Phys. Rev. Lett. **100**, 068102 (2008): *Mechanisms and dynamics of protein clustering on a solid surface*.

[488] H.T.M. Phan, S. Bartelt-Hunt, K.B. Rodenhausen, M. Schubert, and J.C. Bartz, PLoS One. **10**, e0141282 (2015): *Investigation of bovine serum albumin (BSA) attachment onto self-assembled monolayers (SAMs) using combinatorial quartz crystal microbalance with dissipation (QCM-D) and spectroscopic ellipsometry (SE)*.

[489] S. Biffi, R. Cerbino, F. Bomboi, E.M. Paraboschi, R. Asselta, F. Sciortino, and T. Bellini, Proc. Natl. Acad. Sci. U.S.A. **110**, 15633–15637 (2013): *Phase behavior and critical activated dynamics of limited-valence DNA nanostars*.

[490] N.R. Bernardino, and M.M. Telo da Gama, Phys. Rev. Lett. **109**, 116103 (2012): *Reentrant wetting of network fluids*.

[491] M.R. Fries, N. Conzelmann, L. Günter, O. Matsarskaia, M.W.A. Skoda, R.M.J. Jacobs, F. Zhang, and F. Schreiber, Langmuir. **37**, 139–150 (2021): *Bulk phase behaviour vs interface adsorption: Specific multivalent cation and anion effects on BSA interactions*.

[492] M.A. Boegehold, and T.A. Kotchen, Hypertension. **17**, I158–I161 (1991): *Importance of dietary chloride for salt sensitivity of blood pressure*.

[493] A. Grollman, Am. J. Cardiol. **8**, 593–601 (1961): *The role of salt in health and disease*.

[494] L.M. Gaetke, and C.K. Chow, Toxicology. **189**, 147–163 (2003): *Copper toxicity, oxidative stress, and antioxidant nutrients*.

[495] V. Rondeau, D. Commenges, H. Jacqmin-Gadda, and J.F. Dartigues, Am. J. Epidemiol. **152**, 59–66 (2000): *Relation between aluminum concentrations in drinking water and Alzheimer's disease: an 8-year follow-up study*.

[496] J.K. Lanyi, Bacteriol. Rev. **38**, 272–290 (1974): *Salt-dependent properties of proteins from extremely halophilic bacteria*.

[497] S. Yan, Z. Tang, W. Su, and W. Sun, Proteomics. **5**, 235–244 (2005): *Proteomic analysis of salt stress-responsive proteins in rice root*.

[498] F.B. Sheinerman, and B. Honig, J. Mol. Biol. **318**, 161–177 (2002): *On the role of electrostatic interactions in the design of protein-protein interfaces*.

[499] K. Berend, L.H. Van Hulsteijn, and R.O.B. Gans, Eur. J. Intern. Med. **23**, 203–211 (2012): *Chloride: the queen of electrolytes?*

[500] F. Powers, J. Intraven. Nurs. **22**, 286–291 (1999): *The role of chloride in acid-base balance*.

[501] N.M. Yunos, R. Bellomo, D. Story, and J. Kellum, Crit. Care. **14**, 226 (2010): *Bench-to-bedside review: Chloride in critical illness*.

[502] S.M. Koch, and R.W. Taylor, Crit. Care Med. **20**, 227–240 (1992): *Chloride ion in intensive care medicine*.

[503] B.D. Mason, J. Zhang-van Enk, L. Zhang, R.L. Remmele, and J. Zhang, Biophys. J. **99**, 3792–3800 (2010): *Liquid-liquid phase separation of a monoclonal antibody and nonmonotonic influence of Hofmeister anions*.

[504] R.L. Ward, and M.D. Cull, Biochim. Biophys. Acta. **365**, 281–284 (1974): *Active site chloride binding in liver alcohol dehydrogenase*.

[505] R. Winkler, Nat. Sci. **7**, 548–557 (2015): *Iodine—a potential antioxidant and the role of iodine/iodide in health and disease*.

[506] A. De La Vieja, and P. Santisteban, Endocr. Relat. Cancer. **25**, R225–R245 (2018): *Role of iodide metabolism in physiology and cancer*.

[507] F. Ahad, and S.A. Ganie, Indian J. Endocr. Metab. **14**, 13–17 (2010): *Iodine, iodine metabolism and iodine deficiency disorders revisited*.

[508] E.L. Thomas, and T.M. Aune, Antimicrob. Agents Chemother. **13**, 1000–1005 (1978): *Cofactor role of iodide in peroxidase antimicrobial action against Escherichia coli*.

[509] A. Iwata, M.L. Morrison, and M.B. Roth, PLoS One. **9**, e112458 (2014): *Iodide protects heart tissue from reperfusion injury*.

[510] A.J. Fischer, N.J. Lennemann, S. Krishnamurthy, P. Pócza, L. Durairaj, J.L. Launspach, B.A. Rhein, C. Wohlford-Lenane, D. Lorentzen, B. Bánfi, and P.B. McCray, Am. J. Respir. Cell Mol. Biol. **45**, 874–881 (2011): *Enhancement of respiratory mucosal antiviral defenses by the oxidation of iodide*.

[511] P. Lo Nostro, and B.W. Ninham, Chem. Rev. **112**, 2286–2322 (2012): *Hofmeister phenomena: an update on ion specificity in biology*.

[512] R.J.P. Williams, Q. Rev. Chem. Soc. **24**, 331–365 (1970): *The biochemistry of sodium, potassium, magnesium, and calcium*.

[513] C.R. Triggle, and D.J. Triggle, J. Physiol. **254**, 39–54 (1976): *An analysis of the action of cations of the lanthanide series on the mechanical responses of guinea-pig ileal longitudinal muscle*.

[514] P. Heffeter, M.A. Jakupec, W. Körner, S. Wild, N. Graf von Keyserlingk, L. Elbling, H. Zorbas, A. Korynevska, S. Knasmüller, H. Sutterlüty, M. Micksche, B.K. Keppler, and W. Berger, Biochem. Pharmacol. **71**, 426–440 (2006): *Anticancer activity of the lanthanum compound [tris(1,10-phenanthroline) lanthanum(III)]trithiocyanate (KP772; FFC24)*.

[515] Y. Dai, J. Li, J. Li, L. Yu, G. Dai, A. Hu, L. Yuan, and Z. Wen, In Vitro Cell. Dev. Biol. Anim. **38**, 373–375 (2002): *Effects of rare earth compounds on growth and apoptosis of leukemic cell lines*.

[516] T. Sato, M. Hashizume, Y. Hotta, and Y. Okahata, BioMetals. **11**, 107–112 (1998): *Morphology and proliferation of B16 melanoma cells in the presence of lanthanoid and Al^{3+} ions*.

[517] A. Basu, K. Chakrabarty, and G.C. Chatterjee, Toxicol. Lett. **14**, 21–25 (1982): *Neurotoxicity of lanthanum chloride in newborn chicks*.

[518] A. Vaccari, P. Saba, I. Mocci, and S. Ruiu, Neurosci. Lett. **261**, 49–52 (1999): *Lanthanides stimulate [^{3}H]tyramine binding in the rat striatum*.

[519] A. Pałasz, and P. Czekaj, Acta Biochim. Pol. **47**, 1107–1114 (2000): *Toxicological and cytophysiological aspects of lanthanides action*.

[520] C.-M. Xu, B. Zhao, X.-D. Wang, and Y.-C. Wang, Biol. Plant. **51**, 567–570 (2007): *Lanthanum relieves salinity-induced oxidative stress in Saussurea involucrata*.

[521] R.S. Stubbs, R.J. Cannan, and A.W. Mitchell, J. Gastrointest. Surg. **5**, 294–302 (2001): *Selective internal radiation therapy with ^{90}yttrium microspheres for extensive colorectal liver metastases*.

[522] A.T.M. Vaughan, A. Keeling, and S.C.S. Yankuba, Int. J. Appl. Radiat. Isot. **36**, 803–806 (1985): *The production and biological distribution of yttrium-90 labelled antibodies*.

[523] T.J. Webster, C. Ergun, R.H. Doremus, and R. Bizios, J. Biomed. Mater. Res. **59**, 312–317 (2002): *Hydroxylapatite with substituted magnesium, zinc, cadmium, and yttrium. II. Mechanisms of osteoblast adhesion*.

[524] S. Fujihara, and R. Akiyama, J. Mol. Liq. **200**, 89–94 (2014): *Attractive interaction between macroanions mediated by multivalent cations in biological fluids*.

[525] X. Wang, S.Y. Lee, K. Miller, R. Welbourn, I. Stocker, S. Clarke, M. Casford, P. Gutfreund, and M.W.A. Skoda, Langmuir. **29**, 5520–5527 (2013): *Cation bridging studied by specular neutron reflection*.

[526] N. Korkmaz Zirpel, and E.J. Park, Macromol. Biosci. **15**, 1262–1273 (2015): *Trivalent cation induced bundle formation of filamentous fd phages*.

[527] P.A. Gurnev, and S.M. Bezrukov, Langmuir. **28**, 15824–15830 (2012): *Inversion of membrane surface charge by trivalent cations probed with a cation-selective channel*.

[528] A. Martín-Molina, C. Rodríguez-Beas, and J. Faraudo, Phys. Rev. Lett. **104**, 168103 (2010): *Charge reversal in anionic liposomes: experimental demonstration and molecular origin*.

[529] G.A. Vliegenthart, and H.N.W. Lekkerkerker, J. Chem. Phys. **112**, 5364–5369 (2000): *Predicting the gas–liquid critical point from the second virial coefficient*.

[530] K. Schomäcker, D. Mocker, R. Münze, and G.-J. Beyer, Appl. Radiat. Isot. **39**, 261–264 (1988): *Stabilities of lanthanide-protein complexes*.

[531] G.E. Smolka, E.R. Birnbaum, and D.W. Darnall, Biochemistry. **10**, 4556–4561 (1971): *Rare earth metal ions as substitutes for the calcium ion in Bacillus subtilis α-amylase*.

[532] J.E. Gomez, E.R. Birnbaum, and D.W. Darnall, Biochemistry. **13**, 3745–3750 (1974): *Metal ion acceleration of the conversion of trypsinogen to trypsin. Lanthanide ions as calcium ion substitutes*.

[533] P. Mulqueen, J.M. Tingey, and W.D.W. Horrocks Jr., Biochemistry. **24**, 6639–6645 (1985): *Characterization of lanthanide(III) ion binding to calmodulin using luminescence spectroscopy*.

[534] M. Yamasaki, H. Yano, and K. Aoki, Int. J. Biol. Macromol. **13**, 322–328 (1991): *Differential scanning calorimetric studies on bovine serum albumin: II. Effects of neutral salts and urea*.

[535] H.I. Okur, J. Hladílková, K.B. Rembert, Y. Cho, J. Heyda, J. Dzubiella, P.S. Cremer, and P. Jungwirth, J. Phys. Chem. B. **121**, 1997–2014 (2017): *Beyond the Hofmeister series: ion-specific effects on proteins and their biological functions*.

[536] M.W. Washabaugh, and K.D. Collins, J. Biol. Chem. **261**, 12477–12485 (1986): *The systematic characterization by aqueous column chromatography of solutes which affect protein stability*.

[537] A.K. Covington, M. Paabo, R.A. Robinson, and R.G. Bates, Anal. Chem. **40**, 700–706 (1968): *Use of the glass electrode in deuterium oxide and the relation between the standardized pD (pa_D) scale and the operational pH in heavy water*.

[538] L.G. Longsworth, and C.F. Jacobsen, J. Phys. Colloid Chem. **53**, 126–134 (1949): *An electrophoretic study of the binding of salt ions by beta-lactoglobulin and bovine serum albumin*.

[539] M.C. Vaney, I. Broutin, P. Retailleau, A. Douangamath, S. Lafont, C. Hamiaux, T. Prangé, A. Ducruix, and M. Riès-Kautt, Acta Crystallogr. Sect. D. **57**, 929–940 (2001): *Structural effects of monovalent anions on polymorphic lysozyme crystals*.

[540] M. Lund, P. Jungwirth, and C.E. Woodward, Phys. Rev. Lett. **100**, 258105–258106 (2008): *Ion specific protein assembly and hydrophobic surface forces*.

[541] G. Scatchard, J.S. Coleman, and A.L. Shen, J. Am. Chem. Soc. **79**, 12–20 (1957): *Physical chemistry of protein solutions. VII. The binding of some small anions to serum albumin*.

[542] G. Scatchard, I. Herbert Scheinberg, and S. Howard Armstrong Jr., J. Am. Chem. Soc. **72**, 535–540 (1950): *Physical chemistry of protein solutions. IV. The combination of human serum albumin with chloride ion*.

[543] G. Scatchard, I. Herbert Scheinberg, and S. Howard Armstrong Jr., J. Am. Chem. Soc. **72**, 540–546 (1950): *Physical chemistry of protein solutions. V. The combination of human serum albumin with thiocyanate ion*.

[544] M. Lund, R. Vácha, and P. Jongwirth, Langmuir. **24**, 3387–3391 (2008): *Specific ion binding to macromolecules: Effects of hydrophobicity and ion pairing*.

[545] M. Lund, L. Vrbka, and P. Jungwirth, J. Am. Chem. Soc. **130**, 11582–11583 (2008): *Specific ion binding to nonpolar surface patches of proteins*.

[546] J. Dzubiella, J. Am. Chem. Soc. **130**, 14000–14007 (2008): *Salt-specific stability and denaturation of a short salt-bridge-forming α-helix*.

[547] F. Karush, J. Am. Chem. Soc. **72**, 2705–2713 (1950): *Heterogeneity of the binding sites of bovine serum albumin*.

[548] Y. Nozaki, J.A. Reynolds, and C. Tanford, J. Biol. Chem. **249**, 4452–4459 (1974): *The interaction of a cationic detergent with bovine serum albumin and other proteins*.

[549] T. Peters Jr., Serum albumin, in: C.B. Anfinsen, J.T. Edsall, F.M. Richards (Eds.), Adv. Protein Chem. Vol. 37, 1st ed., Academic Press, London (1985): pp. 161–245.

[550] K.B. Rembert, J. Paterová, J. Heyda, C. Hilty, P. Jungwirth, and P.S. Cremer, J. Am. Chem. Soc. **134**, 10039–10046 (2012): *Molecular mechanisms of ion-specific effects on proteins*.

[551] E. Ayranci, and O. Duman, Food Chem. **84**, 539–543 (2004): *Binding of fluoride, bromide and iodide to bovine serum albumin, studied with ion-selective electrodes*.

[552] S.A. Wood, Chem. Geol. **82**, 159–186 (1990): *The aqueous geochemistry of the rare-earth elements and yttrium. 1. Review of available low-temperature data for inorganic complexes and the inorganic REE speciation of natural waters*.

[553] S.A. Wood, Chem. Geol. **88**, 99–125 (1990): *The aqueous geochemistry of the rare-earth elements and yttrium. 2. Theoretical predictions of speciation in hydrothermal solutions to 350°C at saturation water vapor pressure*.

[554] W.W. Rudolph, and G. Irmer, Dalton Trans. **44**, 18492–18505 (2015): *Hydration and ion pair formation in aqueous Y^{3+}-salt solutions*.

[555] W.W. Rudolph, and G. Irmer, Dalton Trans. **44**, 295–305 (2015): *Hydration and ion pair formation in common aqueous La(III) salt solutions-a Raman scattering and DFT study*.

[556] R. Takahashi, and S.-I. Ishiguro, J. Chem. Soc. Faraday Trans. **87**, 3379–3383 (1991): *Inner-sphere and outer-sphere complexes of yttrium(III), lanthanum (III), neodymium(III), terbium(III) and thulium(III) with halide ions in N,N-dimethylformamide*.

[557] J. Dzubiella, J. Phys. Chem. B. **113**, 16689–16694 (2009): *Salt-specific stability of short and charged alanine-based a-helices*.

[558] A. Tiraferri, P. Maroni, and M. Borkovec, Phys. Chem. Chem. Phys. **17**, 10348–10352 (2015): *Adsorption of polyelectrolytes to like-charged substrates induced by multivalent counterions as exemplified by poly(styrene sulfonate) and silica*.

[559] J.L. Jordan, and E.J. Fernandez, Biotechnol. Bioeng. **101**, 837–842 (2008): *QCM-D sensitivity to protein adsorption reversibility*.

[560] M. Rodahl, F. Höök, C. Fredriksson, C.A. Keller, A. Krozer, P. Brzezinski, M. Voinova, and B. Kasemo, Faraday Discuss. **107**, 229–246 (1997): *Simultaneous frequency and dissipation factor QCM measurements of biomolecular adsorption and cell adhesion*.

[561] M.R. Fries, M.W.A. Skoda, N. Conzelmann, R.M.J. Jacobs, R. Maier, N. Scheffczyk, F. Zhang, and F. Schreiber, J. Colloid Interface Sci. under revision (2021): *Bulk phase behaviour vs interface adsorption: Effects of anions and isotopes on beta-lactoglobulin (BLG) interactions*.

[562] S. Bilsborough, and N. Mann, Int. J. Sport Nutr. Exerc. Metab. **16**, 129–152 (2006): *A review of issues of dietary protein intake in humans*.

[563] G.H. Anderson, and S.E. Moore, J. Nutr. **134**, 974S-979S (2004): *Dietary proteins in the regulation of food intake and body weight in humans*.

[564] Y. Guigoz, Int. J. Vitam. Nutr. Res. **81**, 87–100 (2011): *Dietary proteins in humans: basic aspects and consumption in switzerland*.

[565] J. Halkjær, A. Olsen, L.J. Bjerregaard, G. Deharveng, A. Tjønneland, A.A. Welch, F.L. Crowe, E. Wirfält, V. Hellstrom, M. Niravong, J. Linseisen, M. Touvier, J. Linseisen, A. Steffen, M.C. Ocké, P.H.M. Peeters, M.D. Chirlaque, N. Larrañaga, P. Ferrari, P. Contiero, G. Frasca, D. Engeset, E. Lund, G. Misirli, M. Kosti, E. Riboli, N. Slimani, and S. Bingham, Eur. J. Clin. Nutr. **63**, S16–S36 (2009): *Intake of total, animal and plant proteins, and their food sources in 10 countries in the European prospective investigation into cancer and nutrition*.

[566] A. Mansouri, J.L. Guéant, J. Capiaumont, P. Pelosi, P. Nabet, and T. Haertlé, BioFactors. **7**, 287–298 (1998): *Plasma membrane receptor for beta-lactoglobulin and retinol-binding protein in murine hybridomas*.

[567] H.C. Liu, W.L. Chen, and S.J.T. Mao, J. Dairy Sci. **90**, 547–555 (2007): *Antioxidant nature of bovine milk β-lactoglobulin*.

[568] G. Brignon, A. Chtourou, and B. Ribadeau-Dumas, J. Dairy Res. **52**, 249–254 (1985): *Does β-Lactoglobulin occur in human milk?*

[569] K.M. Järvinen, P. Chatchatee, L. Bardina, K. Beyer, and H.A. Sampson, Int. Arch. Allergy Immunol. **126**, 111–118 (2001): *IgE and IgG binding epitopes on α-lactalbumin and β-lactoglobulin in cow's milk allergy*.

[570] Z. Teng, Y. Luo, Y. Li, and Q. Wang, Food Chem. **204**, 391–399 (2016): *Cationic beta-lactoglobulin nanoparticles as a bioavailability enhancer: Effect of surface properties and size on the transport and delivery in vitro*.

[571] T.T. Reddy, L. Lavenant, J. Lefebvre, and D. Renard, Biomacromolecules. **7**, 323–330 (2006): *Swelling behavior and controlled release of theopylline and sulfamethoxazole drugs in β-lactoglobulin protein gels obtained by phase separation in water/ethanol mixture*.

[572] A.S. McAlpine, and L. Sawyer, Biochem. Soc. Trans. **18**, 879 (1990): *β-lactoglobulin: a protein drug carrier?*

[573] M. Yvon, J.-P. Pélissier, P. Guilloteau, and R. Toullec, Reprod. Nutr. Dévelopment. **24**, 835–843 (1984): *In vivo milk digestion in the calf abomasum. II. Milk and whey proteolysis*.

[574] R.S.H. Lam, and M.T. Nickerson, Food Chem. **141**, 975–984 (2013): *Food proteins: a review on their emulsifying properties using a structure-function approach*.

[575] W. He, Y. Tan, Z. Tian, L. Chen, F. Hu, and W. Wu, Int. J. Nanomedicine. **6**, 521–533 (2011): *Food protein-stabilized nanoemulsions as potential delivery systems for poorly water-soluble drugs: Preparation, in vitro characterization, and pharmacokinetics in rats*.

[576] M.C. Yang, H.-H. Guan, J.-M. Yang, C.-N. Ko, M.-Y. Liu, Y.H. Lin, Y.-C. Huang, C.-J. Chen, and S.J.T. Mao, Cryst. Growth Des. **8**, 4268–4276 (2008): *Rational design for crystallization of β-lactoglobulin and vitamin D_3 complex: revealing a secondary binding site*.

[577] A.L. Margolin, and M.A. Navia, Angew. Chem. Int. Ed. **40**, 2204–2222 (2001): *Protein crystals as novel catalytic materials*.

[578] R.A. Miller, and R.C. Hoseney, Cereal Foods World. **53**, 4–6 (2008): *Role of salt in baking*.

[579] S. Jeyarajah, and J.C. Allen, J. Agric. Food Chem. **42**, 80–85 (1994): *Calcium binding and salt-induced structural changes of native and preheated β-lactoglobulin*.

[580] M.E. Richert, G.G. Gochev, and B. Braunschweig, Langmuir. **35**, 11299–11307 (2019): *Specific ion effects of trivalent cations on the structure and charging state of β-lactoglobulin adsorption layers*.

[581] J. Verran, Food Bioprod. Process. **80**, 292–298 (2002): *Biofouling in food processing: Biofilm or biotransfer potential?*

[582] J.L. Nilsson, J. Memb. Sci. **36**, 147–160 (1988): *Fouling of an ultrafiltration membrane by a dissolved whey protein concentrate and some whey proteins*.

[583] B.A. Krantz, A.K. Srivastava, S. Nauli, D. Baker, R.T. Sauer, and T.R. Sosnick, Nat. Struct. Biol. **9**, 458–463 (2002): *Understanding protein hydrogen bond formation with kinetic H/D amide isotope effects*.

[584] P. Cioni, and G.B. Strambini, Biophys. J. **82**, 3246–3253 (2002): *Effect of heavy water on protein flexibility*.

[585] M. Blaber, X.J. Zhang, and B.W. Matthews, Science. **260**, 1637–1640 (1993): *Structural basis of amino acid α helix propensity*.

[586] M.J. Parker, and A.R. Clarke, Biochemistry. **36**, 5786–5794 (1997): *Amide backbone and water-related H/D isotope effects on the dynamics of a protein folding reaction*.

[587] G.C. Kresheck, H. Schneider, and H.A. Scheraga, J. Phys. Chem. **69**, 3132–3144 (1965): *The effect of D_2O on the thermal stability of proteins. Thermodynamic parameters for the transfer of model compounds from H_2O to D_2O*.

[588] R. Keith Cannan, A.H. Palmer, and A.C. Kibrick, J. Biol. Chem. **142**, 803–822 (1942): *The hydrogen ion dissociation curve of lactoglobulin*.

[589] C. Tanford, Proc. Iowa Acad. Sci. **57**, 225 (1950): *Interaction between proteins and chloride ion*.

[590] C.W. Carr, Arch. Biochem. Biophys. **46**, 424–431 (1953): *Studies on the binding of small ions in protein solutions with the use of membrane electrodes. IV. The binding of calcium ions in solutions of various proteins*.

[591] G.B. Jameson, J.J. Adams, and L.K. Creamer, Int. Dairy J. **12**, 319–329 (2002): *Flexibility, functionality and hydrophobicity of bovine β-lactoglobulin*.

[592] P.Å. Albertsson, J. Chromatogr. A. **159**, 111–122 (1978): *Partition between polymer phases*.

[593] C. Tanford, J. Mol. Biol. **67**, 59–74 (1972): *Hydrophobic free energy, micelle formation and the association of proteins with amphiphiles*.

[594] M. Rodahl, P. Dahlqvist, F. Höök, and B. Kasemo, The quartz crystal microbalance with dissipation monitoring (QCM-D), in: E. Gizeli, C.R. Lowe (Eds.), Biomol. Sensors, Taylor & Francis, London (2002): pp. 304–316.

[595] F. Höök, B. Kasemo, T. Nylander, C. Fant, K. Sott, and H. Elwing, Anal. Chem. **73**, 5796–5804 (2001): *Variations in coupled water, viscoelastic properties, and film thickness of a Mefp-1 protein film during adsorption and cross-linking: a quartz crystal microbalance with dissipation monitoring, ellipsometry, and surface plasmon resonance study*.

[596] W. Kunz, Curr. Opin. Colloid Interface Sci. **15**, 34–39 (2010): *Specific ion effects in colloidal and biological systems*.

[597] H. Susi, and D.M. Byler, Appl. Spectrosc. **42**, 819–826 (1988): *Fourier deconvolution of the amide I Raman band of proteins as related to conformation*.

[598] H. Hähl, F. Evers, S. Grandthyll, M. Paulus, C. Sternemann, P. Loskill, M. Lessel, A.K. Hüsecken, T. Brenner, M. Tolan, K. Jacobs, A.K. Hüsecken, T. Brenner, M. Tolan, and K. Jacobs, Langmuir. **28**, 7747–7756 (2012): *Subsurface influence on the structure of protein adsorbates as revealed by in situ X-ray reflectivity*.

[599] A. Kato, T. Matsuda, N. Matsudomi, and K. Kobayashi, J. Agric. Food Chem. **32**, 284–288 (1984): *Determination of protein hydrophobicity using a sodium dodecyl sulfate binding method*.

[600] M. Stamm, 1st ed. Springer Berlin Heidelberg, (2008): *Polymer surfaces and interfaces- characterization, modification and applications*.

[601] L. Schmüser, N. Encinas, M. Paven, D.J. Graham, D.G. Castner, D. Vollmer, H.J. Butt, and T. Weidner, Biointerphases. **11**, 031007 (2016): *Candle soot-based super-amphiphobic coatings resist protein adsorption*.

[602] P. Harder, M. Grunze, R. Dahint, G.M. Whitesides, and P.E. Laibinis, J. Phys. Chem. B. **102**, 426–436 (1998): *Molecular conformation in oligo(ethylene glycol)-terminated self-assembled monolayers on gold and silver surfaces determines their ability to resist protein adsorption*.

[603] R.L.C. Wang, H.J. Kreuzer, and M. Grunze, J. Phys. Chem. B. **101**, 9767–9773 (1997): *Molecular conformation and solvation of oligo(ethylene glycol)-terminated self-assembled monolayers and their resistance to protein adsorption*.

[604] A.L. Eckermann, D.J. Feld, J.A. Shaw, and T.J. Meade, Coord. Chem. Rev. **254**, 1769–1802 (2010): *Electrochemistry of redox-active self-assembled monolayers*.

[605] C. Vericat, M.E. Vela, G. Benitez, P. Carro, and R.C. Salvarezza, Chem. Soc. Rev. **39**, 1805–1834 (2010): *Self-assembled monolayers of thiols and dithiols on gold: new challenges for a well-known system*.

[606] A. Ithurbide, I. Frateur, A. Galtayries, and P. Marcus, Electrochim. Acta. **53**, 1336–1345 (2007): *XPS and flow-cell EQCM study of albumin adsorption on passivated chromium surfaces: Influence of potential and pH*.

[607] T.E. Benavidez, and C.D. Garcia, Langmuir. **29**, 14154–14162 (2013): *Potential-assisted adsorption of bovine serum albumin onto optically transparent carbon electrodes*.

[608] Q. Xie, C. Xiang, Y. Yuan, Y. Zhang, L. Nie, and S. Yao, J. Colloid Interface Sci. **262**, 107–115 (2003): *A novel dual-impedance-analysis EQCM system - investigation of bovine serum albumin adsorption on gold and platinum electrode surfaces*.

[609] B. Beykal, M. Herzberg, Y. Oren, and M.S. Mauter, J. Colloid Interface Sci. **460**, 321–328 (2015): *Influence of surface charge on the rate, extent, and structure of adsorbed bovine serum albumin to gold electrodes*.

[610] R. Sprycha, J. Colloid Interface Sci. **102**, 173–185 (1984): *Surface charge and adsorption of background electrolyte ions at anatase/electrolyte interface*.

[611] A.S. Barnard, and L.A. Curtiss, Nano Lett. **5**, 1261–1266 (2005): *Prediction of TiO_2 nanoparticle phase and shape transitions controlled by surface chemistry*.

[612] R. Maier, G. Zocher, A. Sauter, S. Da Vela, O. Matsarskaia, R. Schweins, M. Sztucki, F. Zhang, T. Stehle, and F. Schreiber, Cryst. Growth Des. **20**, 7951-7962 (2020): *Protein crystallization in the presence of a metastable liquid-liquid phase separation*.

[613] P.J. Flory, J. Chem. Phys. **10**, 51–61 (1942): *Themodynamics of high polymer solutions*.

[614] Y.M. Efimova, S. Haemers, B. Wierczinski, W. Norde, and A.A. Van Well, Biopolymers. **85**, 264–273 (2007): *Stability of globular proteins in H_2O and D_2O*.

[615] A. Mahn, M.E. Lienqueo, and J.C. Salgado, J. Chromatogr. A. **1216**, 1838–1844 (2009): *Methods of calculating protein hydrophobicity and their application in developing correlations to predict hydrophobic interaction chromatography retention*.

[616] M.E. Lienqueo, A. Mahn, and J.A. Asenjo, Mathematical correlations for predicting protein retention times in hydrophobic interaction chromatography, in: J. Chromatogr. A, Elsevier, (2002): pp. 71–79.

[617] A. Kato, and S. Nakai, Biochim. Biophys. Acta. **624**, 13–20 (1980): *Hydrophobicity determined by a fluorescence probe method and its correlation with surface properties of proteins*.

[618] B.H.J. Hofstee, and N.F. Otillio, J. Chromatogr. A. **159**, 57–69 (1978): *Non-ionic adsorption chromatography of proteins*.

[619] D. Sehnal, A.S. Rose, J. Koča, S.K. Burley, and S. Velankar, Eurographics Assoc. **10**, 29-33 (2018): *Mol*: towards a common library and tools for web molecular graphics*.

[620] W.C. Wimley, and S.H. White, Nat. Struct. Biol. **3**, 842–848 (1996): *Experimentally determined hydrophobicity scale for proteins at membrane interfaces*.

[621] B. Jachimska, K. Tokarczyk, M. Łapczyńska, A. Puciul-Malinowska, and S. Zapotoczny, Colloid. Surf. A . **489**, 163–172 (2016): *Structure of bovine serum albumin adsorbed on silica investigated by quartz crystal microbalance*.

[622] K.M.C. Tjørve, and E. Tjørve, PLoS One. **12**, e0178691 (2017): *The use of Gompertz models in growth analyses, and new Gompertz-model approach: an addition to the Unified-Richards family*.

List of Publications

[1] **Multivalent-ion-activated protein adsorption reflecting bulk re-entrant behaviour**

M. R. Fries, D. Stopper, M. K. Braun, A. Hinderhofer, F. Zhang, R. M. J. Jacobs, M. W. A. Skoda, H. Hansen-Goos, R. Roth and F. Schreiber.

Physical Review Letters, 119 (2017) 228001

[2] **Enhanced protein adsorption upon bulk phase separation**.

M. R. Fries, D. Stopper, M. W. A. Skoda, M. Blum, C. Kertzscher, A. Hinderhofer, F. Zhang, R. M. J. Jacobs, R. Roth and F. Schreiber.

Scientific Reports, 10 (2020) 1–9

[3] **Bulk phase behaviour vs interface adsorption: Specific multivalent cation and anion effects on BSA interactions**

M. R. Fries, N. F. Conzelmann, L. Günter, O. Matsarskaia, M. W. A. Skoda, R. M. J. Jacobs, F. Zhang and F. Schreiber.

Langmuir, 37 (2021) 139-150

[4] **Bulk phase behaviour vs interface adsorption: Effects of anions and isotopes on BLG interactions**

M. R. Fries, M. W. A. Skoda, N. F. Conzelmann, R. M. J. Jacobs, R. Maier, N. Scheffczyk, F. Zhang and F. Schreiber.

Under review at *Journal of Colloid and Interface Science*

[5] **Tuneable protein resistance of functionalized surfaces via trivalent ions**

N. F. Conzelmann, M. W. A. Skoda, M. R. Fries, L. Reichart, R. M. J. Jacobs, F. Zhang and F. Schreiber.

In preparation

[6] **About the question of differences and similarities between human and bovine serum albumin in bulk and at interface translating into different crystallization behaviors**

R. Maier, S. da Vela, M. R. Fries, C. Buchholz, P. Rajendran, S. El-Asfar, A. Kikhney, F. Zhang and F. Schreiber.

In preparation

ACKNOWLEDGEMENTS

I use this opportunity to express my gratitude to everyone who supported me during my PhD period. First, I owe my deepest gratitude to Prof. Dr. Frank Schreiber for his constant support, being a mentor, letting me thrive, and making it possible to acquire new skills, providing me with the necessary tools for upcoming challenges.

I would also like to express my very great appreciation to Dr. PD Fajun Zhang and Dr. Alexander Hinderhofer for all the valuable and constructive scientific discussions and experimental ideas concerning the bulk phase behaviour and ellipsometric setup, respectively. I also extend my grateful thanks to my collaborators Dr. Robert Jacobs and Dr. Maximilian Skoda, for our rich discussions and their help during beam times and research visits at Rutherford Appleton Laboratory and the University of Oxford. Their willingness to grant me their time so generously has been very much appreciated. To Prof. Dr. Roland Roth, Dr. Daniel Stopper and Dr. Hendrik Hansen-Goos, I would like to pay my special regards for numerous interesting scientific discussions related to theoretical descriptions of the system investigated. I am immensely proud of the successful establishment of a new model describing the adsorption behaviour.

To all my supervisors, this dissertation would not have been possible without your time, effort and passion for this project and I am more than grateful for the opportunity to work with you and learn from you.

I wish to acknowledge the assistance provided by Prof. Dr. Frank Schreiber, Dr. Robert Jacobs, Dr. Maximilian Skoda, Dr. Alexander Hinderhofer, Dr. Olga Matsarskaia, Simon Schönberg, Nina Conzelmann, Benedikt Sohmen, and Matthias Blum during our numerous beam times at ISIS, ILL, and Diamond, as well as the support by the respective beamline scientists and facility employees.

I would like to thank Dr. Michal Braun for introducing me to the FTIR, Dr. Robert Jacobs for introducing me to single-wavelength ellipsometry, Dr. Maximilian Skoda for introducing me to NR, QCM-D, AFT-FTIR and the preparation of OTS-coatings and Dr. Luke Clifton for providing thiols during our beam times. I wish to thank Ralph Maier and Dr. Olga Matsarskaia for their scientific input regarding the bulk phase behaviour and generous help.

I would like to offer my special thanks to my collaborators, Prof. Dr. Jürgen Geis-Gerstorfer and Prof. Dr. Frank Rupp, for providing me with implant substrates and fascinating scientific discussions in the context of biomaterials and implant modifications, the use of their laboratory and the start of a new interdisciplinary collaboration. To Prof. Dr. Bernd

Speiser, I am grateful for contribution on the electrochemical manipulation of surfaces, as well as providing me with a potentiostat.

To all the students, who contributed to this dissertation, namely Rajat Agarwala, Sevcan Atilgan, Matthias Blum, Christian Exner, Luzie Günter, Amrita das Gupta, Tran Hoang, Christoph Kertzscher, Viktoryia Kim, Ivan Musil, Lara Reichart, Sebastian Rösch, Niels Scheffczyk, Maximilian Senft, Emanual Walter, and especially Nina Conzelmann and Simon Schönberg, I am thankful. Without you, this dissertation would not be as valuable as it is now.

Special thanks go to Bernd Hofferberth and Ralf Zenke, as well as the physical and electronic workshops, for their technical support and clever ideas for experimental setups.

I would particularly like to thank my fellow colleagues for providing me with unforgettable coffee breaks, lunch breaks, and group activities. To Jan Hagenlocher and Clemens Zeiser, I could not have wished for better friends and colleagues to share this experience with.

I am grateful for my proof-readers Nina Conzelmann, Viviane Fries, Anita Girelli, Alessandro Greco, Jan Hagenlocher, Ralph Maier, Frederik Unger, Christoph Theurer, and Clemens Zeiser and the time and effort they invested, which facilitated the finish and quality the dissertation deserved.

To my friends, especially the Nanos, you gave me the motivation to push through and I will always cherish the time together and the support system we established.

Last but not least, my deep and sincere gratitude belongs to my mother and sister for their support and encouragement throughout this process and providing me with the tools I needed to achieve my dreams.